Physics and Design of High-Intensity Circular Accelerators

(June 28, 2002)

(DRAFT)

J. Wei, A. Fedotov, Y. Papaphilippou

Brookhaven National Laboratory

Preface

High-intensity synchrotrons and accumulator rings are essential elements for new-generation accelerator facilities including spallation neutron sources, neutrino factories, and multi-functional applications. This course is to introduce design principle and procedure, beam physics and technology for the high-intensity frontier machines. We will start from the design philosophy and basic functions of the ring and the transport lines, and study machine lattice and optimization, injection and extraction options, and machine aperture determination. We then will emphasize on beam dynamics subjects including space charge, transverse phase space painting, longitudinal beam confinement with single and dual harmonic radio-frequency systems, magnetic nonlinearity and fringe field, and beam collimation. In computer simulation sessions we will study basic tracking and mapping techniques, tune spread and resonance analysis techniques, and statistical accuracy. Finally, we will discuss more advanced topics like transition crossing, intra-beam Coulomb scattering, beam-in-gap cleaning, chromatic and resonance correction, electron cloud effects and instabilities.

Prerequisites: Accelerator fundamentals or Accelerator physics

Contents

1 Introduction

For the five decades since the discovery of the synchrotron [1] and the principle of alternating-gradient focusing [2], the development of accelerator science and technology has sustained exponential growth in both the energy and intensity of the proton beam as shown in the "Livingston chart" ([3, 4] and Figure 1). Combined with an increasing repetition rate, the high proton beam power has extended its use from nuclear and high-energy physics to modern applications including spallation neutron production, kaon factories, nuclear transmutation, energy amplification, neutrino factories and muon collider drivers.

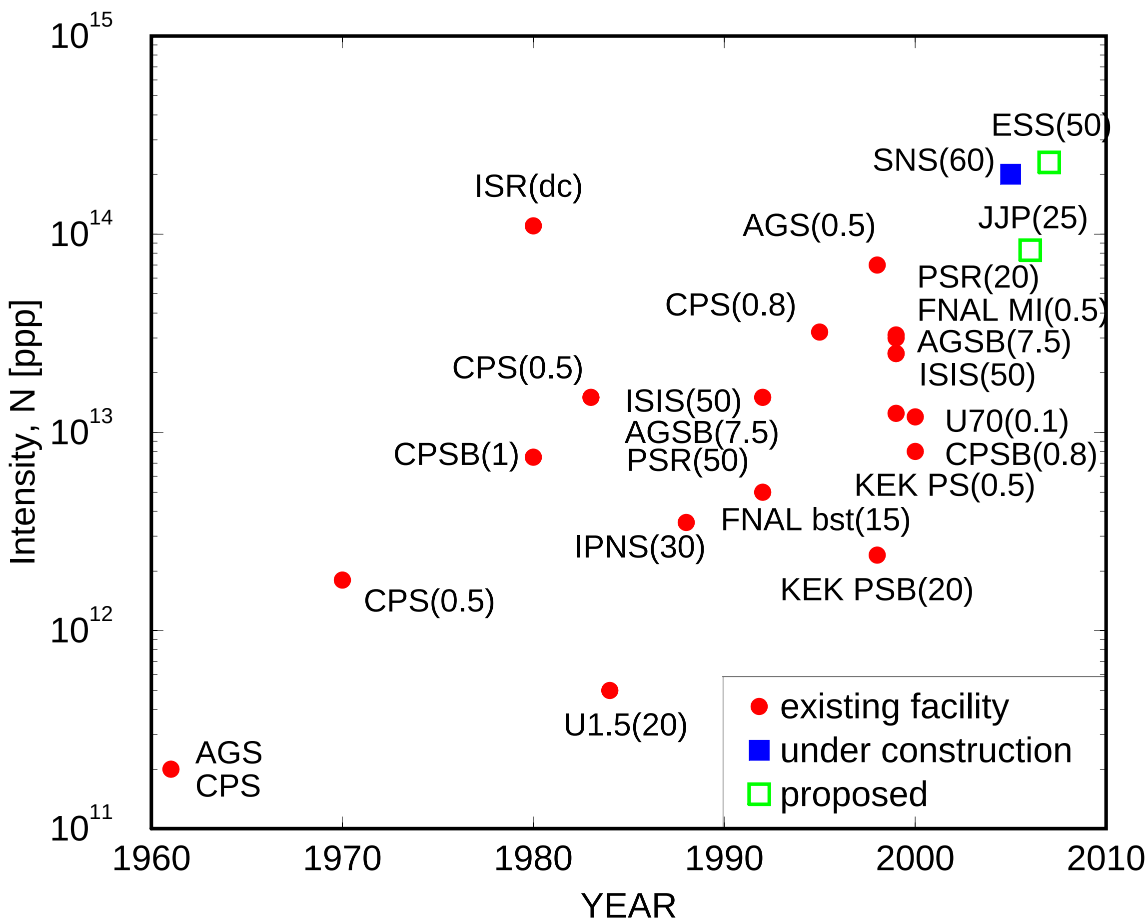

Figure 1: Evolution of ring intensity (particles per pulse). The parentheses indicate repetition rate in Hz.

Several factors have made the use of synchrotrons and accumulators possible for high intensity beams. One is the development of intense, high-duty factor, low emittance H^- and H^+ ion sources. A second is the invention of the Radio-Frequency Quadrupole (RFQ) [5], replacing Cockcroft-Walton as pre-accelerator, combining focusing and acceleration while preserving emittance. A third is the development of linear accelerator technology including permanent magnet quadrupoles for drift-tube linacs and super-conducting technology for operational economy and reliability.

This course discusses mainly the development of synchrotrons and accumulators, emphasizing experiences gained in recent years, current issues, and the future outlook.

1.1 Overview

Generally, there are two types of circular accelerators for high intensity purposes: either an accumulator (LAR) that accepts beams from an injector (usually a full-energy linac) and then compresses them to form pulsed time structure, or a rapid-cycling synchrotron (RCS) that accepts beams from an injector (either a linear accelerator, a cyclotron, or a lower-energy synchrotron) and then compresses and accelerates them to a higher energy.

The LAR scheme has the advantage of a simple ring design with neither field ramping nor acceleration. The time that the beam spends in the ring is relatively short (typically of the order of 1 ms) for many types of instability (e.g. head-tail instability) to fully develop. The field quality of the magnets can be optimized by geometrical compensation at the design excitation current. Therefore, this scheme is often preferred for dedicated high-intensity facilities where beam loss needs to be strictly minimized. Figure 2 shows the schematic layout of the proposed European Spallation Source that consists of a full-energy linac that accelerates the H^- beam to 1.334 GeV, and then two accumulator rings that compress the beam to desired pulsed structure for neutron spallation.

The RCS scheme has the advantage of a lower-cost injector, and the potential for energy and power upgrade by either accelerating to a higher energy or by adding subsequent accelerators. It can also become a good candidate when a bunch of short bunch length is desired (e.g. for neutrino factory and muon collider applications). However, in order to reach a high output power, the entire compression process needs to be completed in a short time (typically in tens of ms). Consequently, a fast ramping is needed demanding a fast magnetic field cycling, a high voltage radio-frequency acceleration system, and a large power supply. Measures needs to be taken to reduce the heating caused by ramping magnetic field without increasing beam coupling impedance caused by the beam image charge. Figure 3 shows the schematic layout of the JAERI/KEK Joint Project under construction at Japan which consists of a 400 MeV linac, a 3 GeV Booster synchrotron, and a 50 GeV synchrotron for multi-purpose applications including nuclear transmutation (linac), neutron spallation (3 GeV ring), and high-energy and nuclear experiments.

Table 1 shows main parameters and machine type of some existing and proposed high-intensity facilities including spallation neutron sources, neutrino-factory proton drivers (NFPD), muon collider drivers, nuclear transmutation, and energy amplifier (EA) [36, 37]. Among them, applications on neutron spallation and neutrino factory/muon collider proton driver are made possible by the high, pulsed beam power achieved with accumulators and rapid-cycling synchrotrons.

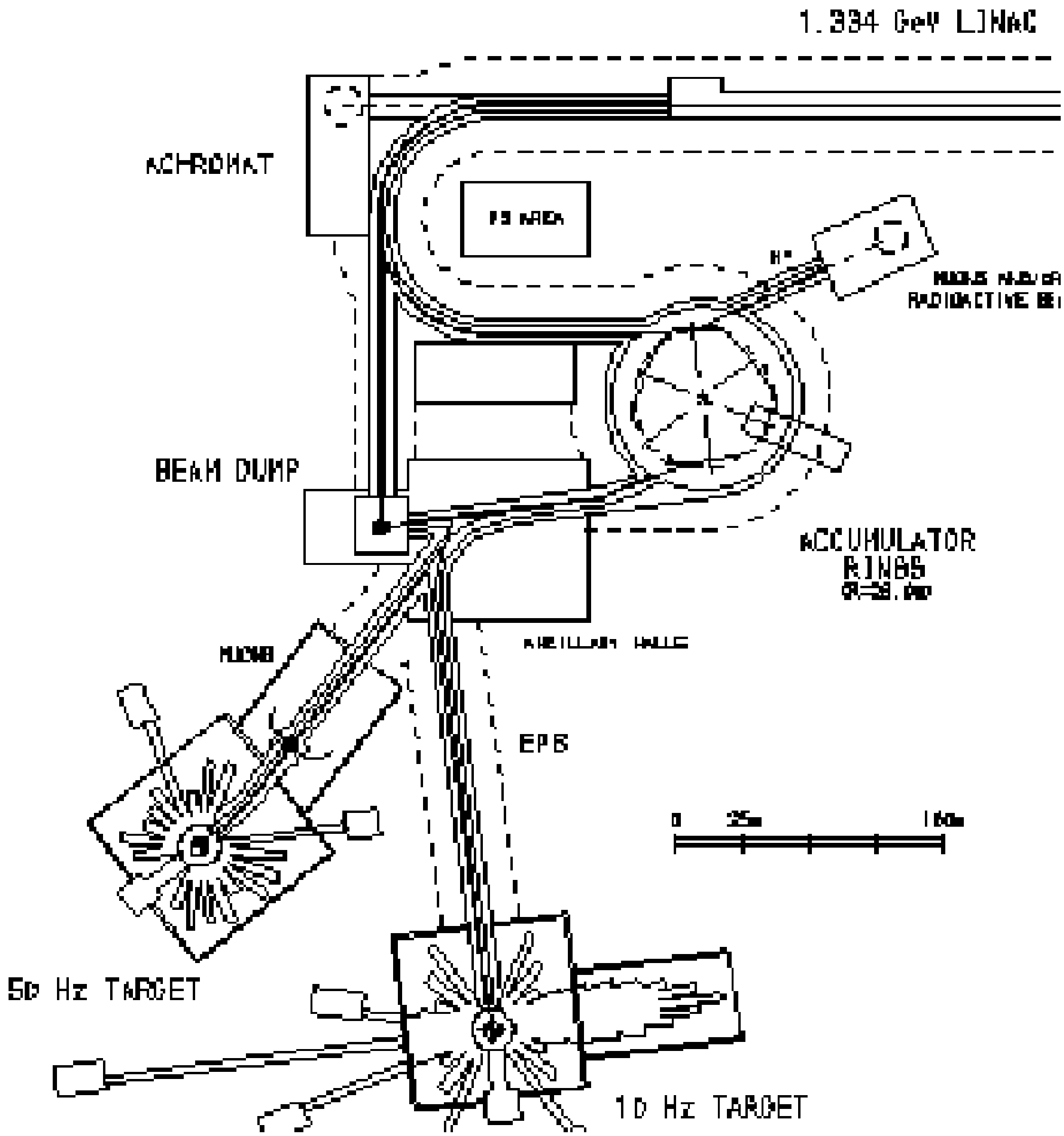

Figure 2: Schematic layout of the proposed European Spallation Source accelerator complex (courtesy G. Rees, C. Prior).

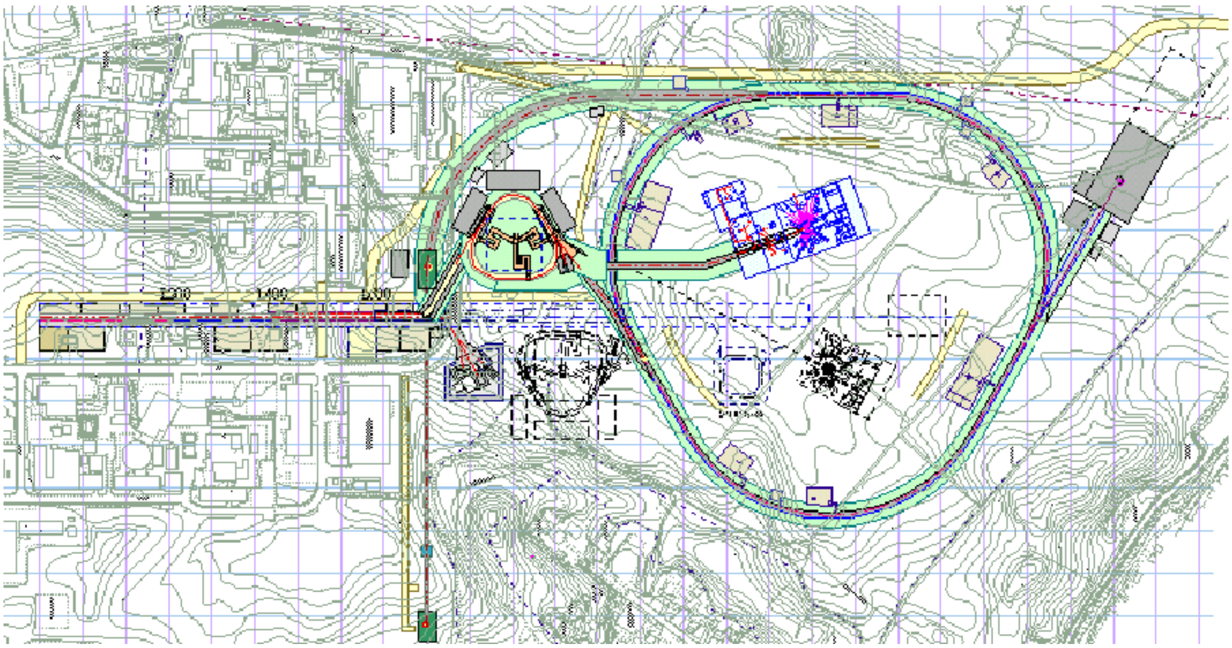

Figure 3: Schematic layout of the proposed JAERI-KEK Joint Project accelerator complex (courtesy Y. Mori, S. Machida).

Table 1: Main parameters of some existing and proposed accelerator-based high-intensity facilities.

Machine	E_k [GeV]	$\langle I \rangle$ [mA]	N_p [ppp]	f_N [Hz]	$\langle P \rangle$ [MW]	Type
Existing:						
LANSCE	0.8		2.3×10^{13}	20	0.07	LAR
ISIS	0.8		2.5×10^{13}	50	0.2	RCS
Proposed:						
JKJ (Japan)	3.0	0.33	8×10^{13}	25	1.0	RCS
SNS (US)	1.0	2	2.1×10^{14}	60	2.0	LAR
ESS (Europe)	1.334	1.8	2.3×10^{14}	50	2.5	LAR (×2)
NFPD (CERN)	2.2	1.8	1.5×10^{14}	75	4	LAR
NFPD (RAL/CERN)	5	0.4	1×10^{14}	25	2	RCS (×2)
NFPD (FNAL)	16	0.125	5×10^{13}	15	2	RCS (×2)
Energy Amplifier	1	10/20	CW	CW	10/20	Cyclotron
APT (LANL)	1.03	100	CW	CW	103	Linac
TRISPAL (CEA)	0.6	40	CW	CW	24	Linac
ADTW (LANL)	0.6/1.2	20/50	CW	CW	> 20	Linac
μ collider PD	30	0.25		15	7.5	RCS

1.2 Beam Power, Current, Time Structure

The usefulness of a high intensity beam is usually measured by the average beam power. The average beam power is defined as the product of the average current of the beam and the kinetic energy of the beam particle.

$$\langle P \rangle \quad [\mathrm{W}] \ = E_k \ \langle I \rangle \ \ [\mathrm{V}\cdot\mathrm{A}] \ = f_N \ N_p \ e \ E_k \quad [\mathrm{s}^{-1}\cdot\mathrm{C}\cdot\mathrm{V}] \tag{1}$$

The average current $\langle I \rangle$ of the accelerator facility introduced above (not to be confused with the average current of the ring) is the product of the number of electrical charge per beam pulse, and the repetition rate f_N of the pulse. The repetition rate, defined as the number of ring machine cycle per unit time, describes the speed of ramping of the accelerator systems (magnet, RF, injection, extraction). Figure 4 shows the time structure of a typical pulsed beam injected from linac observed at locations upstream of ring injection and downstream of ring extraction, respectively. In this example, the repetition rate is 60 Hz. Within each cycle, the time period of ring injection is 1 ms, or 1000 revolution periods. The beam revolution frequency in the ring is 1 MHz. The beam is compressed from the original length of 1 ms to 1μs. Here in the ring, each beam pulse consists of two bunches confined by the RF system.

The average current $\bar{I}$ of the ring is defined as

$$\bar{I} = N e f_s \tag{2}$$

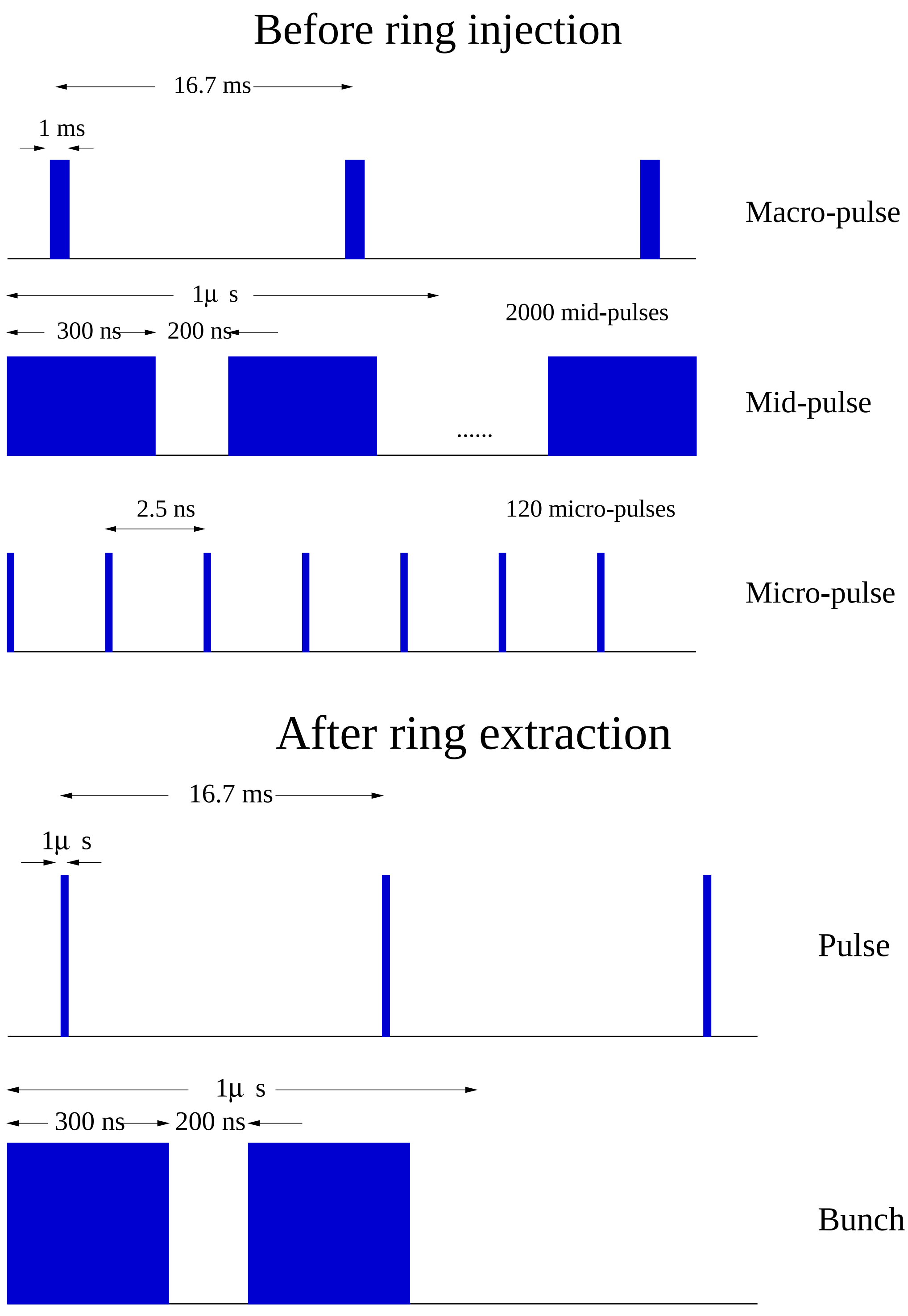

Figure 4: Typical time structure of beam pulses before ring injection and after ring extraction.

where N is the number of charged particle per pulse, e is the electrical charge, and f_s is the synchronous revolution frequency. The peak current $\hat{I}$ of the ring refers to the instantaneous value of the ring current. The bunching factor B is defined as the ratio between the average and the peak current,

$$B = \bar{I}/\hat{I} \leq 1. \tag{3}$$

A high bunching factor is desirable in minimizing peak space charge tune shift and in avoiding instabilities.

1.3 Beam loss, Radiation, Activation, Protection

The primary concern in the design of high-intensity proton facilities is that radio-activation caused by uncontrolled beam loss can limit a machine's availability and maintainability. Typically, hands-on maintenance requires a residual activation level no more than 1 mSv per hour (1 Sievert = 100 rem). Table 2 shows the significance of radiation exposure.

Exposure	Significance
3.5 Sv	50% chance of survival
$>$ Sv	Serious to lethal
$>$ 50 mSv	Requiring medical checks
50 mSv.y^{-1}	Occupational dose limit
15 – 50 mSv.y^{-1}	Strict dose control necessary
5 - 15 mSv.y^{-1}	Professional exposure
$<$ 5 mSv.y^{-1}	Minimum control necessary
1 mSv.y^{-1}	Natural background
10 μSv.y^{-1}	Insignificant

Table 2: Guidelines to the significance of exposure to radiation.

Based on both measurement and computer simulation, it is concluded that a beam loss of 1 Watt beam power per tunnel meter corresponds to a residual radiation exposure of about 1 mSv per hour, measured at a distance of 30 cm from the surface, 4 hours after the shut-down of the machine after a long period (one month or so) of operation. For a facility of 2 MW power, a 1 mSv/h level requires an uncontrolled fractional beam loss of below 0.5×10^{-6} per meter. For a ring of circumference of 200 meters, this corresponds to a total uncontrolled fractional loss of about 10^{-4}.

Figure 5 shows a schematic layout of the Spallation Neutron Source accelerator complex. It accelerates H^- beams from the front end (H^- ion source, Low-Energy-Beam-Transport, RFQ, Medium-Energy-Beam-Transport) through a 1 GeV full-energy linac (Drift-Tube-Linac, Coupled-Cavity Linac, Superconducting RF Linac) and delivers through the High-Energy-Beam-Transport to an accumulator ring, and then strips and compresses the proton beams and delivers through a Ring-Target-Beam Transport to a liquid Mercury target for neutron spallation.

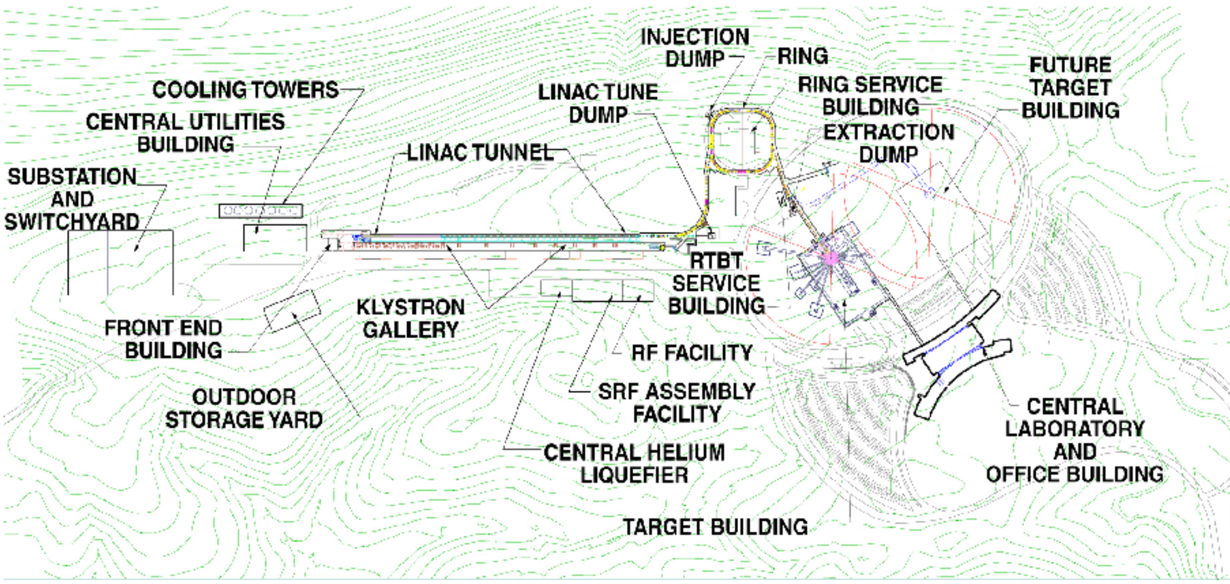

Figure 5: Schematic layout of the Spallation Neutron Source accelerator complex.

Figure 6 shows the estimated distribution of uncontrolled beam loss. For detailed description of this plot see [163]. Some discussion of typical beam loss sources in the ring is provided as a special topic.

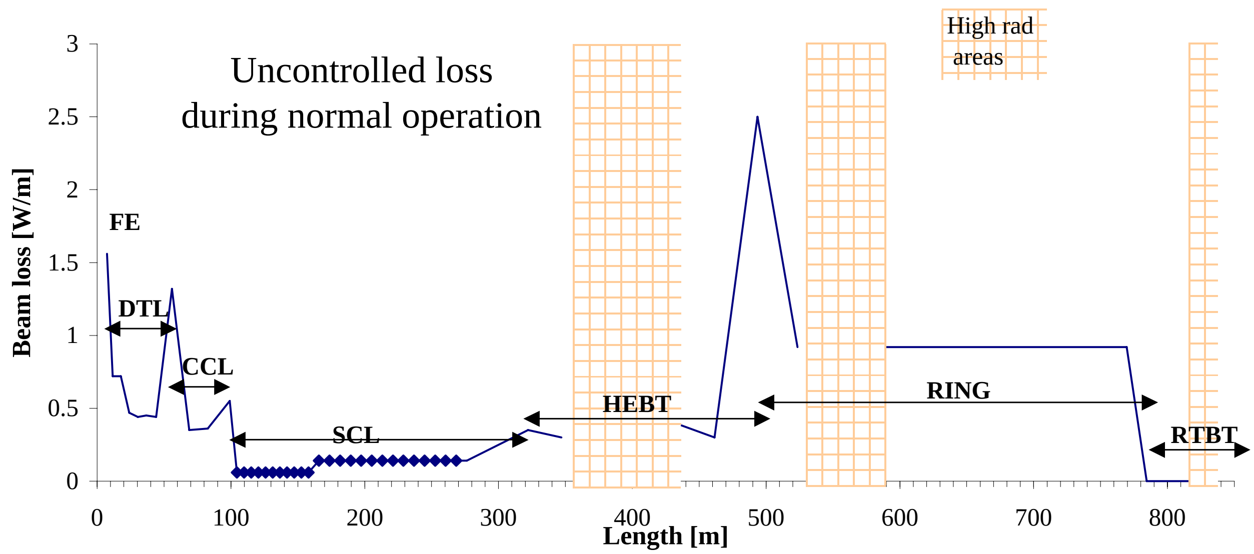

Figure 6: Expected distribution of uncontrolled beam loss.

Problem 1.1 Evaluate beam power on target of a two-ring RCS, and the average allowed beam loss ...

1.4 Design Philosophy

Existing proton synchrotrons and accumulators have beam losses as high as several tens of percent, mostly occurring at injection, capture, initial ramping, transition crossing, and through instabilities. The lowest beam loss is about 3×10^{-3}, achieved at the Proton Storage Ring (PSR) at the Los Alamos National Laboratory [7]. Uncontrolled beam losses are usually attributed to (1) a high space-charge tune shift (0.25 or larger) at injection resulting in resonance crossing; (2) limited physical and momentum acceptance; (3) premature H^- and H^0 stripping and injection foil scattering; (4) large magnet field errors, misalignments and dipole-quadrupole matching errors during ramping; (5) instabilities (*e.g.* head-tail instability, coupled bunch instability, negative mass and microwave instability, PSR instability); and (6) accidental beam loss (ion source and linac malfunction, extraction kicker mis-fire, etc.).

A low-loss design or upgrade must address the above issues. Furthermore, with a large transverse and momentum aperture, multi-stage collimation and momentum cleaning can be incorporated to localize beam loss to shielded locations. Flexibility and robustness (tune adjustment, injection option, ramp-dependent correction, adjustable collimation, foil interchange, spare interchange) need to be reserved for commissioning and operation, and engineering reliability (heat and radiation resistance) and availability (a foil interchange mechanism, quick-disconnect flanges, crane, etc.) need to be addressed at an early design stage.

2 Design Topics

This chapter discusses design aspects of high-intensity rings.

2.1 Key parameters

2.1.1 Ion species

The choice is typically between proton and H^- beam. The advantage of a H^- beam upon ring injection is that multi-turn injection can be effectively facilitated to increase the transverse beam size and to reduce the space charge effects.

Complications caused by using a H^- beam include ionization and magnetic stripping, as well as availability of high-output H^- ion source.

2.1.2 Kinetic energy

The energy range is largely determined by the need of target experiments and the power of applications. From the accelerator point of view, a higher injection energy alleviates space-charge effects by enhancing electro-magnetic force cancellation. A higher extraction energy increases output beam power, and reduces heating on target (longer stopping length). On the other hand, a higher injection energy implies a higher cost on the injector, and demands a lower magnetic field to minimize magnetic stripping and thus even longer magnet length for beam guiding and focusing. A higher extraction energy implies a higher magnetic field, a faster ramping power supply and RF voltage, and demanding field quality control.

2.1.3 Repetition rate

The repetition rate is an important quantity especially for a rapid-cycling synchrotron. It determines the power supply of the magnet system, the peak voltage of the RF system, the achievable magnetic field saturation error and eddy-current error, and the required RF shielding to avoid vacuum chamber heating without increasing the coupling impedance. For an accumulator, the constraint is more from the pre-injector performance (ion source and linac duty cycle, klystron power ...) and less from the ring itself (RF beam loading, injection and extraction kicker power supply ...).

2.1.4 Intensity and bunch length

The bunch length is often pre-determined by the demands of the experiments or applications. From the accelerator point of view, a beam gap must be reserved before the beam is extracted from the ring. This beam gap can be achieved using a radio-frequency system, either confining the beam to the center part of the Rf bucket, or by intentionally leaving empty some RF buckets when the harmonic number of the RF system is much larger than one.

The intensity of the pulse is usually limited by space-charge constraints and instability limits. The intensity of the bunch is partly determined by the bunch length needs, and partly determined by requirements from single-bunch effects (e.g. intra-beam scattering). When the bunch length is not critically defined by the applications, the choice of the number of bunches in the ring is often balanced by the availability of the RF system at specified frequency, the easiness of extraction, the complication of possible coupled-bunch instability, the beam-gap cleaning needs.

2.1.5 Emittance

Unlike an electron machine where synchrotron radiation can cause emittance reduction, in a typical proton or ion accelerator the beam emittance can not be easily reduced. (Beam cooling for high-intensity beam usually takes a long time, not compatible with the usual rapid cycling rate.) Therefore, emittance preservation is usually important.

The transverse beam emittance is often pre-determined by the application's needs. In the case that output emittance is not critical (like neutron spallation applications), a large emittance is often used to reduce space-charge effects. In such cases, the constraint is from practical considerations such as magnet aperture, field, and power supply requirements.

The longitudinal beam emittance is a product of the bunch length and momentum spread. The momentum spread is often limited by the chromatic property of the ring.

2.2 Layout

Modern high-intensity ring is often designed with transport lines that prepares the beam for ring injection, and delivers the beam for final applications.

2.2.1 Transport lines

Figure 7 shows the layout of transport lines for a ring. The transport line that leads the beam to the ring plays the crucial role of transverse and momentum halo cleaning, momentum jitter correction, possibly longitudinal and transverse painting, injection optics matching and optimization, and diagnostics. The transport line that leads the beam from the ring plays the role of accidental damage protection. The various beam dumps are necessary for staged commission, routine operation (injection dump) and machine studies during operation.

2.2.2 Ring

Figure 8 illustrates the layout of a typical ring for high-intensity applications [8]. In order to facilitate robust injection, collimation, and extraction, long uninterrupted straight sections are often preferred. In this example, four straight sections are designed for injection, collimation, radio-frequency (RF) system, and extraction, respectively. For synchrotrons with high repetition rate, long sections are often occupied by radio-frequency cavities.

Double-ring arrangement is sometimes used to alleviate the intensity burden on each ring. For example, the European Spallation Source was designed with two vertically stacked rings of same geometry sharing the same tunnel. The advantage of a two-ring design includes machine availability in the case of component failure, possible savings of tunnel length and machine aperture in comparison with one-ring design of similar performance, and possible sharing of hardware like power supplies. The disadvantage includes complications in installation,

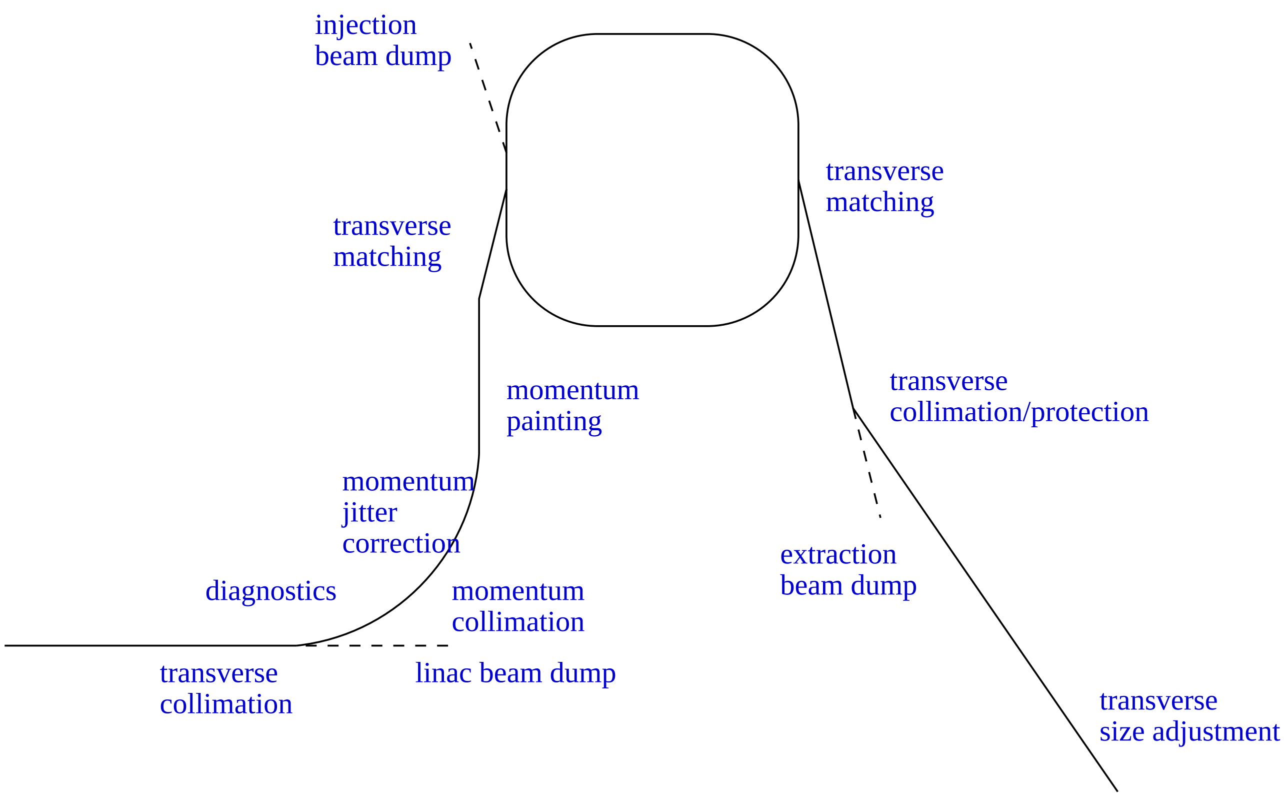

Figure 7: Possible layout and functions of transport lines for a ring.

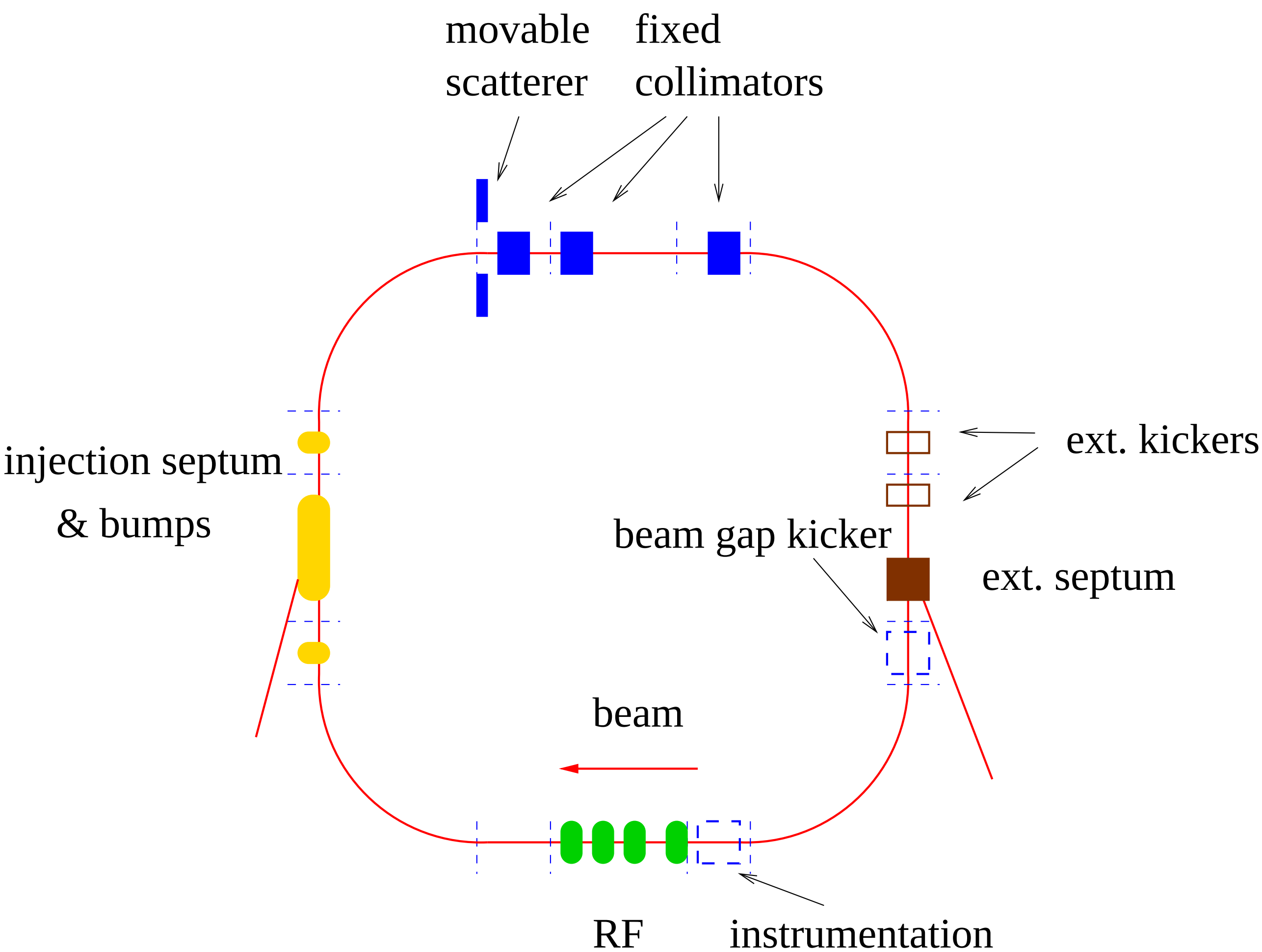

Figure 8: Schematic layout of the Spallation Neutron Source (SNS) accumulator ring.

engineering (e.g. magnet support), and maintenance in a double-ring structure, as well as the net summation of beam loss and activation from both rings.

2.3 Lattice

The lattice is the back-bone of a ring. Recently designed ring lattices often prefer separate-function magnets instead of combined-function magnets for robustness. Tunes are often split by at least half to reduce space-charge coupling and suppress systematic skew quadrupole components.

A traditional choice is the FODO and its variations. FODO structures require modest quadrupole gradients, and the alternating transverse beam amplitudes easily accommodate correction systems. With various arrangements of dipoles, one can create dispersion-free regions for injection, extraction, and RF systems [9, 10], and low momentum compaction to avoid transition crossing [9].

A lattice consisting of doublets/triplets has the advantage of long uninterrupted drifts for flexible injection and optimal collimation. Synchrotrons of this structure also have fewer vacuum chambers and joints [11].

The SNS accumulator ring adopts a hybrid structure with FODO arcs and doublet straights. It combines the FODO structure's simplicity and ease of correction with the doublet structure's long drift (12.5 m) for flexibility [8]. The arcs and straights are optically matched to ensure maximum betatron acceptance. A horizontal phase advance of 360° across each arc makes the straights dispersion free. Each dipole is centered between two quadrupoles so as to maximize the vertical acceptance of the dipoles.

2.3.1 Arc

The most common structure is separate function focusing-drift-focusing-drift, or FODO structure. Using the thin-lens approximation, we can express Courant-Snyder amplitude function $\beta_{x,y}$, $\alpha_{x,y}$, and dispersion $D_{x,y}$ in terms of betatron phase advance per cell μ_c, cell length L_c, and bending angle of the whole cell ϕ_c. The maximum (+) and minimum (−) value of these functions are

$$\beta^{\pm} = \frac{L_c(1 \pm \sin\frac{\mu_c}{2})}{\sin\mu_c} \tag{4}$$

$$\alpha^{\pm} = \frac{\mp 1 - \sin\frac{\mu_c}{2})}{\cos\frac{\mu_c}{2}} \tag{5}$$

$$D^{\pm} = \frac{L_c\phi_c(1 \pm \frac{1}{2}\sin\frac{\mu_c}{2})}{4\sin^2\frac{\mu_c}{2}} \tag{6}$$

The natural chromaticity per FODO cell is

$$\xi_{FODO} = -\frac{1}{\pi}\tan\frac{\mu_c}{\pi} \tag{7}$$

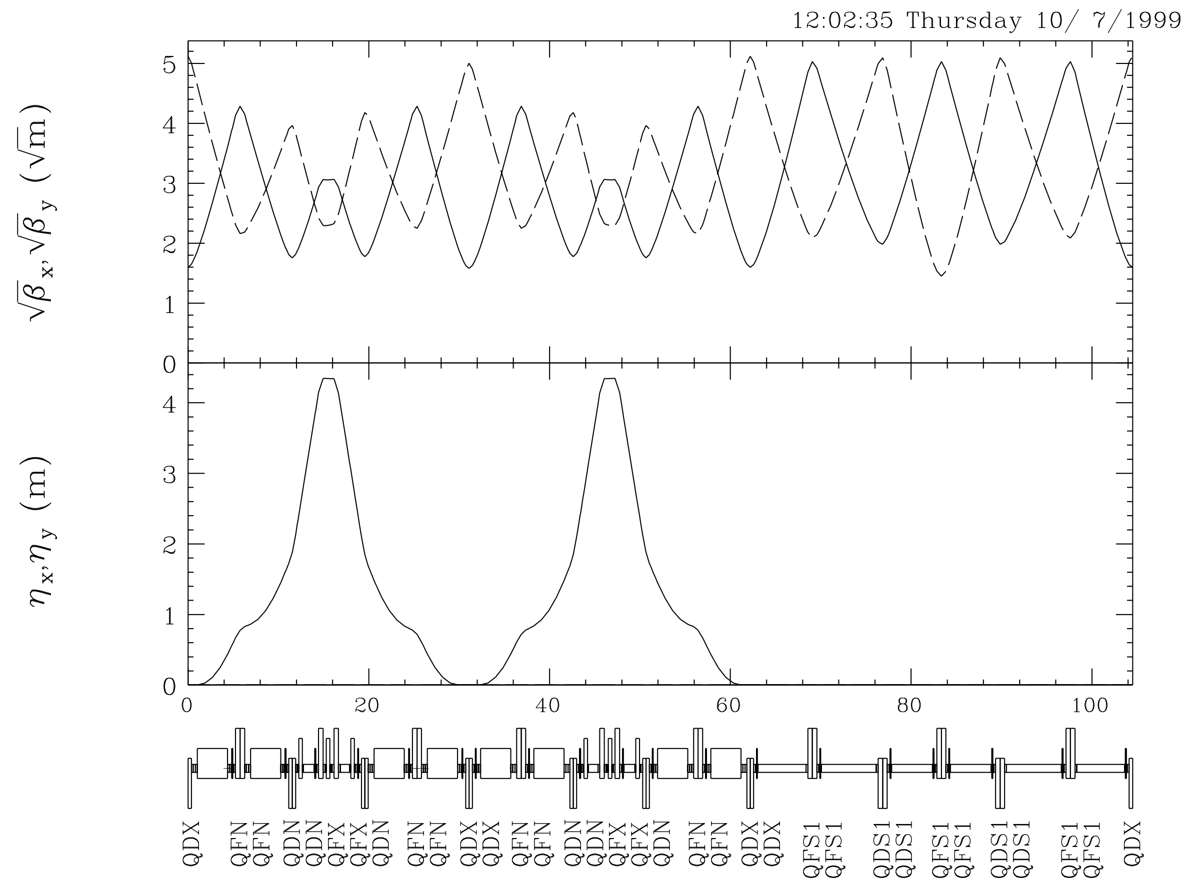

Figure 9: JAERI-KEK Joint Project (JKJ) 3-GeV ring lattice super-period (courtesy S. Machida) of FODO structure. The machine super-periodicity is 3. The split quadrupole creates high-dispersion drift for momentum halo scraping and chromatic adjustment.

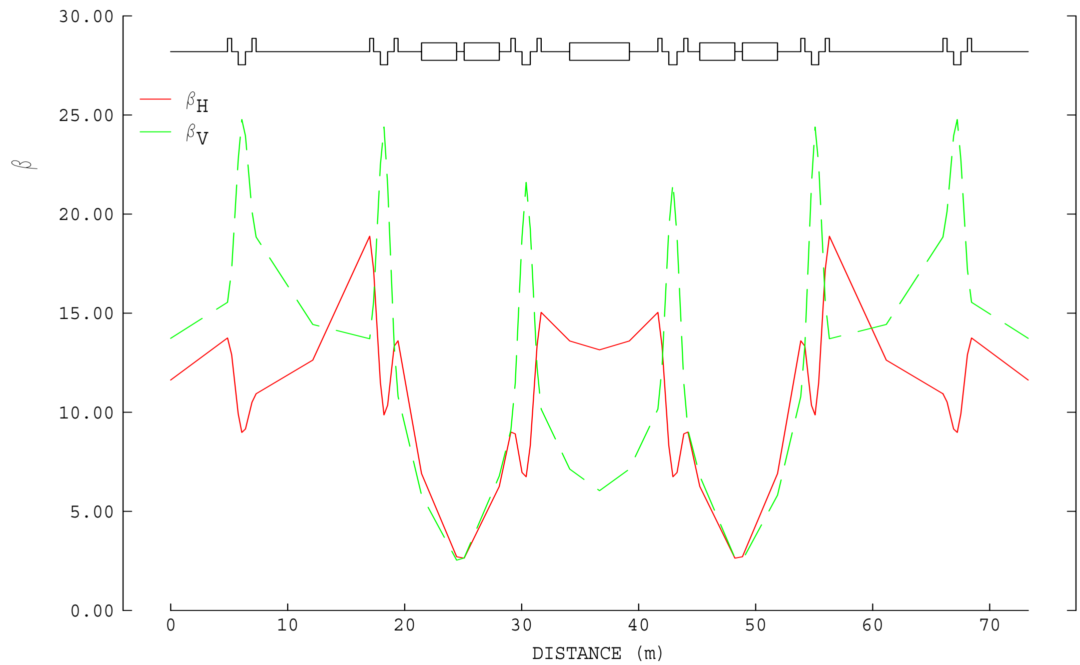

(a) β-functions

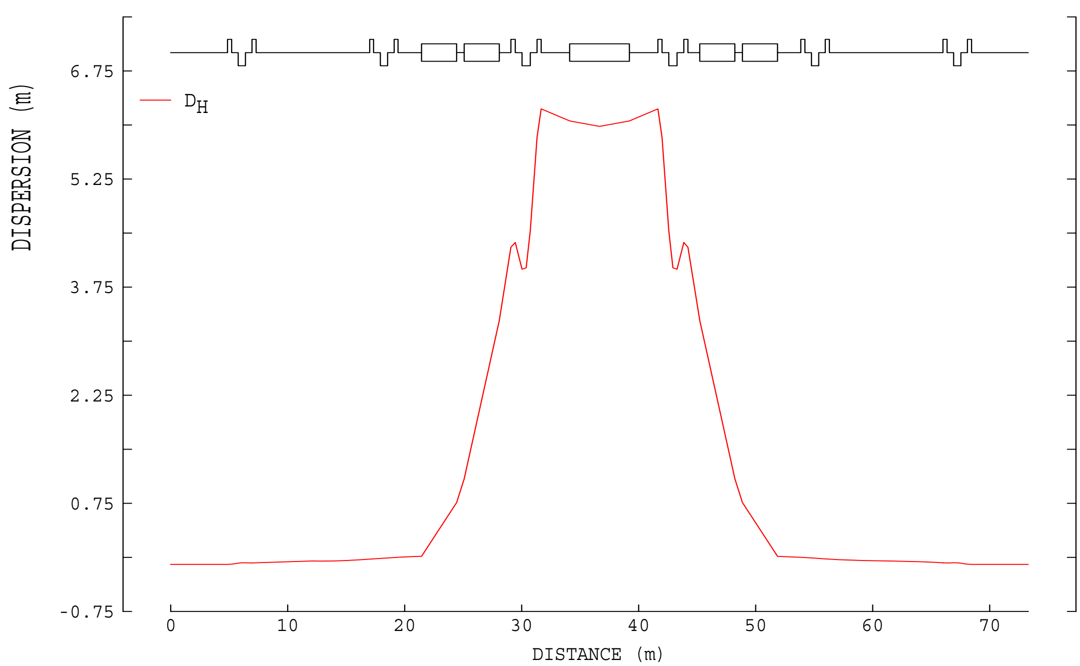

(b) Dispersion function

Figure 10: European Spallation Source (ESS) ring lattice super-period (courtesy G.H. Rees and C.R. Prior) of triplet structure. The machine super-periodicity is 3.

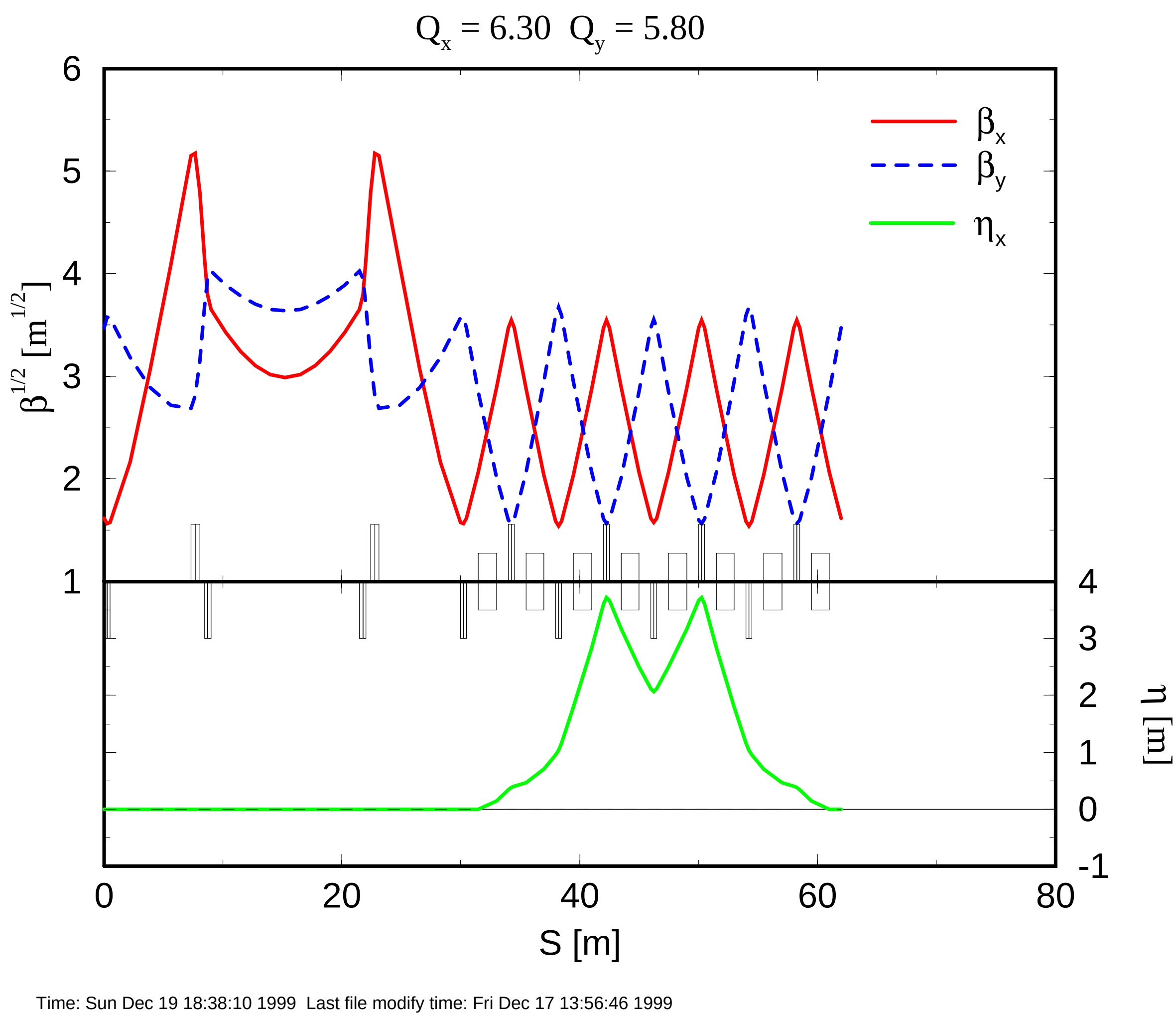

Figure 11: SNS ring lattice super-period of FODO/doublet structure. The machine super-periodicity is 4.

The cell length L_c is usually determined by the drift space needed to accommodate magnets and instruments. The bending angle ϕ_c is usually determined by the overall ring geometry. Normalized to these quantities, Figure 12 shows the dependence of key lattice figure of merits on the cell phase advance. As a design guideline, we usually prefer a low β^+ to maximize betatron acceptance, a low dispersion to maximize momentum acceptance, and a low β^+/β^- ratio to avoid possible beam halo generation. The maximum β-function β^+/L_c reaches a minimum at $\mu_c/2\pi = 0.21$. Typically, phase advance $\mu_c/2\pi$ is selected to be between 0.16 and 0.25 (60 to 90 degrees per cell).

2.3.2 Dispersion suppressor

The goal of dispersion suppression is to eliminate dispersion in the straight section without affecting α and β in the arc. Dispersion suppression for the straight section can be achieved either by a choice of horizontal phase advance of the arc, or by dedicated dispersion suppression insertions.

Achromat By simply locking the total horizontal phase advance across each arc to an integer number of 2π, the dispersion becomes zero outside of the arc. The advantage of this scheme is that the arc is compact, not containing any dispersive drift spaces. The disadvantage of this scheme is the lack of arc tuneability in the horizontal direction.

As shown in Figure 11, the arc achromat consists of 4 DOFO cells with horizontal phase advance $\mu_c = \pi/2$. An alternative is to use 4 FODO cells with the same phase advance per cell. In the later case, the peak dispersion is increased by about 10%.

Suppressor insertion Dispersion suppression using a dedicated insertion is another possibility. A common method is the so-called half-field scheme. By halving the bending kick, a forced dispersion oscillation is launched around half of the FODO value. After a half wavelength, both D and D' are brought to zero.

To illustrate the principle, we consider suppressing the dispersion in M FODO cells. Starting from a zero-dispersion point ($s = 0$) where $D = D' = 0$. The dispersion after M cells can be written as

$$D(ML_c) = S(ML_c)\int_0^{ML_c} \frac{C(s)}{\rho(s)}ds - C(ML_c)\int_0^{ML_c} \frac{S(s)}{\rho(s)}ds \tag{8}$$

$$D'(ML_c) = S'(ML_c)\int_0^{ML_c} \frac{C(s)}{\rho(s)}ds - C'(ML_c)\int_0^{ML_c} \frac{S(s)}{\rho(s)}ds \tag{9}$$

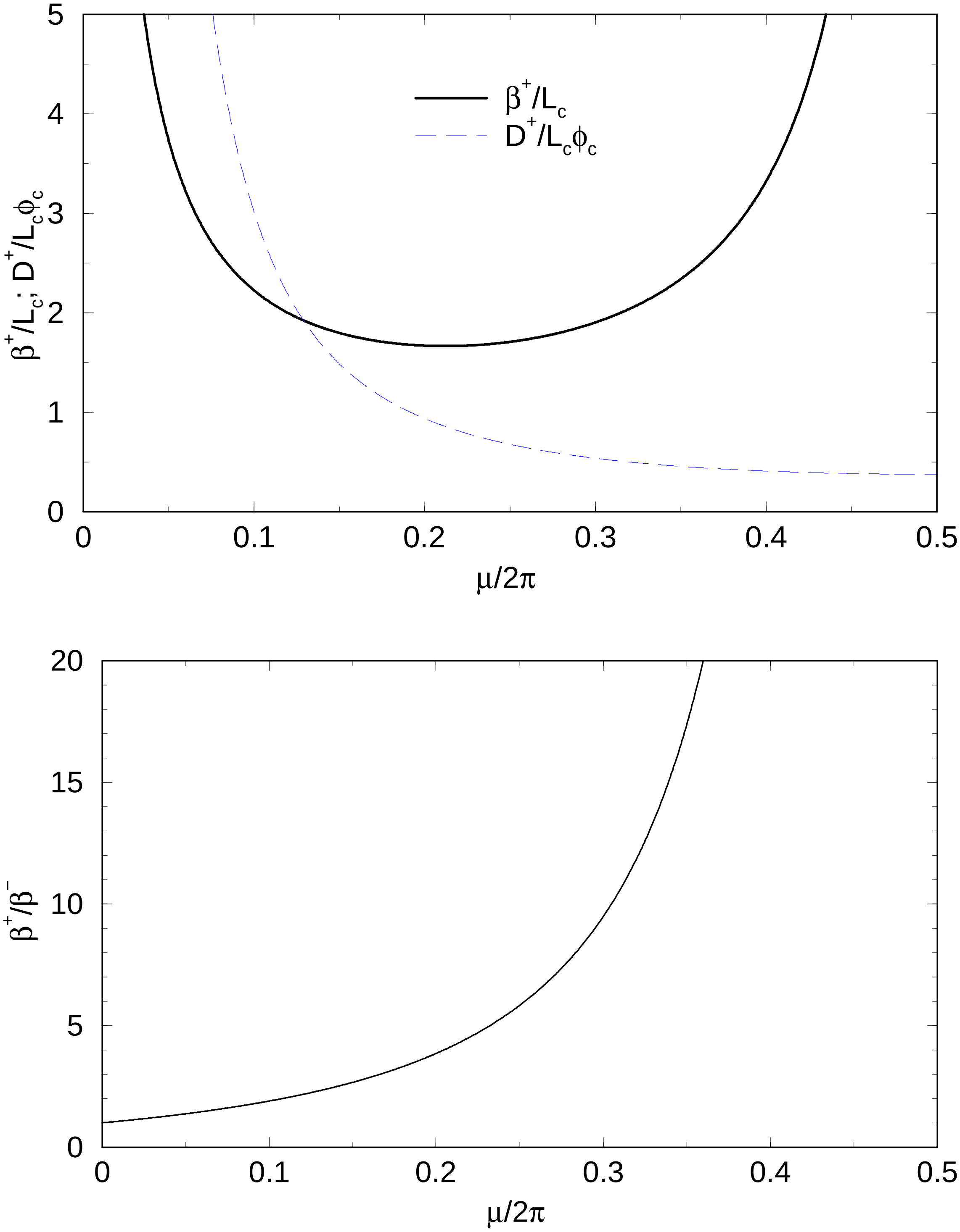

Figure 12: Dependence of Courant-Snyder functions on the phase advance per FODO cell.

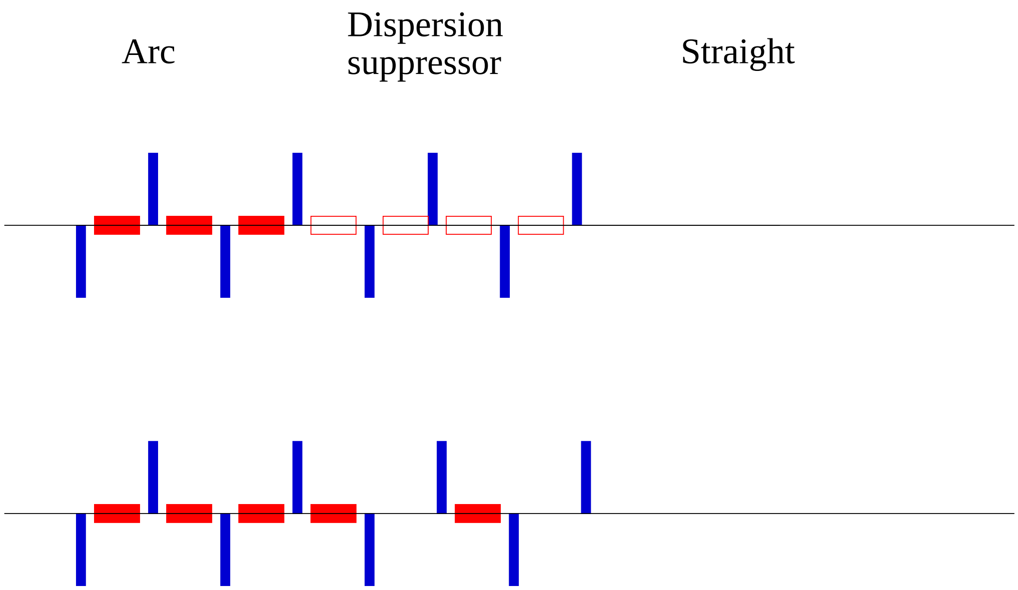

Figure 13: Schematic layout of half-field dispersion suppressors when the betatron phase advance per FODO cell is $\pi/2$.

where C, S, C', S' are components of transfer matrices from point 0 to s,

$$
\begin{aligned}
M(s|0) &= \begin{pmatrix} C(s) & S(s) \\ C'(s) & S'(s) \end{pmatrix} \\
&= \begin{pmatrix} \frac{\beta(s)}{\beta(0)}(\cos\Delta\mu + \alpha(0)\sin\Delta\mu) & \sqrt{\beta(s)\beta(0)}\sin\Delta\mu \\ \\ -\frac{1+\alpha(0)\alpha(s)}{\sqrt{\beta(0)\beta(s)}}\sin\Delta\mu + \frac{\alpha(0)-\alpha(s)}{\sqrt{\beta(0)\beta(s)}}\cos\Delta\mu & \sqrt{\frac{\beta(0)}{\beta(s)}}(\cos\Delta\mu - \alpha(s)\sin\Delta\mu) \end{pmatrix}
\end{aligned}
\tag{10}
$$

and

$$
\begin{aligned}
M(ML_c|0) &= \begin{pmatrix} C(ML_c) & S(ML_c) \\ C'(ML_c) & S'(ML_c) \end{pmatrix} \\
&= \begin{pmatrix} \cos(M\mu_c) & \beta(0)\sin(M\mu_c) \\ \\ -\beta^{-1}(0)\sin(M\mu_c) & \cos(M\mu_c) \end{pmatrix}
\end{aligned}
\tag{11}
$$

The condition $D' = 0$ after a half-wavelength oscillation is satisfied if

$$M\mu_c = \pi \tag{12}$$

That is, the dispersion can be suppressed by π/μ_c FODO cells. If the arc phase advance per FODO cell is $\mu_c = \pi/2$, then 2 FODO cells are needed, as shown in Figure 13. A half-field kick can be realized either by using half-field dipole magnets for bending, or by simply omitting the dipole magnet in one of the two FODO half cells. The later arrangement maximizes the usable dispersion-free drift space.

Table 3: Examples of half-field dispersion suppressors.

Phase advance μ_c	Number of suppressor cells M
$\pi/2$ (90°)	2
$\pi/3$ (60°)	3
$\pi/4$ (45°)	4
$3\pi/5$ (108°)	5

2.3.3 Straight

A long, uninterrupted straight section can be realized by a pair of either doublet or triplet focusing quadrupole packages. The key requirement is to match the Courant-Snyder parameters α and β in both the horizontal and vertical directions.

Figure 14 gives an example of realizing one long, and two short straight sections using a pair of quadrupole doublets. There are seven constraints to be satisfied: α_x, α_y, β_x, and β_y to match the corresponding values of the arc, zero value of α_x and α_y to ensure lattice symmetry, and the specified horizontal phase advance. The adjustment in horizontal phase is often needed in a compact ring without dedicated phase-adjustment section, since the dispersion suppression in the horizontal direction often demands a specific phase advance in the arc and suppressor cells.

In this example, there are seven adjustment parameters available for matching: quadrupole strength of the two doublet quadrupoles, the strength of the quadrupole at the boundary between the straight and the arc (or dispersion suppressor), and the distance between them.

An alternative is to use a pair of quadrupole triplets instead of doublets. In this case, the matching becomes much easier. However, additional number of quadrupoles, quadrupole strength, and tunnel space is needed to accommodate the arrangement.

In the actual design of the SNS ring, the doublet-pair scheme is chosen, with distance l_0 made to be zero to simplify the vacuum chamber design. The β_x and β_y is also constrained to a certain range (about $\pm 10\%$) to provide adequate acceptance for injection and extraction. Operationally, the entire ring is tuned by 5 adjustable quadrupole settings (2 for the arc, 1 at the boundary, 2 in the straight). The 2 quadrupole families in the arc locks horizontal phase to $\pi/2$ per FODO cell while provide vertical tune adjustment, and the 3 straight and boundary quadrupole families provide horizontal tune adjustment while optimizes matching.

2.3.4 Working point selection

Although a wide tuning range is needed to provide operational flexibility, a nominal set of horizontal and vertical tunes (working point in tune space) is usually determined during the design stage, based on which detailed design evolves. Working-point selection is usually based

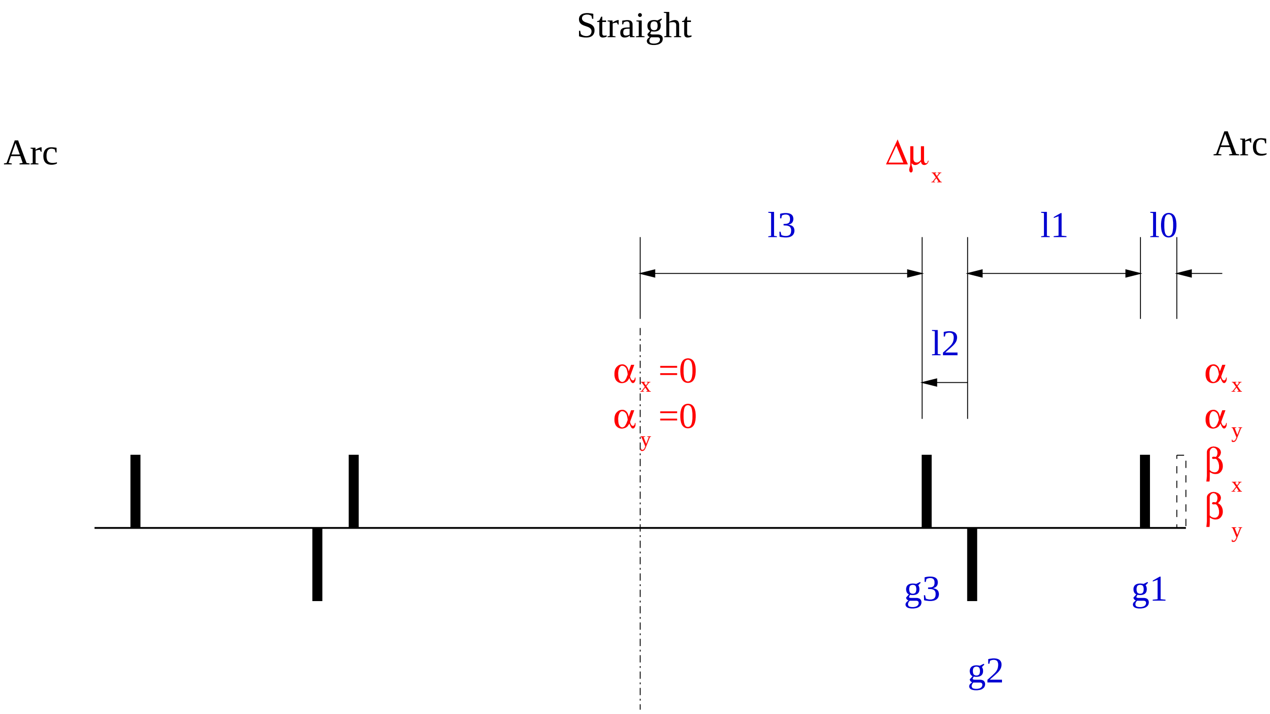

Figure 14: A dispersion-free straight section created by a pair of quadrupole doublets.

on minimizing lower-order, structural, and/or easily excited (e.g. by space charge) resonances, and on avoiding possible instabilities.

Problem 2.1 Evaluate the peak dispersion in both the FODO and DOFO achromat dispersion suppressor arrangements ...

2.4 Acceptance

For new rings, the linac-ring transport is usually designed to clean linac beam halo, prevent source and linac malfunction, and reduce injection activation. Transversely, foils can be used for H^- scraping. Longitudinally, an achromat bend is often used to create dispersion for energy tail cleaning.

Any beam halo and tail generated in the ring can be cleaned with high efficiency using two-stage collimation systems [12]. Momentum cleaning can be achieved in several ways: (1) injecting at a high-dispersion region and collecting at 180° phase advance downstream (ISIS, ESS [11]); (2) scraping at a high-dispersion lattice location (JJP [9]); and (3) using a beam-in-gap (BIG) kicker (SNS [13]). To reduce activation at extraction, the beam in the gap needs to be cleaned either during the initial ramping for synchrotrons, or with BIG kickers for accumulators.

Efficient beam collimation and low beam loss requires an adequate clearance between the beam core and the vacuum chamber limit. Typically, an admittance-to-emittance ratio

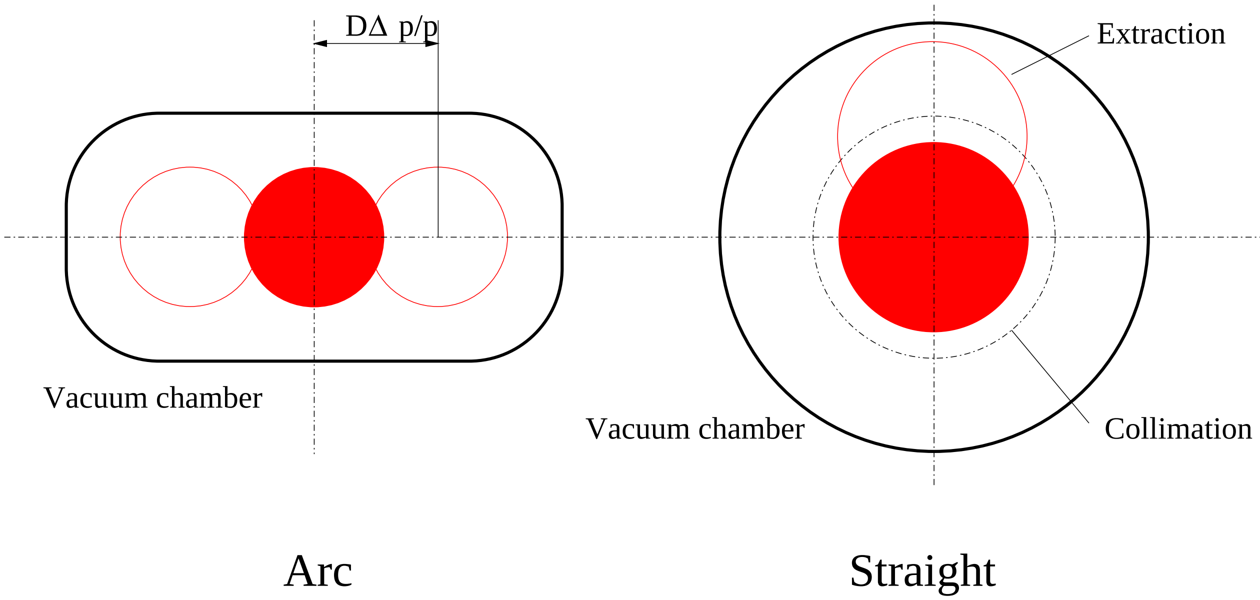

Figure 15: Schematics of the transverse aperture and beam amplitude.

of at least 2 is needed. Momentum collimation using the BIG kicker requires an adequate momentum clearance so that particles can reach the gap without loss.

2.4.1 Transverse acceptance

The transverse admittance is usually defined as the phase space area associated with the largest betatron ellipse that the accelerator accepts. Here in this course, we define the acceptance of the ring in a more general sense addressing not only the finite emittance of the beam, but also the closed-orbit deviation corresponding to a non-zero momentum spread, the design closed-orbit deviation at special region like injection and extraction, the closed-orbit deviation due to magnet alignment errors, and the dynamic acceptance reduction due to nonlinear magnetic errors. Furthermore, to simplify the discussion of beam collimation, the acceptance here refers to the physical aperture of the machine set by generic components like magnets, vacuum chamber wall, and RF cavities, not including dedicated loss-control components like scrapers and collimators.

We express the transverse displacement in terms of betatron oscillation component x_β, dispersive closed orbit x_p, and other closed orbit deviation x_c,

$$x = x_\beta + x_p + x_c = a(s)\cos[\psi(s) + \phi_0] + D(\Delta p/p) + x_c \qquad (13)$$

The betatron admittance is defined as the minimum value of $a(s)/\sqrt{\beta(s)}$ allowed by the accelerator aperture for a specified momentum $(\Delta p/p)$ at design closed orbit x_{c0} across the entire circumference.

Transverse emittance The transverse emittance $\pi\epsilon$ is defined as the $(x,\, x')$ phase space area associated with the betatron ellipse of a certain collection of particles (rms, 90%, 99%

...), as

$$\epsilon = \gamma x^2 + 2\alpha x x' + \beta x'^2 \tag{14}$$

For a Gaussian distribution with density distribution in x normalized as

$$n(x) = \frac{\exp\left(-x^2/2\sigma^2\right)}{\sqrt{2\pi}\sigma} \tag{15}$$

In terms of the rms value σ^2/β, the emittance ϵ is associated with the fraction F of the particles as

$$\frac{\epsilon}{\sigma^2/\beta} = -2\ln(1-F) \tag{16}$$

Table 4 lists some commonly used emittance definition.

Table 4: The fraction F of a Gaussian beam associated with various definitions of the emittance.

ϵ $[\sigma^2/\beta]$	F (%)
1	15
4	87
6	95
9	99

Under the adiabatic condition of acceleration, the quantity

$$\oint x dp_x = \text{constant} \tag{17}$$

is a constant of motion. Since the transverse momentum component p_x is related to the longitudinal momentum component p by the relation $p_x = px'$, we have

$$\epsilon \propto \frac{1}{p} \propto \frac{1}{\beta\gamma} \tag{18}$$

Both the horizontal and vertical (unnormalized) emittance values decrease with energy during acceleration. Thus, injection is usually one of the most critical time when beam loss occurs.

The normalized emittance defined as

$$\epsilon_N = \beta\gamma\epsilon \tag{19}$$

is a constant of motion during acceleration in the absence of diffusion and dilution. Preservation of the normalized emittance is usually a measure of machine performance. The complete uncoupled betatron motion can be expressed as

$$x_\beta = (\epsilon_N \beta(s))^{1/2} \left(\frac{p_0}{p}\right)^{1/2} \cos[\psi(s) + \phi_0] \tag{20}$$

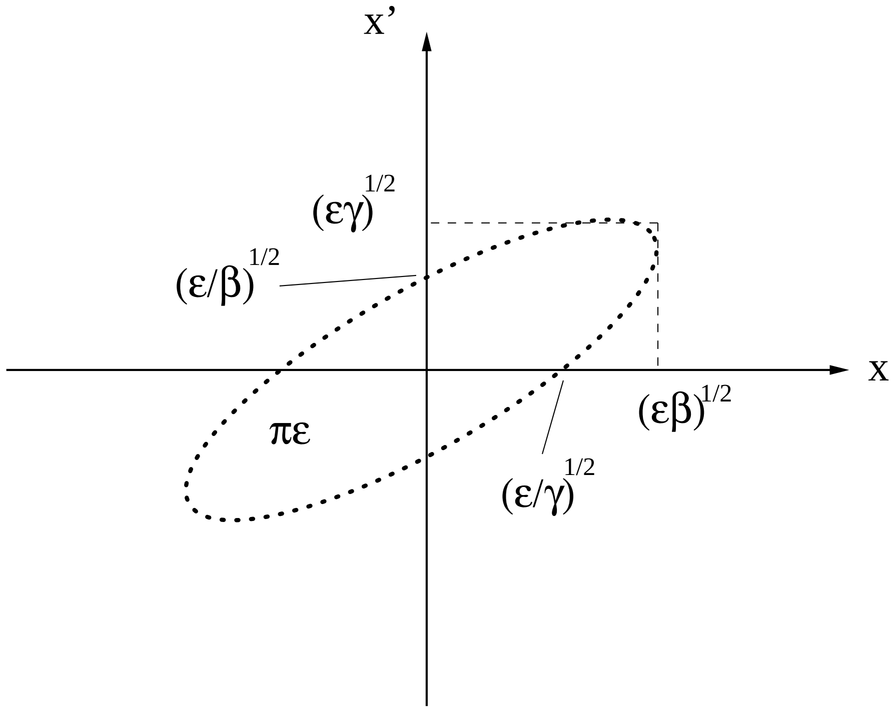

Figure 16: Phase space mapping from turn to turn in a circular accelerator.

Momentum-dependent closed orbit For off-momentum particles, the closed orbit deviation is given by

$$x_p = D(p,s)\frac{\Delta p}{p} \tag{21}$$

The dispersion $D(p,s)$ is a function of both the momentum $\Delta p/p$ and location s. Typically at high-dispersion locations like bending section, the vacuum chamber is widened to accommodate the off-momentum beam trajectory. Bending in the vertical direction is often avoided or carefully compensated to eliminate vertical dispersions.

The fractional circumference change for off-momentum particles is

$$\frac{\Delta C}{C} = \frac{1}{C_0}\oint \frac{D(s)ds}{\rho}\frac{\Delta p}{p_0} \equiv \frac{1}{\gamma_T^2}\frac{\Delta p}{p_0} \tag{22}$$

The slip factor η is

$$\eta = \frac{1}{\gamma_T^2} - \frac{1}{\gamma^2} = \langle\frac{D}{\rho}\rangle - \frac{1}{\gamma^2} \tag{23}$$

Injection and extraction closed orbit Injection and extraction regions are often high in radio-activation due to possible system malfunction. In these regions, the closed orbit is often manipulated to achieve injection painting and to facilitate extraction. Extra clearance must be reserved to accommodate easy-occur malfunction (e.g. extraction kicker misfire), and to accommodate various injection and extraction schemes.

Error-induced closed orbit deviation Deviation in dipole magnetic guiding field produce deviation in the closed orbit of the accelerator. A common cause of such steering error is the misalignment of quadrupole magnets. The closed orbit deviation $x_c(s)$ at a location s produced by dipole kicks $\theta_i = B_i L_i / B_0\rho_0$ at location s_i is expressed as

$$x(s) = \frac{\sqrt{\beta(s)}}{2\sin\pi\nu}\sum_{i=1}^{N}\sqrt{\beta(s)}\theta_i\cos[|\psi(s)-\psi(s_i)|-\pi\nu] \tag{24}$$

where ν is the transverse tune, and ψ is the phase advance. Contributions from steering errors is a linear superposition.

Dipole correctors are usually designed to reduce the closed orbit deviation. The effectiveness of the correction depends the arrangement of the beam position monitors (BPM) and the correctors, as well as the scheme itself.

Beta beating Deviation in quadrupole magnetic focusing field $\Delta K_i = \frac{\partial B_i}{\partial x}/B_0\rho_0$ produces distortion in β function, and effectively reduces the admittance. The distortion $\Delta\beta$ is given

$$\frac{\Delta\beta(s)}{\beta(s)} = \frac{1}{2\sin 2\pi\nu}\sum_{i=1}^{N}\beta(s)\Delta K_i L_i\cos[2|\psi(s)-\psi(s_i)|-2\pi\nu] \tag{25}$$

Due to β modulation, the superposition is nonlinear.

For off-momentum particles, the β distortion exists even for a linear lattice consists of only dipoles and quadrupoles. This "natural" perturbation can be estimated using the relation

$$\nu = \frac{1}{2\pi}\oint\frac{ds}{\beta} \approx \frac{R}{\langle\beta\rangle} \tag{26}$$

where $R = C/2\pi$ is the average radius of the accelerator, and $\langle\beta\rangle$ is the average amplitude function. Recall that the chromaticity ξ is typically equal in value but opposite in sign to the tune ν, we may estimate the average distortion as

$$\langle\frac{\beta(p,s)-\beta(p_0,s)}{\beta(p_0,s)}\rangle \approx -\frac{\Delta\nu}{\nu} = -\frac{\xi}{\nu}\frac{\Delta p}{p} \approx \frac{\Delta p}{p} \tag{27}$$

which is typically of the order of 1%. On the other hand, local off-momentum distprtion depends crucially on the matching of on-momentum lattice. Furthermore, nonlinear elements like the sextupole magnet effectively changes focusing for off-momentum particles, and thus can introduce significantly distortion if not well balanced and compensated.

Dynamic aperture Nonlinearities contributed from magnetic fields of sextupole and higher order introduce complications in particle motion, and can effectively reduces the acceptance of the machine. Computer tracking is often used to determine the actual impact. As a general guideline, a relative field error of below 10^{-4} is often needed to assure a stable particle motion for a relatively long period.

Collimation aperture Beam collimators are not all-around black-body absorbers, but rather devices that can reduce particle's energy and enhances their betatron oscillation at certain direction of the phase space. The function of collimation requires additional aperture to contain the excited particle motion, and to collect them in multi-turns without hitting the rest of the machine aperture.

Hardware clearance Finally, clearance must be reserved on possible intruding septa, electrodes, beam-position-monitor devices, vacuum bellows, and so on.

2.4.2 Longitudinal acceptance

The longitudinal admittance is usually defined as the phase space area provided by the radio-frequency system containing the bunch. The longitudinal or momentum acceptance of the machine here refers to the minimum momentum deviation allowed by the physical aperture of the accelerator for a specified transverse emittance.

RF bucket In terms of the canonically conjugated variables of RF phase ϕ and energy $W \equiv \Delta E/h\omega_s$, the stable phase space area provided by a single-harmonic RF system of peak voltage V and harmonic h is

$$A_B = \frac{16R}{hc}\sqrt{\frac{eVE_s}{2\phi|\eta|}}\kappa(\phi_s) \tag{28}$$

where $0 \leq \kappa(\phi_s) \leq 1$ is the ratio of the area of the bucket with a synchronous phase ϕ_s to the area of the stationary bucket (the one with ϕ_s equal to 0 when below transition and π when above),

$$\kappa(\phi_s) = \frac{1}{4\sqrt{2}}\int_{\min.(\pi-\phi_s,\phi_e)}^{\max.(\pi-\phi_s,\phi_e)} \left[-(\pi-\phi_s)\sin\phi_s + \cos\phi_s + \cos\phi + \phi\sin\phi_s\right]^{\frac{1}{2}} d\phi, \tag{29}$$

with ϕ_e the solution of the transcendental equation

$$\cos\phi_e + \phi_e \sin\phi_s = (\pi - \phi_s)\sin\phi_s - \cos\phi_s. \tag{30}$$

For a rapid-cycling synchrotron, the synchronous phase ϕ_s needs to be quickly increased from 0 at injection to a finite value for fast ramping. The subsequent reduction of the bucket area is a common cause of heavy beam loss at initial ramping.

Momentum acceptance Evolution of momentum and phase deviation can be described in terms of the longitudinal amplitude function β_L. With a normalized time $d\tau = kdt$, $k = qeV|\cos\phi_s|/2\pi h$, the longitudinal motion is described by a Hamiltonian

$$H(\varphi, J; \tau) = \pm J/\beta_L \tag{31}$$

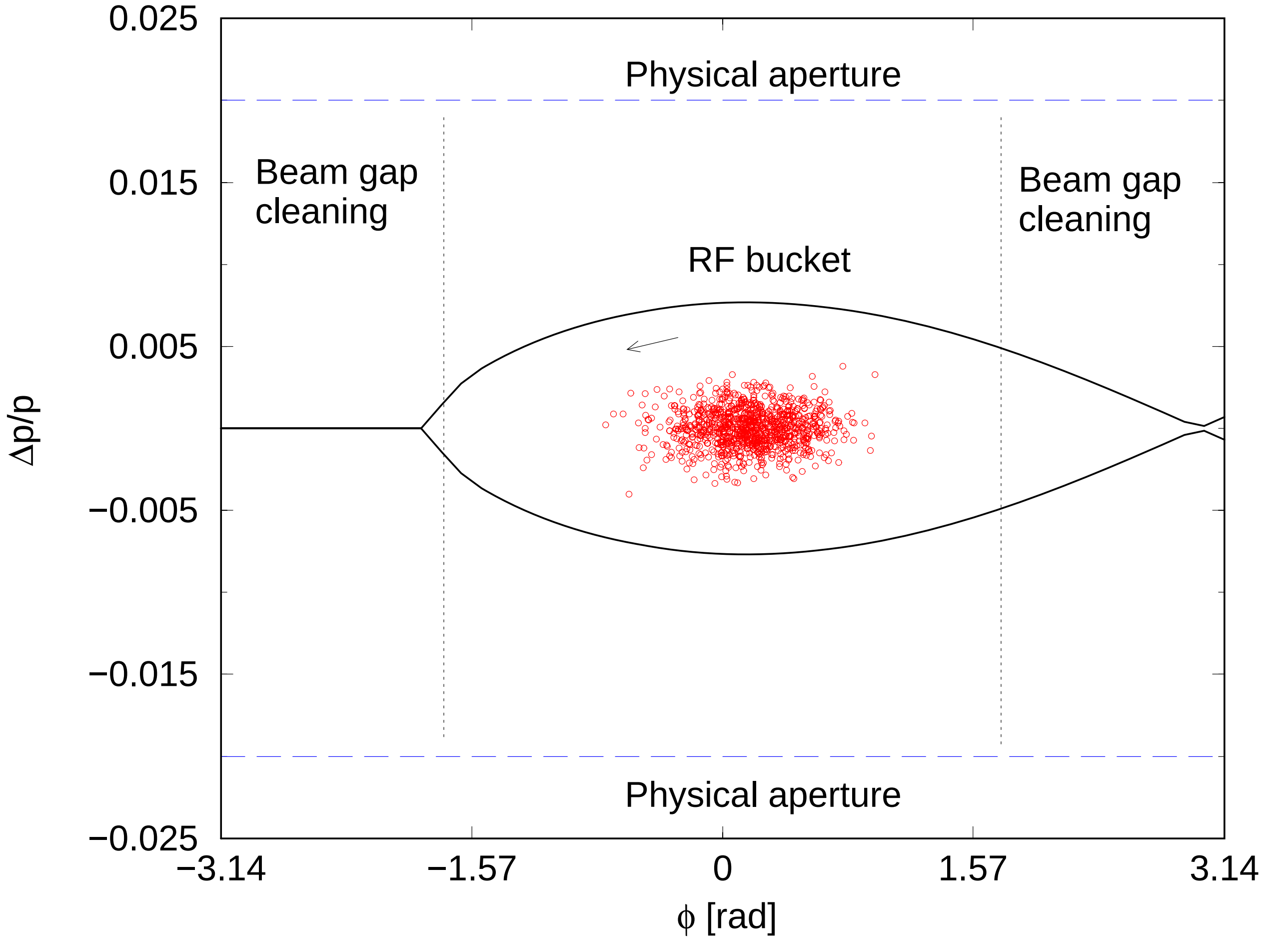

Figure 17: Schematics of the longitudinal RF bucket admittance and accelerator momentum acceptance. The particles circulate in the phase space counter-clockwise below transition energy.

The action-angle variables (φ, J) are related to the rf phase ϕ and $W \equiv -\Delta E/h\omega_s$ by

$$\begin{aligned} \Delta\phi &= \mp\sqrt{2J/\beta_L}(\sin\varphi + \alpha_L\cos\varphi) \\ W &= -\sqrt{2J\beta_L}\cos\varphi \end{aligned}$$

where the upper (or lower) sign is for below (or above) γ_T, $\alpha_L = -\beta_L'/2$, and $'$ denotes the derivative with respect to τ. The amplitude function β_L is given by

$$\frac{1}{2}\beta_L\beta_L'' - \frac{1}{4}\beta_L'^2 + K\beta_L^2 = 1, \;\; K = \frac{-2\pi h^3\omega_s^2\eta_0}{qeV\cos\phi_s E_s\beta_s^2} \tag{32}$$

For a constant $\dot{\gamma}$ near transition,

$$\frac{\beta_L}{kT_c} = \frac{\pi}{3}x\left[\mathrm{J}^2_{-\frac{1}{3}}(y) + \mathrm{N}^2_{-\frac{1}{3}}(y)\right] \approx 1.58 - 1.15x$$

where $y = 2x^{3/2}/3$, $x = |\Delta t|/T_c$, and Δt is the time delay from γ_T. The longitudinal particle motion is non-adiabatic within a characteristic time $\pm T_c$ near transition energy γ_T,

$$T_c = \left(\frac{\pi E_s\beta^2\gamma_T^3}{qeV|\cos\phi_s|\dot{\gamma}h\omega_s^2}\right)^{\frac{1}{3}} \tag{33}$$

where the subscript s denotes the synchronous value. The synchrotron frequency is $\Omega_s = k\beta_L^{-1}$. The maximum excursions in ϕ and W are

$$\hat{\phi} = \sqrt{2\gamma_L J}, \quad \text{and} \quad \hat{W} = \sqrt{2\beta_L J} \tag{34}$$

where $1 + \alpha_L^2 = \beta_L\gamma_L$. For a bunch of rms bunch area $S = 2\pi\langle J\rangle$, the rms phase and momentum deviations at γ_T are

$$\hat{\sigma}_\phi = 0.52\,(S/kT_c)^{1/2} \quad \text{and} \quad \hat{\sigma}_\delta = 0.71h\omega_s\,(kT_cS)^{1/2}/E_s\beta_s^2. \tag{35}$$

The momentum acceptance of the accelerator determined by the physical machine aperture is usually designed to be larger than the maximum momentum admittance of the RF bucket during the entire acceleration cycle. The limiting locations are usually at the high-dispersion area. In addition, momentum-dependant effects, e.g. resonance due to chromaticity, chromatic effects at transition crossing, limit available acceptance. Compensation schemes are often designed to allow a large momentum acceptance.

2.5 Collimation and Collection

2.5.1 Transverse collimation

Collimation of an ion beam containing un-stripped electrons is often performed with adjustable stripping foil scrapers to change the charge state of the particle, and then with collecting devices (shielded collimator block or beam dump) for collection after the scraped particles' trajectory deviates significantly from the un-stripped beam under guiding magnets. Figure 19

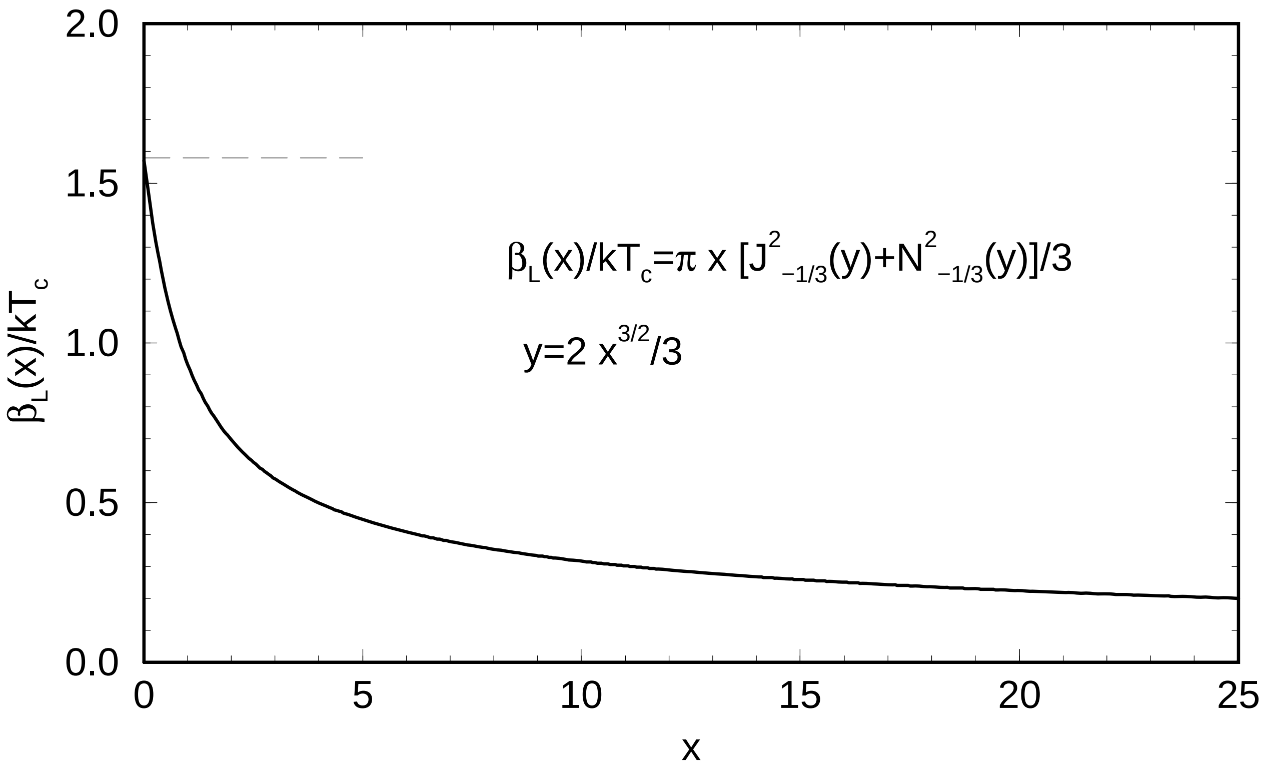

Figure 18: Longitudinal amplitude function. The time $x = 0$ represents transition crossing.

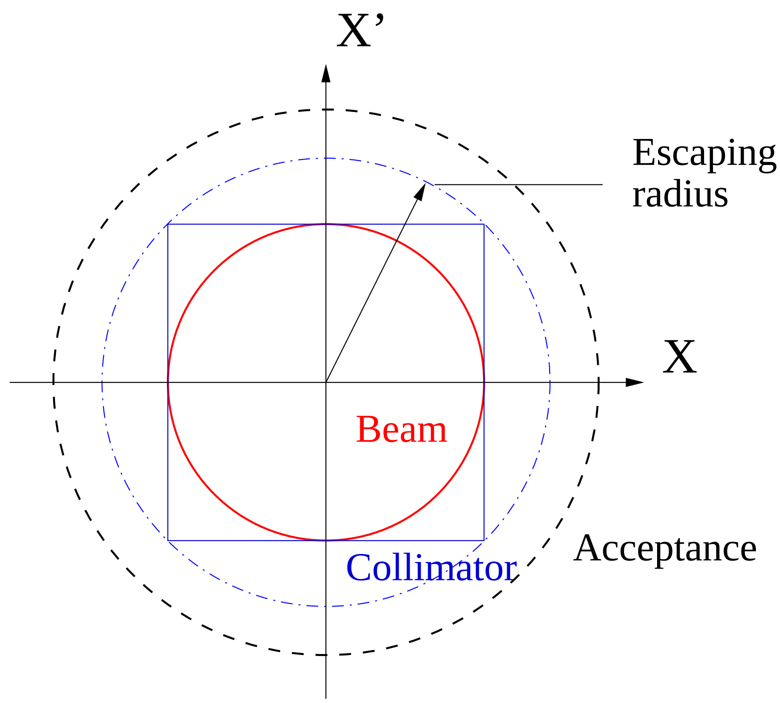

Figure 19: Schematics in normalized phase space of ion collimation with two pairs of scrapers located with a phase advance of $\pi/2$ apart.

shows such a scraping action using two pairs of scrapers location at a betatron advance of $\pi/2$ apart. For the convenience of discussion, we use normalized parameters

$$X \equiv \frac{x}{\sqrt{\beta_x}}, \quad X' \equiv \frac{dX}{d\mu} = \frac{\alpha x + \beta x'}{\sqrt{\beta}} \tag{36}$$

in terms of the phase variable

$$\mu(s) = \int^s \frac{ds'}{\beta} \tag{37}$$

The escaping radius must be less than the acceptance of the accelerator to avoid uncontrolled beam loss.

Collimation of fully stripped particles like protons is usually performed with thin scrapers and thick collimators of solid material. The collimation efficiency is usually not limited by particles that traverse the collimator, but by particles that are out-scattered from the side of the collimator block. The amount of out-scattering depends crucially on the impact parameter (distance of impinging point of incident particle from the edge of collimator), as illustrated in Figure 20.

In order to raise the collimation efficiency, a two-stage scenario is usually preferred: a thin, primary scraper that scatters the incident particle to enhance their impact parameter upon collection by secondary collimators, as shown in Figure 21. The system can consist of several pairs of thin, adjustable scrapers (a few centimeters) approaching the beam in

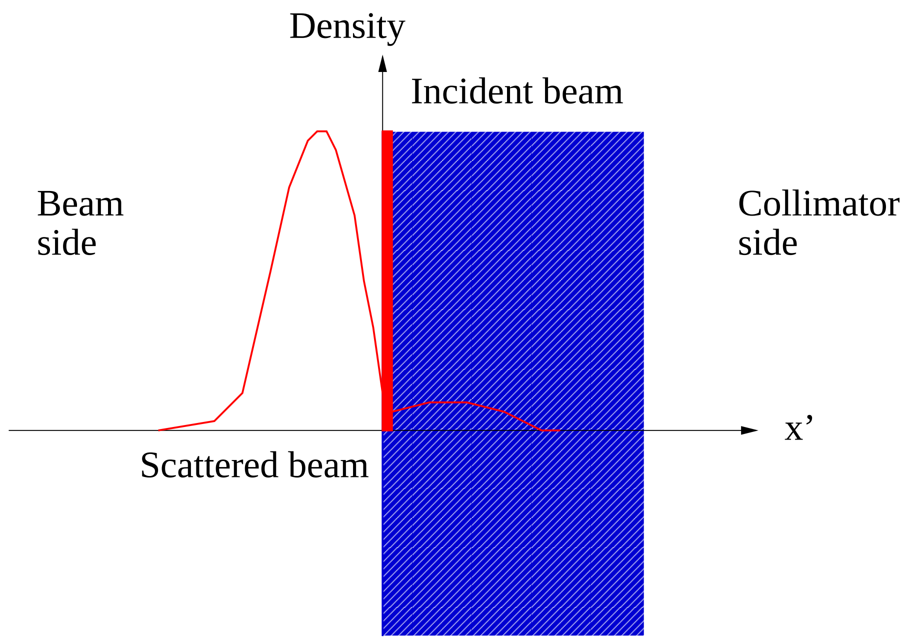

Figure 20: Angular distribution of the out-scattered and transmitted beam upon a collimator block. The incident beam has a uniform impact parameter distribution both in distance and angle just inside the edge of the block.

different directions, and then several thick (several meters) collimators to fully stop the scraped particles. The length of the scraper depends on the beam energy and is an optimization between energy loss and multiple Coulomb scattering. The length of the collimator depends on the stopping distance of the particle which again is a function of the beam energy. Since the transverse collimation is usually done at dispersion-free region, the effect of energy loss in the scraper is usually not critical to the first order.

Figure 22 shows the collimation mechanism in the normalized phase space. With the primary scraper at a distance A away from the beam center, and the secondary collimators at a distance $A+H$ away from the beam center, the optimum phase advance is given by

$$\mu_1 = \cos^{-1}\left(\frac{A}{A+H}\right), \quad \text{and} \quad \mu_2 = \pi - \mu_1 \tag{38}$$

The actual efficiency of the collimation system depends on the design of the accelerator lattice to accommodate the optimum arrangement of the collimation devices. Figure 23 compares the one-pass collimation efficiency in a FODO straight section with $\pi/2$ phase advance per cell, and in a doublet long drift with less-constraint phase limitation.

2.5.2 Momentum collimation and beam-in-gap cleaning

The momentum tail of injected beam, if not cleaned before injection, needs to be collected upon injection to avoid uncontrolled beam loss. The beam gap as well as possible momentum halo generated in the ring needs to be cleaned to assure a clean extraction. For rapid-cycling-synchrotrons, momentum and gap cleaning can be relatively easily done upon initial ramping

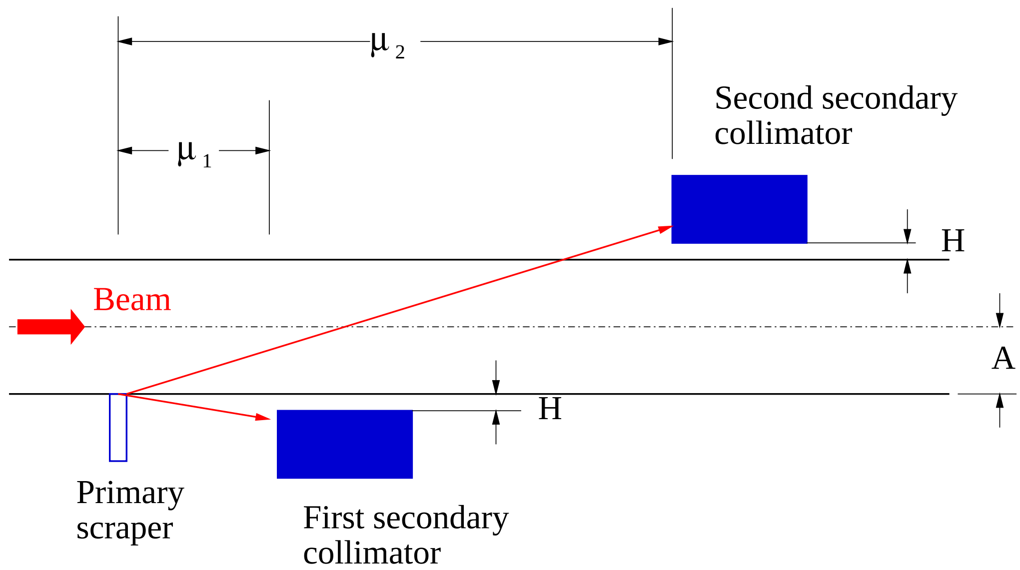

Figure 21: Schematics in normalized phase space of ion collimation with two pairs of scrapers located with a phase advance of $\pi/2$ apart.

using the collimators. Methods proposed or used for longitudinal cleaning include momentum tail collection, beam-in-gap kicker cleaning, and momentum collimation.

Momentum tail collection The beam upon injection often carries a negative momentum tail due to linac output and energy loss at injection foil. This momentum tail can be collected at a distance of betatron phase π downstream of a high-dispersion injection region. This practice has been crucial to the operation of the ISIS synchrotron.

One possible problem of this scenario is the coupling of horizontal and longitudinal particle motion when injection painting is executed.

Beam-in-gap cleaning Various mechanisms, including chopper inefficiency and foil ionization, can produce a residual beam between micro bunches, resulting in uncontrolled loss at extraction. A gap-cleaning kicker is designed to resonantly excite coherent betatron oscillations, driving the gap beam into the primary collimator, where beam loss is measured with a gated fast loss monitor. Complete cleaning of a gap particle needs to by performed in a time much shorter than the synchrotron oscillation period. The process can be complicated if tune spread of the gap particle is large.

Momentum collimation Momentum tail and halo collection can be performed by placing collectors at locations of highest dispersion. The high-dispersion drift space needs to be long enough to accommodate the length of a shielded collector.

Two-stage momentum collimation is possible but needs careful consideration. The momentum scraper needs to be placed at high-dispersion region. Upon scraping, particles of original positive momenta ($\Delta p/p > 0$) will lose energy, resulting in a reduced transverse displacement

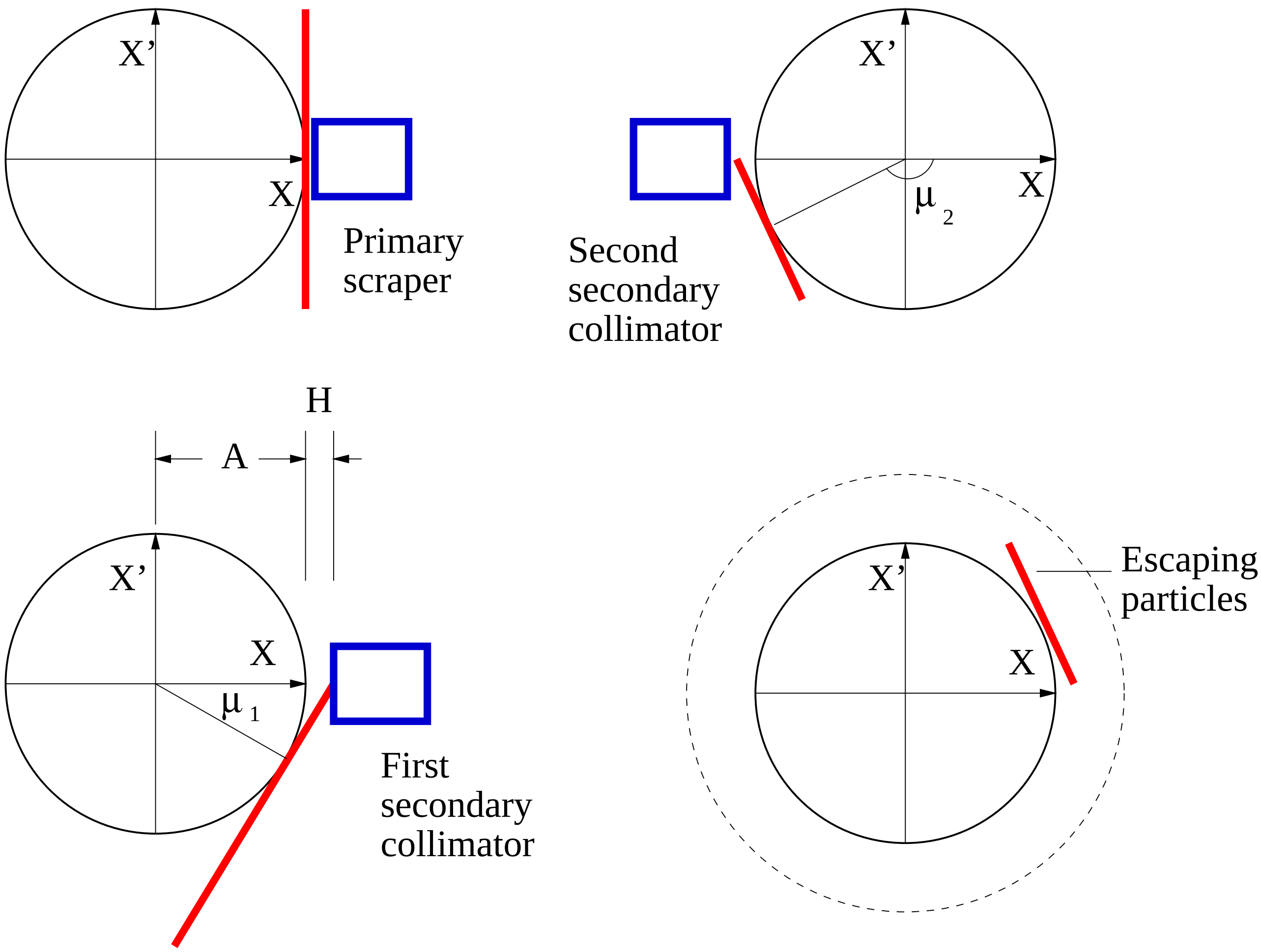

Figure 22: Schematics in normalized phase space of a two-stage collimation with one primary scraper and two secondary collimators located with a phase advance according to Figure 21.

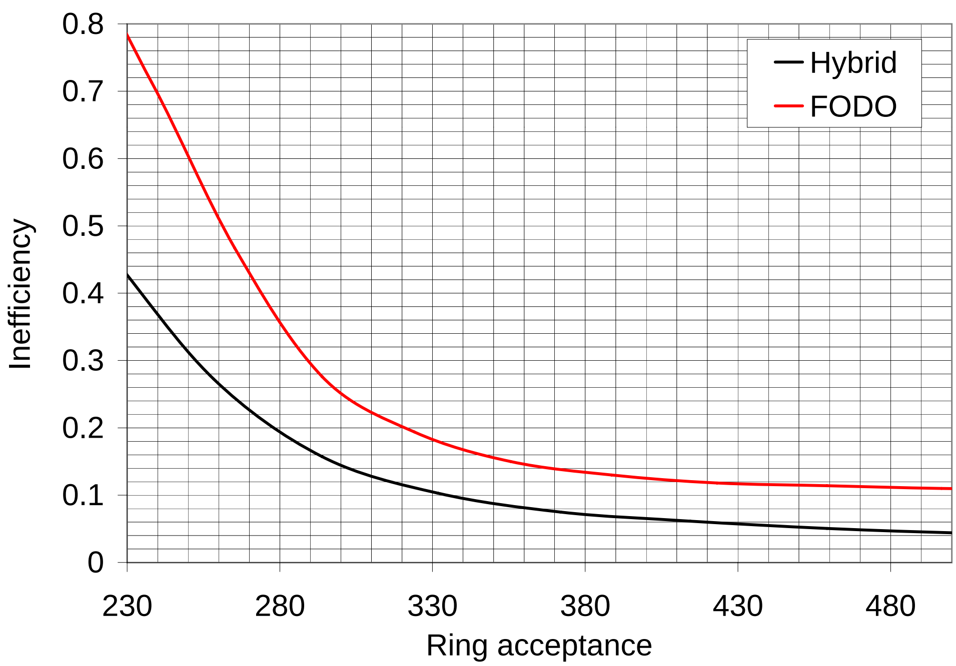

Figure 23: Comparison of collimation inefficiency between the previous all-FODO lattice (upper curve) and the present hybrid lattice (lower curve). The inefficiency is defined as the number of halo particles escaping the collimation system after one turn above a given amplitude.

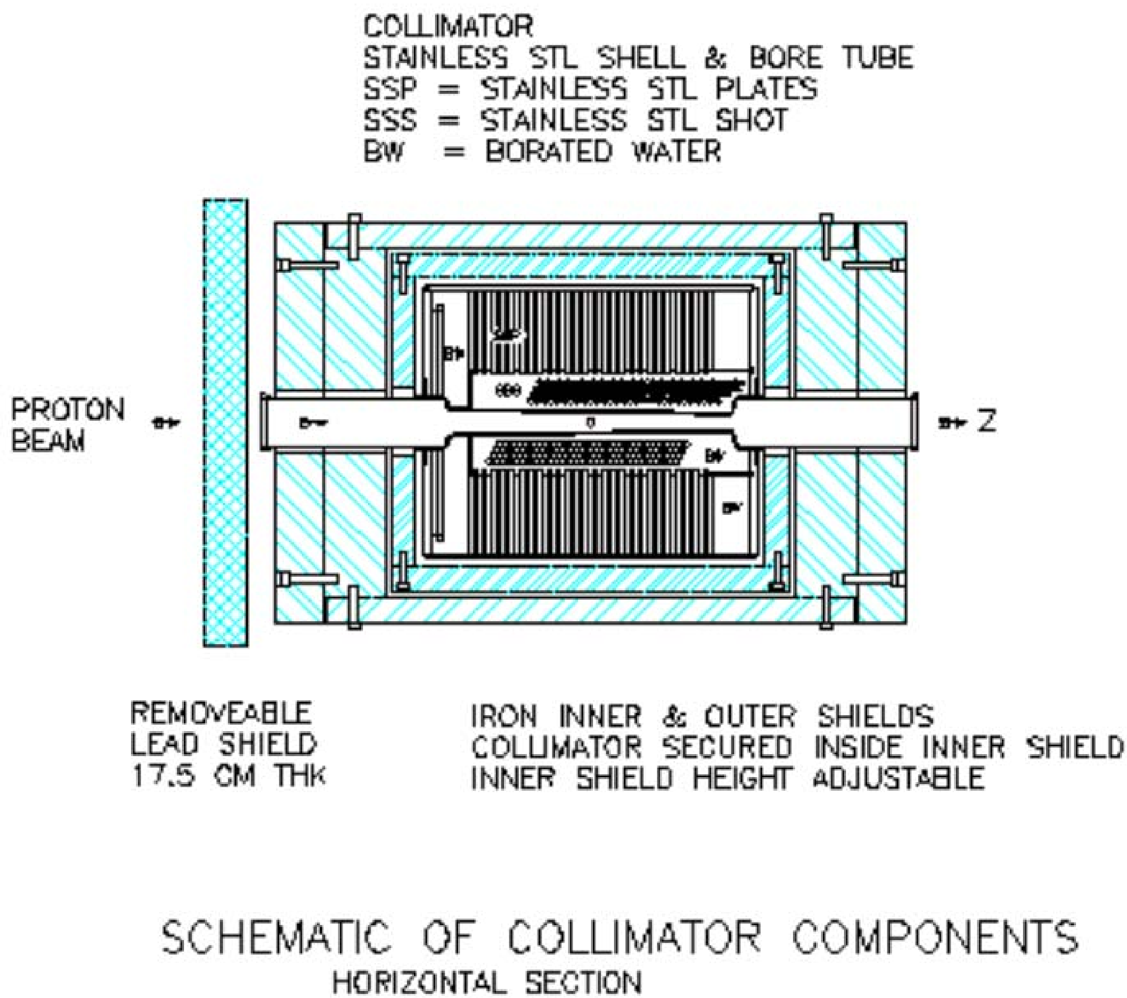

Figure 24: Schematic of the SNS ring collimator showing layers of material for radio-activation containment.

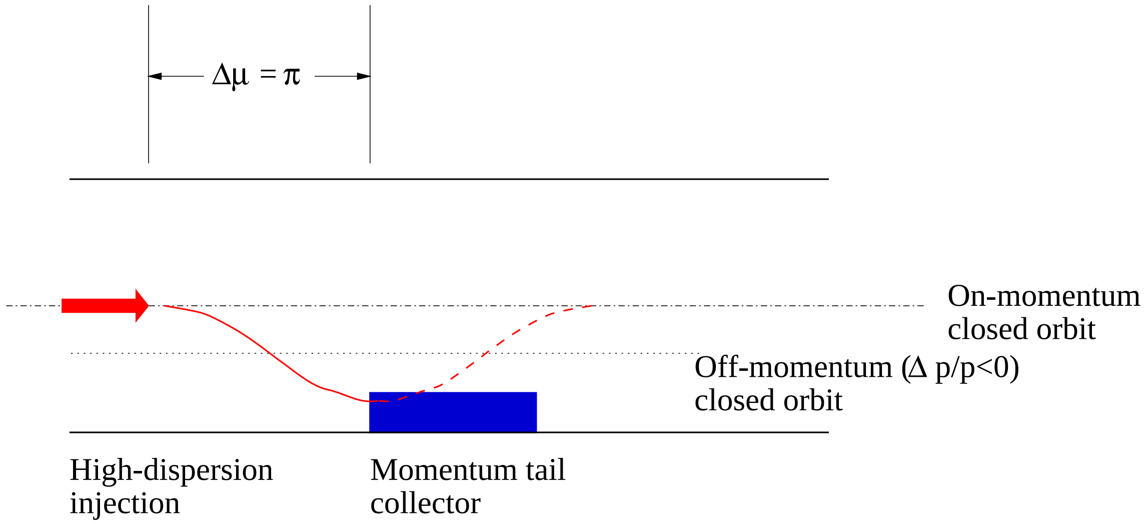

Figure 25: Collection of injection off-momentum tail by injecting at a high-dispersion region.

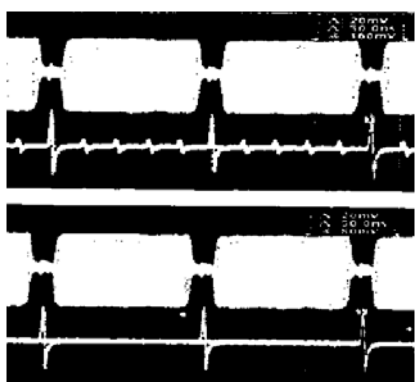

Figure 26: Clearing of stray beam bunches in the National Synchrotron Light Source at the Brookhaven National Laboratory (courtesy R. Nawrocky et al).

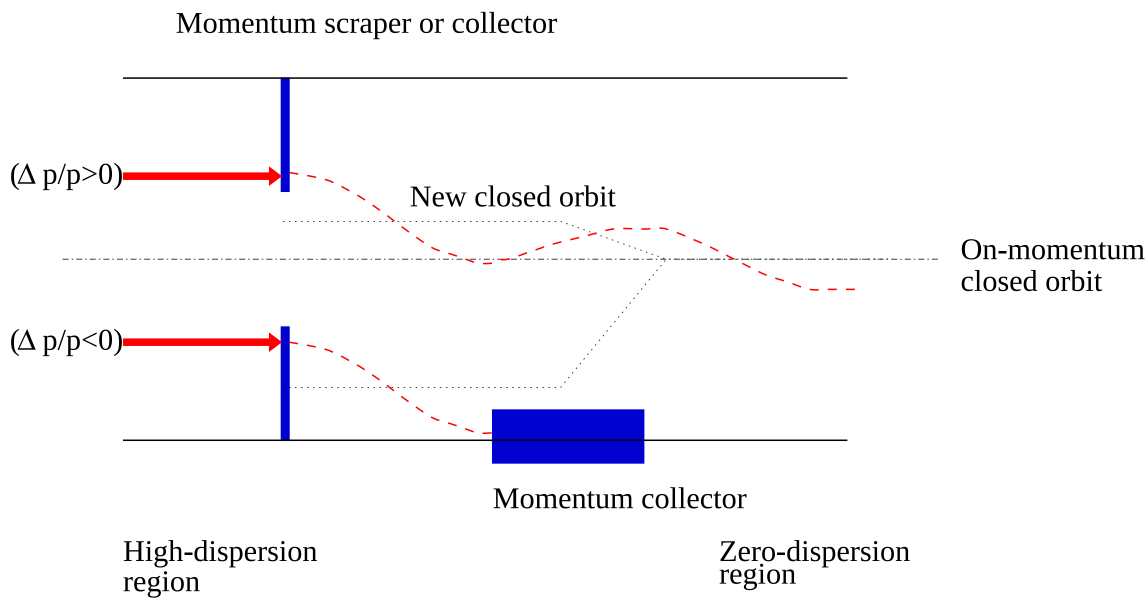

Figure 27: Momentum collimation or collection at high-dispersion region.

due to excited betatron motion and the decreasing dispersion. These particles may escape the secondary momentum collimators and return to the beam core. Particles of original negative momenta ($\Delta p/p < 0$) will further lose energy, resulting in an enhanced transverse displacement to be collected by secondary collimators possibly located also in a high-dispersion region. A lattice design that satisfies the practical conditions can be challenging.

Problem 2.2 Derive Equation 38 ...

2.6 Injection and Painting

Injection refers to the transfer of beam either from a linear to a circular accelerator, or from a circular to another circular accelerator. The design goal is to achieve that transfer with little beam loss and with either a minimum or a controlled dilution of the beam emittance. A successful injection requires the fringe field of the septum and subsequent magnets to be at an acceptable level, the kickers to have a field profile within tolerance and a rise and fall time within a defined fraction of the revolution period, and the RF system to be capable of containing the transient beam loading.

2.6.1 Single-turn injection

Single-turn injection is performed with a septum (dc) and a kicker (ac) located with a betatron (usually horizontal) phase advance of $\Delta\mu$ preferably near $\pi/2$. The injecting beam profile must be matched to the accelerator lattice to preserve the emittance.

Longitudinally, matching implies that the frequency of the RF system must be synchronized, and that the aspect ratio between energy and phase spread matches as much as possible

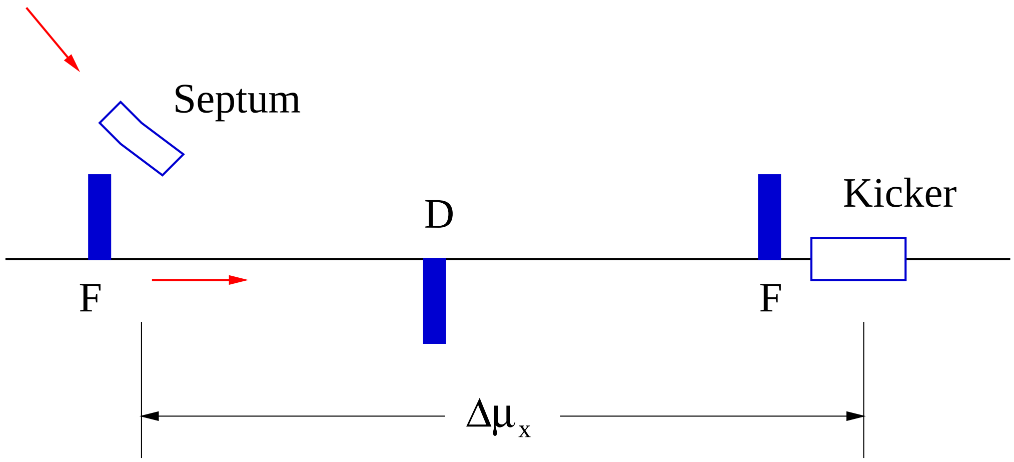

Figure 28: Schematic layout of a single-turn injection system.

to the intrinsically nonlinear RF bucket. Since injection is usually performed at a "flat bottom" without net acceleration, the matched phase-space ellipses are always upright. Matching can be simply done by proper adjustment of the RF frequency and voltage.

Transversely, matching implies that the injected beam must be kicked to the closed orbit of the ring, and that at the exit of the septum the Courant-Snyder parameters of the beam

$$\beta_, \ \alpha_x, \quad D_x, \quad D'_x$$

must be identical to those of the ring lattice. The closed-orbit matching can be conveniently analyzed using the normalized phase space. At the septum exit, the x and x' needs to satisfy

$$\cot \Delta\mu_x = -\frac{X'}{X}, \quad \text{or} \quad x' = -(\alpha_x + \cot \Delta\mu_x)x \tag{39}$$

The amount of deflection θ from the kicker is related to the displacement x at the septum exit as

$$\theta = X/\sin\Delta\mu \quad \text{or} \quad \theta = \frac{x}{\sqrt{\beta_{sep}\beta_{kick}}\sin\Delta\mu_x} \tag{40}$$

The optimum condition is achieved with $\Delta\mu_x = \pi/2$ with

$$\theta = \frac{x}{\sqrt{\beta_{sep}\beta_{kick}}}, \quad \text{and} \quad x' = -\frac{\alpha_x x}{\beta_x} \tag{41}$$

2.6.2 Conventional multi-turn injection

Multi-turn injection is often used to increase the beam intensity in the ring. Conventional multi-turn injection employs a septum and a programmed orbit bump, usually in the horizontal plane in a non-dispersive region. The injection efficiency can be optimized by a specific

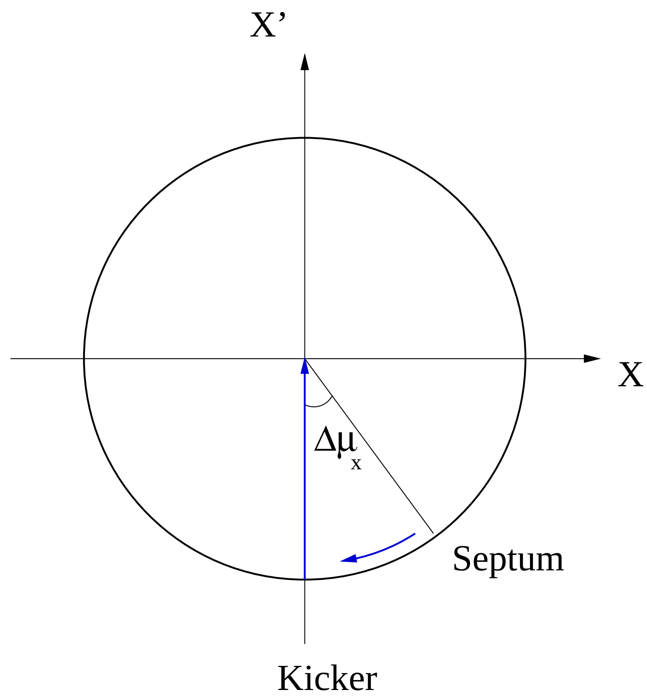

Figure 29: Schematics in the normalized transverse phase space of single-turn injection.

mismatch. Let Courant-Snyder parameters and emittance for the injected beam be (β_i, α_i, ϵ_i), and for the ring (β, α, ϵ); Let input beam center relative to instantaneous injection orbit bump be (x, x'). Then the conditions are

$$\frac{\beta}{\beta_i} = \frac{\alpha}{\alpha_i} = \left(\frac{\epsilon}{\epsilon_i}\right)^{1/3}; \; \frac{\alpha}{\beta} = \frac{\alpha_i}{\beta_i} = -\frac{x'}{x} \tag{42}$$

The number of injection turns is optimized by adjusting fall of the beam bump. According to Liouville's theorem,

$$\epsilon \leq n\epsilon_i \tag{43}$$

Typically, the ratio $\epsilon/(n\epsilon_i)$ is around 0.5.

2.6.3 Charge-exchange multi-turn injection

With multi-turn charge-exchange scheme, it is possible to inject a large number of turns to greatly enhance beam intensity and to control the final beam distribution. The constraints imposed by Liouville's theorem on conventional multi-turn injection do not apply since the stripping of H^- ions occurs within the acceptance of the ring.

The magnetic field must be chosen carefully to prevent premature stripping of both H^- and H^0 [14]. ISIS/ESS prefers injecting at a high-dispersion region (Figure 31). The lattice dipole simplifies the injection magnet arrangement and facilitates momentum halo collection. SNS prefers injection in a zero-dispersion straight (Figure 32). The decoupled longitudinal

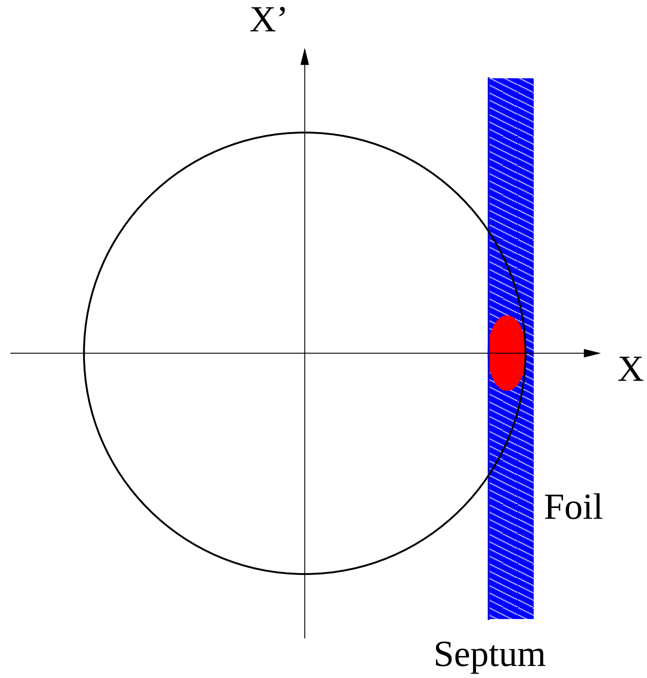

Figure 30: Schematics in the normalized transverse phase space of optimized multi-turn injection.

motion allows independent momentum correction and broadening before injection, and is more tolerant to linac energy deviation. A long, uninterrupted straight is preferred to contain the injection chicane, allowing independent lattice tuning. Intentionally mismatched injection can noticeably reduce the foil hits. Laser stripping [18] has been explored as an alternative but the required power and efficiency are very demanding.

Transverse painting Transverse painting alleviates the fundamental space-charge limit and controls the uniformity and shape of the beam profile. Various beam profiles can be achieved using fast orbit bump or injection steering. Scenario (b) and (c) of Figure 33 ideally produce uniform density beams but practically are susceptible to halo development. Resonance correction and decoupling are crucial in preserving the painted beam shape.

Anti-correlated painting utilizes both the horizontal and vertical orbit bumps programmed anti-parallelly, one with increasing and the other with decreasing closed-orbit deviation (COD) for the injection point. Ideally, such a painting scheme produces a distribution with an elliptical transverse profile and a uniform density distribution. Such a distribution can be also realized by painting in one direction and steering in the other. However, in the presence of space charge this scheme produces an excessive beam halo during the early stage of painting, when the beam is narrow in one direction. Also, the scheme requires extra clearance in the direction of large starting COD amplitude.

Correlated painting using parallel horizontal and vertical orbit bumps produces a rectangular transverse profile. This scheme has the advantage that the beam halo is constantly painted

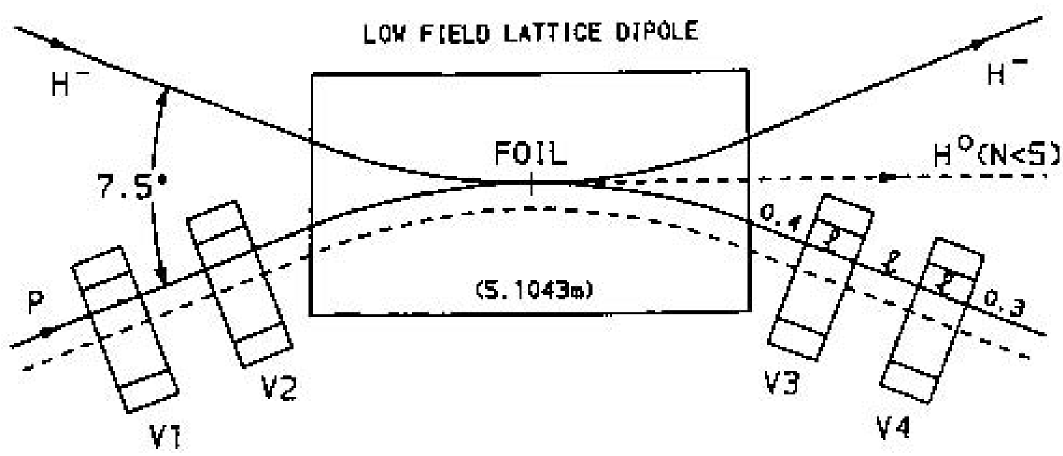

Figure 31: ESS dispersive injection layout.

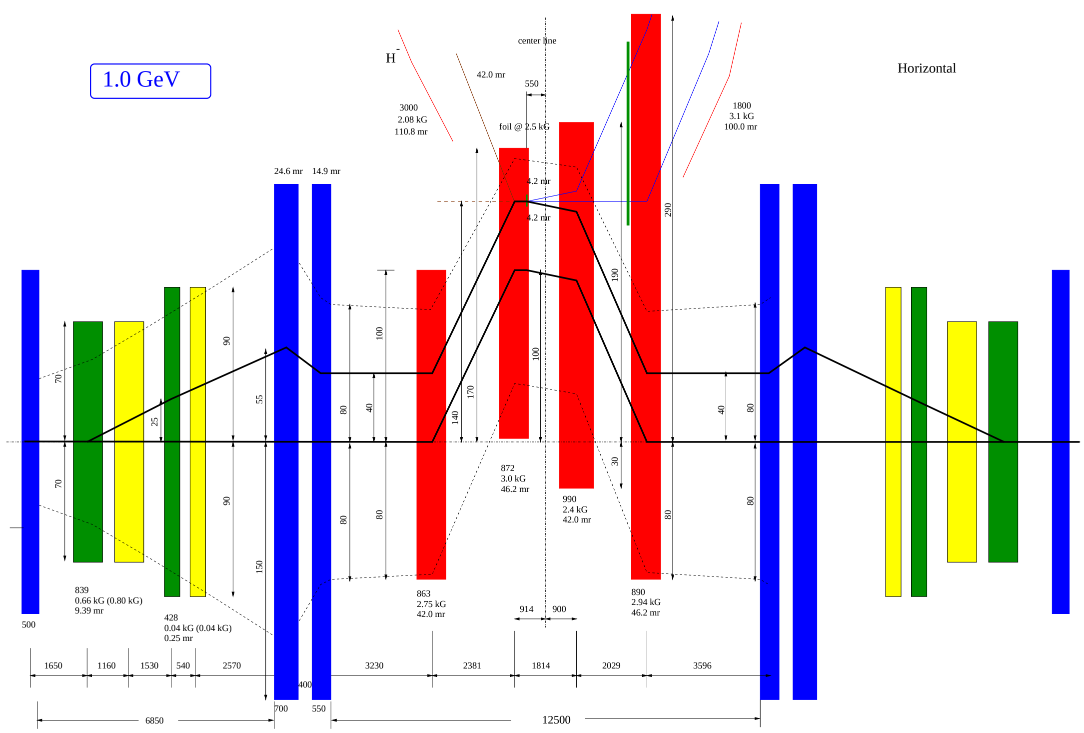

Figure 32: SNS dispersion-free injection. Elements shown are the chicane (red), the ring lattice quadrupoles (blue), and dynamic kickers (yellow H and green V).

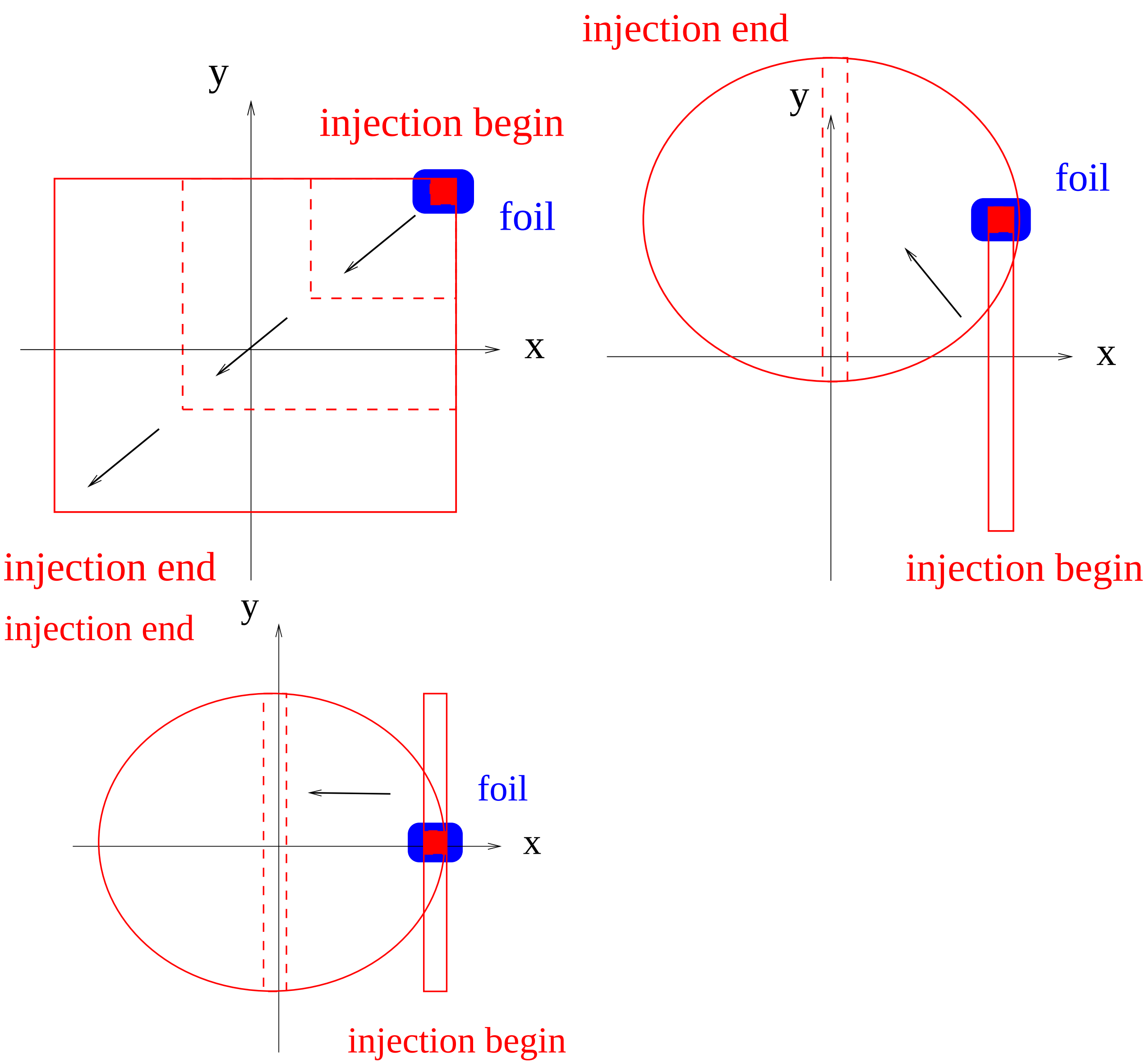

Figure 33: Beam transverse profile of (a) correlated-bump painting (b) anti-correlated bump painting and (c) horizontal painting / vertical steering.

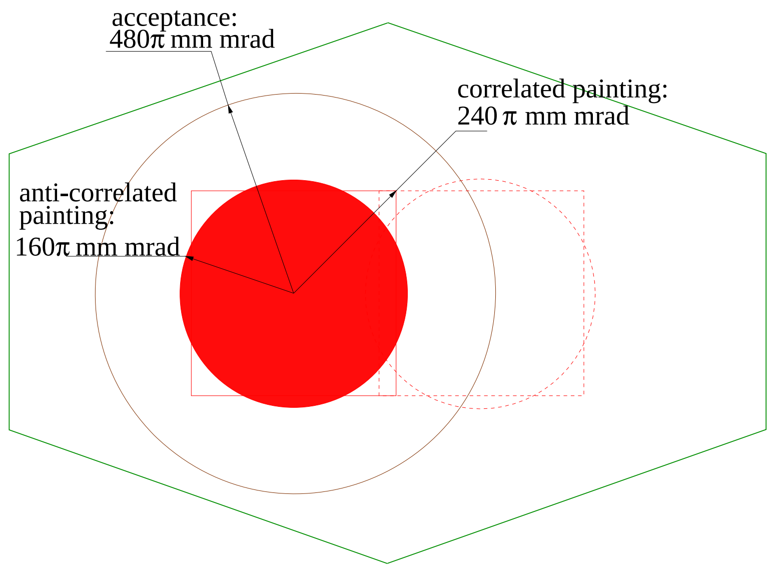

Figure 34: Schematic illustration of the transverse dimensions in the ring. The green hexagonal boundary represents the cross section of the dipole vacuum chamber. The brown circular line corresponds to the minimum aperture in the ring at 480π mm mrad. The beam is represented by the red circle for anti-correlated painting and the red square for correlated painting. The displacement of the beam centroid in the dipole (indicated by the dashed outlines) corresponds to 1% momentum deviation.

over by freshly injected beam. The main concern is whether the rectangular beam profile can be preserved in the presence of coupling produced by space charge and magnet errors. For both anti-correlated and correlated painting, eight fast kickers, four in each direction, are needed to control the orbit bumps.

Hybrid schemes utilizes closed-orbit bump in one direction and injection-angle steering in the other direction. Figure 33 shows a scheme of horizontal orbit painting and vertical angle steering. The four vertical kickers are no longer needed. Instead, a small vertical kicker is used in the transport line at a betatron phase of π upstream of the injection septum to vary the injection beam angle. With such a scheme, a challenging issue is that the foil needs to be supported horizontally to avoid excessive foil traversal and scattering. An alternative scheme is to use vertical orbit painting and horizontal angle steering. However, the beam needs to be injected vertically. In both cases, the acceptance of the injection channel all the way up to the injection dump needs to be designed to accommodate the varying injection beam angle. Operationally, the reliability of the kicker system upstream of injection must be high to avoid injection foil miss, dump over-heating, and injection channel activation.

Longitudinal painting Longitudinal painting provides momentum spread required for beam stability without introducing excessive momentum halo, as shown in Figure 35. With dispersion-free injection, longitudinal painting can be achieved for linac-to-ring injection by using an “energy spreader” RF cavity located in the transport line upstream of injection region, operating at a phase-modulated mode of the linac frequency. In order to facilitate such

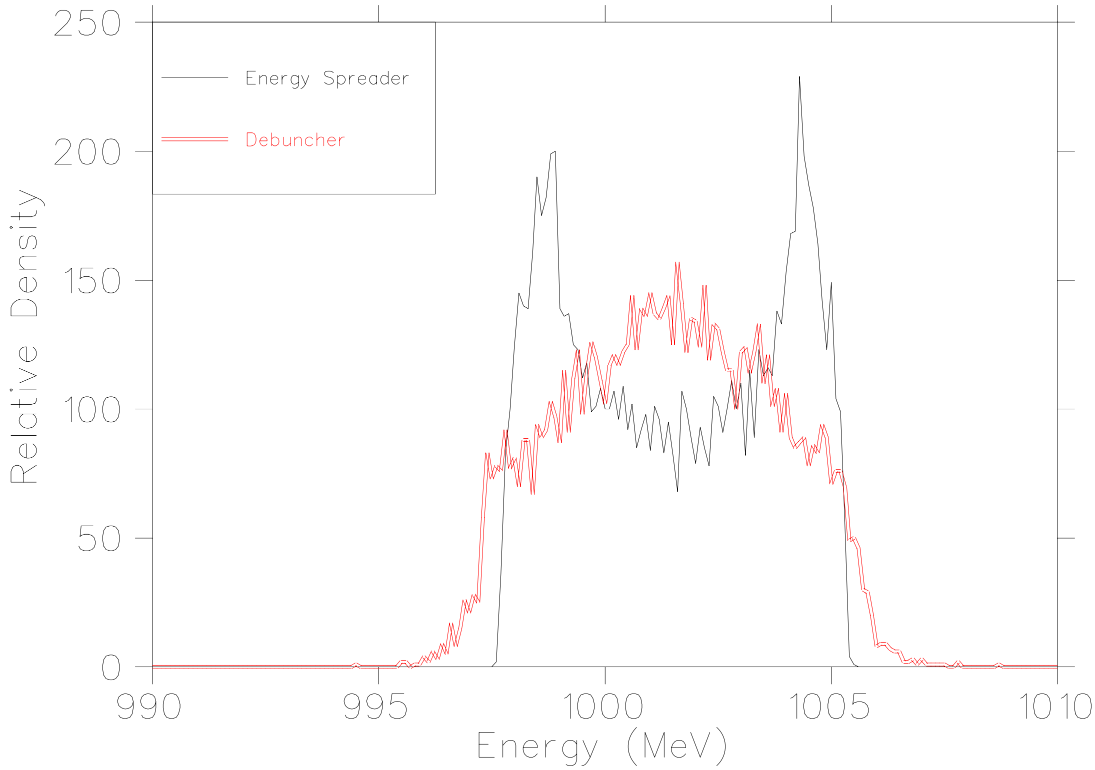

Figure 35: Energy distribution at the injection foil using either an energy spreader or a conventional debuncher. An energy spreader significantly suppresses the beam tail.

a painting scheme, the output momentum jitter and spread need to be strictly controlled possibly by an "energy corrector" RF cavity synchronized to linac frequency, located again in the transport line upstream of injection at an optimized distance from the end of linac to allow for adequate beam-phase slippage and thus moderate RF voltage.

Transverse-longitudinal coupled painting High-dispersion injection couples horizontal and longitudinal beam painting. Instead of introducing an injection "chicane", the bending magnet is itself part of the ring base lattice. The injection layout is clean without the injection septum, various chicane dipole magnets, and four horizontal kickers. Instead, however, the long, low-field injection dipole is repeated at every lattice super-period.

This scheme has the advantage of facilitating momentum-tail collection upon injection. The main disadvantage is the lack of independent control and adjustment in the transverse and longitudinal distribution. The incoming beam momentum spread and jitter must also be strictly controlled.

2.6.4 Other novel injection schemes

Other novel injection schemes include resonance injection, radio-frequency stacking. and beam-cooling stacking, although the process is often slow to accommodate a high repetition rate. Schemes presently under research and development for high-intensity beams includes laser-stripping and plasma-stripping injection.

Problem 2.3 Evaluate possible painting with steering in both planes ... Discuss advantage and disadvantage in comparison with orbit-painting/angle-steering hybrid schemes and correlated/anti-correlated schemes ...

2.7 Longitudinal Beam Capture and Ramping

During initial beam capture and subsequent energy ramping, heavy beam loss often occurs. For multi-turn injection, although in principle even a dc beam can be captured longitudinally when the condition of adiabaticity is satisfied

$$\frac{1}{\Omega_s^2}\frac{d\Omega_s}{dt} \ll 1 \tag{44}$$

in practice the beam loss is often excessive. Beam pre-chopping is commonly performed before ring injection at a low energy.

The bunching factor can be enhanced when RF systems of two or more different frequencies are used. Figure 36 shows the longitudinal phase space of a dual-harmonic RF system at a stationary state. The maximum achievable bunching factor is about 0.5 for an accumulator, and about 0.35 for a RCS. Techniques employing wide-band cavities (barrier cavity) have also been successfully demonstrated to increase beam intensity [20].

Beam loss at initial ramping is usually associated with the reduction of the stable RF bucket phase-space area when the synchronous phase is increased from zero at injection (when below transition) to a finite value in a short time. Both the RF voltage and the synchronous phase need to be carefully programmed to ensure a monotonically increasing bucket area.

Acceleration is typically achieved with ferrite-loaded RF cavities. At a frequency of MHz range, the acceleration gradient is of the order of 10 kV/m. The space required for the installation of a high-voltage (typically several hundred kV) RF system can be significant for an RCS. Cavities using Magnetic Alloy material [21] have been successfully tested at AGS to achieve a gradient of 50 kV/m. The use of IGBT power supplies allows magnet ramping to be programmed, reducing peak ramp rate and current-induced imperfections.

Conventionally, the ring vacuum chamber is either made of metal pipe or is directly attached to magnets (FNAL Booster). For rapid cycling synchrotrons, the vacuum chambers need to be RF shielded to give high impedance to the eddy current but low impedance to the image current. Possible candidates are ceramic chambers with (1) sustained metal wires following the beam envelope (ISIS), (2) printed, internal silver wires (KAON factory [22], SNS RCS [23]), (3) external shielding and internal coating (JJP), and (4) extra thin Inconel chamber (FNAL PD).

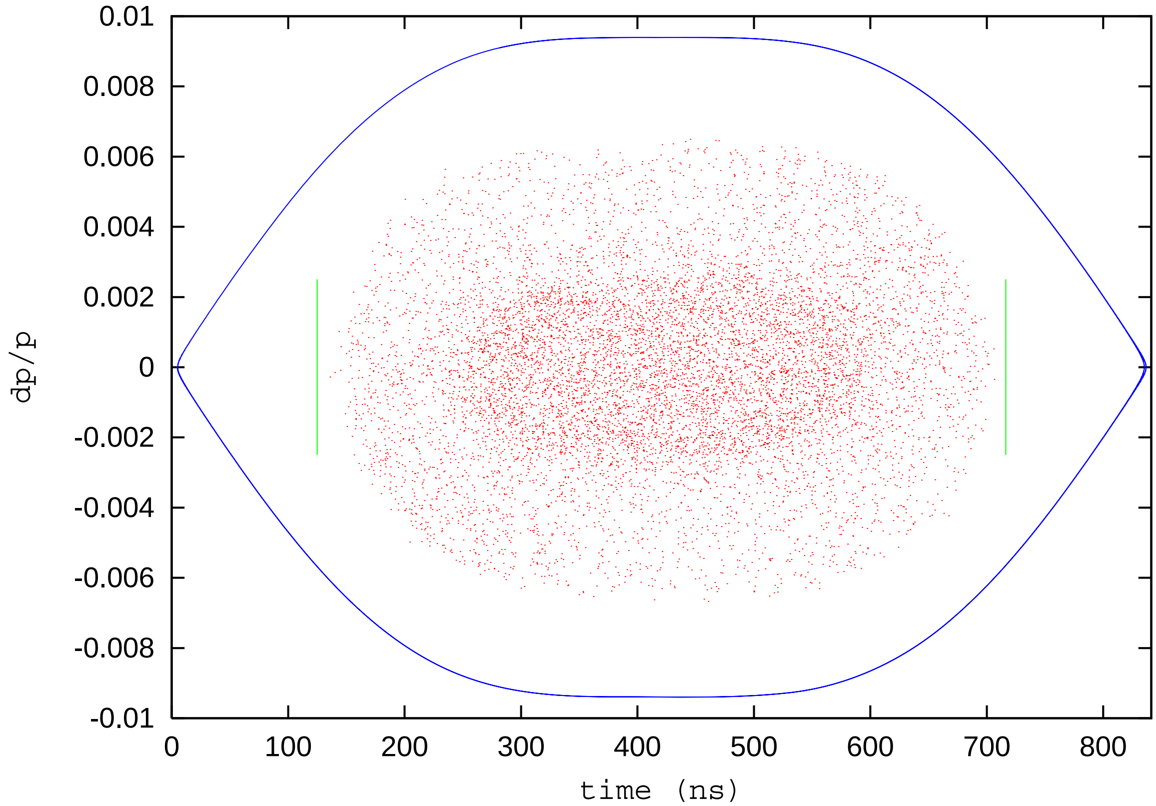

Figure 36: Longitudinal phase space at the end of 2 MW beam accumulation. The blue curve outlines the RF bucket. The vertical lines delineate the edges of a 250 ns gap. The effects of space charge and cavity beam loading are included.

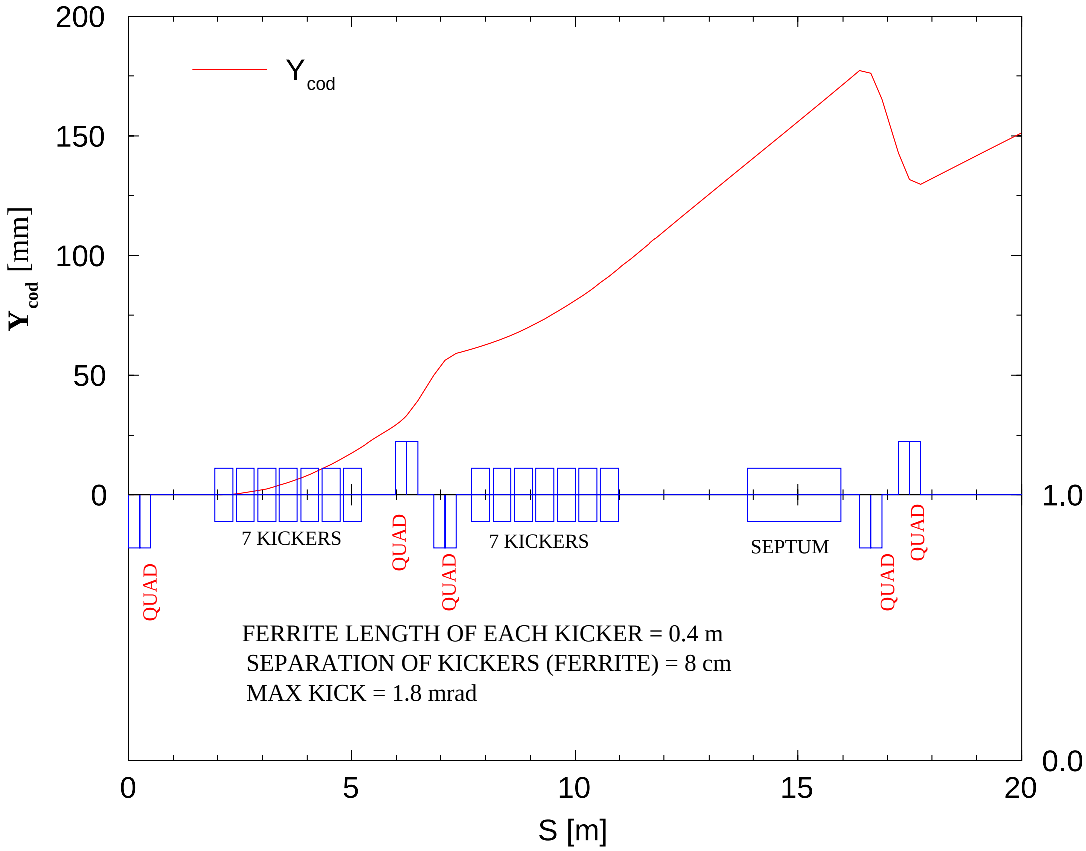

Figure 37: Ring extraction layout and orbit. The beam is kicked vertically by fourteen kicker modules and extracted horizontally by a Lambertson septum magnet.

2.8 Extraction

Extraction is in general a reverse process of single-turn injection. The kick needed is again given by

$$\theta = \frac{x}{\sqrt{\beta_{sep}\beta_{kick}}\sin\Delta\mu} \tag{45}$$

where the optimum phase advance between the kicker and the extraction septum is $\pi/2$.

Extraction is usually an area of heavy radio-activation. In newly designed rings, multiple lumped kickers are used so that beam loss is tolerable when one kicker fails. The pulse forming network is often installed outside of the ring tunnel for easy maintenance. In the case of spallation applications, the phase advance is also chosen so that the beam position on target does not change with kicker failure. In accumulators, cleaning the beam gap with the BIG kicker further reduces uncontrolled extraction loss.

2.9 Magnet System

An accelerator typically consists of dipole magnets for bending, quadrupole magnets for focusing, and sometimes sextupole magnets for chromaticity adjustment. Magnetic correction system typically consists of normal and skew dipole correctors for closed-orbit correction, normal quadrupole correctors for β-wave matching, skew quadrupole correctors for transverse decoupling, and nonlinear (sextupole, octupole ...) correctors for resonance compensation.

Figure 38: Arc bending dipole magnet of the Spallation Neutron Source accumulator ring.

Magnetic errors produce beam orbit deviation, coupling, tune spread, and resonance excitation. For rapid cycling synchrotrons, the leading sources are ramping eddy current and saturation. Ramp rate and peak field need to be moderated, and ramp-dependent corrections need to be implemented to control orbit and coupling.

Accumulators are only susceptible to geometric errors. The leading error components are those allowed by magnet symmetry, and can usually be corrected locally by magnet pole shaping and shimming [25].

Contributions from magnet fringe fields is important for rings of large acceptance and moderate circumference. The relative impulse is approximately equal to the ratio between beam emittance and magnet length [26], which can be corrected by multipole correctors [27].

Chromaticity control is essential for rings operating above transition energy. For rings operating solely below transition, chromatic sextupoles, especially powered in multi-family preserving lattice symmetry, offer tune spread control, instability damping, and off-momentum optics matching. The SNS ring uses four-family chromatic sextupole magnets located in high-dispersion regions, complemented by resonance correction sextupole windings located in zero-dispersion regions [28].

Resonance correction has been used successfully on several machines including CERN PS, AGS and AGS Booster. At the AGS Booster, resonance correction up to normal and skew sextupole has been essential during high-intensity operations (Figure 40) [29].

Neglecting the fringe field and longitudinal components, the magnetic field in a magnet can be expressed using a multipole expansion

$$B_y + iB_x = B_0 \sum_{n=0}^{\infty} (b_n + ia_n)(x + iy)^n \tag{46}$$

For practical convenience, the primed unit is often defined as

$$B_y + iB_x = 10^{-4} B_0 \sum_{n=0}^{\infty} (b'_n + ia'_n) \left(\frac{x + iy}{R_{ref}} \right)^n \tag{47}$$

where B_0 is the nominal guiding field for a dipole, and is equal to $G_0 R_{ref}$ for a quadrupole of gradient G_0. The reference radius R_{ref} is often called the "good-field radius", chosen to specify the extend of the beam. Multipoles allowed by a dipole symmetry are dipole, sextupole, decapole, and so on; multipoles allowed by a quadrupole symmetry are quadrupole, 12-pole (do-decapole), 20-pole, and so on.

Table 5: Integrated quadrupole end field from one magnet end before pole tip end shimming, extracted from a 3D TOSCA calculation (normalized to 10^{-4} of the main field at the reference radius R_{rmref}). For regular ring quadrupoles, $R_{\text{ref}} = 10$ cm; for large ring quadrupoles, $R_{\text{ref}} = 12$ cm (approximately 92% of the quadrupole iron pole tip radius).

n	Normal		Skew	
	$\langle b_n \rangle$	$\sigma(b_n)$	$\langle a_n \rangle$	$\sigma(a_n)$
2	0.4	–	0.0	–
3	0.1	–	0.0	–
4	0.7	–	0.0	–
5	121	–	0.0	–

2.10 Radio-Frequency System

The main purpose of the RF system is to maintain a 250 ns gap for the rise of the extraction kicker. It will also (i) control the peak beam current to prevent space charge stop-band related losses, and (ii) maintain a large momentum spread to prevent coherent instabilities. This momentum spread will also Landau damp coherent quadrupole oscillations which can drive halo formation. Compared with a single harmonic RF, a dual RF system has significant advantages. A barrier bucket RF system maybe even better, but issues such as beam loading still need to be resolved.

The SNS ring will have a dual harmonic system with peak RF amplitudes of 40 kV for harmonic $h = 1$ and 20 kV for $h = 2$. Canonically, the voltages are phased so that the small amplitude synchrotron frequency vanishes. The design of the RF system and power amplifier are driven by beam loading requirements. The power amplifier is designed to fully compensate

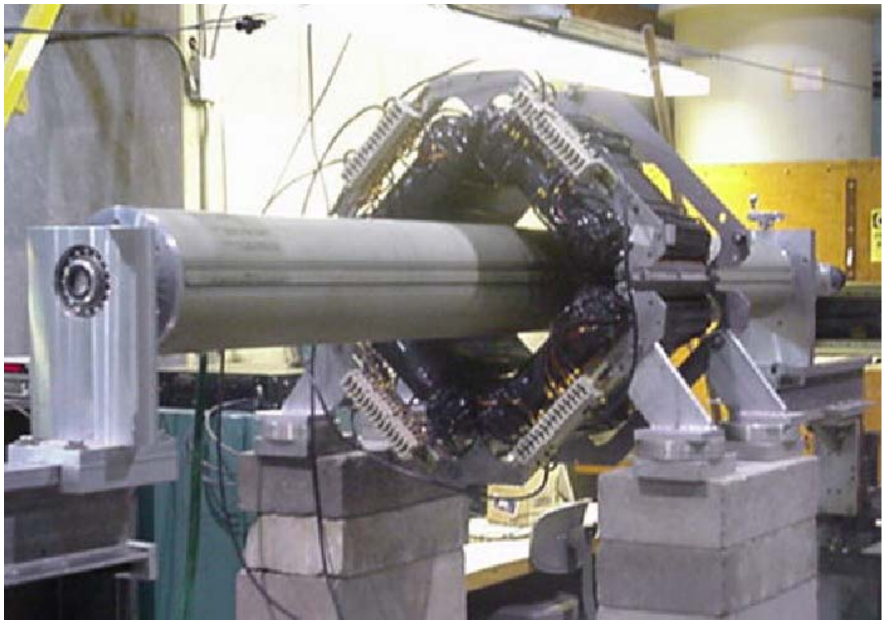

Figure 39: Correction magnet of the Spallation Neutron Source accumulator ring.

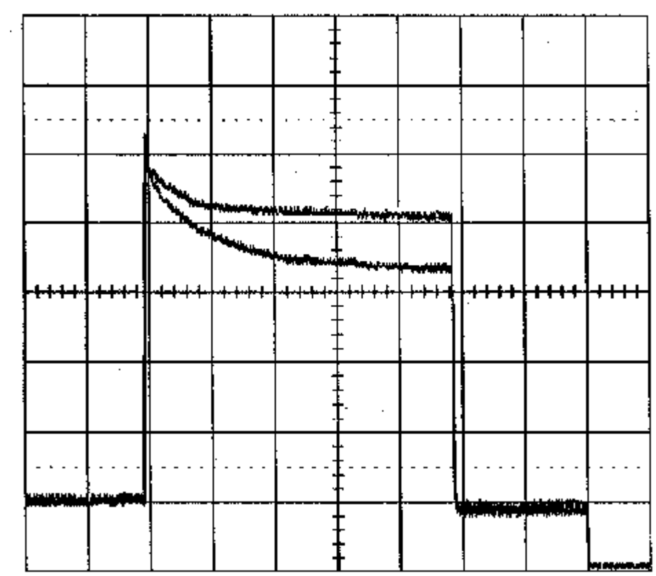

Figure 40: Increase of beam survival with sextupole resonance correction in the AGS Booster (x: 10 ms per box; y: 2×10^{13} ppp at flat top, courtesy C. Gardner).

Table 6: Expected magnetic errors of ring quadrupoles. The multipole strengths are normalized to 10^{-4} of the main field at the reference radius R_{ref}.

n	Normal		Skew	
	$\langle b_n \rangle$	$\sigma(b_n)$	$\langle a_n \rangle$	$\sigma(a_n)$
Body	[unit]			
2	0.0	-2.46	0.0	-2.5
3	0.0	-0.76	0.0	-2.0
4	0.0	-0.63	0.0	1.29
5	0.20	0.0	0.0	1.45
6	0.0	0.02	0.0	0.25
7	0.0	-0.63	0.0	0.31
8	0.0	0.17	0.0	-0.11
9	0.70	0.0	0.0	1.04

Table 7: Expected alignment errors of ring magnets based on the survey measurement of the AGS Booster magnets and the AGS-to-RHIC transfer line magnets.

Item	Value
Integral field variation (rms)	10^{-4}
Integral field, transverse variation (rms)	10^{-4}
Ring dipole sagitta deviation	3 cm
Magnetic center position (rms)	0.1 – 0.5 mm
Magnet longitudinal position (rms)	0.5 mm
Mean field roll angle (rms)	0.2 – 1 mrad

the beam current while providing the quadrature component to drive the gap voltage. As the beam is accumulated in the ring, a feed-forward system will adjust the input into the low-level RF drive.

Shown in Fig. 36 are the results of a simulation using a linac bunch length of 546 ns with the first harmonic voltage ramped from 30 kV to 40 kV over the first 500 turns. The amplitude of the second harmonic was half the amplitude of the first for the entire simulation, which included beam loading and longitudinal space charge. The RF was corrected using both feed forward and low level loops. We note that the full momentum spread ($\Delta p/p$) of the incoming linac beam, after the energy-spreading cavity, is $\pm 0.26\%$. Also, at the end of injection the beam bunching factor is approximately 0.46.

2.11 Instability Control

Instabilities are commonly observed in proton rings. Head-tail instability was observed near injection in KEK PS, CERN PS and AGS, and suspected to be due to chromaticity change caused by eddy current-induced sextupole fields (proportional to $\dot{B}/B$) in the vacuum chamber under dipole magnets. This type of instability can be cured by chamber correction windings (AGS Booster), chromaticity control, octupole field damping, and tune manipulation. Negative mass and microwave instabilities are observed at CERN PS, SPS, AGS, and KEK PS, and can be cured by impedance reduction measures including shielding of vacuum ports and septa, increasing the bunch length and reduction in bunch peak density using dilution cavities. Coupled bunch instability has been observed at CERN PS Booster, PS, SPS, and AGS, and damped by fast feedback systems and Landau damping systems. ISIS programs tunes in each cycle to accommodate natural chromaticity variation, space-charge tune depression, and to avoid resistive-wall head-tail instability [14].

A fast, high-frequency, transverse instability was observed at PSR with both coasting and bunched proton beams, associated with peak intensity-dependent electron accumulation. The electron accumulation is associated with secondary emission from the vacuum chamber, and TiN coating of one straight section suppresses the measured electrons by a factor of about 100. All effective control involves Landau damping [7] (RF voltage and momentum spread increase, inductive insert, sextupole adjustment, etc.). A similar instability was observed at ISR and cured by installing more clearing electrodes [34], and at AGS Booster during coasting beam operation [35].

Impedance minimization is an important measure to prevent instabilities. Improved vacuum chamber by-pass is planned at CERN PS Booster, and shielding of magnet septa and vacuum ports are underway at CERN SPS. ISIS incorporates RF shielding that follows the beam contours and smooth chamber transition, collects stripped electrons, and uses low impedance ferrite extraction kickers.

With the SNS ring, a momentum aperture of $\pm 2\%$ is designed for the beam with $\sim 290\pi$mm$\cdot$mr normalized emittance to allow adequate Landau damping. Vacuum chamber steps are tapered, and bellows and ports are shielded. Chromatic sextupole families are designed for instability control. A relatively high RF voltage and a gap-cleaning (BIG) kicker help preserve a clean beam gap. Magnets near the injection foil are specially tapered to collect stripping electrons. The vacuum chamber's inner surface is coated with TiN to reduce the secondary electron emission yield. Other measures include winding solenoids on straight-section chambers, and reserving space for future wide-band damping systems [8].

2.12 Diagnostics

The ring accumulation and acceleration is often a dynamic process during which the beam intensity increases by several orders of magnitude, and the transverse beam radius increases by more than a factor of 10. The ring diagnostics instrumentation is designed with a wide range of sensitivity and turn-by-turn capability to monitor beam intensity (beam current monitors), position (beam-position monitors), transverse and longitudinal profiles (ionization profile monitor, wall current monitor), and beam loss (loss monitor). Dual-plane beam-position monitors are installed in the critical areas, near the ring straight-section doublets and the middle of the arcs for orbit monitoring and local decoupling. Any beam residual between subsequent micro bunches can be detected by a beam-in-gap monitor, and removed by a beam-in-gap kicker. Electron detectors are planned to monitor the electron cloud in the vacuum chamber. The controls system is designed to immediately shut off subsequent beam pulses when a critical device failure is detected.

Multi-particle effects, such as space-charge, impedence or the electron-cloud are dominating the dynamics of particles in high-intensity rings. On the other hand, for the safe and successfull comissioning of the machine, i.e. when the beam current is still low, single-particle dynamics considerations have to be taken into account. In order to set the basis for a successfull operation towards the high-intensity goal, linear effects such as orbit, coupling and optics functions' distortion, and non-linear ones, such as multi-pole magnet errors and fringe-fields have to be carefully modeled, measured and corrected. In fact, it is the interplay of these single-particle effects with the multi-particle ones that severely limit the performance of a high-intensity machine.

3 Single-Particle Dynamics

3.1 The single-particle relativistic Hamiltonian

The non-linear motion of single particles in an accelerator can be described by the Hamiltonian:

$$H(\mathbf{x},\mathbf{p},t) = c\sqrt{\left(\mathbf{p} - \frac{e}{c}\mathbf{A}(\mathbf{x},t)\right)^2 + m^2c^2} + e\Phi(\mathbf{x},t) \quad , \tag{48}$$

where the vector $\mathbf{x} = (x, y, z)$ represents the positions in the Cartesian coordinate system, $\mathbf{p} = (p_x, p_y, p_z)$ their conjugate momenta, $\mathbf{A} = (A_x, A_y, A_z)$ the magnetic vector potential, Φ the electric scalar potential and, finally, c and e the velocity of light and particle charge, respectively. The Hamiltonian fully describes the motion of relativistic particles in the presence of electro-magnetic fields and can be derived directly from Maxwell equations through the construction of the relativistic Lagrangian (see for example [38, 39]). The first squared term in parentheses inside the square root represents the ordinary kinetic momentum vector

$$\mathbf{P} = \gamma m\mathbf{v} = \mathbf{p} - \frac{e}{c}\mathbf{A} \quad , \tag{49}$$

with $\mathbf{v}$ the particle velocity and $\gamma = (1 - v^2/c^2)^{-1/2}$ the relativistic factor. By replacing the expression (49) in (48) and working out the square root, one can show that the Hamiltonian expresses the total energy of the particle

$$H \equiv E = \gamma mc^2 + e\Phi \quad . \tag{50}$$

Note also that, in the absence of electric fields, the total kinetic momentum can be expressed as:

$$P = \left(\frac{H^2}{c^2} - m^2c^2\right)^{1/2} \quad . \tag{51}$$

The equations of motions are given by Hamilton's equations $(\dot{\mathbf{x}}, \dot{\mathbf{p}}) = [(\mathbf{x}, \mathbf{p}), H]$[1], where the Poisson brackets operation between two functions is defined by:

$$[F, G] = \sum_i \frac{\partial F}{\partial x_i}\frac{\partial G}{\partial p_i} - \frac{\partial F}{\partial p_i}\frac{\partial G}{\partial x_i} \quad ,$$

[1]The dots denote derivatives in the independent variable, i.e. the time t in our case.

with the index i running from 1 to the total number of degrees of freedom of the system N ($N = 3$ in our case). It is straightforward to verify that the equations of particle motion are indeed the Lorentz equations:

$$\frac{d\boldsymbol{P}}{dt} = \boldsymbol{F} = e\left(\boldsymbol{E} + \frac{\boldsymbol{v}}{c}\times\boldsymbol{B}\right) \tag{52}$$

taking into acount that the magnetic field is $\boldsymbol{B} = \boldsymbol{\nabla}\times\boldsymbol{A}$ and the electric field $\boldsymbol{E} = \boldsymbol{\nabla}\cdot\Phi$

For circular accelerators, it is useful to use a coordinate system based on a reference curve defined by the vector $\mathbf{r_0}(s)$, where s now is the distance along the curve. This reference curve is defined to be the closed trajectory of a particle with reference momentum P_0 in the guiding magnetic field B_0. For this, a symplectic transformation is applied from the original variables $(\mathbf{x}, \mathbf{p})$ to the new variables $(\mathbf{x}', \mathbf{p}') = (x, y, s, p_x, p_y, p_s)$ through a mixed variables generating function (e.g. see [40]). The new Hamiltonian takes the form [41]:

$$H(\mathbf{x}', \mathbf{p}', t) = c\sqrt{(p_x - \frac{e}{c}A_x)^2 + (p_y - \frac{e}{c}A_y)^2 + \frac{(p_s - \frac{e}{c}A_s)^2}{(1+\frac{x}{\rho(s)})^2} + m^2c^2} + e\Phi(\mathbf{x}', t) \tag{53}$$

where $A_s = (\mathbf{A}\cdot\hat{\mathbf{s}})(1 + \frac{x}{\rho(s)})$, $p_s = (\mathbf{p}\cdot\hat{\mathbf{s}})(1 + \frac{x}{\rho(s)})$ and $\rho(s)$ is the local radius of curvature.

Taking into account that the motion, is taking place in a circular machine, it is convenient to use the path s as the independent variable instead of the time t. This is a standard transformation where the Hamiltonian is defined now by the variable p_s as

$$\mathcal{H} \equiv -p_s(x, y, t, p_x, p_y, -H)$$

and the new pair of conjugate variables are $(t, -H)$. If there is no electric field, the new Hamiltonian is

$$\mathcal{H} \equiv (-p_s) = -\frac{e}{c}A_s - \left(1 + \frac{x}{\rho(s)}\right)\sqrt{\frac{H^2}{c^2} - m^2c^2 - (p_x - \frac{e}{c}A_x)^2 - (p_y - \frac{e}{c}A_y)^2}\ . \tag{54}$$

Assuming that there is no time dependence in the magnetic fields, the Hamiltonian is a constant of motion. Actually, in a real accelerator, the magnetic fields do change with time and there are longitudinal electric fields produced by the RF cavities to accelerate the particles (as in the high-intensity Rapid Cycling Synchrotrons) or to keep constant the longitudinal bunch length (as in high-intensity accumulators). Most of the times, however, the longitudinal motion is a much slower process than the transverse one. Hence, the longitudinal dynamics can be considered well decoupled with respect to the transverse and treated separately.

3.2 Linear betatron motion

Consider now a ring that has only dipoles to bend the particles and quadrupoles to focus them. Furthermore, let's assume that the magnetic fields have only transverse components[2]

[2]We will see later that this is not true for the field near the magnet edges, which give rise to the so called *fringe-field* effects

and that these components are linear with respect to the transverse variables:

$$\begin{aligned} B_x &= \quad b_1(s)y \\ B_y &= -\, b_0(s) + b_1(s)x \end{aligned} \quad , \tag{55}$$

The main bending field $B_0 \equiv b_0(s)$ is such that the particle with the reference momentum P_0 will follow a trajectory with local radius of curvature, i.e.:

$$B_0(s) = \frac{P_0 c}{e\rho(s)} \quad . \tag{56}$$

The constant quantity $B\rho = \dfrac{P_0 c}{e}$ is called the *magnetic rigidity* of the beam (measured in Tesla $\cdot$ m). It is convenient to define also the normalized quadrupole gradient

$$K(s) = b_1(s)\frac{e}{cP_0} = \frac{b_1(s)}{B\rho} \quad . \tag{57}$$

which has dimensions of $1/\mathrm{m}^2$. By the definition of the magnetic vector potential $\mathbf{B} = \nabla \times \mathbf{A}$, we have that $A_x = A_y = 0$ and

$$A_s(x,y,s) = -\frac{P_0 c}{e}\left[\frac{x}{\rho(s)} + \left(\frac{1}{\rho(s)^2} - K(s)\right)\frac{x^2}{2} + K(s)\frac{y^2}{2}\right] \quad . \tag{58}$$

Thus, the Hamiltonian can be written as:

$$\mathcal{H} \equiv (-p_s) = -P_0\left[\frac{x}{\rho(s)} + \left(\frac{1}{\rho^2} - K(s)\right)\frac{x^2}{2} + K(s)\frac{y^2}{2}\right] - \left(1 + \frac{x}{\rho(s)}\right)\sqrt{P^2 - p_x^2 - p_y^2} \quad . \tag{59}$$

Note that the equations of motion, even with all the simplified assumptions, are still non-linear in the canonical momenta. The usual step taken is to expand the square root in the above expression and keep only terms up to the leading order. Introducing the momentum spread $\delta = \dfrac{\delta P}{P_0} = (\dfrac{P - P_0}{P_0})$, rescaling the Hamiltonian with P and transforming the momenta such that $(p_x, p_y) \mapsto (p_x/P, p_y/P)$, we get the new Hamiltonian:

$$\hat{\mathcal{H}} \equiv (-p_s/P) = \frac{1}{2}\left(p_x^2 + p_y^2\right) + \frac{\delta}{1+\delta}\frac{x}{\rho(s)} + \frac{1}{1+\delta}\left[\left(\frac{1}{\rho(s)^2} - K(s)\right)\frac{x^2}{2} + K(s)\frac{y^2}{2}\right] \quad . \tag{60}$$

In order for the expansion to hold, $p_{x,y}/P \ll 1$, which is true in most of the high-energy accelerators. However, in low-energy high-intensity machines, as we will later see, the "kinematic" higher-order momentum terms should not be neglected as they introduce a noticeable non-linear effect. Note also that by rescaling the Hamiltonian, the new momentum is just the slope of the positions , *e.g.* $p_x = \dfrac{dx}{ds} \equiv x'$

The equations of motion are now given by

$$\begin{aligned} x'' + \frac{1}{1+\delta}\left(\frac{1}{\rho(s)^2} - K(s)\right) x &= \frac{\delta}{1+\delta}\frac{1}{\rho(s)} \\ y'' + \frac{1}{1+\delta}K(s)y &= 0 \end{aligned} \quad , \tag{61}$$

where the primes denote derivatives with respect to s. They are independent with each other, linear in the transverse variables, with periodic coefficients on s with period the circumference of the ring C. These are the usual Hill's equations describing the betatron motion.

It is now useful to make a last transformation which centers the coordinate system on the closed orbit. The closed orbit for the vertical plane is $y_0(s) = 0$. On the other hand for the horizontal plane the solution $x_0(s)$ is not zero, due to the existence of the linear term in the Hamiltonian which comes from the horizontal bending of the trajectory and the existence of off-momentum particles. The same would have been the case for the vertical plane if we have imposed also vertical bending of the trajectory and/or vertical displacement due to other steering errors. It is useful now to introduce the horizontal *dispersion* function $D_x(s) = x_0/\delta$. By replacing the periodic solution to the Hill's equation describing the horizontal motion we get a differential equation from which the dispersion can be computed

$$D_x'' - \frac{1}{1+\delta}K_x(s)D_x = \frac{1}{\rho(s)} \quad ,$$

where we set $K_x(s) \equiv \dfrac{1}{\rho(s)^2} - K(s)$ and $K_y(s) \equiv K(s)$.

Now we perform a symplectic transformation from the old variables (x, p_x) to the new variables $x_\beta, p_{x\beta}$ through the mixed variables generating function $F_2(x, p_{x\beta}) = (x - x_0)(p_{x\beta} + p_{x0})$. One can easily show that this transformation just shifts the coordinates origin on the closed orbit and eliminates the linear term from the Hamiltonian. These are called Legendre transformations and they always preserve the symplectic structure of the system. The equations of motion have the form:

$$x'' + K_x(s)x, = 0 \qquad \text{and} \qquad y'' + K_y(s)y = 0 \quad . \tag{62}$$

which are homogeneous equations with periodic coefficients $K_{x,y}(s) = K_{x,y}(s+C)$. It is worth noticing that the imposed periodicity by the design of the lattice is usually stronger. By Floquet theory [42] we know that homogeneous equations with periodic coefficients (61), have solution of the form:

$$x = \sqrt{A_x\beta_x(s)}\cos(\psi_x(s) + \psi_{0x}) \qquad \text{and} \qquad y = \sqrt{A_y\beta_y(s)}\cos(\psi_y(s) + \psi_{0y}) \quad . \tag{63}$$

where the Courant-Snyder amplitude function $\beta_{x,y}(s)$ is the periodic solution of the equation

$$\beta_{x,y}''' + 4K_{x,y}(s)\beta_{x,y}' + 2K_{x,y}'(s)\beta_{x,y} = 0 \quad , \tag{64}$$

with the additional condition

$$\beta_{x,y}\beta_{x,y}'' + (\beta_{x,y}'/2)^2 + K_{x,y}(s)\beta_{x,y}^2 = 1 \quad , \tag{65}$$

It is useful to introduce the alpha $\alpha_{x,y} = -\beta'_{x,y}/2$ and gamma $\gamma_{x,y} = (1+\alpha^2_{x,y})/\beta'_{x,y}$ functions. These solutions describe the *betatron oscillations*. The quantity $A_{x,y}$ is called the Courant-Snyder invariant and $\psi_{0x,y}$ the initial phase. The phase advance is

$$\psi_{x,y}(s) = \int_0^s \frac{d\tau}{\beta_{x,y}(\tau)} \quad . \tag{66}$$

and the tunes:

$$Q_{x,y} = \frac{1}{2\pi}\int_0^C \frac{ds}{\beta_{x,y}(s)} \quad . \tag{67}$$

Note that, in the presence of non-linear terms in the equation of motion the periodic solution and as consequence the dispersion and the beta functions are not the same and they have to be recalculated from the full non-linear system of equations of motion.

3.3 Action-angle variables

In the language of Hamiltonian dynamical systems, the Hamiltonian (60) is *integrable*, i.e. there exist as many independent integrals of motion in involution (their Poisson brackets vanish) as the degrees of freedom of the system. In our case, the system has 3 degrees of freedom, with the one degree being periodic. In the case of integrable Hamiltonians one can perform a symplectic transformation to the action-angle variables, and the Hamiltonian will only depend on the actions $H = H_0(J_x, J_y)$. The actions represent the volume enclosed by the trajectories in each degree of freedom, i.e. $J_x = \oint p_x dx$. In our case, we use the generating functions

$$F_1(x,\phi_x,y,\phi_y,s) = -\frac{x^2}{2\beta_x(s))}\left[\tan\left(\phi_x+\theta_x(s)\right)+\alpha_x(s)\right] - \frac{y^2}{2\beta_y(s))}\left[\tan\left(\phi_y+\theta_y(s)\right)+\alpha_y(s)\right] \tag{68}$$

The transformation equations are:

$$\begin{aligned} x(s) =& \sqrt{2\beta_x(s)J_x}\cos\left(\phi_x(s)+\theta_x(s)\right) \\ p_x(s) =& -\sqrt{\frac{2J_x}{\beta_x(s)}}\left[\sin\left(\phi_x(s)+\theta_x(s)\right)+\alpha_x(s)\cos\left(\phi_x(s)+\theta_x(s)\right)\right] \end{aligned} \tag{69}$$

The quantity

$$\theta_x(s) = -\arctan\left[\frac{\beta_x(s)x'+\alpha_x(s)x}{x}\right] - \phi_x(s) \quad . \tag{70}$$

is used in order to have a phase which advances linearly with s. The new Hamiltonian is:

$$H_0(J_x,J_y) = \frac{1}{R}(Q_xJ_x+Q_yJ_y) \quad , \tag{71}$$

where $R = 2\pi/C$ is the average radius of the ring. The equations of motion are

$$\begin{aligned} J_x &= \text{constant} \quad , \qquad J_y = \text{constant} \\ \phi_x(s) &= \phi_{x0}(s) + \frac{Q_x(s-s_0)}{R} \quad , \qquad \phi_y(s) = \phi_{y0}(s) + \frac{Q_y(s-s_0)}{R} \quad , \end{aligned} \tag{72}$$

and describe a 2-torus in the phase space $(\phi_x, \phi_y, J_x, J_y)$. Solving the new action in terms of the old variables we have:

$$J_x = \frac{1}{2\beta_x(s)}\left[x^2 + (\beta_x(s)p_x + \alpha_x(s)x)^2\right] \quad , \tag{73}$$

and an equivalent expression for J_y.

3.4 Generalized non-linear Hamiltonian

3.4.1 Transverse field expansion

Up to now, we neglected all non-linear terms in the accelerator, which unfortunately is far from being true. Let assume again a two dimensional transverse field. In that case one can apply the theory of analytic functions (e.g. see [43]). From the basic law of magneto-statics which implies the absence of magnetic mono-poles we have that $\boldsymbol{\nabla}\cdot\boldsymbol{B} = 0$. It follows that it exists a magnetic vector potential $\boldsymbol{A}$ such that $\boldsymbol{B} = \boldsymbol{\nabla}\times\boldsymbol{A}$. Because of the fact that we assumed a two-dimensional field, the vector potential has only one component A_z. On the other hand, the Ampére's law in vacuum (that is inside the beam pipe) is $\boldsymbol{\nabla}\times\boldsymbol{B} = 0$. Then, it exists a scalar potential V such that $\boldsymbol{B} = \boldsymbol{\nabla}V$. Combining the equations defining the vector and scale potential we have:

$$B_x = -\frac{\partial V}{\partial x} = \frac{\partial A_z}{\partial y} \qquad \text{and} \qquad B_y = -\frac{\partial V}{\partial y} = \frac{\partial A_z}{\partial s} \tag{74}$$

The equations (74) represent the Cauchy-Riemann conditions for the real and imaginary part of an analytic function. Thus, we may define a complex potential of $x + iy$ as

$$\mathcal{A}(x+iy) = A_z(x,y) + iV(x,y) = \sum_{n=1}^{\infty}(\kappa_n + i\lambda_n)(x+iy)^n \tag{75}$$

and this expansion is convergent inside a circle of radius $|z| = r_c$ which is the closest distance to an iron yoke or collar where the Eqs. (74) are not satisfied any more and so does the analyticity of the function. The coefficients κ_n and λ_n can be associated with the normal and skew multipole coefficients

$$b_{n-1} = -\frac{n\kappa_n r_0^{n-1}}{B_0} \qquad \text{and} \qquad a_{n-1} = \frac{n\lambda_n r_0^{n-1}}{B_0} \tag{76}$$

where r_0 is the reference radius which is chosen to be the outermost conceivable deviation of the beam particles (a few cm for the high intensity rings) and B_0 the main field. Thus the vector potential component becomes:

$$A_z(x,y) = -B_0 r_0 \Re e \sum_{n=0}^{\infty} \frac{b_n - ia_n}{n+1} (\frac{x+iy}{r_0})^{n+1} \tag{77}$$

Note that with this definition, for $n = 0$ we have the dipole terms, $n = 1$ the quadrupole, $n = 2$ the sextupole, $n = 3$ the octupole, etc. (US convention).

3.4.2 Derivation of the Hamiltonian

We start from the relativistic Hamiltonian (54). Setting $A_x = A_y = 0$, rescaling with P and expanding the square root up to leading order we get

$$\mathcal{H} \equiv (-p_s/P) = \frac{1}{2}\left(p_x^2 + p_y^2\right) - \frac{x}{\rho(s)} - \frac{e}{cP} A_s \tag{78}$$

The vector potential component A_s is:

$$\begin{aligned} A_s &= (\mathbf{A} \cdot \hat{\mathbf{s}})(1 + \frac{x}{\rho(s)}) \\ &= (1 + \frac{x}{\rho(s)}) B_0 \Re e \sum_{n=0}^{\infty} \frac{b'_n - ia'_n}{n+1} (x+iy)^{n+1} \end{aligned} \tag{79}$$

Now, as before, one may want to center the coordinate system to the closed orbit. Orbit distortions are produced by steering errors and also by the momentum spread of the beam. Thus, we may replace x by $x_\beta + D_x\delta + x_0$ and y by $y_\beta + D_y\delta + y_0$ where $\delta = \delta P/P_0$ and $D_{x,y}$ the dispersion function. Using the generating function $F_2(x, p_{x\beta}, y, p_{y\beta}) = (x - D_x\delta - x_c)p_{x\beta} + (y - D_y\delta - y_c)p_{y\beta}$. The Hamiltonian takes the form:

$$\mathcal{H}' = H_0 + \sum_{k_x,k_y} h_{k_x,k_y}(s) x^{k_x} y^{k_y} \tag{80}$$

where H_0 is the integrable Hamiltonian (60). The terms $h_{k_x,k_y}(s)$ are periodic and depend on the multi-pole coefficients and the closed orbit displacements $\Delta_x = D_x\delta + x_0$ and $\Delta_y = D_y\delta + y_0$.

3.5 Classical perturbation theory

The Hamiltonian (78) is not integrable. However, if the non-integrable part is small compared to the integrable, one can expand the generating function and the Hamiltonian and try to solve the equations of motion order by order. This is the purpose of classical perturbation theory. The technique was initially developed by Linstead [44] and put in terms of canonical transformations by Poincaré [45] and Von-Zeipel [46]. A general discussion of the method can be also found in [47].

First consider a general Hamiltonian with n degrees of freedom and time dependence. After transformation in the n-dimensional action-angle variables $\boldsymbol{J}, \boldsymbol{\varphi}$ of the integrable system, it can be brought to the general form

$$H(\boldsymbol{J}, \boldsymbol{\varphi}, \theta) = H_0(\mathbf{J}) + \epsilon H_1(\boldsymbol{J}, \boldsymbol{\varphi}, \theta) + \mathcal{O}(\epsilon^2) \tag{81}$$

where the non-integrable part $H_1(\boldsymbol{J}, \boldsymbol{\varphi}, \theta)$ is 2π-periodic on θ and φ. The motion now does not take place on tori, as in the case of the integrable Hamiltonian. Assuming that the perturbation is small, distorted tori still persist the perturbation. One may try then to "straighten up" the distorted tori, by seeking a transformation in some new action angle variables $(\bar{\boldsymbol{J}}, \bar{\boldsymbol{\varphi}})$, in order for the new Hamiltonian to be written as a function of the new actions alone $\bar{H}(\bar{\boldsymbol{J}})$. For this we introduce a near-identity mixed variables generating function

$$S(\bar{\boldsymbol{J}}, \boldsymbol{\varphi}, \theta) = \bar{\boldsymbol{J}} \cdot \boldsymbol{\varphi} + \epsilon S_1(\bar{\boldsymbol{J}}, \boldsymbol{\varphi}, \theta) + \mathcal{O}(\epsilon^2) \tag{82}$$

our purpose it to find a suitable representation for $S_1(\bar{\boldsymbol{J}}, \boldsymbol{\varphi}, \theta)$. The old action, new angle and new Hamiltonian can be found by the canonical transformation equations:

$$\begin{aligned} \boldsymbol{J} &= \bar{\boldsymbol{J}} + \epsilon \frac{\partial S_1(\bar{\boldsymbol{J}}, \boldsymbol{\varphi}, \theta)}{\partial \boldsymbol{\varphi}} + \mathcal{O}(\epsilon^2) \\ \bar{\boldsymbol{\varphi}} &= \boldsymbol{\varphi} + \epsilon \frac{\partial S_1(\bar{\boldsymbol{J}}, \boldsymbol{\varphi}, \theta)}{\partial \bar{\boldsymbol{J}}} + \mathcal{O}(\epsilon^2) \end{aligned} \tag{83}$$

Then, we can express the old variables in terms of the new ones by inverting the previous equations:

$$\begin{aligned} \boldsymbol{J} &= \bar{\boldsymbol{J}} + \epsilon \frac{\partial S_1(\bar{\boldsymbol{J}}, \bar{\boldsymbol{\varphi}}, \theta)}{\partial \bar{\boldsymbol{\varphi}}} + \mathcal{O}(\epsilon^2) \\ \boldsymbol{\varphi} &= \bar{\boldsymbol{\varphi}} - \epsilon \frac{\partial S_1(\bar{\boldsymbol{J}}, \bar{\boldsymbol{\varphi}}, \theta)}{\partial \bar{\boldsymbol{J}}} + \mathcal{O}(\epsilon^2) \end{aligned} \tag{84}$$

Note that S_1 is now expressed in terms of the new variables. Then the new Hamiltonian is:

$$\bar{H}(\bar{\boldsymbol{J}}, \bar{\boldsymbol{\varphi}}, \theta) = H(\boldsymbol{J}(\bar{\boldsymbol{J}}, \bar{\boldsymbol{\varphi}}), \boldsymbol{\varphi}(\bar{\boldsymbol{J}}, \bar{\boldsymbol{\varphi}}), \theta) + \epsilon \frac{\partial S_1(\bar{\boldsymbol{J}}, \bar{\boldsymbol{\varphi}}, \theta)}{\partial \theta} + \mathcal{O}(\epsilon^2) \tag{85}$$

Now, we may expand term by term the old Hamiltonian in the right hand side of (85), in a power series of ϵ, using the expressions of the old variables as a function of the new (see Eq. (84)). Hence, we have for each term to leading order in ϵ:

$$\begin{aligned} H_0(\boldsymbol{J}(\bar{\boldsymbol{J}}, \bar{\boldsymbol{\varphi}})) &= H_0(\bar{\boldsymbol{J}}) + \epsilon \frac{\partial H_0(\bar{\boldsymbol{J}})}{\partial \bar{\boldsymbol{J}}} \frac{\partial S_1(\bar{\boldsymbol{J}}, \bar{\boldsymbol{\varphi}}, \theta)}{\partial \bar{\boldsymbol{\varphi}}} + \mathcal{O}(\epsilon^2) \\ \epsilon H_1(\boldsymbol{J}(\bar{\boldsymbol{J}}, \bar{\boldsymbol{\varphi}}), \boldsymbol{\varphi}(\bar{\boldsymbol{J}}, \bar{\boldsymbol{\varphi}}), \theta) &= \epsilon H_1(\bar{\boldsymbol{J}}, \bar{\boldsymbol{\varphi}}) + \mathcal{O}(\epsilon^2) \end{aligned} \tag{86}$$

Inserting these equations in the expression of the new Hamiltonian and equating the terms of equal order in ϵ, we get in zero order $\bar{H}_0 = H_0(\bar{\boldsymbol{J}})$ and in first order:

$$\bar{H}_1 = \frac{\partial S_1(\bar{\boldsymbol{J}}, \bar{\boldsymbol{\varphi}}, \theta)}{\partial \theta} + \boldsymbol{\omega}(\bar{\boldsymbol{J}}) \cdot \frac{\partial S_1(\bar{\boldsymbol{J}}, \bar{\boldsymbol{\varphi}}, \theta)}{\partial \bar{\boldsymbol{\varphi}}} + H_1(\bar{\boldsymbol{J}}, \bar{\boldsymbol{\varphi}}) \tag{87}$$

where $\boldsymbol{\omega}(\bar{\boldsymbol{J}}) = \dfrac{\partial H_0(\bar{\boldsymbol{J}})}{\partial \bar{\boldsymbol{J}}}$ is the frequency vector of the unperturbed system. Since we made this transformation in order for the new Hamiltonian H_1 to be a function of the new actions

$\bar{\boldsymbol{J}}$ only, we should try to eliminate the $\bar{\boldsymbol{\varphi}}$ dependence in equation (87). For this, we introduce the average part of the leading order perturbation term of the old Hamiltonian H_1 over all the angles $\bar{\boldsymbol{\varphi}}$:

$$\langle H_1 \rangle_{\bar{\varphi}} = \left(\frac{1}{2\pi}\right)^n \oint H_1(\bar{\boldsymbol{J}}, \bar{\boldsymbol{\varphi}}) d\bar{\boldsymbol{\varphi}} \tag{88}$$

and the oscillating part of H_1 is defined as:

$$\{H_1\} = H_1 - \langle H_1 \rangle_{\bar{\varphi}} \tag{89}$$

Inserting the equations (88),(89) in (87) we have:

$$\bar{H}_1 = \frac{\partial S_1(\bar{\boldsymbol{J}}, \bar{\boldsymbol{\varphi}}, \theta)}{\partial \theta} + \boldsymbol{\omega}(\bar{\boldsymbol{J}}) \cdot \frac{\partial S_1(\bar{\boldsymbol{J}}, \bar{\boldsymbol{\varphi}}, \theta)}{\partial \bar{\boldsymbol{\varphi}}} + \langle H_1(\bar{\boldsymbol{J}}, \bar{\boldsymbol{\varphi}}) \rangle_{\bar{\varphi}} + \{H_1(\bar{\boldsymbol{J}}, \bar{\boldsymbol{\varphi}})\} \ . \tag{90}$$

We can now choose S_1 such that the $\bar{\boldsymbol{\varphi}}$ dependence is eliminated, that is

$$\bar{H}_1(\bar{\boldsymbol{J}}) = \langle H_1(\bar{\boldsymbol{J}}, \bar{\boldsymbol{\varphi}}) \rangle_{\bar{\varphi}} \qquad \text{and} \qquad \frac{\partial S_1(\bar{\boldsymbol{J}}, \bar{\boldsymbol{\varphi}}, \theta)}{\partial \theta} + \boldsymbol{\omega}(\bar{\boldsymbol{J}}) \cdot \frac{\partial S_1(\bar{\boldsymbol{J}}, \bar{\boldsymbol{\varphi}}, \theta)}{\partial \bar{\boldsymbol{\varphi}}} = -\{H_1(\bar{\boldsymbol{J}}, \bar{\boldsymbol{\varphi}})\} \ , \tag{91}$$

and now the new Hamiltonian is a function of the new actions only, to leading order in ϵ

$$\bar{H}(\bar{\boldsymbol{J}}) = H_0(\bar{\boldsymbol{J}}) + \epsilon \ \langle H_1(\bar{\boldsymbol{J}}, \bar{\boldsymbol{\varphi}}) \rangle_{\bar{\varphi}} + \mathcal{O}(\epsilon^2) \ . \tag{92}$$

with the new frequency vector

$$\bar{\boldsymbol{\omega}}(\bar{\boldsymbol{J}}) = \frac{\partial \bar{H}(\bar{\boldsymbol{J}})}{\partial \bar{\boldsymbol{J}}} = \boldsymbol{\omega}(\bar{\boldsymbol{J}}) + \epsilon \frac{\partial \langle H_1(\bar{\boldsymbol{J}}, \bar{\boldsymbol{\varphi}}) \rangle_{\bar{\varphi}}}{\partial \bar{\boldsymbol{J}}} + \mathcal{O}(\epsilon^2) \ . \tag{93}$$

The second term in the equation above is the first order correction to the frequency vector. Indeed, this is true if we are able to solve the second part of (91) and recover the appropriate generating function term S_1 which eliminates the angle dependence. To do this, first remember that the perturbation of the original Hamiltonian H_1 is a 2π-periodic on θ and $\bar{\boldsymbol{\varphi}}$. The same should stand for the oscillating part of the perturbation transformed in the new variables. Hence it can be expanded in a Fourier series

$$\{H_1(\bar{\boldsymbol{J}}, \bar{\boldsymbol{\varphi}})\} = \sum_{\boldsymbol{k},p} H_{1\mathbf{k}}(\bar{\boldsymbol{J}}) e^{i(\boldsymbol{k}\cdot\bar{\boldsymbol{\varphi}} + p\theta)} \ , \tag{94}$$

with $\boldsymbol{k} \cdot \bar{\boldsymbol{\varphi}} = k_1\bar{\varphi}_1 + \cdots + k_n\bar{\varphi}_n$. In order to have a solution for (91), the leading order term of the generating function $S_1(\bar{\boldsymbol{J}}, \bar{\boldsymbol{\varphi}}, \theta)$ should be also periodic on θ and $\bar{\boldsymbol{\varphi}}$ and can be expressed as a Fourier series

$$S_1(\bar{\boldsymbol{J}}, \bar{\boldsymbol{\varphi}}, \theta) = \sum_{\boldsymbol{k},p} S_{1\mathbf{k}}(\bar{\boldsymbol{J}}) e^{i(\boldsymbol{k}\cdot\bar{\boldsymbol{\varphi}} + p\theta)} \ , \tag{95}$$

The amplitudes of $S_{1k}(\bar{\boldsymbol{J}})$ are the unknowns and we may get them through (91) by equating same order terms of the two Fourier series:

$$S_{1k}(\bar{\boldsymbol{J}}) = i\frac{H_{1k}(\bar{\boldsymbol{J}})}{\boldsymbol{k}\cdot\boldsymbol{\omega}(\bar{\boldsymbol{J}})+p} \qquad \text{with} \qquad \boldsymbol{k}, p \neq \boldsymbol{0} \ , \tag{96}$$

which gives us the final form of the generating function

$$S(\bar{\boldsymbol{J}},\bar{\boldsymbol{\varphi}}) = \bar{\boldsymbol{J}}\cdot\bar{\boldsymbol{\varphi}} + \epsilon i \sum_{\mathbf{k}\neq\mathbf{0}} \frac{H_{1\mathbf{k}}(\bar{\mathbf{J}})}{\boldsymbol{k}\cdot\boldsymbol{\omega}(\bar{\boldsymbol{J}})+p} e^{i(\boldsymbol{k}\cdot\bar{\boldsymbol{\varphi}}+p\theta)} + \mathcal{O}(\epsilon^2) \ , \tag{97}$$

Now we may substitute the generating function in (84) and get the new invariant actions and angles.

Sometimes, the first order perturbation theory is not enough, either for computational purposes and the demand for increased precision or because the first order correction associated to the average of the perturbation is zero (as in the case of a sextupole magnet perturbation in the accelerator Hamiltonian). In principle, the Poincaré-Von-Zeipel method can be carried out in arbitrary order in ϵ, but the disentangling of the old with the new variables becomes cumbersome, even for the second order. Modern perturbation methods exist, like the Lie transformations, where the complete inversion of variables is not needed and the whole procedure can be done in a completely algorithmic way (e.g. see [48]) employing the power of computers. These methods were applied for the first time in accelerator dynamics by Dragt and Finn [49].

The equation (97) is very important to understand the effect of resonances in a Hamiltonian dynamical system. In general, for any actions $\bar{\boldsymbol{J}}$ there can be found an integer combinations of $\boldsymbol{k}$ and p such that the denominator of the Fourier amplitudes is close to zero. These small denominators prevent the global convergence of (97). Resonances $\boldsymbol{k}\cdot\boldsymbol{\omega}(\bar{\boldsymbol{J}})+p=0$ do not only represent a mathematical culprit but have also physical meaning. The phase space trajectories close to a resonance change their topology and an exact resonance condition blows up the oscillation amplitude of a particle as in the case of a forced pendulum, where the frequency of oscillation equals the forcing frequency.

On the other hand, one may try to apply perturbation techniques that take the singularity to higher order and converge more rapidly at least for some regions of the phase space. These super-convergent perturbation techniques proposed by Kolmogorov [50] are the basis of the KAM theory [51] which states that under certain conditions of the Hamiltonian and provided that the trajectories are far enough from the resonance conditions, we can still find solutions that evolve on invariant tori. However, due to the severe mathematical restrictions of the theory, the applicability to realistic physical systems is limited.

3.5.1 Application to the accelerator Hamiltonian - Resonance driving terms

The classical perturbation techniques were first applied in beam dynamics by Schoch [52] and Hagedorn [53] and it was influenced by the work of Jurgen Moser, who spend some time at CERN during the fifties. They were finally popularized twenty years after by Guignard [54, 55].

In order to apply the classical perturbation techniques in the non-linear Hamiltonian used to describe the motion in a ring under the influence of magnetic imperfections (see Eq. (80)), we first rewrite the transverse variable in the following form:

$$x(s) = \sqrt{\frac{J_x \beta_x(s)}{2}} \left(e^{i(\phi_x(s)+\theta_x(s))} + e^{-i(\phi_x(s)+\theta_x(s))} \right) \tag{98}$$

and the equivalent expression for y. Then, we may transform the Hamiltonian in action-angle variables as described in section 3.3. The Hamiltonian takes the form:

$$\mathcal{H}'(J_x, J_y, \phi_x, \phi_y) = H_0(J_x, J_y) + H_1(J_x, J_y, \phi_x, \phi_y) \tag{99}$$

where the integrable part is given by (71) and the perturbation is

$$H_1(J_x, J_y, \phi_x, \phi_y; s) = \sum_{k_x, k_y} J_x^{k_x/2} J_y^{k_y/2} \sum_j^{k_x} \sum_l^{k_x} g_{j,k,l,m}(s) e^{i[(j-k)\phi_x + (l-m)\phi_y]} \tag{100}$$

with

$$g_{j,k,l,m}(s) = \frac{h_{k_x,k_y}(s)}{2^{\frac{j+k+l+m}{2}}} \binom{k_x}{j} \binom{k_y}{l} \beta_x^{k_x/2}(s) \beta_y^{k_y/2}(s) e^{i[(j-k)\theta_x(s) + (l-m)\theta_y(s)]} \tag{101}$$

and the indexes j, k, l, m satisfy the relations $k_x = j + k$ and $k_y = l + m$. As the perturbed part of the Hamiltonian is periodic in the "time" variable s through the coefficients $h_{k_x,k_y}(s)$, it can be expanded in a Fourier series so that,

$$H_1(J_x, J_y, \phi_x, \phi_y; s) = \sum_{k_x, k_y} J_x^{k_x/2} J_y^{k_y/2} \sum_j^{k_x} \sum_l^{k_x} \sum_{p=-\infty}^{\infty} g_{j,k,l,m;p} e^{i[(j-k)\phi_x + (l-m)\phi_y - p\frac{s}{R}]} \tag{102}$$

with

$$g_{j,k,l,m;p} = \binom{k_x}{j} \binom{k_y}{l} \frac{1}{2^{\frac{j+k+l+m}{2}}} \frac{1}{2\pi} \oint h_{k_x,k_y}(s) \beta_x^{k_x/2}(s) \beta_y^{k_y/2}(s) e^{i[(j-k)\theta_x(s) + (l-m)\theta_y(s) + p\frac{s}{R}]} ds \quad . \tag{103}$$

As shown in the previous chapter, in order to find a generating function which will take us from the unperturbed action variables to the new ones, we will have to expand it in a Fourier series which will not be convergent when $(j-k)\phi_x + (l-m)\phi_y - p\frac{s}{R} = 0$. Setting $n_x = j-k$, $n_y = l-m$ and using (72), we have the resonance condition in the unperturbed tunes $n_x Q_x + n_y Q_y = p$. The coefficients $g_{j,k,l,m;p}$ are called the resonance driving terms. One tries to find ways to minimize them either by changing the magnet design so that the coefficients $h_{k_x,k_y}(s)$ which come from magnet imperfections are small or by introducing magnetic elements that are capable of creating a cancelling effect.

3.6 Tune Shift and Tune Spread

In order to find the first order correction to the tunes (see (93)), we have to compute the derivatives with respect to the action variables of the average part of the perturbation in the Hamiltonian. For a given term $h_{k_x,k_y}(s)x^{k_x}y^{k_y}$ of the polynomial in the perturbation part (80), we have that:

$$\begin{aligned}\delta Q_x &= \frac{J_x^{k_x/2-1}J_y^{k_y/2}}{4\pi^2}\sum_j^{k_x}\sum_l^{k_x}\bar{g}_{j,k,l,m}\oint e^{i[(j-k)\phi_x+(l-m)\phi_y]}d\phi_x d\phi_y \\ \delta Q_y &= \frac{J_x^{k_x/2}J_y^{k_y/2-1}}{4\pi^2}\sum_j^{k_x}\sum_l^{k_x}\bar{g}_{j,k,l,m}\oint e^{i[(j-k)\phi_x+(l-m)\phi_y]}d\phi_x d\phi_y\end{aligned} \tag{104}$$

where $\bar{g}_{j,k,l,m}$ is the average of the coefficient $g_{j,k,l,m}(s)$ around the ring. It can be shown that the integral vanishes for $k_x = j+k$ or $k_y = l+m$ an odd number. This means that we have to go to higher order in the perturbation in order to compute the leading order frequency change. The change of the tunes due the perturbation is called tune shift (or spread) or detuning in the language of accelerator physics. The computation of leading order tune-shift is very useful for characterizing the importance of the non-linear effects in an accelerator ring. Typical values for the tune spread due to different mechanisms in a high-intensity ring are given in Table 8, taking the example of the SNS.

Table 8: Tune spread produced by various mechanisms on a 2 MW beam with transverse emittance of 480 π mm mrad and momentum spread of $\pm1\%$.

Mechanism	Full tune spread
Space charge	0.15-0.2 (2 MW beam)
Chromaticity	±0.08 (1% $\Delta\ p/p$)
Kinematic nonlinearity (480π)	0.001
Fringe field (480π)	0.025
Uncompensated ring magnet error (480π)	±0.02
Compensated ring magnet error (480π)	±0.002
Fixed injection chicane	0.004
Injection painting bump	0.001

3.7 The single resonance treatment - Secular perturbation theory

Consider the general two dimensional Hamiltonian $H(\mathbf{J},\boldsymbol{\varphi}) = H(J_1, J_2, \varphi_1, \varphi_2)$ written in the usual form:

$$H(\mathbf{J},\boldsymbol{\varphi}) = H_0(\mathbf{J}) + \varepsilon H_1(\mathbf{J},\boldsymbol{\varphi}) \tag{105}$$

with the perturbed part being periodic in angles, so that it can be expanded in a Fourier series

$$H_1(\mathbf{J},\boldsymbol{\varphi}) = \sum_{k_1,k_1} H_{k_1,k_2}(J_1,J_2)\exp[i(k_1\varphi_1 + k_2\varphi_2)] \tag{106}$$

A resonance of the form $n_1\omega_1 + n_2\omega_2 = 0$, with $\omega_2 < \omega_1$ will blow up the convergence of the perturbation series and leads to a secular growth of the solution. In order to remove this behavior, we can perform a canonical transformation $(\mathbf{J}, \boldsymbol{\varphi}) \longmapsto (\hat{\mathbf{J}}, \hat{\boldsymbol{\varphi}})$ so as to eliminate one of the original actions. We choose the generating function

$$F_r(\hat{\mathbf{J}}, \boldsymbol{\varphi}) = (n_1\varphi_1 - n_2\varphi_2)\hat{J}_1 + \varphi_2\hat{J}_2 \tag{107}$$

with the transformed Hamiltonian

$$\hat{H}(\hat{\mathbf{J}}, \hat{\boldsymbol{\varphi}}) = \hat{H}_0(\hat{\mathbf{J}}) + \varepsilon\hat{H}_1(\hat{\mathbf{J}}, \hat{\boldsymbol{\varphi}}) \tag{108}$$

ant the perturbation

$$\hat{H}_1(\hat{\mathbf{J}}, \hat{\boldsymbol{\varphi}}) = \sum_{k_1,k_2} H_{k_1,k_2}(\hat{\mathbf{J}}) \exp\left\{\frac{i}{n_1}\left[k_1\hat{\varphi}_1 + (k_1n_2 + k_2n_1)\hat{\varphi}_1\right]\right\} \quad . \tag{109}$$

The relations between the variables are:

$$\begin{array}{rcl} J_1 = n_1\hat{J}_1 & , & J_2 = \hat{J}_2 - n_2\hat{J}_1 \\ \hat{\varphi}_1 = n_1\varphi_1 - n_2\varphi_2 & , & \hat{\varphi}_2 = \varphi_2 \end{array} \quad . \tag{110}$$

This transformation puts the observer in a rotating frame in which the rate of change of the new variable $\dot{\hat{\varphi}}_1 = n_1\dot{\varphi}_1 - n_2\dot{\varphi}_2$ measures the deviation from the resonance. We can now average over the "slow" angle $\hat{\varphi}_2 = \varphi_2$ and to first order we get

$$\bar{H}(\hat{\mathbf{J}}, \hat{\boldsymbol{\varphi}}) = \bar{H}_0(\hat{\mathbf{J}}) + \varepsilon\bar{H}_1(\hat{\mathbf{J}}, \hat{\varphi}_1) \tag{111}$$

with $\bar{H}_0(\hat{\mathbf{J}}) = \hat{H}_0(\hat{\mathbf{J}})$ and

$$\bar{H}_1(\hat{\mathbf{J}}, \hat{\varphi}_1) = \langle\hat{H}_1(\hat{\mathbf{J}}, \hat{\varphi}_1)\rangle_{\hat{\varphi}_2} = \sum_{p=-\infty}^{+\infty} H_{-pn_1,pn_2}(\hat{\mathbf{J}}) \exp(-ip\hat{\varphi}_1) \tag{112}$$

The averaging eliminated one angle and thus

$$\hat{J}_2 = J_2 + J_1\frac{n_2}{n_1} \tag{113}$$

is an invariant of motion. Now, assuming that the Fourier harmonics that dominate the series (112) are the leading ones (i.e for $p = 0, \pm 1$ and and taking into account that $H_{-n_1,n_2} = H_{n_1,-n_2}$ we get the Hamiltonian

$$\bar{H}(\hat{\mathbf{J}}, \hat{\theta}_1) = \bar{H}_0(\hat{\mathbf{J}}) + \varepsilon\bar{H}_{0,0}(\hat{\mathbf{J}}) + 2\varepsilon\bar{H}_{n_1,-n_2}(\hat{\mathbf{J}})\cos\hat{\varphi}_1 \tag{114}$$

Let $\hat{J}_1 = \hat{J}_{10}$ the location of the fixed point inside the resonant island. We introduce the new variable $\Delta\hat{J}_1 = \hat{J}_1 - \hat{J}_{10}$, which positions the coordinate system on the fixed point. Expanding

$\bar{H}(\hat{\mathbf{J}})$ in the vicinity of the fixed point, we get the Hamiltonian describing the motion near the resonance

$$\bar{H}_r(\Delta\hat{J}_1,\hat{\theta}_1) = \left.\frac{\partial^2\bar{H}_0(\hat{\mathbf{J}})}{\partial\hat{J}_1^2}\right|_{\hat{J}_1=\hat{J}_{10}} \frac{(\Delta\hat{J}_1)^2}{2} + 2\varepsilon\bar{H}_{n_1,-n_2}(\hat{\mathbf{J}})\cos\hat{\varphi}_1 \tag{115}$$

This is a remarkable result that suggests that the motion near a typical resonance is like that of the pendulum, with a libration part, a separatrix and a rotation part of the motion.

The libration frequency is as in the case of the pendulum

$$\hat{\omega}_1 = \left(2\varepsilon\bar{H}_{n_1,-n_2}(\hat{\mathbf{J}})\left.\frac{\partial^2\bar{H}_0(\hat{\mathbf{J}})}{\partial\hat{J}_1^2}\right|_{\hat{J}_1=\hat{J}_{10}}\right)^{1/2} \tag{116}$$

The maximum excursion $\Delta\hat{J}_{1\,max}$ occurs on the separatrix and is given by the resonance half width

$$\Delta\hat{J}_{1\,max} = 2\left(\frac{2\varepsilon\bar{H}_{n_1,-n_2}(\hat{\mathbf{J}})}{\left.\frac{\partial^2\bar{H}_0(\hat{\mathbf{J}})}{\partial\hat{J}_1^2}\right|_{\hat{J}_1=\hat{J}_{10}}}\right)^{1/2} \tag{117}$$

3.7.1 Resonance overlap criterion

The secular perturbation theory is the basis for the Chirikov resonance overlap criterion [56, 57]. In fact, as the perturbation grows, the width of resonance island grows. One can imagine then that at some point the separatrices of the two islands overlap. This will permit orbits from the one resonance to diffuse through the separatrices, across the other resonance. Taking that the distance between two resonances is

$$\delta\hat{J}_{1\,n,n'} = \frac{2\left(\frac{1}{n_1+n_2} - \frac{1}{n_1'+n_2'}\right)}{\left|\left.\frac{\partial^2\bar{H}_0(\hat{\mathbf{J}})}{\partial\hat{J}_1^2}\right|_{\hat{J}_1=\hat{J}_{10}}\right|} \tag{118}$$

we get the simple resonance overlap criterion

$$\Delta\hat{J}_{n\,max} + \Delta\hat{J}_{n'\,max} \geq \delta\hat{J}_{n,n'} \tag{119}$$

Actually the mechanism is much more complicated because of the existence of secondary islands that tend to overlap also with the main resonance and the fact that the separatrix when the perturbation is getting bigger and bigger forms a chaotic layer, whose width has to be taken into account. Considering these two effects, we have the modified criterion by the "two thirds" rule.

$$\Delta\hat{J}_{n\,max} + \Delta\hat{J}_{n'\,max} \geq \frac{2}{3}\delta\hat{J}_{n,n'} \tag{120}$$

However, due to the pure geometrical aspect of the criterion, it is quite difficult to extent it in Hamiltonian systems with 3 or more degrees of freedom.

3.7.2 Single resonance treatment for the accelerator Hamiltonian - Resonance widths

We can apply the secular perturbation theory to the accelerator Hamiltonian (99) (see [54, 55]). Consider a resonance term $n_xQ_x+n_yQ_y = p$, which we suppose is the dominant so as to neglect the rest of the expansion (102). Then, we have the single resonance Hamiltonian

$$H(J_x, J_y, \phi_x, \phi_y, s) = \frac{1}{R}(Q_xJ_x + Q_yJ_y) + g_{n_x,n_y}\frac{2}{R}J_x^{\frac{k_x}{2}}J_y^{\frac{k_y}{2}}\cos(n_x\phi_x + n_y\phi_y + \phi_0 - p\frac{s}{R}) \quad (121)$$

where $g_{n_x,n_y}e^{i\phi_0} = g_{j,k,l,m;p}$. Using the generating function (see (107))

$$F_r(\phi_x, \phi_y, \hat{J}_x, \hat{J}_y, s) = (n_x\phi_x + n_y\phi_y - p\frac{s}{R})\hat{J}_x + \phi_y\hat{J}_y \quad (122)$$

we get the Hamiltonian

$$\hat{H}(\hat{J}_x, \hat{J}_y, \phi_x) = \frac{(n_xQ_x + n_yQ_y - p)\hat{J}_x + \hat{J}_y}{R} + g_{n_x,n_y}\frac{2}{R}(n_x\hat{J}_x)^{\frac{k_x}{2}}(n_y\hat{J}_x + \hat{J}_y)^{\frac{k_y}{2}}\cos(\hat{\phi}_x + \phi_0) \quad (123)$$

Thus, we get the two invariants, namely the action $\hat{J}_y$ and the new Hamiltonian $\hat{H}$ (see (113)). Expressing them in the old variables, we get:

$$\begin{aligned} c_1 &= \frac{J_x}{n_x} - \frac{J_y}{n_y} \\ c_2 &= (Q_x - \frac{p}{n_x+n_y})J_x + (Q_y - \frac{p}{n_x+n_y})J_y + 2g_{n_x,n_y}J_x^{\frac{k_x}{2}}J_y^{\frac{k_y}{2}}\cos(n_x\phi_x + n_y\phi_y + \phi_0 - p\frac{s}{R}) \ . \end{aligned} \quad (124)$$

Note that from the first invariant if n_x and n_y have opposite sign, the motion is bounded. This of course is a result of a first order approach and it does not apply in general. These resonances are called *difference* resonances whereas the ons for which n_x and n_y have the same sign are called *sum* resonances. Setting $e = n_xQ_x + n_yQ_y - p$ the distance from the resonance we can compute the resonance stop band width $\Delta e = n_x\Delta Q_x + n_y\Delta Q_y$, which yields:

$$\Delta e = \frac{g_{n_x,n_y}}{R}J_x^{\frac{k_x-2}{2}}J_y^{\frac{k_y-2}{2}}(k_xn_xJ_x + k_yn_yJ_y) \quad (125)$$

3.8 The choice of the working point

Up to know we have not considered a periodicity other than the one coming from the ring circumference. In the process of the design of the lattice, we usually try to impose a periodic structure which is stronger than this one. Then, the resonance condition can be written as $n_xQ_x + n_yQ_y = p = mN$, where m is the super-periodicity of the lattice. One can easily understand that now the only resonance conditions that can take place are the ones that the harmonic p is an integer multiple of m. These resonances are called *structural* or *systematic* resonances, because they are the only ones that are allowed by the structure of the lattice. All

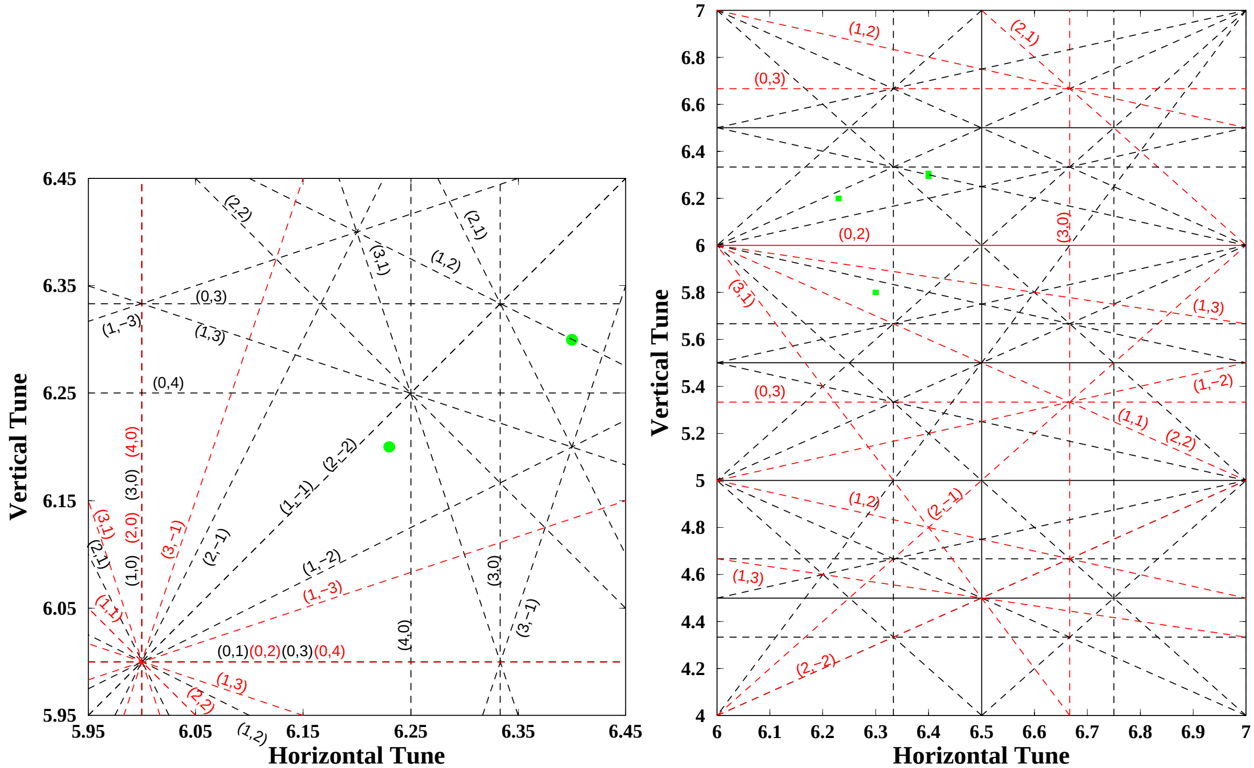

Figure 41: Tune spaces for a lattice with super-period four. The red lines are the structural resonances and all the black are the non-structural ones (up to 4th order).

other resonances are called *non-structural* or *random*. Indeed, it is very important to avoid the break of the super-periodicity of the lattice which will result in the excitation of these resonances, e.g. by random errors. The primary concern when choosing the working point for a high-intensity is to be far from the structural resonances. In Figure 41, we illustrate this by giving an example of a tune-space of a lattice with super-period 4. Here we plot the resonant lines only up to 4th order. One can observe directly that the choice of a working point is much easier if non-structural resonances (black lines) are not excited.

3.9 Linear Imperfections and correction

3.9.1 Steering error, closed orbit distortion and correction

The control of the position of the closed orbit is one of the major concerns in high intensity rings. The effect of the orbit errors in beam dynamics can be identified directly from equation of the magnetic vector potential (77), by replacing x and y by $x+\delta_x$ and $y+\delta_y$ and expanding the polynomials inside the sum. Taking a normal multi-pole of order n, for example, we have:

$$A_{nz}(x,y) = -\frac{B_0}{r_0^n}\frac{b_n}{n}\sum_{k=0}^{n/2}\sum_{l=0}^{n-2k}\sum_{m=0}^{2k} C_{k,l,m} x^{n-2k-l} y^{2k-m} {\delta_x}^l {\delta_y}^m \tag{126}$$

where $C_{k,l,m} = (-1)^l \binom{n}{2l}\binom{n-2k}{l}\binom{m}{2k}$. Note that now the vector potential contains polynomials in the transverse variables of order 1 to n. In fact, at first order, the orbit displacement will result to a polynomial of order $n-1$, at second order to a polynomial of order $n-2$, etc. This effect is usually called multi-pole "feed-down" and it is most harmful, especially when an important orbit displacement appears in areas where the associated multi-pole coefficient is strong.

In order to evaluate the effect of closed orbit distortion in the linear equations of motion we follow Courant and Snyder [41]. An horizontal or vertical $\delta_{x,y}$ orbit distortion is given by

$$\delta_{x,y}(s) = -\frac{\sqrt{\beta_{x,y}}}{2\sin(\pi Q_{x,y})}\int_s^{s+C}\frac{\Delta B(\tau)}{B\rho}\sqrt{\beta_{x,y}}\cos(|\pi Q_{x,y} + \psi_{x,y}(s) - \psi_{x,y}(\tau)|)d\tau \tag{127}$$

where $\Delta B(\tau)$ is the equivalent magnetic field error at the location $s=\tau$. Approximating the errors as delta functions in n locations around the ring, the integral (127) becomes a sum:

$$\delta_{x,y;i} = -\frac{\sqrt{\beta_{x,y;i}}}{2\sin(\pi Q_{x,y})}\sum_{j=i+1}^{i+n}\phi_{x,y;j}\sqrt{\beta_{x,y;j}}\cos(|\pi Q_{x,y} + \psi_{x,y;i} - \psi_{x,y;j}|) \tag{128}$$

where $\delta_{x,y;i}$ is the distortion produced at the location i and $\phi_{x,y;j}$ the kick produced by the jth element. There are several effects that can produce these kicks and displace an orbit from its ideal trajectory. Typically, we consider errors in the dipole guiding field, random rotations of the dipoles around the beam axis (rolls), random dipole displacements and finally horizontal and vertical misalignments of the quadrupoles. For an error in the guiding field of a dipole ΔB_j, with length L_j the kick is:

$$\phi_j = \frac{\Delta B_j L_j}{B\rho} \tag{129}$$

This will be an horizontal or vertical kick depending on the type of dipole. For the roll of a dipole the kick is

$$\phi_j = \frac{B_j L_j \sin\theta_j}{B\rho} \tag{130}$$

where θ_j is the roll angle. The kick will be horizontal if the dipole is vertical and vice-versa. A horizontal or vertical displacement $\Delta x, y_j$ of a quadrupole will give a kick in the horizontal or vertical plane

$$\phi_j = \frac{G_j L_j \Delta x, y_j}{B\rho} \tag{131}$$

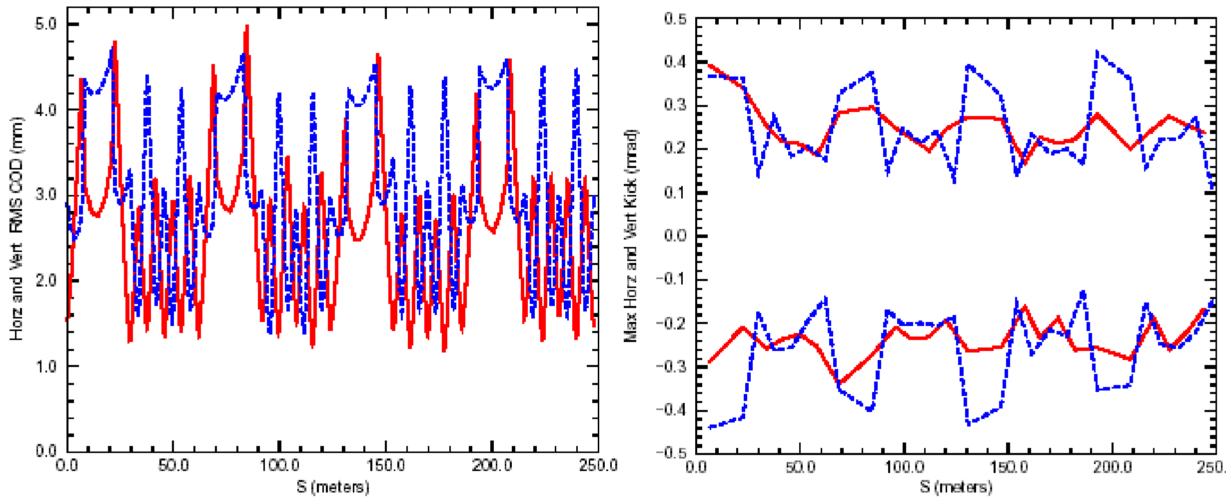

Figure 42: Horizontal and vertical closed orbit rms displacement for 101 error distributions in the SNS accumulator ring and maximum kicks required for correction (courtesy of C.J. Gardner)

where G_j is the quadrupole gradient.

In order to correct the closed orbit distortion, dipole correctors are introduced in the ring lattice. These correctors are able to produce dipole kicks in both the horizontal and vertical plane. In order to correct the closed orbit distortion, we include the kicks given by the correctors as unknowns in (128) and try to minimize the expression by a multi-variable minimization routine (see [58]). This will provide a global orbit correction. In figure 42 we show a typical closed orbit displacement for the SNS accumulator ring and the kicks needed to correct the orbit. Sometimes, it is necessary to provide a local correction scheme. A standard method to do so is based on the so called *three-bumps*: using three steering correctors producing kicks, we try to produce an orbit displacement which will compensate the orbit distortion between the first and third corrector. There is also a variant of this method using four correctors, in order to control both the position and the phase at a certain location.

The determination of the location of the dipole correctors is imposed by the lattice structure in order to get maximum kicks with minimum dipole fields: horizontal dipole correctors are placed near horizontal beta function maxima (usually adjacent to focusing quads) and vertical dipole correctors are placed near vertical beta function maxima (adjacent to defocusing quads). Especially in the injection and extraction sections of high-intensity rings, where the orbit control becomes critical, the dipole correctors are designed as combined function magnets able to produce both horizontal and vertical dipole kicks.

In the design process of the ring, the errors resulting orbit distortions are unknown. Statistical methods are employed, with random distributions of errors with rms values based on previous experience with existing machines and taking into account the mechanical tolerances and magnetic field design characteristics of the magnets. For the SNS accumulator ring a typical value for the error of the dipole field is a few 10^{-4} of the main field. Random dipole displacements and quadrupole misalignments have a rms value of 0.5mm and dipoles' random roll rms value is about 0.5mrad. For the 1GeV design of the SNS accumulator ring, the integrated dipole field of the arc correctors under design is around 6.7×10^{-4} T m which gives the capability of 1.2 mrad kicks for each corrector. The dipole correctors in the straight sections are able to produce approximately twice this integrated field and kick, both in the horizontal and vertical direction.

3.9.2 Gradient error and correction

As already pointed out in 3.8, the preservation of the lattice super-periodicity is essential for the good performance of high-intensity rings. A lattice with perfect symmetry does not allow the excitation of resonances other than "structural". On the other hand, when the super-periodicity is broken, e.g. by random errors in the magnets, "non-structural" resonances can be excited as well. The combination of lattice perturbation in the presence of large space-charge forces in a high-intensity ring, can lead to excessive beam loss. This effect was already observed [59] and analyzed theoretically [61] in the KEK PS, where a 4th order "non-structure" space-charge induced resonance was excited, as the super-periodicity was broken due to errors in the quadrupole strengths.

The direct observable for a broken super-periodicity is the distortion of the tune and linear optics functions by random and systematic errors in the quadrupole strengths. Another perturbation of the super-periodicity may be attributed to the injection regions where special injection devices (injection chicanes) perturbed the perfect lattice symmetry.

In a first order approximation, the shift of the tune due to gradient error $\delta K_{x,y}$ can be found by averaging the derivative of the associated perturbation terms after transformation to action angle variables (see e.g. [41])

$$\delta Q_{x,y} = \frac{1}{4\pi} \oint \beta_{x,y}(s) \delta K_{x,y}(s) ds \tag{132}$$

The introduction of a gradient error results to a beta variation at a location s, which at first order is:

$$\frac{\delta \beta_{x,y}(s)}{\beta_{x,y}(s)} = -\frac{1}{2\sin(2\pi Q_{x,y})} \int_s^{s+C} \beta_{x,y}(\tau) \delta K_{x,y}(\tau) \cos[-2(\pi Q_{x,y} + \psi_{x,y}(s) - \psi_{x,y}(\tau))] d\tau \tag{133}$$

where $Q_{x,y}$ is the perturbed tune. In the language of dynamical systems this beta function variation can be translated as a change in the action variables and can be calculated order by order with the help of the perturbation methods used above, through a generating function passing from the old to new action-angle variables.

A gradient perturbation can also excite integer resonances $Q_{x,y} = N$ and half-integer resonances $2Q_{x,y} = N$. Following the single resonance theory described in 3.7.2 we can calculate the resonances width [41] by setting these conditions in equation (103).

In order to compensate these effects and allow a fine tuning of the lattice, quadrupole strings are mounted on the core of quadrupole magnets and powered independently from the main quadrupole magnets. These are called TRIM windings. During the design process, as in the case of the steering error, we estimate a rms error in the quadrupole magnets' gradients by the magnet design tolerances. Then, we consider random error distributions in the quadrupole magnets' gradient with this rms value and use the TRIM windings in order to re-tune the lattice to the unperturbed working point by minimizing the tune-shift (132) and the beta-beating (133).

In order to minimize the integer and half-integer resonance widths, the usual procedure is to move the working point close to these resonances. Due to the proximity to the resonances, the beta beating should be significant. In fact, depending to the integer harmonic N of the resonance, only strings connected in a certain way are able to provide an equivalent harmonic that can balance out the effect of this resonance. The quadrupole strings are powered than accordingly in order to minimize this effect. To give an example of the order of magnitude, the SNS ring quadrupole TRIM windings are able to produce around 1% of the quadrupole gradient which is of the order of 5×10^{-2} T/m, for 1GeV operation.

It is often desirable to have individual power supplies for each quadrupole TRIM winding. Apart from the evident flexibility in the correction schemes, they can be used in the early commissioning stages to assist the orbit correction and to allow the beam-based alignment of the beam position monitors.

3.9.3 Linear coupling and correction

Linear coupling of the two dimensions in the particle motion is characterized by an xy term in the vector potential. This means that the Hill's equations of betatron motion are modified to the ones of linearly coupled oscillators. Note that this perturbation as the previous ones are completely integrable, in the sense that we can still find new action integrals that are associated with the two degrees of freedom of the system. The problem arises because the original tunes of the machine are distorted and so do all the optics functions of the uncoupled lattice, which is mostly dangerous for the safe operation of the ring. On the other hand, whenever the motion is strongly coupled, instabilities in the horizontal plane of motion can be "mirrored" to the vertical plane and vice versa. For a Hamiltonian formulation of linear coupling, one may refer to Ripken [62].

Linear coupling is attributed usually to random rolls in the quadrupole magnets, whose rms values can be as large as 1 mrad. A smaller contribution comes from random and systematic skew quadrupole errors in the magnetic elements or offsets in sextupole magnets.

Apart from the linear optics perturbations such as beta and dispersion beating, skew quadrupole errors can excite the coupling resonances $Q_x \pm Q_y = N$. Especially for working points that are close to a structural coupling resonance, it was found essential that a very careful correction has to be applied in order to compensate the effect of random quadrupole rolls [143]. In a quite similar way as for quadrupole errors, the large space-charge tune-shift pushes the particles in the resonance and the result is a quite steep increase of beam loss.

A way to quantify the coupling perturbation is by the usual classical first order perturbation theory approach. The driving terms associated with coupling resonances in the Fourier expansions of the perturbing part of the Hamiltonian:

$$g_{\pm} = \frac{1}{R} \oint \sqrt{\beta_x \beta_y} k_s(s) e^{i[\psi_x \pm \psi_y - (Q_x \pm Q_y - pN)\theta]} d\theta \tag{134}$$

where $\pm$ stands from the sum and difference resonance respectively and k_s is the coefficient associated with xy term in the vector potential. For example, in the case of a quadrupole roll by a rotation angle of $\delta\phi$ the skew quadrupole strength introduced is $k_s(s) = K(s)\sin(2\delta\phi)$.

Note that the driving term is as always a complex quantity and we need two independent nobes to correct the contribution for each resonance. Skew quadrupole strings correctors are placed accordingly around the ring to globally minimize the coupling coefficients. One can also imagine that a local coupling correction can be achieved by locally minimizing the coupling coefficients in each cell, especially when it is critical for the good performance of the machine. This latest scheme is being tested in the SNS ring. In order to save space, the four skew quadrupole strings per super-period are mounted in the cores of the dipole correctors and are powered independently in order to achieve a quasi-local correction. To give an order of magnitude the integrated skew quadrupole gradient of each corrector is about 2.25×10^{-2} T

3.10 Chromaticity

We saw that even the linear equations of motion depend on the energy of the individual partial through the momentum deviation $\delta p/p$. This means that for particles with different energy, the tunes and the other optics functions should be dependent on the particle energy. The chromaticity function of a ring is defined as the shift of the tune as a function of the momentum

$$\xi_{x,y} = -\frac{\Delta Q_{x,y}}{\delta p/p} \ . \tag{135}$$

The chromaticity function can be computed by the first order perturbation theory approach of Courant and Snyder [41]. In the case of a linear lattice, the natural chromaticity is:

$$\xi_{x,y,N} = -\frac{1}{4\pi}\oint \beta_{x,y}(s)K_(s)ds \ , \tag{136}$$

where $\beta_{x,y}$ are the horizontal and vertical beta functions of the ring, $K(s) = G/B\rho$ is the ratio of the quadrupole gradient G along the ring over the beam rigidity $B\rho$ and the integration is along the central orbit of the beam. This chromaticity function is also called the "natural chromaticity" of the ring. In a synchrotron with a regular FODO lattice and no straight sections (apart from those included in the FODO cell), the natural chromaticities $\xi_{x,y,N}$ are equal and opposite to the tunes $Q_{x,y}$.

The control of the chromaticity is very important, especially if the momentum spread of the beam is large. Then, the tune-spread of off-momentum particles can be quite important. This means that the particles can approach dangerous resonances which can enhance the beam loss. On the other hand, the chromaticity control is an efficient way to correct collective instabilities by triggering the Landau dumping mechanism (see following chapter).

A method to control the natural chromaticity, while keeping the tunes constant, is to introduce two families of multi-poles (higher then quadrupole) in non-zero dispersion areas along the ring. Let us remind that the off-momentum orbit on a $2n$-pole magnet gives an equivalent $2n-1$-pole effect in the equation of particle motion at first order. This means that an off-momentum particle orbit on a sextupole will give an equivalent quadrupole effect.

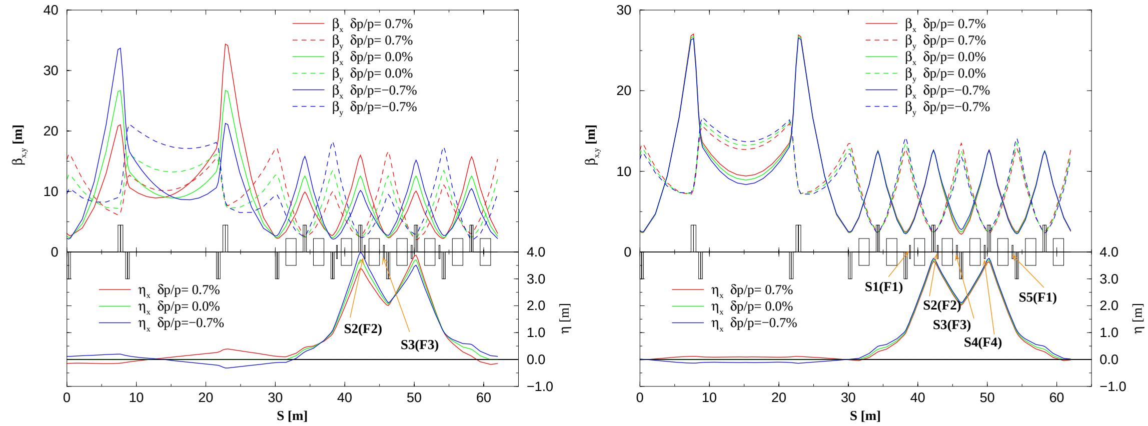

Figure 43: Lattice functions of a ring lattice using two (left) and four (right) families of sextupoles.

Thus, two families of "chromaticity" sextupoles, for example, placed at locations of the ring where the dispersion function is nonzero, will affect the chromaticity by an amount [41]:

$$\xi_{x,y,S} = -\frac{1}{2\pi}\oint \beta_{x,y}(s) b_2(s)\eta_x(s) ds \ , \tag{137}$$

where $b_2(s)$ is the sextupole multipole strength measured in T/m^2 and η_x is the horizontal dispersion of the ring (the vertical dispersion η_y is assumed here to be zero, which is true as long as we do not introduce vertical dipole fields or vertical orbit distortions). Now, the total horizontal and vertical chromaticity is the sum of the "natural" and the "sextupole generated" chromaticity $\xi_{x,y,T}$ and can be controlled by varying the strength of the chromaticity sextupoles. In order to achieve higher values of chromaticity correction with lower sextupole field, two families of sextupoles should be placed at high-beta, high-dispersion regions of the ring.

As we mentioned in the introduction, when non-linear elements are introduced the optics functions are distorted and have to be recalculated by the full non-linear equation of motion. Thus, the sextupoles may strongly affect the beta and dispersion functions as well as the second order dependence of the tunes to the momentum spread (higher-order chromaticity). Explicit expressions on the first and higher order terms of the chromaticity are given in [41].

This dependence of the optics functions on the momentum spread may introduce strong "beta/dispersion waves", which will perturb the dynamics of the ring. For example, in figure 43, we show the optical function of the SNS accumulator ring after introduction of the two families of sextupoles to correct the natural chromaticity and set it to zero. There is an obvious distortion of the beta and dispersion function, whereas in the case of the linear lattice the distortion of the optical functions functions for particles with nonzero momentum spread was quite small. Another aspect of the distortion can be observed in the dependence of the chromaticities with the momentum spread (Fig. 44).

In order to minimize the dependence of the beta, the dispersion functions and the chromaticity on the $\delta p/p$, we can place two families of sextupoles in adequate locations such that the second order effect is eliminated. However, this solution does not give enough flexibility

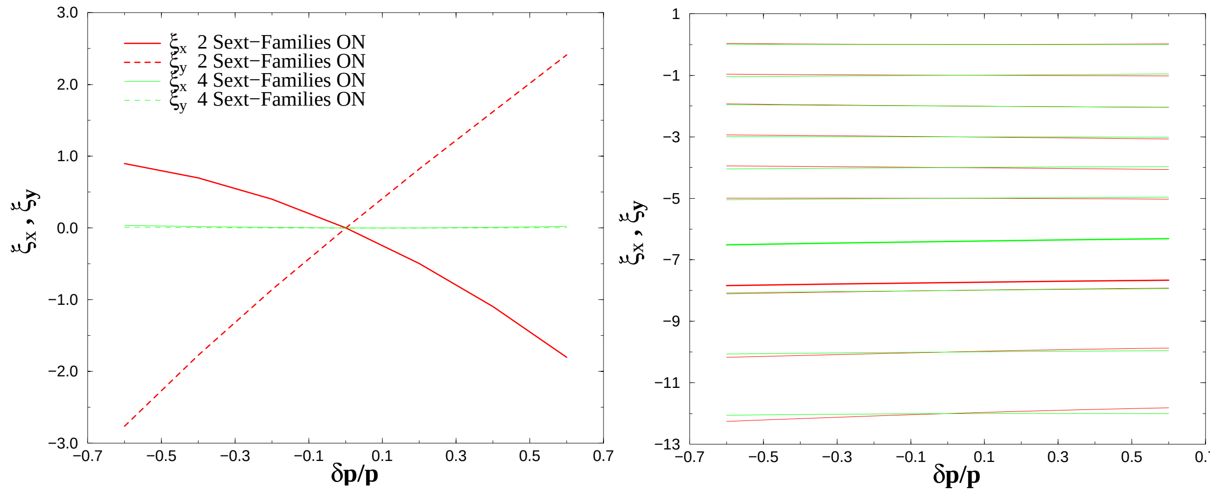

Figure 44: Plot of the chromaticities $\xi_{x,y,T}$ as a function of momentum spread, when four families of sextupoles are used. The natural chromaticities are also plotted (distinct red and green lines in the middle of the plot. This plot reflects the successful minimization of the first and second order chromatic terms, accomplished by the four sextupoles families' scheme.

in the lattice tuning. The preferred solution is to place additional families of sextupoles and try to minimize with their help the second order chromatic effect. Returning to the example of the SNS, two additional families of sextupoles were used in order to compensate the off-momentum optical distortion. In Fig. 43, we show the optics functions for a four-family chromaticity correction scheme. Now the optical distortion is eliminated. This can be also seen in the dependence of the chromaticity with respect to the momentum spread.

3.11 Non-linear effects

3.11.1 Kinematic effect

Note that, even in the absence of any field, the motion of a relativistic particle in free space is a non-linear function of the canonical momentum $\mathbf{p}$. The "kinematic non-linearity" refers to these high-order terms in the expansion of the classical relativistic Hamiltonian which contain only the transverse momenta, p_x and p_y. This non-linearity is negligible in high-energy colliders (*e.g.* RHIC, LHC), where $p_{x,y} \ll p_z$ but it cannot be neglected in low-energy high-intensity.

In fact, a measure of the impact of this non-linearity is given by the first-order tune-shift. By keeping all the kinematic terms in the expansion of the Hamiltonian, we obtain a general expression for the first-order tune-shift they induce [27]:

$$\delta Q_{x,y} = \frac{1}{2\pi} \sum_{k=2}^{\infty} \frac{(2k-3)!!}{2^k (2k)!!} \times \sum_{\lambda=0}^{k} \lambda \binom{2\lambda}{\lambda} \binom{k}{\lambda} \binom{2(k-\lambda)}{k-\lambda} J_{x,y}^{\lambda-1} J_{y,x}^{k-\lambda} G_{x,y} \tag{138}$$

where $G_{x,y} = \oint_{\text{ring}} \gamma_{x,y}^{\lambda} \gamma_{y,x}^{k-\lambda} ds$ depends on the usual Twiss gamma functions. The first, usually dominant, term in the series gives an octupole-like tune-shift, *i.e.* linear in the actions. For a high-intensity rings, where the emittance is large and the gamma functions in the straight sections exceed unity, the kinematic terms give a non-negligible tune-shift. For the SNS accumulator ring it is about 10^{-3} at 480 π mm mrad.

3.11.2 Magnet fringe field

In the multi-pole expansion (77), we neglected any contribution from a longitudinal dependence of the field components. Nevertheless, in order to satisfy Maxwell's equation, the gradual drop of the field at the edges of the magnet has to be taken into account. On high-energy colliders, the transverse field approximation is valid and the fringe-field effect can be entirely neglected especially in the magnets populating the arcs (e.g.. see [63]). On the other hand, on low-energy high-intensity machines where the beam emittance is large and the magnets are short with wide apertures, this longitudinal dependence of the field becomes the most important magnet non-linearity [27, 64].

General field expansion We developed [26] a general multipole expansion that is applicable for magnetic fields that depend arbitrarily on the longitudinal coordinate z. Being a power series in the transverse coordinates x and y, is valid only close to the centerline. The expansion is intended to describe an arbitrary "multipole" magnet along with its fringe field. This expansion generalizes an approach described by Steffen and reduces to formulas he gives in the case of dipoles and quadrupoles [65].

In the current free regions to which the beams are restricted, the magnetostatic field $\mathbf{B}(x, y, z)$ can be expressed as the gradient of a scalar potential $\Phi(x, y, z)$;

$$\mathbf{B}(x,y,z) = \nabla\Phi(x,y,z) = \frac{\partial\Phi}{\partial x}\mathbf{x} + \frac{\partial\Phi}{\partial y}\mathbf{y} + \frac{\partial\Phi}{\partial z}\mathbf{z} \ , \tag{139}$$

where Φ satisfies

$$\nabla^2\Phi(x,y,z) = \frac{\partial^2\Phi}{\partial x^2} + \frac{\partial^2\Phi}{\partial y^2} + \frac{\partial^2\Phi}{\partial z^2} = 0 \ . \tag{140}$$

An appropriate expansion for the intended calculation is [66, 67]

$$\Phi(x,y,z) = \sum_{m=0}^{\infty}\sum_{n=0}^{\infty}\mathcal{C}_{m,n}(z)\frac{x^n\, y^m}{n!\, m!} \ , \tag{141}$$

where the coefficients $\mathcal{C}_{m,n}(z)$ depend on the longitudinal position z. The spatial dependence of function Φ can guide the shaping of the pole pieces of iron magnets to match, as closely as possible, equipotentials of Φ. This is discussed by Steffen [65], for the case of quadrupoles.

Substituting Eq. (141) into Eq. (140), we get a recursion relation for the coefficients;

$$\mathcal{C}_{m+2,n} = -\mathcal{C}_{m,n+2} - \mathcal{C}_{m,n}^{[2]} \ , \tag{142}$$

where in this and subsequent formulas a superscript $[l]$ denotes l differentiations with respect to z; in this case $l = 2$. Now, we can evaluate the gradient of the potential and get the field components in the three Cartesian directions;

$$\begin{aligned}
B_x(x,y,z) &= \sum_{m=0}^{\infty}\sum_{n=0}^{\infty}\mathcal{C}_{m,n+1}(z)\frac{x^n\,y^m}{n!\,m!} && (143)\\
B_y(x,y,z) &= \sum_{m=0}^{\infty}\sum_{n=0}^{\infty}\mathcal{C}_{m+1,n}(z)\frac{x^n\,y^m}{n!\,m!} \quad , && (144)\\
B_z(x,y,z) &= \sum_{m=0}^{\infty}\sum_{n=0}^{\infty}\mathcal{C}_{m,n}^{[1]}(z)\frac{x^n\,y^m}{n!\,m!} && (145)
\end{aligned}$$

The coefficients can be expressed in terms of the usual normal and skew multipole coefficients which, as well as being conventional, have only one index, while $\mathcal{C}_{m,n}$ has two;

$$\begin{aligned}
b_n(z) =&\mathcal{C}_{1,n}(z) = \left(\frac{\partial^n B_y}{\partial x^n}\right)(0,0,z)\\
a_n(z) =&\mathcal{C}_{0,n+1}(z) = \left(\frac{\partial^n B_x}{\partial x^n}\right)(0,0,z) \quad .
\end{aligned} \tag{146}$$

We next seek a representation of the field as a function of these coefficients and their derivatives. We turn to the recursion relation (142) and try to write it in a general form. In fact, we may observe that

$$\mathcal{C}_{m,n} = \sum_{l=0}^{k}(-1)^k\binom{k}{l}\mathcal{C}_{m-2k,n+2k-2l}^{[2l]} \quad . \tag{147}$$

The last equation can be proved by recurrence. In order to have the dependence on the multipole coefficients (see Eq. (146)), we have to distinguish two cases for m, namely $m=2k$ (even) or $m=2k+1$ (odd), and we have

$$\begin{aligned}
\mathcal{C}_{2k,n} &= \sum_{l=0}^{k}(-1)^k\binom{k}{l}a_{n+2k-2l-1}^{[2l]} \;,\ \text{for } n+2k-2l-1\geq 0\\
\mathcal{C}_{2k+1,n} &= \sum_{l=0}^{k}(-1)^k\binom{k}{l}b_{n+2k-2l}^{[2l]}
\end{aligned} \quad . \tag{148}$$

Note that the upper bound of the first series involving skew coefficients has to be modified accordingly in the case of a "dipole" magnet ($n=0$) in order to fulfill the restriction $n+2k-2l-1\geq 0$. Moreover, the coefficients n and k cannot be simultaneously 0 due to the fact that these relations stand only for non-solenoidal magnets, *i.e.* $\mathcal{C}_{0,0}=0$.

We can now put the representation of the coefficients in the magnetic field. After having rearranged the m summation the field components can be written in a compact form as

$$
\begin{aligned}
B_x(x,y,z) &= \sum_{n=0}^{\infty}\sum_{m=0}^{\infty}\sum_{l=0}^{m}(-1)^m \binom{m}{l}\frac{x^n\,y^{2m}}{n!\,(2m)!}\left(b_{n+2m+1-2l}^{[2l]}\frac{y}{2m+1}+a_{n+2m-2l}^{[2l]}\right)\\
B_y(x,y,z) &= \sum_{n=0}^{\infty}\sum_{m=0}^{\infty}(-1)^m\frac{x^n\,y^{2m}}{n!\,(2m)!}\left[\sum_{l=0}^{m}\binom{m}{l}b_{n+2m-2l}^{[2l]}\right.\\
&\qquad\left.-\sum_{l=0}^{m+1}\binom{m+1}{l}a_{n+2m+1-2l}^{[2l]}\frac{y}{2m+1}\right] \qquad , \\
B_z(x,y,z) &= \sum_{n=0}^{\infty}\sum_{m=0}^{\infty}\sum_{l=0}^{m}(-1)^m \binom{m}{l}\frac{x^n\,y^{2m}}{n!\,(2m)!}\left(b_{n+2m-2l}^{[2l+1]}\frac{y}{2m+1}+a_{n+2m-1-2l}^{[2l+1]}\right)
\end{aligned}
\tag{149}
$$

keeping in mind the restrictions given in Eq. (148). In an idealized model of a magnet, only one (or in the case of combined function magnets, two) of the multipole coefficients will be non-vanishing in the body of the magnet (length $L_{\rm eff}$) and in this region only the $l=0$ terms in the expansions survive. One can make many useful remarks about symmetries of the skew and normal multipole coefficient in a quite straightforward way through these expressions.

In order to investigate the impact of the fringe field to the particle motion, one should know the exact shape of the multi-pole components along the edges of the magnet and integrate the equations of motion. This can be done by accurately modeling the magnet with 3D Poisson solver codes [68]. On the other hand, the fringe effect can be represented as a non-linear map which transports the transverse coordinates through the fringe. For this, different approaches exist, using either direct numerical evaluation with exact integration of the magnetic field [69, 70] or parameter fit of an adequate function [71, 72, 73] (e.g. the Enge function [74]). A good approximation can be given by computing the integrals involved in the "hard-edge" approximation, *i.e.* taking the limit for which the fringe-field length goes to zero (see [75, 76]. In what follows we will study the impact of the fringe-fields on dipoles and quadrupoles, taking this approximation.

Dipole: Consider a "straight" dipole magnet. In that case, the configuration of poles and coils is symmetric about the $x=0$ and $y=0$ planes, and the coils are excited with alternating signs and equal strength. The magnetic field will satisfies the following symmetry conditions: B_x is odd in x and odd in y; B_y is even in both x and y; B_z is even in x and odd in y. Using a general z-dependent field expansion we get:

$$
\begin{aligned}
B_x &= \sum_{m,n=0}^{\infty}\sum_{l=0}^{m}\frac{(-1)^m x^{2n+1}y^{2m+1}}{(2n+1)!(2m+1)!}\binom{m}{l}b_{2n+2m+2-2l}^{[2l]}\\
B_y &= \sum_{m,n=0}^{\infty}\sum_{l=0}^{m}\frac{(-1)^m x^{2n}y^{2m}}{(2n)!(2m)!}\binom{m}{l}b_{2n+2m-2l}^{[2l]}\\
B_z &= \sum_{m,n=0}^{\infty}\sum_{l=0}^{m}\frac{(-1)^m x^{2n}y^{2m+1}}{(2n)!(2m+1)!}\binom{m}{l}b_{2n+2m-2l}^{[2l+1]}
\end{aligned}
\tag{150}
$$

Taking the field expansion up to leading order, we get:

$$\begin{aligned} B_x &= b_2 xy + O(4) \\ B_y &= b_0 - \frac{1}{2} b_0^{[2]} y^2 + \frac{1}{2} b_2 (x^2 - y^2) + O(4) \\ B_z &= y\ b_0^{[1]} + O(3) \end{aligned} \tag{151}$$

where b_2 represents a sextupole field component allowed by the symmetry of the "dipole" magnet (for an ideally designed magnet $b_2 = 0$) and $O(3)$ and $O(4)$ contain all the allowed terms of higher orders.

Note the $b_0^{[2]} y^2$ in the representation of the B_y field. This means that the dipole fringe-field is associated with a sextupole like effect which usually has a big contribution to vertical chromaticity.

Quadrupole: The configuration of poles and coils in a quadrupole magnet is symmetric about the four planes $x = 0; y = 0;\ x = y;\ x = -y$ and if the coils are excited with alternating signs and equal strength, the magnetic field will satisfy the following symmetry conditions: B_x is even in x and odd in y; B_y is odd in x and even in y; B_z is odd in both x and y; and $B_z(x, y, z) = B_z(y, x, z)$. As before, we may express the field components as:

$$\begin{aligned} B_x &= \sum_{m,n=0}^{\infty} \sum_{l=0}^{m} \frac{(-1)^m x^{2n} y^{2m+1}}{(2n)!(2m+1)!} \binom{m}{l} b_{2n+2m+1-2l}^{[2l]} \\ B_y &= \sum_{m,n=0}^{\infty} \sum_{l=0}^{m} \frac{(-1)^m x^{2n+1} y^{2m}}{(2n+1)!(2m)!} \binom{m}{l} b_{2n+2m+1-2l}^{[2l]} \quad . \\ B_z &= \sum_{m,n=0}^{\infty} \sum_{l=0}^{m} \frac{(-1)^m x^{2n+1} y^{2m+1}}{(2n+1)!(2m+1)!} \binom{m}{l} b_{2n+2m+1-2l}^{[2l+1]} \end{aligned} \tag{152}$$

The field expansion can be written as

$$\begin{aligned} B_x &= y \left[b_1 - \frac{1}{12}(3x^2 + y^2) b_1^{[2]} \right] + O(5) \\ B_y &= x \left[b_1 - \frac{1}{12}(3y^2 + x^2) b_1^{[2]} \right] + O(5) \\ B_z &= xy b_1^{[1]} + O(4) \end{aligned} \tag{153}$$

where $b_1(z)$ is the transverse field gradient at the quadrupole axis, and $O(4), O(5)$ contain all the higher order terms. Note also that $b_3 = -b_1^{[2]}/2$, due to the field symmetry.

For a quadrupole one can evaluate the fringe-field contribution in the limit of zero fringe length. The corresponding Hamiltonian for a single fringe (to leading order) is [75, 76]

$$H_f = \frac{\pm Q}{12 B\rho (1 + \frac{\delta p}{p})} (y^3 p_y - x^3 p_x + 3x^2 y p_y - 3y^2 x p_x), \tag{154}$$

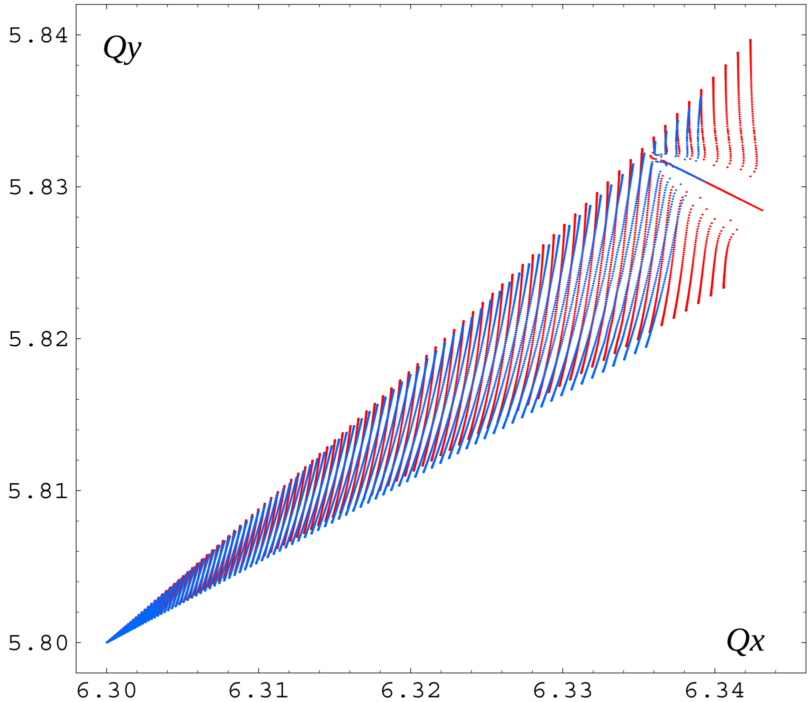

Figure 45: Tune footprints of the SNS ring, based on realistic (blue) and hard-edge (red) quadrupole fringe fields.

where Q_i is the quadrupole strength, and the $+$ and $-$ signs are used at, respectively, the entrance and exit of the magnet. It follows, as was shown by Lee-Whiting [87], that a quadrupole fringe-field induces an octupole-like transverse kick.

To study the non-linear effect of the fringe-field, maps can be built quadrupole maps based on either (154) or an exact representation [114]. Figure 45 represents the tune-shift given by quadrupole fringe fields in the case of the the SNS ring. It seems that the hard-edge model slightly overestimates the fringe-field effect and therefore represents a conservative estimate. On the other hand, the fringe-field tune spreads are of about (0.04,0.03) at 1000π mm mrad, roughly one-third the space-charge tune spread.

The tune spread can be accurately represented by the results of first-order perturbation theory:

$$\begin{pmatrix} \delta\nu_x \\ \delta\nu_y \end{pmatrix} = \begin{pmatrix} a_{hh} & a_{hv} \\ a_{hv} & a_{vv} \end{pmatrix} \begin{pmatrix} 2J_x \\ 2J_y \end{pmatrix}, \tag{155}$$

where the normalized anharmonicities are given by

$$\begin{aligned} a_{hh} &= \frac{-1}{16\pi B\rho} \sum_i \pm Q_i \beta_{xi} \alpha_{xi}, \\ a_{hv} &= \frac{1}{16\pi B\rho} \sum_i \pm Q_i (\beta_{xi}\alpha_{yi} - \beta_{yi}\alpha_{xi}), \\ a_{vv} &= \frac{1}{16\pi B\rho} \sum_i \pm Q_i \beta_{yi} \alpha_{yi}. \end{aligned} \tag{156}$$

Here the index i runs over the entrances and exits of all quadrupoles in the ring, and the $+$ and $-$ signs are as in (154). Note that the entrance and exit fringe fields do *not* cancel one another: even if the β functions are equal at the entrance and exit, the α functions usually change sign, leading to an additive effect. For the SNS lattice we find $(a_{hh}, a_{hv}, a_{vv}) \approx (49, 22, 42)[m^{-1}]$, and these values closely match (apart from the obvious resonance) the results shown in Fig. 45.

3.11.3 High order multipole errors

For a given magnet with a perfect $2(n+1)$-pole geometry, the scalar potential should satisfy the following symmetry condition:

$$\Phi(r, \theta, z) = \Phi(r, \frac{\pi}{n+1} - \theta, z) \quad , \tag{157}$$

which is interpreted in a relation between the index n and the multipole order $(n+1)$:

$$n = (2j+1)(n+1) - 1 \quad . \tag{158}$$

Thus, for a normal dipole ($n = 0$) the multipole coefficients allowed by the magnet symmetry are of the form b_{2j}, for a normal quadrupole ($n = 1$) b_{4j+1}, for a normal sextupole ($n = 2$) b_{6j+2}, etc. In a high-intensity ring lattice with dipoles and quadrupoles the main contributions are coming from the lower multipole field allowed components, i.e. the sextupole and decapole in the dipoles and the dodecapole and twenty-pole in the quadrupoles.

3.12 Non-linear Correction

3.12.1 Sextupole correction

The main sextupole non-linearities in a ring are usually introduced by the chromaticity sextupole, the sextupole errors in the main dipoles and the dipole fringe-fields.

By using classical perturbation theory, we can show that sextupoles introduce a second order (quadratic in the sextupole strength) tune-shift with amplitude which is linear with the particles' emittance, equivalent to a first order octupole effect. This tune-shift may be quantified by the anharmonicity coefficients. To give an example, we display in Fig. 46, these three quantities in the case of the SNS ring for different ranges of chromaticity values (i.e. different values of the sextupole strengths). The maximum anharmonicity values are found to be a factor of five smaller than the ones introduced by the quadrupole fringe-fields, indicating that the introduction of chromatic sextupoles will not have an important non-linear impact on the SNS ring. This residual octupole-like tune-shift can be corrected by dedicated octupole correctors.

On the other hand, the sextupoles may excite sextupole type of resonances defined by the condition $3Q_x = N$ or $Q_x \pm 2Q_y = N$ where N is an integer number. The main functionality of the sextupole correctors is the correction of erect sextupole resonances, which can be excited by sextupole errors in the dipoles, dipole fringe-fields at leading order and the non-linear effect of the chromaticity sextupoles. As all non-linear correctors, they should be located in non-dispersive areas in order to avoid "feed-downs" due to closed-orbit displacements giving a quadrupole effect at first order. This avoids the perturbation of the chromaticity.

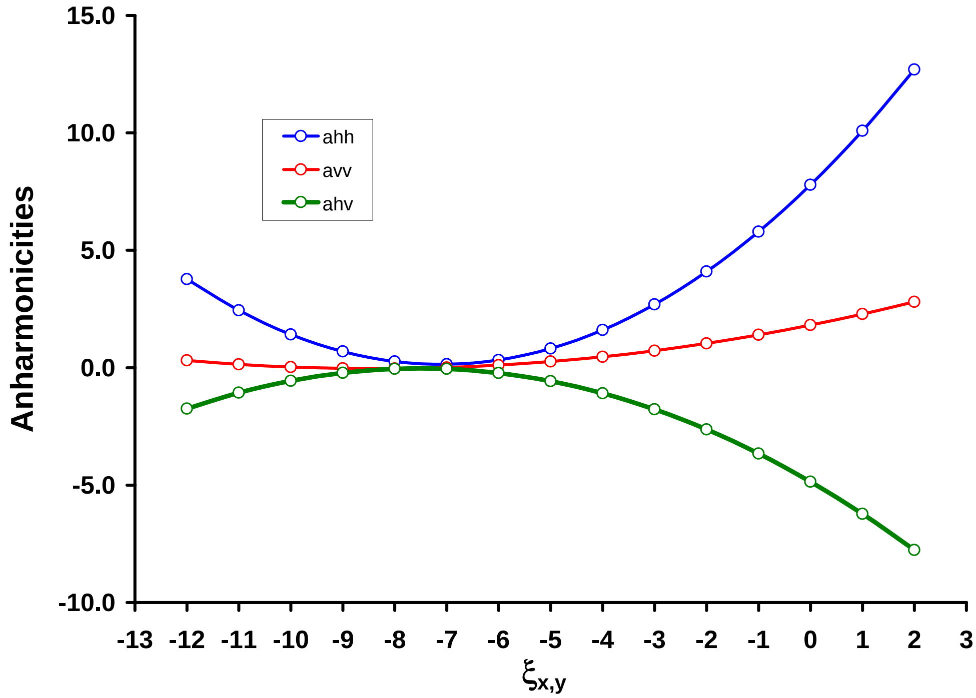

Figure 46: Anharmonicities versus the chromaticity. The maximum values are within 5% of the ones produced by the quadrupole fringe-fields.

One can try to compensate the resonance effect by tuning the sextupole correctors to cancel the sextupole resonance driving terms $g_{3,0}$, $g_{1,2}$ and $g_{1,-2}$, depending on which one is the most important. A global resonance correction can also be followed, by trying to minimize the norm of all sextupole resonances. An example is given in figure 47, where we present the norm $\sqrt{g_{3,0}^2 + g_{1,2}^2 + g_{1,-2}^2}$ of the resonance driving terms for the SNS accumulator ring, before and after correction. In the case of the SNS ring the sextupole correctors are eight in total (two per super-period) and are powered independently in order to produce any possible harmonic. To give an order of magnitude, the integrated sextupole gradient produced by the correctors in SNS ring is about 2.6 T/m.

3.12.2 Skew-sextupole correction

The excitation of skew sextupole resonances was found to be one of the most important limitations in high intensity machines like the AGS booster. Skew sextupole resonances of the type $2Q_x \pm Q_y = N$ and $3Q_y = N$ can be excited by skew sextupole errors coming from rolls in the main dipoles or other geometrical errors in the magnet elements of the SNS ring. In order to correct this effect skew sextupole correctors are needed. In the case of the SNS ring, windings able to produce a skew-sextupole component are mounted on the dipole correctors along with the main dipole coils and the skew quadrupole components. The integrated gradient is 6.6×10^{-2} T/m. The correction schemes followed in the case of skew sextupole correctors are very much equivalent to the ones followed in the case of normal sextupoles.

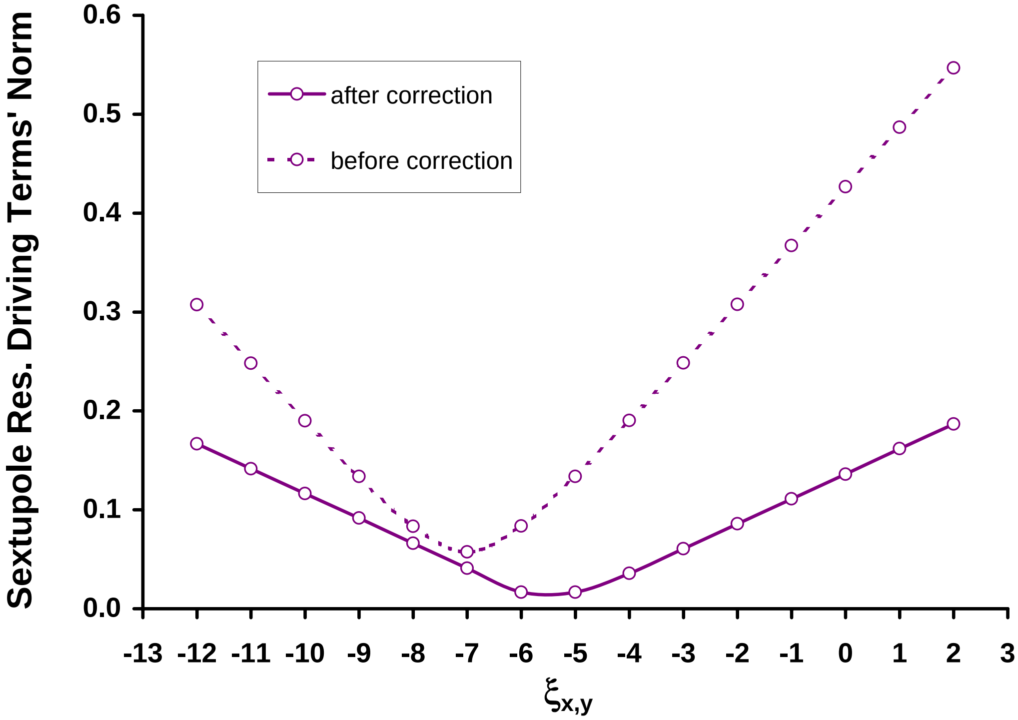

Figure 47: Norm of sextupole resonance driving terms before correction (dashed line) and after correction (solid line) with dedicated sextupole correctors. The resonance norms are reduced after the correction by as much as a factor of four.

3.12.3 Octupole correction

Octupole magnets can modify the tune-spread caused by quadrupole fringe-fields, kinematic non-linearity, chromatic sextupoles, and other octupole-like effects. If octupoles are placed in non-dispersive areas, the anharmonicities (156) become

$$\begin{aligned}
A_{hh} &= a_{hh} + \frac{3}{16\pi B\rho}\sum_j O_j\beta_{xj}^2, \\
A_{hv} &= a_{hv} - \frac{6}{16\pi B\rho}\sum_j O_j\beta_{xj}\beta_{yj}, \\
A_{vv} &= a_{vv} + \frac{3}{16\pi B\rho}\sum_j O_j\beta_{yj}^2.
\end{aligned} \tag{159}$$

Here O_j denotes integrated octupole strength, and the index j runs over all octupoles in the ring. Complete cancellation of the tune-spread requires three families of octupoles to drive the anharmonicities (159) to zero. In some cases, when one anharmonicity is much smaller than the others, two families of octupoles can reduce the tune-spread. This is not the case for the SNS ring, however. The octupole strengths required to drive the anharmonicities (159) to zero depend on the octupole locations. Figure 48 shows the integrated strengths of the octupole correctors in the SNS ring versus the position of a third family in one of the SNS

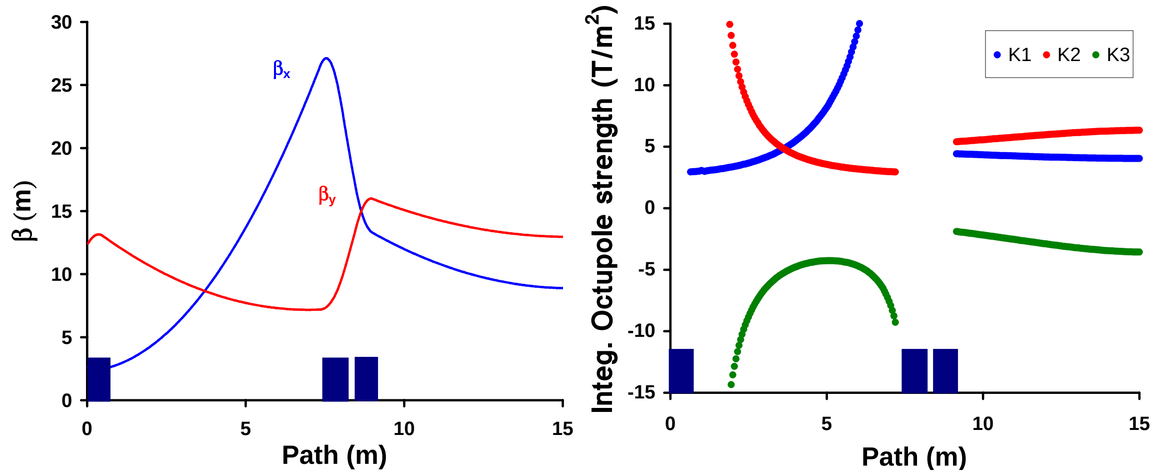

Figure 48: Top: the β functions in the first half of the SNS straight section. Bottom: integrated strengths of three families of octupoles versus location of the third family.

ring straight sections. The first two families, at the ends of each arc, are located where β_x and β_y take extremal values. Then the optimal position for the third corrector is where the β functions are roughly equal, *i.e.* either in the middle of the straight section or just after the doublet. Unfortunately, the addition of this third family is not possible to a first stage due to the tight space of the ring.

On the other hand, it would be impossible to correct all octupole type resonances of the form $4Q_x = N$, $2Q_x \pm 2Q_y = N$ and $4Q_y = N$ with a two-family scheme. For this reason, it is usually preferred to power the correctors individually powering, in much the same way as for the other non-linear correctors. To give an order of magnitude the integrated octupole gradient given by the correctors of the SNS ring is 2.9 T/m^2.

3.12.4 Error compensation in magnet design - An example

In a magnet with normal quadrupole symmetry the first allowed multipole error is the normal dodecapole, b_5. In the absence of pole-tip shaping, this error can be exceedingly large: for the SNS 21 cm quadrupole (see Fig. 49), an OPERA-3d [68] simulation (with un-shaped ends) gives a dodecapole component of about 120 (in units of 10^{-4}, normalized with respect to the main, quadrupole, component).

Because the dodecapole error is quite localized, its effect can be computed using a thin-element approximation. Applying first-order perturbation theory, one finds the tune-spread induced by dodecapole errors is given by

$$\begin{pmatrix} \delta\nu_x \\ \delta\nu_y \end{pmatrix} = \sum_i \frac{b_{5i} Q_i}{8\pi B\rho} \mathcal{D}_i \begin{pmatrix} J_x^2 \\ J_x J_y \\ J_y^2 \end{pmatrix}, \tag{160a}$$

where $\mathcal{D}_i$ denotes the 3×2 matrix

$$\begin{pmatrix} \beta_{xi}^3 & -6\beta_{xi}^2\beta_{yi} & 3\beta_{xi}\beta_{yi}^2 \\ -3\beta_{xi}^2\beta_{yi} & 6\beta_{xi}\beta_{yi}^2 & -\beta_{yi}^3 \end{pmatrix}. \tag{160b}$$

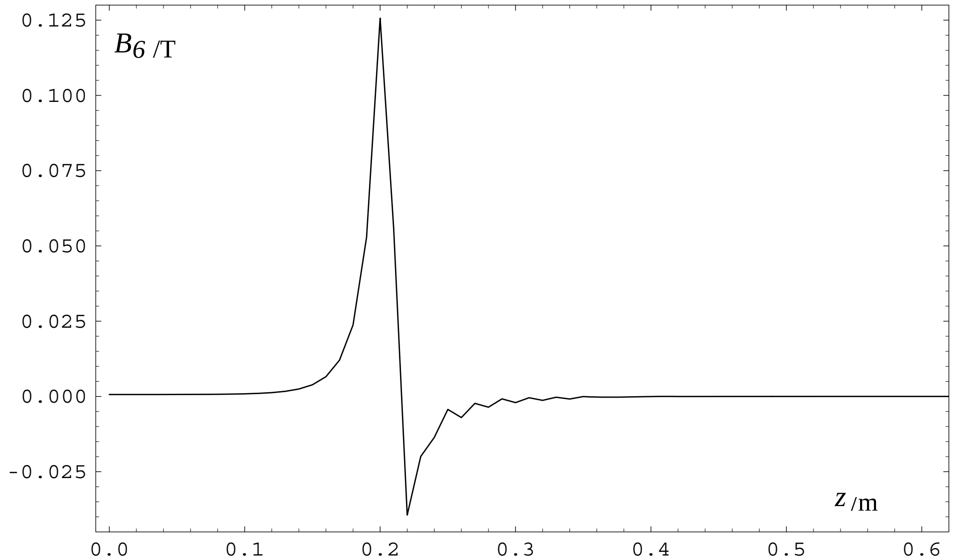

Figure 49: Dodecapole component in a 21 cm quadrupole with un-shaped ends. The reference radius is 10 cm, and the origin, $z = 0$, is at the magnet's center.

Here the index i runs over all dodecapole kicks in the ring, *i.e.* over the entrances and exits of all quadrupoles. Note that this effect depends linearly on the error strength, but quadratically on the amplitude. In Fig. 50 a comparison of this analytic result with tracking data and shows a striking agreement. Figure 50 also shows that the very large uncorrected dodecapole error gives a tune-spread (at 1000π mm mrad) roughly twice that caused by the quadrupole fringe fields.

By shaping the ends of the quadrupoles, one can reduce the b_5 error to 1 unit or less [65]. Such shaping reduces the peak and the trough seen in Fig. 49, and makes those two areas roughly cancel one another. This constitutes *local* compensation. One might also correct the b_5 error by adding a small negative dodecapole component through the body of the magnet. In Fig. 51 we compare the tune-spreads (160) after local and body compensation. In this example, the compensation works well in both cases, with local compensation being slightly better. But, in fact, it is essential to use local compensation: because the tune-spreads (160) depend cubically on the β functions, the results of body compensation will be very sensitive to the ring optics.

3.12.5 Dynamic aperture

An ultimate check of the validity of the correction schemes and the good performance of the beam is given by single-particle tracking. There are several tracking programs that are able to propagate the single particle along the ring lattice, including all the linear and non-linear imperfections mentioned above.

A tracking example is given in Figures. 52, where we study the detrimental effect of the natural chromaticity in the dynamic aperture of the SNS ring. In these figures, we plot the maximum survival amplitude (in terms of total emittance) of particles launched in 5

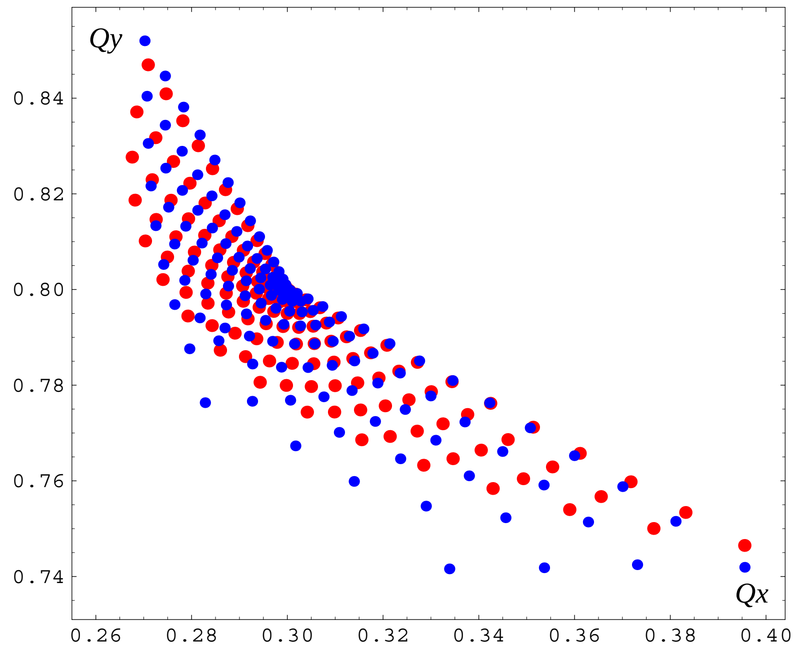

Figure 50: Tune footprints of a ring lattice with a dodecapole error in the quadrupoles of $b_5 = 60$ units; results are from tracking data (blue) or the analytic estimate (160) (red).

different initial ratios of the transverse emittances, with three different momentum spreads ($\delta p/p = 0, \pm 0.2$). The momentum spread of ± 0.2 is indeed higher than the actual RF bucket size of ± 0.7. Nevertheless, it corresponds to the momentum acceptance of the ring and halo particles can reach this level before they are "cleaned" by the Beam-In-Gap kicker. Through Figures 52, one observes the unacceptable reduction in the dynamic aperture of the SNS ring below the physical aperture of 180 π mm mrad for a momentum spreads of -0.2 (green curve on the left). This is attributed to the fact that the chromaticity pushes the particles' vertical tune towards the very dangerous integer resonance, at $Q_y = 6$ and the particles get rapidly lost. A less pronounced reduction of the dynamic aperture can be attributed to the half-integer resonance at $2Q_y = 11$ for particles with momentum spread of 0.2 (red curve on the left). Finally, the on momentum particles have very similar dynamic aperture (blue curves).

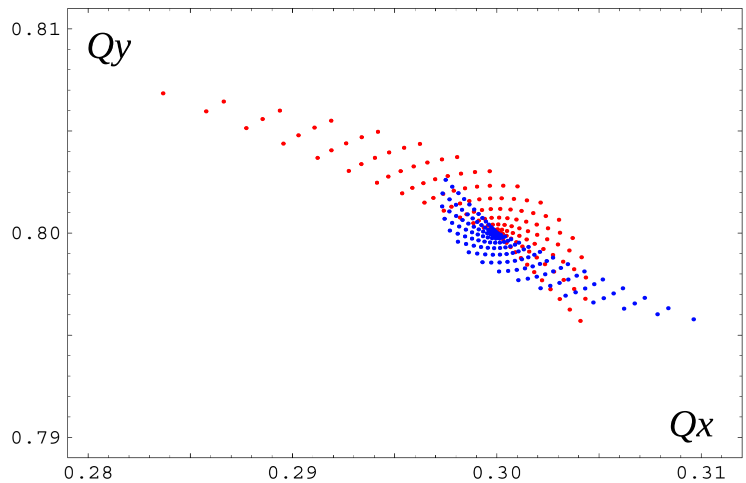

Figure 51: Comparison of tune-shift plots using body (red) and local (blue) compensation of the dodecapole component in the SNS ring quadrupoles.

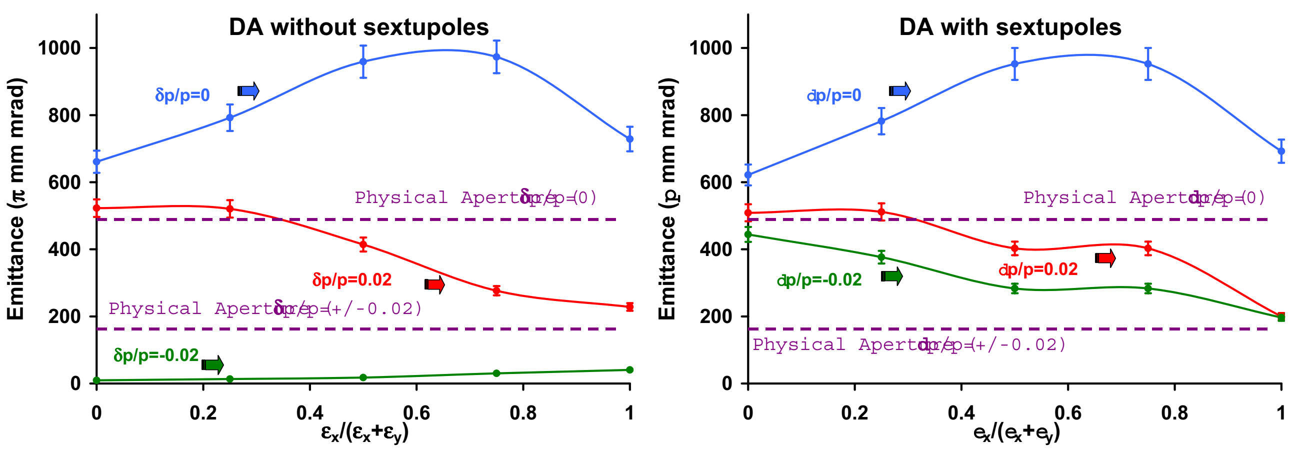

Figure 52: Dynamic aperture for the working point (6.3,5.8), without (left) and with (right) sextupoles.

4 Multi-Particle Dynamics

4.1 Introduction

When the beam currents are high enough the self fields of the beam can no longer be neglected in comparison to the applied fields. The mutual interaction of the charged particles in a beam can be represented by the sum of a "collisional" force and a "smooth" force. The collisional part of the total interaction force arises when a particle "sees" its immediate neighbors and is therefore affected by their individual positions. Such a force is responsible for small random displacements of the particle's trajectory and statistical fluctuations in the particle distribution as a whole. In most practical beams this is a relatively small effect. Thus, the mutual interaction between particles can be described mainly by a smoothed force. As a result, one can consider the motion of a single particle under the influence of the surrounding "space charge".

A simple theory can be built using the smooth or weak approximation for the single-particle unperturbed betatron motion. The influence of the other particles in the beam on the test particle is then added as a transverse Lorentz force.

A self-consistent approach, typically required for the treatment of coherent instabilities, can be built using the Vlasov equation which we introduce at a later stage.

4.2 Space-charge effects

4.2.1 Transverse space-charge force

A good description of space-charge effects can be found in [95],[96]. We will use material from these books in our analysis.

We start with the equation of motion in the smooth approximation, for example, in the vertical direction:

$$y'' + \frac{\nu_{y0}^2}{R^2} y = \frac{F}{m\gamma v^2}, \tag{161}$$

where R is the radius of the ring, and ν_{y0} is an unperturbed tune defined as betatron frequency ω_{y0} divided by the particle revolution frequency ω_0. Here $y' = dy/ds$.

By considering various contributions to F we can explore several collective effects. For example, contribution of the **self fields** to F will describe direct incoherent tune shift; the contribution from **image fields** will modify the incoherent tune shift and also introduce the coherent tune shift; while the contribution from **wake fields** will address the question of coherent transverse instabilities.

The function F can be expanded to first order in terms of the test particles motion y and its average position $\bar{y}$:

$$F = \left[\frac{\partial F}{\partial y}\right]_{\bar{y}=0} y + \left[\frac{\partial F}{\partial \bar{y}}\right]_{y=0} \bar{y}. \tag{162}$$

When $\bar{y}(t) = 0$, the beam and its associated fields are static. This term can be considered as an additional focusing term, and thus it will cause an incoherent tune shift.

The coherent motion can be solved by choosing $y = \bar{y}$, i.e. the test particle is at the beam center with zero betatron amplitude.

When $dy/dt \neq 0$, the beam and its fields are time varying, and $\partial F/\partial \bar{y}$ will in general be complex. This will take into account the wake fields left by other particles at various azimuthal positions in the accelerator and will lead to the concept of a complex coupling impedance and associated coherent instabilities.

4.2.2 Direct incoherent tune shift

We now consider the contribution to the space-charge force from the **self field** of the beam. Assume an unbunched beam that has a longitudinal line charge density λe and moves with speed βc ($\lambda = N/2\pi R$, where N is the total number of particles in the beam and R is the radius of the ring). For a round beam of radius a with uniform distribution, using Gauss's law we obtain:

$$E_r = \frac{2\lambda e}{a^2} r, \qquad r < a. \tag{163}$$

To find the magnetic field we use Ampere's law which gives

$$B_\theta = \frac{2\lambda e\beta}{a^2} r, \qquad r < a. \tag{164}$$

Problem 4.1 Derive E_r and B_θ for both $r > a$ and $r < a$.

The Lorentz force experienced by the particles in the radial direction is

$$F_r = e(E_r - \beta B_\theta) = \frac{2\lambda e^2}{a^2\gamma^2} r. \tag{165}$$

One sees that the electric and magnetic forces will cancel one another in the ultrarelativistic limit $\gamma >> 1$. In other words, the direct space-charge effect is essentially nonrelativistic, and thus becomes very important at low energies.

We now introduce the concept of a tune shift by assuming a perturbation which affects the focusing in the vertical direction:

$$y'' + \frac{\nu_{y0}^2}{R^2} y = Ky. \tag{166}$$

The perturbed ("depressed" since K is subtracted) tune is given by

$$\nu_y^2 = \nu_{y0}^2 - KR^2, \tag{167}$$

$$\nu_y \approx \nu_{y0} - \frac{KR^2}{2\nu_{y0}}, \tag{168}$$

for small K. We thus can define the tune shift as

$$\Delta\nu = \frac{KR^2}{2\nu_{y0}}. \tag{169}$$

Using the space-charge perturbation given in Eq. 165, we obtain the direct incoherent space-charge tune shift:

$$\Delta\nu = \frac{F_y R^2}{2\nu_0 m\gamma\beta^2 c^2} = \frac{\lambda e^2 R^2}{mc^2 a^2\gamma^3\beta^2\nu_0} = \frac{N r_0^2 R}{2\pi a^2\beta^2\gamma^3\nu_0} = \frac{N r_0^2}{2\pi\beta^2\gamma^3\epsilon}, \tag{170}$$

where $r_0^2 = e^2/mc^2$ is the classical radius of the particle (in *cgs* units), and ϵ is the beam emittance.

Similarly, for a Gaussian distribution we get

$$F_r = \frac{2\lambda e^2}{a^2\gamma^2 r}\left(1 - \exp^{-r^2/2\sigma^2}\right), \tag{171}$$

and for r values small compared with σ we have

$$F = \frac{2\lambda e^2}{a^2\gamma^2 2\sigma^2} r, \tag{172}$$

which gives the maximum tune shift for a Gaussian beam:

$$\Delta\nu_G = \frac{N r_0^2 R}{4\pi\sigma^2\beta^2\gamma^3\nu_0}. \tag{173}$$

To compare tune shifts for various distributions we will need to introduce the concept of equivalent beams and rms beam parameters. We will do this in Section 4.4. Here we jump ahead by stating that for the uniform distribution $a = 2\sigma$, where σ is rms beam radius. We therefore rewrite the expression for the tune shift due to a uniform distribution as

$$\Delta\nu_U = \frac{N r_0^2 R}{8\pi\sigma^2\beta^2\gamma^3\nu_0}. \tag{174}$$

We can see that the tune shift of a uniform beam is a factor of two smaller than the maximum tune shift of a Gaussian beam.

We note that the tune shift expression can also be obtained using beam optics which gives

$$\Delta\nu = \frac{1}{4\pi}\int k(s)\beta(s)ds, \tag{175}$$

where $k(s)$ is small gradient perturbation. Using $k(s) = \frac{1}{m\gamma}\frac{dF_r}{dr}$ and F_r for a uniform distribution, we obtain an expression for the tune shift of a uniform beam identical to Eq. 170.

We note that the above formulas were based on the assumption of a circular beam cross section. For an elliptical beam our expression for the vertical tune shift of a uniform beam is rewritten as

$$\Delta\nu_U = \frac{N r_0^2 R}{\pi\beta^2\gamma^3\nu_0}\frac{1}{a_V(a_H + a_V)}, \tag{176}$$

where a_H and a_V are the horizontal and vertical semi-axis of the ellipse, respectively.

4.2.3 Effect of images on incoherent tune shift

Cancelation between electric and magnetic fields is perturbed due to the beam surroundings, which contribute to a tune shift. The electric field distribution will be influenced by the conducting boundary while the magnetic field distribution will be influenced by the presence of magnet materials within a magnet.

We begin with a simple example of "rectangular" chamber approximated by two parallel plates. Let such plates be made of a perfect conductor and located at $y = \pm h$. Assuming $h >> a$, the image charge contribution can be calculated as coming from series of image like charges of density $-\lambda e$ at $y = \pm 2h, \pm 6h, etc.$ and density λe at $y = \pm 4h, \pm 8h$, etc. A particle at location y on the $y-$axis will thus experience an electric field:

$$E_y = 2\lambda e\left(\frac{1}{2h-y} - \frac{1}{4h-y} + ... - \frac{1}{2h+y} + \frac{1}{4h+y} - ..\right). \tag{177}$$

For $|y| << h$, it becomes

$$E_y \approx -\frac{\lambda e}{h^2} y \sum_{n=1}^{\infty} \frac{(-1)^n}{n^2} = \frac{\pi^2}{12}\frac{\lambda e}{h^2} y. \tag{178}$$

We now consider magnetic part of the problem. Let magnet pole be presented by two plates at $y = \pm g$. The image currents are $\lambda e \beta c$ at $y = \pm 2g, \pm 4g$, etc. This gives

$$B_x = 2\lambda e\beta\left(\frac{1}{2g-y} + \frac{1}{4g-y} + ... - \frac{1}{2g+y} - \frac{1}{4g+y} - ..\right), \tag{179}$$

$$B_x \approx \frac{\lambda e\beta}{g^2} y \sum_{n=1}^{\infty} \frac{1}{n^2} = \frac{\pi^2}{6}\frac{\lambda e\beta}{g^2} y. \tag{180}$$

The total incoherent tune shift of a uniform beam in the vertical direction becomes:

$$\Delta\nu_y = -\frac{\lambda r_0 R^2}{\nu_{y0}\beta^2\gamma}\left(\frac{1}{a^2\gamma^2} + \frac{\pi^2}{24h^2} + \frac{\pi^2\beta^2}{12g^2}\right). \tag{181}$$

Problem 4.2 Repeat analysis for image effects for the x-motion and obtain expression for the tune shift in horizontal direction $\Delta\nu_x$.

For a bunched beam the maximum tune shift due to direct self-fields is obtained with λ replaced by a peak density at the beam center $\hat{\lambda}$. Similarly, the maximum electric field is obtained by replacing λ with $\hat{\lambda}$ in the case of conducting boundary. For the case of magnetic field one has to distinguish between "dc" ($\bar{\lambda}$) and "ac" ($\tilde{\lambda}$) component of the current. The "dc" contains frequencies at which the skin depth is greater than the vacuum chamber wall thickness. The "ac" component has a skin depth which is small compared to the wall thickness.

The vertical tune shift should be rewritten as

$$\Delta\nu_y = -\frac{r_0 R^2}{\nu_{y0}\beta^2\gamma}\left[\frac{1}{\gamma^2}\left(\frac{1}{a^2} + \frac{\pi^2}{24h^2}\right)\hat{\lambda} + \beta^2\left(\frac{\pi^2}{24h^2} + \frac{\pi^2}{12g^2}\right)\bar{\lambda}\right]. \tag{182}$$

We can rewrite the expression above in a more general form using the Laslett coefficients:

$$\Delta\nu_{inc} = -\left[\frac{Nr_0}{\pi\beta^2\gamma}\right]\left(\frac{\bar{\beta}}{B_f}(\frac{1}{\gamma^2}-n_e)\frac{\epsilon_{sc}}{a^2}+\sum_i C_i\bar{\beta}_i\left[\frac{(1-n_e)}{B_f}\frac{\epsilon_{1,i}}{h_i^2}+\beta^2\frac{\epsilon_{2,i}}{g_i^2}-\beta^2(\frac{1}{B_f}-1)\frac{\epsilon_{1,i}}{h_i^2}\right]\right), \tag{183}$$

where we use B_f for bunching factor defined as a ratio of average beam current to a peak current, include the neutralization parameter n_e, and keep the structure parameter C_i which represents the fraction of the circumference occupied by each type of component. Here $\bar{\beta} \approx R/\nu_0$ is an average beta function, and ϵ_{sc} is the self-field coefficient which is equal to 1/2 in our case of circular beam cross section and uniform density. In this expression, the first term under the $\sum$ sign comes from the electric image, the second term comes from "dc" magnetic image, and the third term comes from "ac" magnetic image due to axial bunching. The Laslett (image) coefficients $\epsilon_{1,2}$ will depend on the geometry of beam pipe. These coefficients were computed for various geometries [96],[97],[98],[99], and are given in Table 9. In Table 9, $K(k)$

Table 9: Image coefficients for various beam pipe geometries

Image Coefficients	Parallel Plates	Circular	Elliptical
$\epsilon_{1,x}$	$-\frac{\pi^2}{48}$	0	$-\frac{h^2}{6d^2}\left[2(2-k^2)K^2/\pi^2-1\right]$
$\epsilon_{1,y}$	$\frac{\pi^2}{48}$	0	$\frac{h^2}{6d^2}\left[2(2-k^2)K^2/\pi^2-1\right]$
$\epsilon_{2,x}$	$-\frac{\pi^2}{24}$	-	-
$\epsilon_{2,y}$	$\frac{\pi^2}{24}$	-	-
$\xi_{1,x}$	0	$\frac{1}{2}$	$\frac{h^2}{4d^2}\left[1-4K^2(1-k^2)/\pi^2\right]$
$\xi_{1,y}$	$\frac{\pi^2}{16}$	$\frac{1}{2}$	$\frac{h^2}{4d^2}\left[4K^2/\pi^2-1\right]$
$\xi_{2,x}$	0	-	-
$\xi_{2,y}$	$\frac{\pi^2}{16}$	-	-

is the complete elliptic integral of the 1st kind, v and h are the major and minor axes of the elliptical tube, and $d=\sqrt{v^2-h^2}$. Symbol ϵ is used for the coefficients associated with the incoherent part, while for the coherent part we use additional coefficients ξ with the subscripts $1,2$ referring to the electric or magnetic problems, respectively. The image coefficients ϵ_2 and ξ_2 for closed magnetic boundaries (such as circular or elliptic) cannot be calculated for $\mu\to\infty$ because the induced magnetic field would not permit a charged beam to pass through. Closed magnet yokes are used in superconducting magnets, but there the coefficients $\epsilon_2 = \xi_2 \to 0$ since the magnet material is driven completely into saturation $\mu \to 1$. For more discussion on image coefficients see [96],[99].

4.2.4 Coherent tune shift

We now go back to Section 4.2.1, and expression for the force in Eq. 162. In this case the average position $\bar{y}$ is varying in time due to the coherent oscillation of the beam. The equation of motion can be solved by choosing $y = \bar{y}$. We thus have

$$\bar{y}'' + \left(\frac{\nu_{y0}^2}{R^2} - \frac{1}{m\gamma v^2}\left(\left[\frac{\partial F}{\partial y}\right]_{\bar{y}=0} + \left[\frac{\partial F}{\partial \bar{y}}\right]_{y=0}\right)\right)\bar{y} = 0. \tag{184}$$

We can now introduce the coherent tune shift:

$$\Delta\nu_{coh} = -\frac{R^2}{2\nu_{y0} m\gamma v^2}\left(\left[\frac{\partial F}{\partial y}\right]_{\bar{y}=0} + \left[\frac{\partial F}{\partial \bar{y}}\right]_{y=0}\right). \tag{185}$$

Such coherent motion is called the rigid dipole mode. Higher order modes also exist. These modes govern beam cross-sectional form and will also contribute to beam tune shift even in the absence of beam surroundings, while the coherent tune shift of dipole mode is a result of image fields. For this reason, we will refer to the tune shift of high order modes as "effective" to distinguish from the coherent tune shift caused by the dipole mode.

Similarly to the incoherent motion, we can find contribution to the force F from image field and obtain the general expression for the coherent tune shift. Boundary conditions now depend upon whether the oscillating field of the beam is of a low enough frequency to penetrate the vacuum chamber and to reach the magnetic poles or not. Electric fields are always considered as non-penetrating. However, for magnetic field both penetrating and non-penetrating fields are possible. For the non-penetrating fields, the magnetic image should be decomposed into its "dc" part, which is bounded on the poles, and "ac" part, which is bounded on the vacuum chamber. In the case of the penetrating magnetic fields, we have:

$$\Delta\nu_{coh}^{p} = -\left[\frac{Nr_0}{\pi\beta^2\gamma}\right]\sum_i C_i\bar{\beta}_i\left[\frac{(1-n_e)}{B_f}\frac{\xi_{1,i}}{h_i^2} + \beta^2\frac{\xi_{2,i}}{g_i^2} - \beta^2(\frac{1}{B_f}-1)\frac{\xi_{1,i}}{h_i^2}\right]. \tag{186}$$

Once again, the first term under the $\sum$ sign comes from the electric image, the second term comes from "dc" magnetic image, and the third term comes from "ac" magnetic image due to axial bunching. In the case of the non-penetrating magnetic fields, we have:

$$\Delta\nu_{coh}^{non-p} = -\left[\frac{Nr_0}{\pi\beta^2\gamma}\right]\sum_i C_i\bar{\beta}_i\left[\frac{(1-n_e)}{B_f}\frac{\xi_{1,i}}{h_i^2} + \beta^2\frac{\epsilon_{2,i}}{g_i^2} - \beta^2(\frac{1}{B_f}-1)\frac{\xi_{1,i}}{h_i^2} - \beta^2\frac{(\xi_{1,i}-\epsilon_{1,i})}{h_i^2}\right], \tag{187}$$

where additional term comes from "ac" magnetic image due to the transverse motion. The correspondent Laslett coefficients are given in Table 9.

4.2.5 Effect on image coefficients due to finite beam size

In our analysis we used the image coefficients derived in the assumption that distances between a beam and its images are much greater than the transverse beam size. This assumption allows us to approximate the beam and its images by line charges and currents which is not quite accurate for some beams in high-intensity rings, for example, for the SNS beam parameters.

Below we underline the principle difference due to Zotter [97]. For a pencil beam at x_0 in a circular vacuum chamber of radius h, the electric image coefficient evaluated at point x is given by

$$\epsilon_1 = -\frac{\phi_0^2}{2(1-\phi_0\phi)^2}, \tag{188}$$

where $\phi_0 \equiv x_0/h$ and $\phi \equiv x/h$. For a beam at the center of vacuum chamber ($\phi_0 = 0$), and thus we have $\epsilon_1 = 0$ as we used in our estimates. For a uniform flat beam of width $2a$ we have [97]:

$$\epsilon_1(\phi, \phi_0, \alpha) = -\frac{1}{2\phi^2}\left[1 + \frac{1}{u^2 - v^2} + \frac{1}{v}\ln\frac{u-v}{u+v}\right], \tag{189}$$

where $u \equiv 1 - \phi\phi_0$, $v \equiv \alpha\phi$ with $\alpha \equiv a/h$. For $\phi \to 0$ this expression becomes indeterminate. Thus this limit should be obtained directly from integration over a beam of finite width. Final result is the following:

$$\epsilon_1(0, \phi_0, \alpha) = -\frac{1}{2}\left(\phi_0^2 + \frac{\alpha^2}{3}\right). \tag{190}$$

Now, at $\phi_0 = 0$, $\epsilon_1 \neq 0$, and, for example, for $\alpha^2 = 1/2$ (SNS example) we have $\epsilon_1 = -1/12$.

We can see that for the final-size (at the end of multi-turn injection) SNS beam at full-intensity our estimates based on pencil beams are not quite accurate. However, we should note that, due to the multi-turn injection painting, beam size increases gradually. The significant value of α is reached only at the end of painting just before extraction.

4.2.6 Summary of major points

- Space-charge effect is of non-relativistic nature with direct incoherent tune shift having energy dependence of $1/\beta^2\gamma^3$.
- For a beam with non-uniform density the space-charge tune shift depends on the amplitude. Particles with small amplitudes will have maximum tune shift. Such maximum tune shift can be estimated using the concept of equivalent beams.
- For bunched beams space-charge force depends on the longitudinal distance from the bunch center. This leads to a tune spread and tune modulation for particles executing a synchrotron oscillations.
- Cancellation between electric and magnetic forces in the beam is perturbed due to the beam surroundings which can lead to important tune shift due to image fields.

• The estimates of the image coefficients are typically derived in the assumption that beam size is much smaller than the distance between the beam and its images. For very large beam sizes one has to take into account correction due to the beam size.

• Beams can get partially neutralized. In this case the electric space-charge field is reduced and cancellation between forces is perturbed.

4.3 Self-consistent treatment of beams

4.3.1 The Vlasov Equation

Here we closely follow the description of this subject given in [100]. The accepted method of describing self-consistent equilibria is the Vlasov model. It applies to all systems for which Liouville's theorem is applicable and where collisions between particles can be neglected. A system of identical charged particles is defined by the distribution function $f(q_i, p_i, t)$ in six-dimensional phase space, where q_i and p_i represent the conjugate canonical space and momentum coordinates. Liouville's theorem states that

$$\frac{df}{dt} = \frac{\partial f}{\partial t} + \sum_{i=1}^{3} \left(\frac{\partial f}{\partial q_i} \dot{q}_i + \frac{\partial f}{\partial p_i} \dot{p}_i \right) = 0. \tag{191}$$

This is equivalent to the statement that the volume occupied by a given number of particles in phase space remains constant:

$$\int d^3q d^3p = const. \tag{192}$$

The phase-space coordinates q_i, p_i obey Hamilton's equation of motion:

$$\dot{q}_i = \frac{\partial H}{\partial p_i}, \quad \dot{p}_i = -\frac{\partial H}{\partial q_i}, \tag{193}$$

where $H(q_i, p_i, t) = c(m^2c^2 + (\mathbf{p} - Q\mathbf{A})^2)^{1/2} + Q\phi$ is the relativistic Hamiltonian. Here the scalar potential ϕ and the vector potential $\mathbf{A}$ represent the sum of the applied fields and the self fields of the beam. The self-field contribution is determined by the space-charge density ρ and current density $\mathbf{J}$. These quantities are obtained by integrating the distribution function in momentum spaces

$$\rho = Q \int f(q_i, p_i, t) d^3p, \tag{194}$$

$$\mathbf{J} = Q \int \mathbf{v} f(q_i, p_i, t) d^3p. \tag{195}$$

Then, in the case of explicit time dependence ($\partial f / \partial t \neq 0$), one has to solve the wave equations for ϕ and $\mathbf{A}$:

$$\bigtriangledown^2 \phi - \mu_0 \epsilon_0 \frac{\partial^2 \phi}{\partial t^2} = -\frac{\rho}{\epsilon_0}, \tag{196}$$

$$\nabla^2 \mathbf{A} - \mu_0 \epsilon_0 \frac{\partial^2 \mathbf{A}}{\partial t^2} = -\frac{\mathbf{J}}{\epsilon_0}. \tag{197}$$

Using Hamilton's equation, we rewrite the Liouville equation as

$$\frac{\partial f}{\partial t} + \sum_{i=1}^{3} \left(\frac{\partial f}{\partial q_i} \frac{\partial H}{\partial p_i} - \frac{\partial f}{\partial p_i} \frac{\partial H}{\partial q_i} \right) = 0, \tag{198}$$

which is the Vlasov equation. This equation can be rewritten as

$$\frac{\partial f}{\partial t} + \sum_{i=1}^{3} \left(\frac{\partial f}{\partial q_i} \dot{q}_i + Q(\mathbf{E} + \mathbf{v} \times \mathbf{B})_i \frac{\partial f}{\partial P_i} \right) = 0, \tag{199}$$

where P is a mechanical momentum, with electric and magnetic field determined self consistently by Maxwell's equations.

To construct a stationary ($\partial/\partial t = 0$) solution it is necessary to know the constants of motion C_i, taking into account both external focusing and self fields. Then, any distribution function which is an arbitrary function of these constants $f(C_1, C_2, ..)$ satisfies the Vlasov equation

$$\frac{df}{dt} = \sum_i \frac{\partial f}{\partial C_i} \frac{\partial C_i}{\partial t} = 0, \tag{200}$$

since $dC_i/dt = 0$, for $i = 1, 2, ...$

For constant focusing, one can choose the Hamiltonian to describe a stationary solution with an arbitrary $f(H)$. The potential in H must be found self-consistently from the charge density.

For periodic focusing, the Hamiltonian is not a constant. The only stationary solution known in this case is the Kapchinsky-Vladimirsky (KV) distribution.

4.3.2 KV distribution

In statistical mechanics, the distribution in which the forces are linear and the phase-space areas remain constant is known as the microcanonical distribution. This distribution, which was used by Kapchinsky and Vladimirsky to study the effects of space charge on transverse dynamics, is referred to in the accelerator community as the KV distribution.

We start with the equations of motion for a quadrupole focusing channel:

$$x'' + k_x(z)x = 0, \tag{201}$$

$$y'' + k_y(z)y = 0, \tag{202}$$

where the focusing functions also include the linear space-charge force:

$$k_x(z) = k_{x,0}(z) - \frac{2\kappa}{X(X+Y)}, \tag{203}$$

where X and Y are the semiaxes of elliptical cross section of the beam, and κ is the space-charge parameter. Solutions of these equations are

$$x(z) = A_x W_x(z) \cos(\psi_x(z) + \phi_x), \tag{204}$$

$$y(z) = A_y W_y(z) \cos(\psi_y(z) + \phi_y), \tag{205}$$

with $\psi_x' = 1/W_x^2$, $\psi_y' = 1/W_y^2$, and the following equation for $W_{x,y}$:

$$W'' + kW - \frac{1}{W^3} = 0. \tag{206}$$

$$A_x^2 = \frac{x^2}{W_x^2} + (W_x x' + W_x' x)^2, \tag{207}$$

with $A_{x,max}^2 = \epsilon_x$ being the beam emittance. The quantities A_x^2, A_y^2 are the constants of the motion. One can define a new integral of the motion

$$F = A_x^2 + \frac{\epsilon_x}{\epsilon_y} A_y^2, \quad or \quad G = \frac{A_x^2}{\epsilon_x} + \frac{A_y^2}{\epsilon_y}. \tag{208}$$

As discussed above, any distribution function $f(F)$ or $f(G)$ satisfies the stationary Vlasov equation. However, only the special microcanonical distribution produces linear equations of motion. This distribution has the following form:

$$f = \bar{f}_0 \delta(F - F_0), \quad f = f_0 \delta(G - 1), \tag{209}$$

where $\delta(x)$ is Dirac's delta function. For such a distribution, all particles in the beam lie on the surface of the 4-dimensional (4-D) hyperellipsoid

$$\frac{1}{\epsilon_x}\left[\frac{x^2}{W_x^2} + (W_x x' - W_x' x)^2\right] + \frac{1}{\epsilon_y}\left[\frac{y^2}{W_y^2} + (W_y y' - W_y' y)^2\right] = 1. \tag{210}$$

The projection of this hyperellipsoid in the (x, x') plane gives $\frac{x^2}{W_x^2} + (W_x x' - W_x' x)^2$, which may be rewritten in terms of the Courant-Snyder parameters as

$$\gamma_x x^2 + 2\alpha_x x x' + \beta_x x'^2 = \epsilon_x. \tag{211}$$

In fact, all 2-D projections $(x, x';\ x, y;$ etc.) are ellipses with uniform particle density. The charge density can be found from the distribution function as

$$\rho = Q f_0 \int \delta(G-1) dx' dy' = Q f_0 \pi \sqrt{\frac{\epsilon_x \epsilon_y}{\beta_x \beta_y}}. \tag{212}$$

The total current in the longitudinal z-direction is given by

$$I = v_z \int \rho dx dy = v \rho X Y \pi, \tag{213}$$

where beam cross section is an ellipse $XY\pi$. We then have

$$\rho(z) = \frac{I}{\pi v X(z) Y(z)}, \quad f_0 = \frac{I}{\pi^2 Q v \epsilon_x \epsilon_y}. \tag{214}$$

By knowing the charge density, the electrostatic potential Φ can be found from Poisson's equation for any given position z, approximating the beam as an infinite elliptical cylinder with semiaxes X, Y:

$$\Phi = -\frac{\rho}{4\epsilon_0}\left[x^2 + y^2 - \frac{X(z) - Y(z)}{X(z) + Y(z)}(x^2 - y^2)\right] + const, \tag{215}$$

which gives a linear field inside the beam.

4.3.3 Stationary distributions in a constant focusing channel

For a uniform focusing channel the KV distribution can be represented as a delta function of the transverse Hamiltonian:

$$f(H_\perp) = f_1 \delta(H_\perp - H_0). \tag{216}$$

We then have

$$n(r) = 2\pi f_1 \int \delta(H_\perp - H_0) dH_\perp = 2\pi f_1 = n_0. \tag{217}$$

Using the Poisson equation

$$\frac{1}{r}\frac{d}{dr}\Big(r\frac{d\phi}{dr}\Big) = -\frac{Qn_0}{\epsilon_0} = -\frac{\rho_0}{\epsilon_0}, \tag{218}$$

we get

$$\phi(r) = \frac{\rho_0}{4\epsilon_0}(a^2 - r^2) = \frac{I}{4\pi\epsilon_0 v}\Big(1 - \frac{r^2}{a^2}\Big), \tag{219}$$

and

$$E_r = -\frac{d\phi}{dr} = \frac{\rho_0}{2\epsilon_0} r, \tag{220}$$

with linear beam self fields.

The KV distribution is the easiest one to perform analytic studies. However, it is not a realistic one. In fact, a sufficient condition for the distribution function to be stable is to have a monotonically decreasing $f(H)$ [101]. The KV distribution, on the contrary, often becomes unstable due to density fluctuations because of the $\delta(H - H_0)$ dependence.

Clearly, a more realistic distribution is the one where the ellipsoid is filled inside also. Such a distribution is called a "Waterbag" (WB) distribution:

$$f = f_2 \theta(H_0 - H_\perp). \tag{221}$$

The density is proportional to the potential $W(r)$:

$$n(r) = 2\pi f_2 \Big[W(a) - W(r)\Big]. \tag{222}$$

This results in a linear Poisson equation in the form

$$\frac{1}{r}\frac{\partial}{\partial r}\left(r\frac{\partial u}{\partial r}\right) = \kappa^2 u, \tag{223}$$

in terms of a new variable u for the potential. The solution of this equation is the modified Bessel-function $I_0(\kappa r)$. We thus obtain:

$$n(r) = n_0\left(1 - \frac{I_0(\kappa r)}{I_0(\kappa a)}\right), \tag{224}$$

which gives the zero-current parabolic density profile for $\kappa = 0$, and a square profile for $\kappa a \to \infty$.

One can construct a family of stationary distributions in the general form

$$f(\mathbf{r}, \mathbf{p}) = f_0(H_0 - H)^n, \tag{225}$$

$$n = -1, \quad (like \;\; KV), \quad 4 - D, \tag{226}$$

$$n = 0, \quad (WB), \quad 4 - D, \tag{227}$$

$$n \to \infty, \; H_0 \to \infty, \quad (Maxwell - Boltzman), \quad 4 - D. \tag{228}$$

In six dimensions (6-D), it is not possible to get a distribution with linear forces inside the beam but it is possible to get an analytically tractable distribution [102]:

$$n = -1/2, \quad (analytically \;\; tractable), \quad 6 - D, \tag{229}$$

$$n \to \infty, \quad (Maxwell - Boltzman), \quad 6 - D. \tag{230}$$

In 6-D, we have

$$\rho(\mathbf{r}) = Q\int d\mathbf{p} f(\mathbf{r}, \mathbf{p}), \tag{231}$$

$$H_0 - H = \left[H_0 - \sum_i \frac{k_i x_i^2}{2} - e\Phi_{sc}(\mathbf{r})\right] - \frac{p^2}{2m}. \tag{232}$$

If we now define the expression in the square brackets as $G(\mathbf{r})$, we obtain

$$\rho(\mathbf{r}) = \frac{QG^{n+3/2}(\mathbf{r})}{\int d\mathbf{r} G^{n+3/2}(\mathbf{r})}, \tag{233}$$

so that a choice of $n = -1/2$ gives us a linear equation for the potential (similar to the WB case in 4-D) which is solvable analytically. Such a distribution function was proposed and used for studies of the 6-D beam halo in high-intensity linacs [102]. Subsequently, it was employed to study the effect of particle collisions on beam halo formation [103].

4.4 Envelope description of non-KV beams

Envelope equations for a continuous beam with uniform charge density and elliptical cross-section were first derived by Kapchinsky and Vladimirsky (KV). It was later shown [104] that KV equations are not restricted to uniformly charged beams, but are equally valid for any charge distribution with elliptical symmetry, provided the boundary and emittance are defined by rms (root-mean-square) values. This follows because

- the second moments of particle distribution depend only on the linear part of the force.
- this linear part of the force in turn depends only on the second order moments of the distribution.

This is also true in practice for three-dimensional bunched beams with ellipsoidal symmetry, and allows the formulation of envelope equations that include the effect of space charge on bunch length and energy spread [104].

Consider a stationary or non-stationary distribution $f(x, y, x', y')$ in 4-D. The second moment of the particle distribution x is defined by

$$\bar{x^2} = \int x^2 f(x, y, x', y') dx dx' dy dy', \tag{234}$$

and the rms width in the x-direction

$$x_{rms} \equiv \tilde{x} = \sqrt{\bar{x^2}}. \tag{235}$$

Similarly, one can define the other second order moments such as $\bar{x'^2}, \bar{xx'}, \bar{y^2}$, etc.

Problem 4.3 Show that for a uniform distribution in 2-D $x_{rms} = a/2$ and in 3-D (spherical beam) $x_{rms} = a/\sqrt{5}$, where a is the maximum beam radius.

We now derive the rms version of the envelope equation by starting with equation of the motion

$$p' + k^2 x = f_x. \tag{236}$$

We then construct the following expressions:

$$< x^2 >' = 2 < xx' > = 2 < xp >, \tag{237}$$

$$< xp >' = < x'p + p'x > = < p^2 > - k^2 < x^2 > + < x f_x >, \tag{238}$$

$$< p^2 >' = 2 < pp' > = -2k^2 < xp > + 2 < p f_x > . \tag{239}$$

From Eqs. 237 and 238 we have

$$< x^2 >'' = 2 < p^2 > - 2k^2 < x^2 > + 2 < x f_x > . \tag{240}$$

By defining the rms emittance $\tilde{\epsilon}_x^2 = < x^2 >< p^2 > - < xp >^2$, we obtain

$$< p^2 > = \frac{\tilde{\epsilon}^2}{< x^2 >} + \frac{< xp >^2}{< x^2 >} = \frac{\tilde{\epsilon}^2}{< x^2 >} + \frac{(< x^2 >')^2}{4 < x^2 >}. \tag{241}$$

We now define $\sigma_x^2 =< x^2 >$ and put Eq. 241 in Eq. 240:

$$< \sigma_x^2 >'' = \frac{2\tilde{\epsilon}^2}{\sigma_x^2} + \frac{2((\sigma_x^2)')^2}{4\sigma_x^2} - 2k^2\sigma_x^2 + 2 < xf_x >, \tag{242}$$

which can be rewritten in the final form, known as the rms envelope equation:

$$\sigma_x'' + k^2\sigma_x - \frac{\tilde{\epsilon}^2}{\sigma_x^3} = \frac{< xf_x >}{\sigma_x}. \tag{243}$$

We should note that rms envelope equation was derived on the assumption that the rms emittance is either constant or its time dependence is known a priori. It has been shown by Sacherer that the term $< xf_x >$ is approximately independent of the distribution and has the same value as for the KV equivalent distribution.

$$< xf_x > = \frac{\kappa}{2}\frac{\sigma_x}{\sigma_x + \sigma_y}, \tag{244}$$

which gives

$$\sigma_x'' + k^2\sigma_x - \frac{\tilde{\epsilon}^2}{\sigma_x^3} - \frac{\kappa}{2(\sigma_x + \sigma_y)} = 0, \tag{245}$$

with a similar envelope equation in the y-direction. By introducing the beam width $X = 2\sigma_x$, $Y = 2\sigma_y$ and $\epsilon_x = 4\tilde{\epsilon}_x$, $\epsilon_y = 4\tilde{\epsilon}_y$, we recover the KV envelope equations:

$$X'' + k^2X - \frac{2\kappa}{X+Y} - \frac{\epsilon_x^2}{X^3} = 0, \tag{246}$$

$$Y'' + k^2Y - \frac{2\kappa}{X+Y} - \frac{\epsilon_y^2}{Y^3} = 0. \tag{247}$$

One can analyze the behavior of various distributions using the concept of equivalent beams. According to this concept, two beams composed of the same particle species (with the same current and kinetic energy) are equivalent in an approximate sense if the second moments of the distribution are the same. This implies that the rms beam widths and rms emittances in the two orthogonal directions are identical. As a result, one can describe the average or rms behavior of non-KV beam by solving the rms envelope equation. Note that the rms envelope equations are not closed for non-KV distributions since the rms emittance is not a conserved quantity in the presence of non-linear forces. As a result, the rms envelope equations can be applied for realistic beams with non-linear forces with the exception of situations where the rms emittance growth occurs.

4.5 Resonance condition and space charge

In a circular machine the effect of magnet field errors in beam optics can accumulate. This results in an instability if betatron tunes have resonant values. For example, in the absence of coupling, the resonance condition for the tune would be $\nu_0 = n/m$, where n is the harmonic content of the errors and m is the resonance order. The resonance order m can be associated with the multipole spectrum of the lattice errors, with $m = 2$ corresponding to gradient errors, $m = 3$ - sextupole errors, etc.

If we now think about space charge as a perturbation producing a tune shift of individual particles (incoherent tune shift) the resonance condition would become $n/m = \nu_0 - \Delta\nu_{sc}$, with $\Delta\nu_{sc}$ being the maximum space-charge tune shift. Such a criterion is widely used when one wants to choose the best working point in the tune space by avoiding dangerous resonances. However, this condition is only approximate. It can be still applied for high-order resonances or in the limit of very small space charge (high energy) keeping in mind that it is based on incorrect physics. For high-intensity accelerators this condition would give too conservative an estimate for low-order resonances which are most important in consideration of the resonance condition. This, in turn, could strongly underestimate the maximum achievable current. A correct treatment requires one to take into account the collective behavior of the beam.

The fact that the incoherent tune (do not confuse it with single-particle tune without space charge ν_0) is irrelevant for integer resonances was first emphasized by D. Morin [105] and P. Lapostolle [106]. It was then L. Smith [107] who used the envelope equation to prove that the half-integer resonance does not occur at the incoherent frequencies either. Smith's analysis was extended to high-order resonances by F. Sacherer [108] using the Vlasov equation in 1-D. The theoretical framework was later extended to 2-D by R.L. Gluckstern [109]. This theory was subsequently confirmed with computer simulations by I. Hofmann [110] and S. Machida [111]. Recently, a very good overview was presented by R. Baartman [112].

In general, the integer resonance can be investigated using the equation of motion of the first moments. The half-integer resonance studies require the equation of motion of second order moments or envelope equations. High-order resonances would require solution of the correspondent equations of high-order moments. Also, high-order resonances can be treated using the Vlasov equation as was shown by F. Sacherer [108].

4.5.1 Integer resonances

Assume that the space-charge force is given by $F_{sc} = \frac{\kappa}{a^2}x \equiv \tilde{\kappa}x$. We then write the equation of the motion as

$$x'' + \nu_0^2 x = \tilde{\kappa}x + F(x,\theta), \tag{248}$$

where $F(\theta)$ represents lattice errors. We need to take into account the fact that space-charge forces are centered on the beam:

$$x'' + \nu_0^2 x = \tilde{\kappa}(x - \bar{x}) + F(\theta), \tag{249}$$

where $\bar{x}$ is the coordinate of the center of the beam charge. Taking the average, we have:

$$\bar{x}'' + \nu_0^2 \bar{x} = F(\theta), \tag{250}$$

which is an obvious finding that the center of the charge is not affected by the space-charge forces. We now subtract Eq. 250 from Eq. 249 and obtain an equation for the incoherent motion:

$$(x - \bar{x})'' + \nu_0^2 (x - \bar{x}) = \tilde{\kappa}(x - \bar{x}) \tag{251}$$

or

$$(x - \bar{x})'' + \nu_{inc}^2 (x - \bar{x}) = 0, \tag{252}$$

with the incoherent tune defined as $\nu_{inc}^2 = \nu_0^2 - \tilde{\kappa}$. This shows that the incoherent equation of the motion does not have a driving term at an integer resonance. As a result, the incoherent motion is not affected by dipoles errors. Obviously, the coherent motion becomes unstable when the coherent tune ν_0 in Eq. 250 becomes an integer, which is also true for individual particle motion if space-charge forces are not considered.

4.5.2 Half-Integer resonance

The incoherent space-charge approach to the resonance condition fails because it is based on the assumption that the beam size remains constant. However, the beam envelope depends on the oscillation amplitude of the individual particles. Thus, if the gradient error causes these amplitudes to grow, the beam size also grows which in turn reduces the space-charge effect (this, of course, applies to high-order multipole errors also). Clearly, the incoherent space-charge approach is not self-consistent. More than that, using the KV beam, it is easy to show [113], [108] that the effect of gradient errors in the lattice is exactly compensated by the space-charge perturbation induced by those errors if $\nu_{inc} = n/2$. Here we present this interesting cancelation effect, assuming for simplicity a symmetric mode of envelope oscillations. We start with the following equation of motion

$$x'' + \nu^2 x = \alpha_n \nu_0^2 x \cos n\theta, \tag{253}$$

where $\nu^2 \equiv \nu_{inc}^2 = \nu_0^2 - \kappa/a_0^2$, and the envelope equation:

$$a'' = \frac{\epsilon^2}{a^3} - \nu_0^2 a + \frac{\kappa}{a} + \alpha_n \nu_0^2 a \cos n\theta. \tag{254}$$

We now assume small oscillations of the beam radius $a = a_0(1 + u)$ and obtain

$$u'' + p^2 u \approx \alpha_n \nu_0^2 \cos n\theta, \tag{255}$$

with p being the frequency of the symmetric envelope oscillations. Using the particular solution for u, we get

$$a = a_0 \left[1 + \frac{\alpha_n \nu_0^2 \cos n\theta}{p^2 - n^2} \right]. \tag{256}$$

Taking the variation of beam radius into account, Eq. 253 becomes

$$x'' + \nu^2 x = \left(- \frac{2\kappa}{a_0^2} \alpha_n \frac{\nu_0^2}{p^2 - n^2} + \alpha_n \nu_0^2 \right) x \cos n\theta, \tag{257}$$

which gives, after applying a phase-amplitude analysis, the following resonance condition:

$$2\nu(2\nu - n) = \alpha_n \nu_0^2 \left(1 - \frac{2\kappa}{a_0^2(p^2 - n^2)}\right). \tag{258}$$

Using $p^2 = 4\nu^2 + 2\kappa/a_0^2$, the resonance condition becomes

$$2\nu(2\nu - n) = \alpha_n \nu_0^2 \frac{(4\nu^2 - n^2)}{p^2 - n^2}. \tag{259}$$

Thus, we have exact cancelation for the $\nu = n/2$ resonance. There is no "quadrupole" resonance at the incoherent tune. In a similar analysis for an antisymmetric envelope mode, or in a general case for resonance of any order, this cancelation effect can be shown using the Vlasov equation [114]. We also find that the half-integer resonance occurs at the coherent frequency Ω_2 (where we used $\Omega_2 \equiv p$). The frequencies of second order coherent modes can be easily obtained by linearizing the envelope equations for small perturbation. The expressions are especially simple for a round beam with the same external focusing in both transverse directions:

$$\Omega^2_{2,symm} = 2\nu_0^2 + 2\nu_{inc}^2 \approx 4\nu_0^2 - 4\nu_0\Delta\nu, \tag{260}$$

$$\Omega^2_{2,antisymm} = \nu_0^2 + 3\nu_{inc}^2 \approx 4\nu_0^2 - 6\nu_0\Delta\nu, \tag{261}$$

where the first part of these expressions are derived without the approximation of small space-charge. As a result, they are extensively used in high-intensity linac studies.

Problem 4.4 Derive expressions given by Eqs. 260-261, assuming small oscillations of the beam envelopes (use Eq. 245).

In circular machines, transverse tunes are typically split to avoid coupling. If this split $|\nu_{0x} - \nu_{0y}|$ is not small compared to $\Delta\nu/4$, instead of the coupled modes described above we have essentially decoupled motion with

$$\Omega_2^2 \approx 4\nu_0^2 - 5\nu_0\Delta\nu. \tag{262}$$

We can now write the correct half-integer resonance condition. For example, for the symmetric second order mode, it becomes

$$n = \Omega_2 \approx 2(\nu_0 - \frac{1}{2}\Delta\nu). \tag{263}$$

4.5.3 High-order resonances

In general, the resonance condition (here we use Baartman's notation) can be rewritten as

$$\frac{n}{m} = \nu_0 - C_m\Delta\nu. \tag{264}$$

For the half-integer resonance we obtained $C_{2,symmetric} = 1/2$, $C_{2,antisymmetric} = 3/4$ for the case of similar tunes. Therefore, for the antisymmetric case the effective tune shift $\Delta\nu_{eff} = \frac{3}{4}\Delta\nu$ is significantly smaller than one would expect based on the incoherent tune shift. For the split tune case the difference is even bigger since $\Delta\nu_{eff} = \frac{5}{8}\Delta\nu$. The concept of "effective" tune shift is introduced here in order not to confuse it with the coherent tune shift of the rigid-dipole mode, which arises from image effects. This effective tune shift arises from high-order collective beam modes, which have nothing to do with the effect of images. The coefficients C_m can be easily obtained from high-order coherent frequencies which were derived for a round beam by R.L. Gluckstern [109], and later extended to non-round beams by I. Hofmann [115]. Here we list coefficients for the low-order modes of a round beam in the case of similar tunes:

$m = 2 -> C_{symm} = 1/2,\ C_{asymm} = 3/4,$

$m = 3 -> C = 3/4, 11/12,$

$m = 4 -> C = 7/8, 13/16, 31/32.$

$m \to \infty -> C = 1.$

From these coefficients it is clear that the standard approach of using the incoherent tune shift for the resonance condition would not give an accurate predictions for low-order resonances, especially for the half-integer resonance. For this reason, it seems possible to accumulate more current in high-intensity machines than predicted using the simplified (incoherent) resonance condition.

4.5.4 Non-KV distributions

The coherent beam modes were derived using the KV beam. However, in the previous section we showed that one can use rms envelope equation for non-KV distributions also, using the rms quantities. This allows us to use second order coherent modes for non-KV beams. This concept of KV equivalent beams has been used in studies of high-order resonances as well [116], [112], [111].

4.5.5 Effect of images

In Section 4.2 we derived the contribution to the incoherent tune shift from images. Clearly, if image effects are important they can add to the effective tune shift which would make the resonance condition look similar to the incoherent one. Thus one has to estimate the importance of image effects when one intends to analyze the resonance condition in the presence of space charge for a specific machine of interest.

4.5.6 Discussion

Space-charge induced tune spread causes the beam foot-print to span imperfection resonances. For a coasting beam, there is general agreement that Sacherer's theory is correct so that the resonance condition is defined by the coherent frequencies. However, several effects should be taken into account (including the effect of images) when one wants to apply it to experimental observations. For bunched beams there is no good conceptual analytic framework. For long ellipsoidal bunches the transverse modes are decoupled from the longitudinal one but it is not clear to what extent the synchrotron motion will impact the resonance condition of the transverse coherent modes. This question is currently under study but in some accelerators where synchrotron motion is negligible (in the SNS the full injection process of 1000 turns takes about one synchrotron oscillation) it seems reasonable to assume that the impact of synchrotron motion will not be important. In fact, some recent experiments and simulations for the bunched beam in the LANL Proton Storage Ring (PSR) seem to support the above discussion [117], [118].

4.6 Halo formation and emittance growth

The importance of space charge and halo formation in high-intensity linacs has been widely recognized (see extensive literature in [127]; also some new developments were recently reported [128]). In rings, however, an understanding of these issues appears to be even more important: for economic reasons, in a linac one may have a sufficiently large bore to accept the halo, while in a ring one must try to avoid halo formation because of a relatively small beam pipe acceptance / beam size ratio. A discussion of halo formation issues in circular accelerators was recently presented [113]. Here we briefly discuss various mechanisms of halo formation in circular accelerators and their application to the SNS [148].

4.6.1 Development of parametric halo

The parametric resonance mechanism, which could be one of the major sources of space-charge induced halo in linacs, is not necessarily the main source of halo in rings. The physics of this resonance is described by the following equation:

$$x'' + \nu^2 x = \mu \frac{2\kappa}{a^2} x \cos ps, \tag{265}$$

where ν is the depressed tune, κ is the space-charge parameter, μ is the mismatch parameter which describes small envelope oscillations, and p is the frequency of these envelope oscillations. The mechanism of halo formation is therefore the parametric resonance between p and ν, with $\nu = p/2$ being the dominant one. This resonance between the motion of individual ions and collective beam oscillations is governed by the rms beam mismatch. It can be shown that the main 1:2 parametric resonance is possible for any non-zero space charge. The halo extent associated with this resonance is large not only for very strong tune depressions of the order of $\eta \sim 0.5$ (typical in linacs) but also for tune depressions of only a few percent $\eta \sim 0.98$ (typical in high-intensity rings). The separatrix width of this 1:2 resonance is governed mainly by the beam mismatch, although some dependence on tune depression does exist. In the limit of zero space charge, the motion near the core is very regular, and the rate at which particles are driven to the 1:2 resonance becomes very small; in addition, the unstable fixed points of the 1:2 resonance move further from the origin. Therefore, for the space charge typical in high-intensity rings ($\eta \sim 0.98$), it will take much more time for particles to be trapped in the 1:2 resonance than for typical linac tune depressions. The rate of halo development thus becomes the most important question when one tries to estimate the effect of the parametric resonance on halo formation in rings. Computer simulations with a full-intensity KV beam confirm both the existence of parametric halo at $\eta \sim 0.98$ and a very slow growth rate [129]. However, in the SNS the use of multi-turn injection makes the situation quite different from the simplified assumption of a full-intensity beam. First, the final intensity is reached only at the end of injection, just before extraction; this leaves no time for a parametric halo to develop. Second, the mismatched modes of the beam may be damped by the phase mixing associated with multi-turn injection. To summarize, mechanisms other than parametric resonance may be more important for halo development in high-intensity rings. Thorough studies of various mechanisms that can lead to beam tail growth are required because of the low tolerance for uncontrolled beam loss.

4.6.2 Effect of resonances

Machine resonances play a major role in halo formation. Most of the analytic studies can be done using single-particle dynamics. When space charge is included one has to use the correct resonance condition described in the previous section. The realistic prediction of emittance growth, of course, has to rely on computer simulations which are described in Section 4.8.

Besides machine resonances there are also space-charge induced resonances. Their importance was first shown for the dominant coupling resonance [130], and then for some non-coupling resonances [111, 131]. Therefore, the choice of working point should also take into account space-charge induced resonances. For the SNS the dominant space-charge coupling resonance, $2\nu_x - 2\nu_y = 0$, was observed in numerical simulations with full-intensity beams and multi-turn injection. An important question associated with this resonance is the instability of high-order coherent beam modes, which was recently addressed [134].

Working points with tune split of the half-integer or more help to avoid coupling caused by the space-charge forces and systematic magnet errors. However, the region close to the same tune coupling resonance line is the largest region free of the imperfection resonances. Thus, trying to avoid coupling necessarily increases the impact of various imperfection resonances. Finding the best compromise between these effects requires to consideration of all these effects in combination, and thus again heavily relies on realistic computer simulations.

4.6.3 Other mechanisms

The development of a beam halo also depends strongly on the choice of the painting scheme and beam profile. As an example, we briefly discuss two painting schemes proposed for the SNS.

Anti-correlated painting is designed to produce an elliptical transverse beam profile of uniform density, but, in the presence of space charge, it generates an excessive halo [132, 149]. Thus, special schemes are required to minimize halo production [149]. Correlated painting has the advantage of constantly painting over the beam halo, but even in this case careful bump optimization is needed to achieve low beam loss.

In the case of correlated painting, the beam is painted to a square shape; this results in a “singular” distribution along the diagonals [148], [133]. The inclusion of space charge leads to rapid azimuthal diffusion and some spreading in the radial direction. For this case the 2-D beam densities, based on simulations, agree well with analytic predictions [133].

4.7 Coherent Instabilities

In an accelerator, the beam of particles does not propagate in a free space. Beam surroundings (pipes, cavities, pumping holes, etc.) influence the fields around the beam, which may make the beam unstable. We already started to consider the beam environment by discussing image effects in Section 4.2. However, in our previous description fields remained in phase with the motion of single particles or with the beam centroid, which resulted in simple incoherent or coherent tune shifts, respectively.

Clearly, the beam-environment interaction is more complex. For example, assume a beam passing through a cavity. It will excite fields in the cavity which can in turn act on the remaining portion of the beam or on a subsequent beam bunch. Such fields are typically referred to as wake fields. Therefore, the beam-environment interaction involves a study of the wake fields or coupling impedance which is an inverse Fourier transform of the wake field.

The subject of coherent instabilities is very important but also is very advanced. For detailed description we refer the interested reader to Alex Chao book [95] and K.Y. Ng lectures [158]. The typical electron bunch length can be of the same order or even shorter than the wavelength of the instability driving force which requires taking in consideration a bunch structure. On the other hand, the length of proton bunches are usually larger than the wavelength of perturbation or instability driving force which allows to consider them locally as a coasting beam. For this reason, we mostly limit our discussion to the stability condition of coasting beams which has direct application for a very long beam bunch in high-intensity machines under design. We adopt our quick introduction to this subject from [96]. The bunched beam structure would support oscillation modes within the bunch similar to those of a coasting beam. However, the bunch length sets the resonance condition for the standing wave rather than the machine circumference. In addition, there would be coupled-bunch modes which are characterized by definite phase relation between the oscillations from bunch to bunch.

4.7.1 Coupling Impedance

In our discussion of stability conditions we will use the concept of the coupling impedance, which is defined below. Assume a harmonic excitation current of amplitude $I(\omega)$ which excites a harmonic field with complex amplitude $E_z(\omega)$. The longitudinal coupling impedance is then defined as

$$Z_{||}(\omega) = \frac{\int E_z exp(jkz)dz}{I}. \tag{266}$$

The transverse coupling impedance is defined as the integral of the deflecting fields over one turn normalised by the dipole moment of the excitation beam current

$$Z_{\perp}(\omega) = j\frac{\int \left[E_r + \beta c B_\theta\right] exp(j\omega z/v)dz}{I\Delta y}, \tag{267}$$

where Δy is the horizontal or vertical offset of the beam from the axis.

At low frequency the impedance is dominated by the skin effect of the vacuum chamber; at medium and higher frequencies the impedance behaves as that of a broad band resonator - thus the word “broadband” impedance. At certain high frequencies there will be strong local resonances, for example, from cavities. A typical example of impedance budget for a high-intensity proton machine is shown in Table 10, using the SNS case.

Table 10: SNS impedance budget (low frequency (below 10MHz) approximation.)

	$\mathbf{Z_{\parallel}/n}$	$\mathbf{Z_{\perp}}$
Space charge	-j196	-j7,720
Extraction kicker (50 Ω termination)	35+j42	21·n+j200
RF cavity	requires damping of parasitic modes and active feedback system	-
Resistive wall (at ω_0)	(j+1)0.69	(1+j)6.23
Broadband		
BPM	j4.0	j58.0
Bellows	j1.53	j13.8
Steps	j1.60	j14.4
Ports	j0.49	j4.42
Valves	j0.15	j1.35
Collimator	j0.22	j1.98
Total BB	j8.0	j94.0
Unit	Ω	**kΩ/m**

4.7.2 Landau damping

From the knowledge of the impedance seen by the beam it is possible to predict whether the beam is stable or not. The natural stabilizing mechanism against collective instabilities is the synchrotron or betatron frequency spread of particles in the beam. This stabilization is known as Landau damping [152]. In an accelerator, the spread in natural frequencies of the beam comes from various sources. Such a spread occurs due to the dependence of the betatron frequencies on the energy of the particles together with the energy spread of the beam. Another source of the spread are nonlinearities in the focusing system as well as in self-fields of the beam which cause a dependence of betatron frequencies on particles’s amplitude. In the longitudinal case the source of frequency spread depends on whether the beam is bunched or unbunched. For bunched beams, a spread of synchrotron frequency can result from nonlinearities in the rf focusing voltage. For unbunched beams, the spread comes from the dependence of the revolution frequency on the particle energy. If a large spread of frequencies provides a fast decay of center-of-mass response the effect of the impedance can be compensated and the instability is suppressed. The Landau damping mechanism is automatically included in stability analysis when one applies the Vlasov equation as demonstrated in the next section.

4.7.3 Longitudinal instability in a coasting beam

It is natural to describe particle distributions in a circulating beam in terms of the angular position and the angular momentum. Let $f(\Theta, p, t)$ be a function describing the beam distribution with azimuthal angle $\Theta = 2\pi s/C_0$ and longitudinal momentum p. We start with the Vlasov equation

$$\frac{\partial}{\partial t} f(\Theta, p, t) + \dot{\Theta} \frac{\partial}{\partial \Theta} f(\Theta, p, t) + \dot{p} \frac{\partial}{\partial p} f(\Theta, p, t) = 0. \tag{268}$$

A particle at position s sees a wake force from all beam particles that passed the same location earlier. This force, averaged over the ring circumference, is

$$\dot{p} = -\frac{eZ_{\parallel}}{C_0} I_1 e^{j(\Omega t - n\Theta)}, \tag{269}$$

where we used the fact that the beam-induced voltage experienced by a particle during one turn is $Z_{\parallel} I_1 e^{j(\Omega t - n\Theta)}$ with $I(s) = I_0 + I_1 e^{j(\Omega t - n\Theta)}$. It is reasonable to make a trial function solution with the same form as the current perturbation:

$$f(\Theta, p, t) = f_0(p) + f_1(p) e^{j(\Omega t - n\Theta)}. \tag{270}$$

Inserting this trial function into Eqs. 268- 269 gives

$$j(\Omega - n\omega) f_1(p) e^{j(\Omega t - n\Theta)} - \frac{eZ_{\parallel}}{C_0} I_1 e^{j(\Omega t - n\Theta)} \frac{d}{dp} f_0(p) = 0, \tag{271}$$

with $\omega = \dot{\Theta}$. Here, f_1 in the last term was neglected since it is small compared to f_0.

If we now integrate over the momentum spread in the beam we obtain an expression for coherent beam behavior

$$I_1 e^{j(\Omega t - n\Theta)} = \frac{j}{C_0} e^2 \omega_0 Z_{\parallel} I_1 e^{j(\Omega t - n\Theta)} \int_{beam} \frac{df_0(p)/dp}{n\omega - \Omega} dp, \tag{272}$$

which simplifies in the linear approximation to

$$1 = \frac{j}{C_0 p_0} e^2 \omega_0^2 Z_{\parallel} \eta \int_{beam} \frac{df_0/d\omega}{n\omega - \Omega} d\omega, \tag{273}$$

which is the dispersion relation linking the frequency of the disturbance Ω with its wavelength represented by n. Here, the compaction factor η is defined as $\Delta\omega = \eta\omega_0 \Delta p/p_0$. Using the dispersion relation, it is possible to investigate beam stability. The collective frequency has to be solved from the dispersion relation for each revolution frequency. If there is no energy spread the dispersion relation given by Eq. 273 is easily solved. Above transition ($\eta > 0$), the solution will be unstable for capacitive impedance $Z_{\parallel} = jZ_i$. As a result, the longitudinal space-charge impedance becomes the source of instability known as "negative mass" instability. The stability criterion with momentum spread was first derived for an rf cavity. The dispersion integral in Eq. 273 was solved by assuming that the perturbation frequency has a small imaginary part and assuming a Lorentz beam distribution:

$$Z_{\|,cavity} < \frac{nZ_0|df_{rev}/dE|\Delta E^2_{hwhm}}{m_0c^2r_0Nf^2_{rev}}, \tag{274}$$

where Z_0 is the impedance of free space, r_0 is the classical radius of the beam particle and ΔE is half of the energy spread at half maximum of the distribution. The dispersion relation can also be rewritten in a compact form

$$1 = sign(\eta)(U' - jV')S, \tag{275}$$

where S represents the normalized dispersion integral. The parameters U', V' were introduced by Ruggiero and Vaccaro to have a compact form for the dispersion relation. These parameters are proportional to the parameters U, V introduced earlier by Neil and Sessler, which have the advantage of being closely related to the induced voltage ($Z_\| = j(U + jV)/eI_0$). The dispersion integral depends greatly on the particle distribution in momentum or revolution-frequency space. The stability curves in the U', V' space (impedance plane) were studied by Ruggiero and Vaccaro for various distributions [119]. Then an approximate condition was proposed [120], which is known as Keil-Schnell criterion:

$$|Z_\|/n| < F_1\frac{\beta^2E_0}{e}\frac{\eta}{I_0}\Big[\frac{\Delta p_{fwhm}}{p_0}\Big]^2, \tag{276}$$

where F_1 is a form factor depending on beam distribution. Thus, for beam stability the impedance seen by the beam should be minimized. One can see that large value of the momentum compaction η helps, as well as large value of $\Delta p/p_0$. The stabilization effect by momentum spread is called Landau damping. Figure 53 shows schematic plot of the longitudinal stability diagram for a Gaussian distribution.

The Keil-Schnell approximation, which uses a circle assumption in the impedance plane (see Fig. 53), works well for energies above transition. Below transition, on the other hand, the main source of the longitudinal impedance is the space charge (only imaginary contribution) so that the real part of the impedance could be orders of magnitude smaller. This results in a significant deviation from the circle approximation, and is the reason why for energies below transition Keil-Schnell condition was significantly overcome. Also, in such a “space-charge regime” in the stability diagram (in U', V' space) one could expect stabilization due to nonlinear behavior [121]. For additional discussion see, for example [122].

The wavelegth of such instabilities is much smaller than the length of the bunch. Therefore, the high-frequency growth is called microwave instability. Microwave instabilities predicted by Eq. 276 are rare or nonexistent below transition.

4.7.4 Transverse instability in a coasting beam

The underlying physics for transverse instabilities is similar to that for the longitudinal case. The calculations of the transverse coupling impedances are more complicated than those of the longitudinal impedances. However, in many cases a simple approximate relationship between

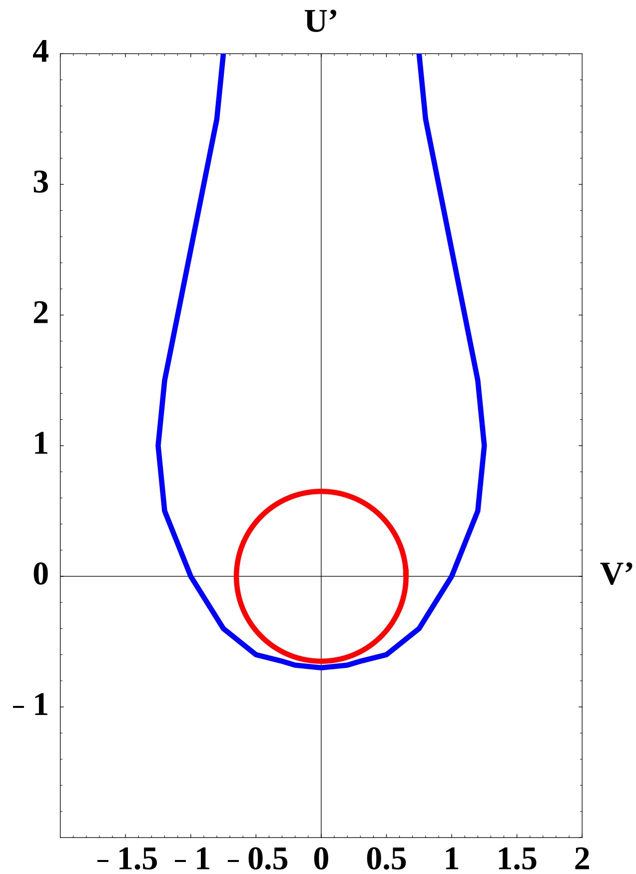

Figure 53: Schematic longitudinal stability diagram of a beam with Gaussian distribution.

transverse and longitudinal impedances can be applied which allows one to avoid complicated calculations. If the transverse impedance is found, then the stability condition can be again obtained using the Vlasov equation [123]. The transverse stability condition is given by

$$|Z_\perp| < F_2 \frac{E_0}{e} \frac{4\nu_0\gamma\beta}{IR} \frac{\Delta p_{fwhm}}{p_0} \Big[(n-\nu_0)\eta - \xi\Big], \tag{277}$$

where F_2 is a form factor close to unity for well-behaved distributions. Here we used the convention ν for the tune, and ξ for the chromaticity, which is the tune change due to momentum ($\delta\nu = \xi\Delta p/p_0$). In case the instability growth rate is much faster than the synchrotron oscillation, one may obtain a stability criterion against transverse microwave instability for bunched beams [124]. This is done by simply replacing the unperturbed beam density of an unbunched beam by the peak density of a bunched beam because, in the fast growing regime, the instability occurs locally and thus the peak beam density would determine the stability condition.

The Landau damping (necessary for stability) can be enhanced by introducing the amplitude dependent tune spread with chromatic sextupoles and octupoles. There is still discussion in the community as to how to include correctly the space charge in the transverse instabilities models, and the interested reader is referred to [125], [126].

The typical measures aimed to prevent instabilities consist of minimization of the coupling impedance of the vacuum chamber by screening any abrupt cross section changes (bellows, vacuum manifolds, etc.) and proper design of protruding elements like pick up and cleaning electrodes.

4.7.5 Other single-bunch instabilities

Here we briefly describe some other basic instabilities in addition to the microwave instabilities discussed above.

Robinson instability This instability addresses the question of phase stability in circular accelerator. The RF cavities are tuned so that the resonance frequency of the fundamental mode ω_R is very close to an integral multiple of the revolution frequency ω_0 of the beam. As a result, the wake field excited by the beam in the cavities contains a major frequency component near $\omega_R \approx h\omega_0$, where integer h is called harmonic number. Above the transition energy, the beam will be unstable if w_R is slightly above $h\omega_0$ and stable if below [153]. Below transition energy the dependence of the revolution frequency on energy is reversed which changes the stability criterion.

Negative mass instability The revolution frequency increases with energy gain below transition and decreases above it. In other words, above transition energy the particle slows down if it gain energy ("negative longitudinal mass"). As a result, some spontaneous longitudinal density fluctuation is enhanced above transition resulting in negative mass instability. The unbunched beams are intrinsically unstable longitudinally above transition. This requires damping mechanisms such as Landau damping, which was discussed in the previous section on longitudinal stability.

Head-tail instability Short-range transverse wake fields excited by particles at the head of a bunch may excite oscillations at its tail. Synchrotron motion brings these particles again to the head and they continue to excite particles behind. Such oscillations will grow if they add in phase. If the chromaticity is negative the only unstable azimuthal mode is $m = 0$ with all other high-order beam modes being stable. Such unstable beam mode can be damped with a beam damper. Also, chromaticity correction is typically required which is achieved with chromatic sextupoles. Various head-tail modes of oscillations can be excited shifting the chromaticity to the unstable directions. These modes were first observed in the CERN PS Booster [154]. Some recent observations of head-tail instability at RAL ISIS, CERN PS and KEK PS were reported at BNL's workshop on instabilities in hadron machines [126]. The head-tail instability can be cured with the tune spread, appropriate choice of natural chromaticity, reduction of wall impedance and dedicated feedback system.

Transverse mode coupling instability (TMCI) The TMCI instability is also called fast/strong head-tail instability. Such instability occurs when the frequencies of two neighboring head-tail modes approach each other due to detuning with increasing current during acceleration. The fast head-tail was observed at PEP, LEP, SPS and electron machines with short bunches but not so far in hadron machines with long bunches. It was recently reported that space-charge tune shift can strongly damp TMCI [155].

E-P instability The electron-proton (e-p) instability was first diagnosed in the CERN ISR [156] and LBL Bevatron [157]. This instability is believed to be responsible for the fast transverse instability observed at LANL PSR. The e-p instability is considered a possibility for the proposed high-intensity machines. Among possible cures are coating of the vacuum chamber to reduce secondary electron emission and effective control by Landau damping.

4.8 Computer Simulations

4.8.1 Overview

Simulation of space-charge effects is one of the most computer intensive problems in particle tracking. The most widely used method for modeling intense charged particle beams is the particle simulation technique [135]. In this approach, one integrates the equation of motion for individual particles taking into account both the external fields of the system and collective fields of the beam. The collective fields may be obtained using Particle-Mesh methods, which are referred to as Particle-in-Cell (PIC) methods. This approach consists of placing the charge on a numerical grid and solving the field equations on the grid. The required steps are:

- **Charge deposition** : Place charges on a numerical grid.
- **Field solution** : Solve the field equations on the grid.
- **Field interpolation** : Interpolate the fields at the particle position based on values at the grid locations.

Although PIC methods are the basis of most of the codes, they suffer from the presence of statistical noise. The approach to avoid this is to use Vlasov/Poisson direct solvers, where one defines the particle distribution function on a grid in phase space. However, such simulations require large memory resources. For example, the memory requirement in a 2-D simulation grows as the fourth power of the grid size in one dimension (such simulations are now possible with parallel computing). For comparison, 2-D simulation with 128^4 grid requires 268 million grid points, while the 3-D case with 128^6 would require 4 trillion grid points, which is still beyond present-day computer resources. In this section we limit our discussion to particle simulation codes.

In particle simulation codes space charge may be treated in the full 6-dimensional phase space of the particles (3-D code), in the 4-dimensional transverse space with correction for the longitudinal dimension ($2\frac{1}{2}$-D code) or only in the 4-dimensional transverse space (2-D code). It is not always possible, as well as necessary, to use fully 3-D space-charge codes. Clearly, it depends on the parameters of the beam for which the code is intended. For example, for high-intensity linacs, which can have tune depression as high as 50%, space-charge effects becomes the crucial. Beam bunches with small aspect ratio (sometimes almost a spherical bunch) require 3-D space-charge codes, with correct modeling of space-charge coupling. This was shown to be important for detailed prediction of beam halo and emittance growth. Also, the necessity to predict beam losses at the 10^{-6} level in high-intensity linacs under design pushed the number of particles in simulations to a level where a single particle in simulation already corresponds to just a few real particles. This became possible due to recent development of parallel computing and the DOE Grand Challenge in Computational Accelerator Physics. An example of a beam dynamics code developed under this program is IMPACT, specifically written to model beam dynamics in high-intensity linacs [136].

For high-intensity circular machines one still needs to use the macro particle approach since tracking with a realistic number of particles ($10^{13} - 10^{14}$) is far beyond the present-day computer capabilities. Also, in most of the high-intensity circular machines the beam aspect ratio is quite different from the one in linacs. For example, in the SNS, the beam transverse size is a few cm while its length is around 200 m. Clearly, implementing a fully 3-D space-charge algorithm for such a beam would be very challenging. However, because of the large beam aspect ratio, the transverse and longitudinal space-charge forces are essentially decoupled. As a result, most questions may be answered without full 3-D space-charge representation. Nevertheless, the correction due to the longitudinal motion should still be taken into account. Here we list some of the codes developed for high-intensity circular machines which are widely used for particle tracking with space charge and a realistic machine lattice.

- ORBIT [137] (in $C++$), ORNL/BNL - developed for the SNS project.
- ACCSIM [138] (in Fortran), TRIUMF, Canada - developed for Kaon Factory project.
- SIMPSONS [111] (in Fortran), KEK, Japan - originally developed for the SSC; now used for Japanese Neutron Spallation Source project.
- WARP [139] (in Fortran), LLNL - developed for heavy-ion Fusion project.
- Track2D, Track3D [140] (in Fortran), Rutherford Appelton Lab, UK - now used for the European Neutron Spallation project.

The beam power of the proposed high-intensity circular machines is an order of magnitude above that of existing accelerator facilities, which imposes extremely strict requirement on uncontrolled beam loss at the 10^{-4} level. In order to address such low-level losses we need to closely reproduce all complex physics of a realistic machine. This includes not just the space-charge treatment but also realistic representation of magnet errors and non-linear particle motion. For example, the environment of the Unified Accelerator Libraries (UAL) suits such purposes [141]. The UAL's environment allows one to develop the project-specific packages which can include the best available codes and algorithms. Therefore, such a package was also developed for the SNS project [142], and it is currently used for beam dynamics studies [143]. For detailed description of this SNS package we refer the interested reader to [143]. As an example, in the next section we describe some basic features of the SNS/UAL simulation package.

4.8.2 The SNS simulations using UAL

Some of the important features which were implemented, benchmarked, and used in the SNS/UAL package are: injection painting, magnet fringe fields, magnet non-linearities and space charge.

Injection painting. During the multi-turn injection into the SNS ring, the beam is painted over a large phase space volume in order to reduce the space-charge tune shift and to minimize the number of traversals through the stripping foil. The development of beam halo depends strongly on the choice of painting scheme [148, 149]. Implementation of this dynamical process is based on the ACCSIM approach. However, the control of different scenarios is programmed directly with the Perl Application Programming Interface (API) that provides simple access to the UAL packages.

Fringe fields. Since the aperture of the ring magnets is comparable to the magnet lengths, fringe field impact is very important. The fringe fields are included through the Taylor maps extracted from the fringe field models. Both realistic three-dimensional (3-D) fringe field calculations with MARYLIE [145] and "hard-edge" approximation show the importance of the longitudinal field derivatives, and produce very similar behavior [146]. Currently, we are using maps (up to 5th order) based on both the "hard-edge" formulas and the realistic 3-D fields.

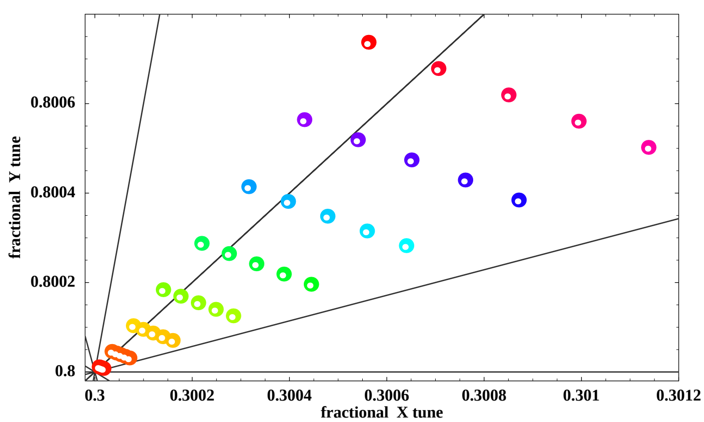

Figure 54: Kinematic non-linearity X-Y tune foot-print. Particles are launched in five different transverse directions with the amplitudes going up to 480 π mm mrad. Data obtained with MARYLIE is presented by color circles, while UAL's data is given by white dots inside the color circles.

Single-particle dynamics and non-linearities. Special characteristics of the SNS ring are large beam emittances (up to 240 π mm mrad), and large beam pipe apertures. Not surprisingly, this brings a variety of non-linear effects which are a direct consequence of large particle amplitudes. Such non-linearities can shift particles in undesired directions, dramatically decreasing the dynamic aperture. The study and understanding of these effects thus becomes very important. The simulation of non-linear magnet fields and misalignments were done with the TEAPOT [144] approach. TEAPOT approximates magnet elements by thin multipoles but treats the non-linear equation of motion exactly. To be confident in our non-linear dynamics studies, the UAL was benchmarked against MARYLIE 3.0 [145], which is a thick element code with an approximate treatment of equations of the motion. Some results of this benchmarking were presented in [147]. Figure 54 shows excellent agreement between these two codes for the tune shift due to the kinematic non-linearity, which arises from high order terms proportional to the transverse momenta p_x, p_y in the expansion of the standard square-root relativistic Hamiltonian. This plot is generated by launching particles in five different transverse directions with the amplitudes going up to 480 π mm mrad (neither non-linear elements nor magnet errors are present in the lattice). Data obtained with MARYLIE is presented by colored circles, while UAL's data is given by white dots inside the colored circles.

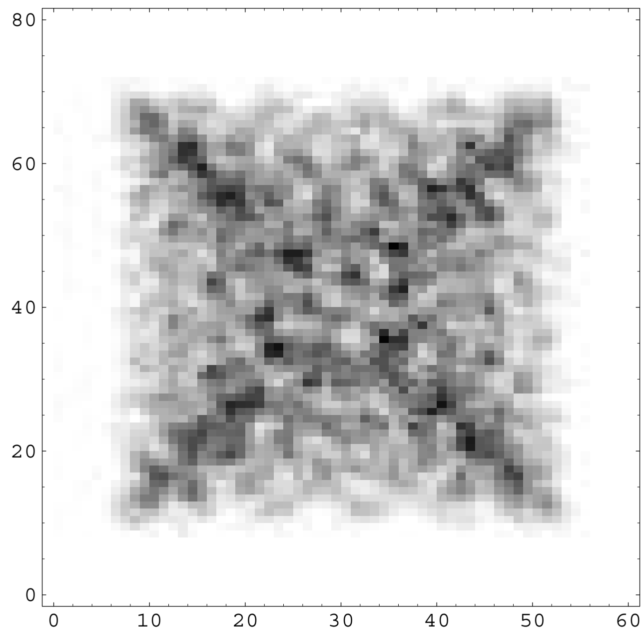

Figure 55: 2-D density plot (X-Y) for correlated painting with the square-root bump function (without the space charge), using SCMapper/ORBIT algorithm.

Multi-particle dynamics with space charge. The space-charge effect has the largest impact on beam dynamics and halo growth in the SNS accumulator ring, and has to be included in the common model. It is currently implemented through the ORBIT space-charge module, detailed description of which may be found, for example, in [129]. Briefly, this module is based on a Particle-in-cell (PIC) method employing a bilinear distribution of macroparticles on the nodes of a rectangular grid with subsequent use of a fast-Fourier-transform method to approximate the full non-linear space-charge force.

For the space-charge studies two independent integrators were developed [143]: SCMapper and SCTracker. The SCMapper, which adopts linear matrices approach for ring element treatment, was extensively used to ensure perfect agreement between the UAL and ORBIT codes. The SCTracker contains the ORBIT space-charge algorithm but treats ring elements based on the TEAPOT approach which allows one to include magnet errors in a consistent manner. Similar to a single-particle dynamics, it includes all non-linear features of the motion

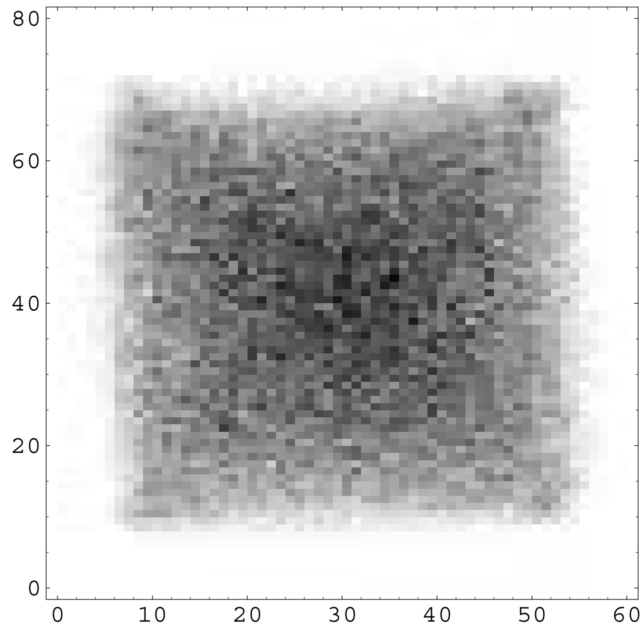

Figure 56: 2-D density plot (X-Y) for correlated painting with the square-root bump function (with the space charge), using SCMapper/ORBIT algorithm.

even in the absence of magnet errors.

Here we present examples based on correlated painting which results in a square shape beam desired by the target requirements. In Figs. 55 and 56 we present 2-D density plots (X-Y) for the resulting beam distribution based on the square-root bump function without and with space charge, respectively. Simulations were done with the SCMapper without magnet errors. The inclusion of the space charge leads to a rapid azimuthal diffusion with some spreading in the radial direction. For this case the 2-D beam densities, based on simulations, agree well with analytic predictions [133]. Exact treatment of non-linear motion (without magnet errors) via the SCTracker package leads to an additional spreading along the diagonals [143].

Computational efficiency The requirement of beam loss predictions at $10^{-3} - 10^{-4}$ level forces us to use a large number of macro-particles in our simulations to obtain good statistics. Our primary goal was to include all necessary physics in simulations rather than use large number of particles but with simplified physics (improvement of some algorithms is currently in progress [151]). The standard compromise between speed of calculation and physics is not quite applicable to our case since the requirements on beam losses is an order of magnitude smaller than those achieved in existing high-intensity machine. We thus need to keep all required physics in order to produce credible predictions of beam loss. At this point we note that the speed of the integrator becomes very slow with most of the physics correctly included. The typical run for 50K particles with the full-injection scenario, space charge, fringe fields and magnet errors takes about 50 hours of 1 CPU time on a Sun station. This resulted in our decision to deploy UAL on the parallel cluster. A parallel version of UAL was recently successfully developed and we now perform the SNS space-charge simulations on the parallel cluster [150].

5 Measurement, Correction, Commissioning

6 Design Example: Spallation Neutron Source Accumulator

6.1 Layouts

Schematic layout of the Spallation Neutron Source accumulator ring is given in Figures 5, 7, and 8.

6.2 List of Parameters

Table 11 lists the major parameters of the Spallation Neutron Source accumulator ring.

Table 11: Major machine parameters for the original hybrid lattice Spallation Neutron Source ring.

Quantity	Value	unit
Circumference	220.88	m
Average radius	35.154	m
Injection energy	1	GeV
Extraction energy	1	GeV
Beam power	2	MW
Repetition rate per ring	60	Hz
Number of protons	2.08	10^{14}
Ring dipole field	0.7406	T
RF harmonics	1, 2	
Peak RF voltage, $h = 1$	40	kV
Peak RF voltage, $h = 2$	20	kV
Unormalized emittance in x or y (cor. painting)	120	π mm mrad
Unnormalized emittance (99%) (anti-cor. painting)	160	π mm mrad
Betatron admittance	480	π mm mrad
Momentum acceptance (160 π mm mrad)	$\pm$ 2	%
Momentum acceptance (zero amplitude)	$\pm$ 3.8	%
Magnetic rigidity, $B\rho$	5.6574	Tm
Bending radius, ρ	7.6389	m
Horizontal tune	5.8 – 6.8	
Vertical tune	4.8 – 5.8	
Transition energy, γ_T	4.95	GeV
Horizontal natural chromaticity	-7.5	
Vertical natural chromaticity	-6.3	
Number of super-periods	4	

6.3 Lattice

```
! Lattice of the SPallation Neutron Source Accumulator Ring
! (draft)
  ANG:= 2*PI/32
  EE := ANG/2
  Brho := 5.6575
  lbnd := 1.5
  lq := 0.5
! matching value
  BEXD := 2.428
  BEYD := 13.047
  OZ : DRIFT, L = 0.0
  OQ1 : DRIFT, L = 0.0
  OQ2 : DRIFT, L = 0.0
  OQ3 : DRIFT, L = 0.0
  BL:  Sbend, L=lbnd/2, Angle=EE, E1=0., E2=0.
  BR:  Sbend, L=lbnd/2, Angle=EE, E1=0., E2=0.
  BND: Sbend, L=lbnd, Angle=ANG, E1=0.0, E2=0.0
! for achromat in x
  KF      := 4.65962
  KD      :=-4.94124
  QH      :=6.3
  QV      :=5.8
  MUH     := QH/4.0
  MUV     := QV/4.0
  QDH     : QUADRUPOLE, L = lq/2, K1 = KD/Brho
  QF      : QUADRUPOLE, L = lq, K1 = KF/Brho
  QFH     : QUADRUPOLE, L = lq/2, K1 = KF/Brho
  QD      : QUADRUPOLE, L = lq, K1 = KD/Brho
  OARC    : DRIFT, L = 1
  DM      : DRIFT, L = 3.8
  KMAT    := -3.405
  KS2     :=  4.298150
  KS3     := -4.586139
  lq1     := 0.25/2
  lq2     := 0.7/2
  lq3     := 0.55/2
  O1      : DRIFT, L = 6.85
  O11     : DRIFT, L = O1[L]/4
  O2      : DRIFT, L = 0.4
  O3      : DRIFT, L = 6.25
  O31     : DRIFT, L = O3[L]/12
  QMAT    : QUADRUPOLE, L = lq/2, K1 = KMAT/Brho
```

```
Q2       : QUADRUPOLE, L = lq2, K1 = KS2/Brho
Q3       : QUADRUPOLE, L = lq3, K1 = KS3/Brho

acd     : line = (QDH,OARC,BND,OARC,QFH)
acf     : line = (QFH,OARC,BND,OARC,QDH)
acfl    : line = (QFH,OARC,BND,OARC)
ac      : line = (acd,acf)
arc     : line = (ac,ac,ac,ac)
sc      : line = (QMAT,QMAT,O11,O11,O11,O11,Q2,OQ2,Q2,O2,Q3,&
     OQ3,Q3,O31,O31,O31,O31,O31,O31,O31,O31,O31,O31,O31,O31)
insert : line = (sc,OZ,-sc)
SP    : line = (insert,-acfl,-acd,ac,ac,acd,acfl)
ring  : line = (4*SP)

Use, SP
SELECT, OPTICS, RANGE = #S/#E
OPTICS,FILENAME = "sp.optics",&
      COLUMNS = NAME, KEYWORD, S, L, K1L, BETX,DX, BETY,DY
PRINT,  FULL

use, ring
SELECT, OPTICS, RANGE = #S/#E
OPTICS,FILENAME = "ring.optics",&
      COLUMNS = NAME, KEYWORD, S, L, K1L, BETX,DX, BETY,DY
PRINT,  FULL
TWISS, TAPE

stop
end
```

7 Special Topics

7.1 Beam Loss Mechanisms

Here we briefly describe some of the typical beam loss mechanisms which apply to the high-intensity proton rings.

7.1.1 "First-turn" losses

There are two major causes of beam loss which are usually referred to as "first-turn" losses [159]:

Scattering at the foil First mechanism is nuclear and large-angle Coulomb scattering of the circulating beam in the injection stripping foil. Before a recent upgrade at LANL PSR this type of loss accounted for 0.3% beam loss. By choosing the direct H^- injection scheme and minimizing beam foil traversals this loss can be significantly decreased [159].

Excited H^0 states A fraction of injected beam interacts in the stripper foil and is converted to excited states of H^0. As those neutrals pass through the magnetic field required to separate the different charge states, they can be stripped by the Lorentz force. Depending on when they strip, their subsequent trajectories can be outside the beam core. The H^0s that exit the foil will populate the various hydrogen states n, where n denotes principal quantum number. The behavior of excited states of H^0 is well understood and can be calculated to good accuracy by a number of methods. A widely used approach is the fifth-order perturbation theory of Damburg and Kolosov [162]. The probability $P(z)$ for $H^0(n)$ to survive to a point located at coordinate z in the fringe field of the magnet is given by solution of the basic loss rate equation

$$\frac{dP(z)}{dz} = \frac{-P(z)}{\tau(z)\beta\gamma c} = -\frac{P(z)\Gamma(z)}{\hbar\beta\gamma c}, \tag{278}$$

where Γ is the width of a given parabolic Stark state and τ its field-dependent lifetime. This give

$$P(z) = \exp\Big(- \frac{1}{\hbar\beta\gamma c} \int_{\infty}^{z} \Gamma(s) ds \Big). \tag{279}$$

The production of H^0 states can be strongly reduced by choosing an appropriate foil thickness. An upgraded design of the injection scheme at LANL PSR allowed to reduce this loss from 0.3% to $0.1 - 0.17$% (with 0.05% calculated) [159]. In the SNS design, to prevent stripping of H^0 in $n = 4$ and lower excited states the injection stripping foil is located at the downstream end of the injected dipole with the field of subsequent dipole magnet 2.4 kG. The fringe field of the injected dipole is shaped so that stripped electrons spiral down to where they can be easily collected. With such a design further reduction of this type of loss below 10^{-4} level is expected [160].

7.1.2 Imperfection resonances

Machine resonances are a fundamental source of beam halo in circular accelerators. A very careful choice of the working point and appropriate corrections schemes are required to reduce beam loss to a 10^{-3} level and below.

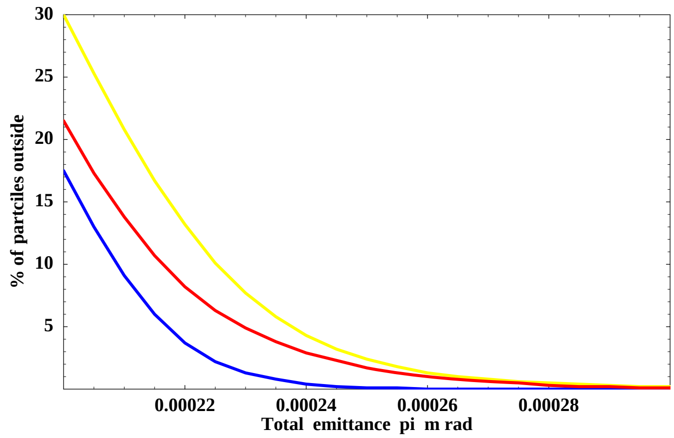

Figure 57: Beam halo at the end of multi-turn injection for $(\nu_x, \nu_y) = (6.4, 6.3)$; a) blue color shows halo due to the space charge alone b) red color corresponds to the case of both systematic and random magnet field errors at a few units at 10^{-4} level, chromatic sextupoles and quadrupole fringe fields c) yellow color shows an additional effect of x, y misalignment of 0.5 mm and magnet tilt of 1 mrad.

As an example, we show resulting beam halo for two different working points of the SNS [161]. Figure. 57 shows the case for $(\nu_x, \nu_y) = (6.4, 6.3)$ where several imperfection resonances (including 3rd order skew-sextupole resonance) are crossed. This results in a significant halo at the end of multi-turn injection requiring careful correction of resonances. Figure 58 demonstrates the case of $(\nu_x, \nu_y) = (6.23, 6.20)$ when no major imperfection resonances are excited. As a result, beam halo at the end of multi-turn injection is insignificant.

7.1.3 Space-charge effects

After machine imperfection resonances are corrected most of the "storage" beam losses are associated with space-charge effects. For example, space-charge driven resonances could be an important source of halo formation. The choice of working point should be done by taking these type of resonances into account. Particle-core parametric resonance, which is believed to be an important source of halo generation in a proton linac, is expected to be unimportant in a ring with multi-turn injection [148]. In general, space charge can be alleviated by longitudinal manipulation (double RF, barrier cavity, etc) to enhance bunching factor, painting and controlled injection or by simply raising the injection energy.

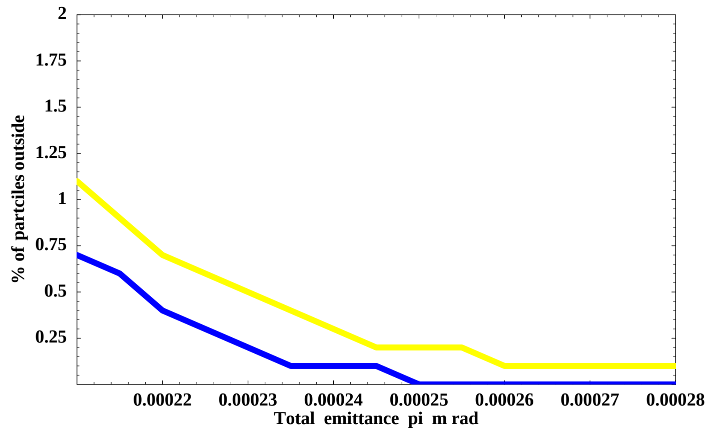

Figure 58: Beam halo for $(\nu_x, \nu_y) = (6.23, 6.20)$; a) blue color shows halo due to the space charge alone b) yellow color shows halo when magnet errors of expected magnitude are included.

7.1.4 Coherent instabilities

An attempt to reach the highest intensity possible is typically a long accelerator project struggle with coherent instabilities. Such instabilities (some of which are described in the section on instabilities) can strongly limit the high-intensity operation of a machine. This results in a number of preventive measures which minimize the coupling impedance of the vacuum chamber, design of feedback damping systems and other cures depending on the specifics of the instability.

7.1.5 Ramping loss

If instead of an accumulator ring the synchrotron approach is chosen, one has to deal with an additional significant beam losses due to ramping and RF capture. Compared with rapid cycling synchrotron, an accumulator ring simplifies the capture process and avoids ramping complications. The next generation of high-intensity machines set limitation on allowed beam loss at 10^{-4} level. Trying to get beam losses to such a low level in s synchrotron will be a very challenging task.

7.2 Scaling law for magnet fringe-field impact

7.2.1 Rms momentum kicks, general multipolarity

Following the symmetry condition (158), we can rewrite the field components (149), keeping terms of the expansion to leading order:

$$\begin{aligned}
B_x(x,y,z) =& \Im m \left\{ \frac{(x+iy)^n b_n(z)}{n!} - \frac{(x+iy)^{n+1}\left[(n+3)x - i(n+1)y\right] b_n^{[2]}(z)}{4(n+2)!} + O(n+4) \right\} \\
B_y(x,y,z) =& \Re e \left\{ \frac{(x+iy)^n b_n(z)}{n!} - \frac{(x+iy)^{n+1}\left[(n+1)x - i(n+3)y\right] b_n^{[2]}(z)}{4(n+2)!} + O(n+4) \right\} \ , \\
B_z(x,y,z) =& \Im m \left\{ \frac{(x+iy)^{n+1} b_n^{[1]}(z)}{(n+1)!} + O(n+3) \right\}
\end{aligned} \tag{280}$$

where the functions $O(j)$ represent polynomial terms in the transverse variables x, y of order greater or equal to j. These expressions stand for $n > 0$. The special case of the dipole will be treated in a subsequent section.

For a particle traversing the magnet with a horizontal deviation x and vertical deviation y from the center, the impulse (i.e. change of transverse momentum) imparted by the nominal field component is

$$\begin{aligned}
\Delta p_x^b =& - \ e \int_{\text{body}} v_z B_y(x,y,z)dz \approx - \ e v_z \overline{b_n} L_{\text{eff}} \frac{\Re e\left\{(x+iy)^n\right\}}{n!} \\
\Delta p_y^b =& \ e \int_{\text{body}} v_z B_x(x,y,z)dz \approx \ e v_z \overline{b_n} L_{\text{eff}} \frac{\Im m\left\{(x+iy)^n\right\}}{n!}
\end{aligned} \tag{281}$$

where $L_{eff} = \int_{\text{body}} b_n(z)dz/\overline{b_n}$ is the effective length of the magnet, and $\overline{b_n}$ is the nominal field coefficient in the body of the multipole magnet.

The impulse due to the fringe field at one end of a magnet is defined as the effect of field deviation from nominal, from well inside (where the nominal multipole coefficient is assumed to be independent of z) to well outside the magnet (where all field components are assumed to vanish.) These will be the limits for subsequent integrals.

The momentum kick imparted by the fringe field can be represented as follows:

$$\Delta p_{x,y}^f = \Delta p_{x,y}^f(\|) + \Delta p_{x,y}^f(\perp) \ , \tag{282}$$

where

$$\begin{aligned}
\Delta p_x^f(\|) =& \ e \int_{\text{fringe}} v_z y' B_z(x,y,z)dz \\
\Delta p_y^f(\|) =& - \ e \int_{\text{fringe}} v_z x' B_z(x,y,z)dz
\end{aligned} \ , \tag{283}$$

are the momentum increments of the particle caused by the longitudinal component of the magnetic field and

$$\begin{aligned} \Delta p_x^f(\perp) &= - \quad e \int_{\text{fringe}} v_z B_y(x,y,z)dz \\ \Delta p_y^f(\perp) &= \quad e \int_{\text{fringe}} v_z B_x(x,y,z)dz \end{aligned} \quad , \tag{284}$$

are the momentum increments of the particle caused by the transverse components of the magnetic field. Using the leading order expressions of the magnetic field, we obtain the following relations

$$\begin{aligned} \Delta p_x^f(\|) &\approx \quad \frac{ev_z\overline{b_n}}{(n+1)!}\Im m\left\{(x+iy)^{n+1}\right\}y' \\ \Delta p_y^f(\|) &\approx - \quad \frac{ev_z\overline{b_n}}{(n+1)!}\Im m\left\{(x+iy)^{n+1}\right\}x' \end{aligned} \quad . \tag{285}$$

and

$$\begin{aligned} \Delta p_x^f(\perp) &\approx \frac{-ev_z\overline{b_n}}{4(n+1)!}\Re e\left\{(x+iy)^n\left[(n+1)xx'+(n+3)yy'+i(n-1)xy'-i(n+1)yx'\right]\right\} \\ \Delta p_y^f(\perp) &\approx \frac{ev_z\overline{b_n}}{4(n+1)!}\Im m\left\{(x+iy)^n\left[(n+3)xx'+(n+1)yy'+i(n+1)xy'-i(n-1)yx'\right]\right\} \end{aligned} \quad , \tag{286}$$

for the momentum increments due to the longitudinal and transverse component of the field, respectively. The total momentum increments due to the fringe field are therefore

$$\begin{aligned} \Delta p_x^f &\approx - \quad \frac{ev_z\overline{b_n}}{4(n+1)!}\Re e\left\{(x+iy)^n\left[(n+1)(x-iy)(x'+iy')+2iy'(x+iy)\right]\right\} \\ \Delta p_y^f &\approx \quad \frac{ev_z\overline{b_n}}{4(n+1)!}\Im m\left\{(x+iy)^n\left[(n+1)(x-iy)(x'+iy')-2x'(x+iy)\right]\right\} \end{aligned} \quad . \tag{287}$$

In order to evaluate the contribution coming from the fringe part as compared to the body of the magnet, we first have to compute the total rms transverse momentum kick imparted by the fringe field $(\Delta p_\perp^f)_{rms} = \sqrt{\langle(\Delta p_x^f)^2\rangle + \langle(\Delta p_y^f)^2\rangle}$, where the operator $\langle . \rangle$ denotes the average over the angle variables. An equivalent expression stands for the deflection due to the body part of the field. After averaging over the angles and some lengthy calculations(see [26], the rms transverse momentum kicks can be expressed as:

$$
\begin{aligned}
(\Delta p_\perp^f)_{rms} &\approx \frac{ev_z\overline{b_n}}{2^{n+3}(n+1)!}\left[\sum_{l=0}^{n}\binom{2(n-l)}{n-l}\binom{2l}{l}\beta_x^{n-l}\beta_y^{l}\epsilon_x^{n-l}\epsilon_y^{l}\sum_{m=0}^{2} g_{n,l,m}(\alpha_{x,y},\beta_{x,y})\epsilon_x^m\epsilon_y^{2-m}\right]^{1/2}, \\
(\Delta p_\perp^b)_{rms} &\approx \frac{ev_z\overline{b_n}L_{\text{eff}}}{2^n n!}\left[\sum_{l=0}^{n}\binom{n}{l}\binom{2(n-l)}{n-l}\binom{2l}{l}\overline{\beta_x^{n-l}\beta_y^{l}}\epsilon_x^{n-l}\epsilon_y^{l}\right]^{1/2}
\end{aligned}
\tag{288}
$$

where the bars on the β's denote their average values over the body of the magnet. The coefficients $g_{n,l,m}$, given by

$$
\begin{aligned}
g_{n,l,0}(\alpha_{x,y},\beta_{x,y}) &= \frac{\left[(n^2+1)(2l+1)\binom{n}{l}-2l(2n+1)(-1)^l\binom{2n}{2l}\right]\left[1+(2l+3)\alpha_y\right]}{(l+1)(l+2)} \\
&\quad -\frac{8(n+1)(n-l)(2l+3)(-1)^l\binom{2n}{2l}\alpha_x\alpha_y\beta_y}{\beta_x(l+1)(l+2)} \\
g_{n,l,1}(\alpha_{x,y},\beta_{x,y}) &= \frac{\left[(n^2+4n+5)(2l+1)\binom{n}{l}+2(5n+2ln+2)(-1)^l\binom{2n}{2l}\right]\left[1+(2n-2l+1)\alpha_x\right]\beta_y}{\beta_x(n-l+1)(l+1)} \\
&\quad +\frac{\left[(n^2+4n+5)\binom{n}{l}-2(n+2)(-1)^l\binom{2n}{2l}\right](2n-2l+1)[1+(2l+1)\alpha_y]\beta_x}{\beta_y(n-l+1)(l+1)} \\
&\quad -\frac{8(n+1)\left[(2l+1)\binom{n}{l}+(n-l)(-1)^l\binom{2n}{2l}\right](2n-2l+1)\alpha_x\alpha_y}{(n-l+1)(l+1)}, \\
g_{n,l,2}(\alpha_{x,y},\beta_{x,y}) &= \frac{\left[(n^2+1)\binom{n}{l}+2n(-1)^l\binom{2n}{2l}\right](2n-2l+1)[1+(2n-2l+3)\alpha_x]}{(n-l+1)(n-l+2)}
\end{aligned}
\tag{289}
$$

depend on the twiss functions and on the multipole order n. One may note that rms transverse momentum kick of the fringe is represented by the square root of a polynomial of order $n+1$ in the transverse emittances ϵ_x and ϵ_y as compared to the square root of a polynomial of order p representing the body contribution (see also [76]). Thus their ratio should be proportional to the transverse emittance. We will show that this scaling law is indeed exact for the case of the dipole and quadrupole. For higher order multipoles, due to the complexity of these formulas, one can have approximative estimates considering special cases of beam shapes.

Flat beam For a flat beam, one of the transverse degrees of freedom (e.g. the vertical y, y') vanishes. Thus, the total transverse rms momentum increment for the body is

$$
(\Delta p_\perp^b)_{rms} \equiv \sqrt{\langle(\Delta p_x^b)^2\rangle} \approx \frac{ev_z\overline{b_n}L_{\text{eff}}}{2^n n!}\sqrt{\binom{2n}{n}\overline{\beta^n}\epsilon_\perp^n}\ , \tag{290}
$$

where $\overline{\beta^n}$ represents the average of the β^n on the body of the magnet and $\epsilon_\perp$ is the rms beam transverse emittance. The total transverse rms momentum increment for the fringe is

$$(\Delta p_\perp^f)_{rms} \equiv \sqrt{\langle(\Delta p_x^f)^2\rangle} \approx \frac{ev_z\overline{b_n}}{2^{n+3}n!}\sqrt{\binom{2n+2}{n+1}\frac{\beta^n[1+(2n+3)\alpha^2]}{2(n+2)}\epsilon_\perp^{n+2}} \quad , \tag{291}$$

where β and α represent the beta and alpha functions, at the fringe location. The ratio of the rms momentum transverse kicks is:

$$\frac{(\Delta p_\perp^f)_{rms}}{(\Delta p_\perp^b)_{rms}} \approx \frac{\epsilon_\perp}{8L_{\text{eff}}}\sqrt{\frac{(2n+1)\beta^n[1+(2n+3)\alpha^2]}{(n+1)(n+2)\overline{\beta^n}}} \quad , \tag{292}$$

Considering that the beta functions are not varying rapidly, if the magnets are in non-critical locations (which is to say most magnets), the square root can be neglected, so a crude estimate of the impulse is given by

$$\frac{(\Delta p_\perp^f)_{rms}}{(\Delta p_\perp^b)_{rms}} \approx \frac{\epsilon_\perp}{L_{\text{eff}}} \quad , \tag{293}$$

The case in which fringe deflections are likely to be most important is when α is anomalously large, for example in the vicinity of beam waists such as at the location of intersection points in colliding beam lattices. In this case, the deflections can be approximated by

$$\frac{(\Delta p_\perp^f)_{rms}}{(\Delta p_\perp^b)_{rms}} \approx \alpha\frac{\epsilon_\perp}{L_{\text{eff}}} \quad , \tag{294}$$

(The same scaling law is obtained by setting $\beta_x >> \beta_y$ in Eqs. (288).)

Often the relative deflection is so small as to make neglect of the fringe field deflection entirely persuasive. The simplicity of the formula is due to the fact that the fringe contribution is expressed as a fraction of the dominant contribution. Note that, as stated before, this formula applies to each end separately, and does not depend on any cancellation of the contribution from two ends. In fact, nonlinear analysis shows that fringe-field contributions tend to add up instead of canceling [76].

Round beam For a round beam, the two transverse emittances are equal $\epsilon_x = \epsilon_y = \epsilon_\perp$. For simplicity, we may also consider that the optics functions of the horizontal and vertical plane are close and thus $\beta_x \approx \beta_y = \beta$ and $\alpha_x \approx \alpha_y = \alpha$. One may also consider that $\overline{\beta^n} \approx \overline{\beta}^n$, i.e. the beta functions do not vary significantly in the body of the magnet. Taking into account the previous hypotheses, the total transverse rms momentum increment for the body becomes:

$$(\Delta p_\perp^b)_{rms} \approx \frac{ev_z\overline{b_n}L_{\text{eff}}}{2^{n/2}n!}\overline{\beta}^{n/2}\epsilon_\perp^{n/2}\left[{}_3F_2(1/2,-n,-n;1,1/2-n;1)\frac{(2n-1)!!}{n!}\right]^{1/2} \quad , \tag{295}$$

where the function in the square root represents the generalized Hyper-geometric function (see [88] for details). Applying the same simplifications, the rms momentum kick given by the fringe field is:

$$(\Delta p_\perp^f)_{rms} \approx \frac{e v_z \overline{b_n} \beta^{n/2} \epsilon_\perp^{n/2+1}}{2^{n+3}(n+1)!} \left[\sum_{l=0}^{n} \binom{2(n-l)}{n-l} \binom{2l}{l} g_{n,l}(\alpha) \right]^{1/2} , \tag{296}$$

where we considered $\beta_x \approx \beta_y = \beta$ and the same for the α functions. Notice now that the sum of the coefficients $g_{n,l} = g_{n,l,0} + g_{n,l,1} + g_{n,l,2}$ depends only on α. The series involving them can be also written as a sum of a few generalized Hyper-geometric functions. The ratio of the rms momentum transverse kicks is:

$$\frac{(\Delta p_\perp^f)_{\rm rms}}{(\Delta p_\perp^b)_{\rm rms}} \approx \frac{\epsilon_\perp}{L_{\rm eff}} \frac{\beta^{n/2}}{\overline{\beta}^{n/2}} C_n(\alpha) \ , \tag{297}$$

where the coefficient C_n is:

$$C_n(\alpha) = \frac{1}{8(n+1)} \left[\frac{n! \sum_{l=0}^{n} \binom{2(n-l)}{n-l} \binom{2l}{l} g_{n,l}(\alpha)}{{}_3F_2(1/2, -n, -n; 1, 1/2-n; 1)(2n-1)!!} \right]^{1/2} , \tag{298}$$

Let us consider two cases, as before: one where α is small and one where α is large, as in the case of interaction points of large colliders. For the first case (α small), we may neglect the terms having α as a factor in the coefficient $g_{n,l}$ and in the second case, we can pull out α from the square root and neglect terms in the coefficient $g_{n,l}$ having now the α function in the denominator. In this way, the coefficients C_n of Eq.(298) will depend only on the order n. The behavior of these coefficients as a function of the multipole order n, for large and small α, is dominated by $(1/(n+1)$. For all practical cases (multipole orders up to 20), C_n lies between 1/2 and 1/10. Considering now that the average β in the body of the magnet is not so different from β in the fringe, one gets for small α functions:

$$\frac{(\Delta p_\perp^f)_{\rm rms}}{(\Delta p_\perp^b)_{\rm rms}} \approx \frac{\epsilon_\perp}{L_{\rm eff}} \ , \tag{299}$$

as in Eq. (293), and for α large:

$$\frac{(\Delta p_\perp^f)_{\rm rms}}{(\Delta p_\perp^b)_{\rm rms}} \approx \alpha \frac{\epsilon_\perp}{L_{\rm eff}} \ , \tag{300}$$

as in Eq. (294).

7.3 Frequency maps and diffusion maps

The application of high-order perturbation theory has been extensively used in beam physics [77, 78] in order to give some insight regarding the systems' non-linear dynamics. However, the construction of some optimal set of variables (normal forms or action-angle) for the evaluation of the phase space distortion cannot be applied in the parts of the phase space which are close to instabilities, such as resonances or chaotic regions. In fact, an approach giving in a direct way a global view of the phase space structure is needed. This later can be achieved by the Frequency Map Analysis (F.M.A), a method extensively used in celestial mechanics [79, 80] and in Hamiltonian toy models [81, 82, 83] but only recently in real accelerators, as the ALS [84] or the LHC [86]. The method relies on the high precision calculation [85] of another fixed feature of KAM orbits, the associated frequencies of motion and can be directly applied in short term tracking data. Moreover, the variation of the frequencies over time [82, 83, 86] can provide an early stability indicator as good as, if not better than, the Lyapounov exponent.

The first step is to derive through the NAFF algorithm [79] or variants of this code, a quasi-periodic approximation, truncated to order N,

$$f'_j(t) = \sum_{k=1}^{N} a_{j,k} e^{i\omega_{jk} t} , \tag{301}$$

with $f'_j(t), a_{j,k} \in \mathbb{C}$ and $j = 1, \ldots, n$, of a complex function $f_j(t) = q_j(t) + ip_j(t)$, formed by a pair of conjugate variables of a n degrees of freedom Hamiltonian system, which are determined by usual numerical integration, for a finite time span $t = \tau$. The next step is to retain from the quasi-periodic approximation the frequency vector $\boldsymbol{\nu} = (\nu_1, \nu_2, \ldots, \nu_n)$ which, up to numerical accuracy [85], parameterizes the KAM tori in the stable regions of a non-degenerate Hamiltonian system. Then, the construction of the frequency map can take place [81, 82, 83, 84], by repeating the procedure for a set of initial conditions which are transversal to the orbits of interest. As an example, we may keep all the $\boldsymbol{q}$ variables constant, and explore the momenta $\boldsymbol{p}$ to produce the map $\mathcal{F}_\tau$:

$$\mathcal{F}_\tau \ : \begin{array}{ccc} \mathbb{R}^n & \longrightarrow & \mathbb{R}^n \\ \boldsymbol{p}|_{\boldsymbol{q}=\boldsymbol{q}_0} & \longrightarrow & \boldsymbol{\nu} \ . \end{array} \tag{302}$$

The dynamics of the system is then analyzed by studying the regularity of this map.

The F.M.A is applied to the tracking data ($\tau = 500$ turns), for a large number of initial conditions ($\approx 10^4$). We select an arbitrary section of the phase space, setting the initial transverse momenta to zero. The particle coordinates are chosen equally spaced in the transverse linear Courant-Snyder invariants I_{x0} and I_{y0}, at different ratios I_{x0}/I_{y0}. Hence, we construct the map

$$\mathcal{F}_\tau \ : \begin{array}{ccc} \mathbb{R}^2 & \longrightarrow & \mathbb{R}^2 \\ (I_x, I_y)|_{p_x,p_y=0}, & \longrightarrow & (\nu_x, \nu_y) \end{array} , \tag{303}$$

and proceed to the dynamical analysis of the accelerator model.

To give an example, in Figures 59, we display frequency maps [82, 86], for the working point (6.3,5.8) of the SNS accumulator ring. The maps are produced by injecting $\tilde{1}000$ particles with different amplitudes up to a maximum emittance of 480 π mm mrad and five different momentum spreads ($\delta p/p = 0, \pm 0.1, \pm 0.15$). Small field errors in the quadrupoles and dipoles were included, in the $10^{-}{-}4$ level. Finally, quadrupole fringe fields were simulated like "hard-edge" kicks at the entrance and the excite of the magnets.

The two maps correspond to two different cases: on the left the chromaticity sextupoles are switched off and the machine has its natural chromaticities $(\xi_x, \xi_y) = (-7.7, -6.4)$. Thus, there is a huge tune-spread of the order of 0.3 associated with of off-momentum particles motion. In addition, the quadrupole fringe-fields produce an "octupole-like" tune-shift linear with amplitude, which corresponds to the triangular shape of the foot-prints. This tune-shift pushes large amplitude off-momentum particles into dangerous resonances, as the structural coupling resonances in the middle of the plot $Q_x + Q_y = 12$. This resonance can be excited by linear coupling errors due to magnet tilts and misalignments [143]. Moreover this line corresponds to an octupole resonance of the type $2Q_x + 2Q_y = 24$ which can be excited by the quadrupole fringe-fields. The detrimental effect of this resonance is reflected in the irregularity of the map at bottom corner of the plot corresponding to particles with momentum spread of $\delta p/p = 0.15$. The map on the right corresponds to a case where the sextupoles are tuned in order to set the chromaticities to 0. As expected, the chromatic tune spread is eliminated.

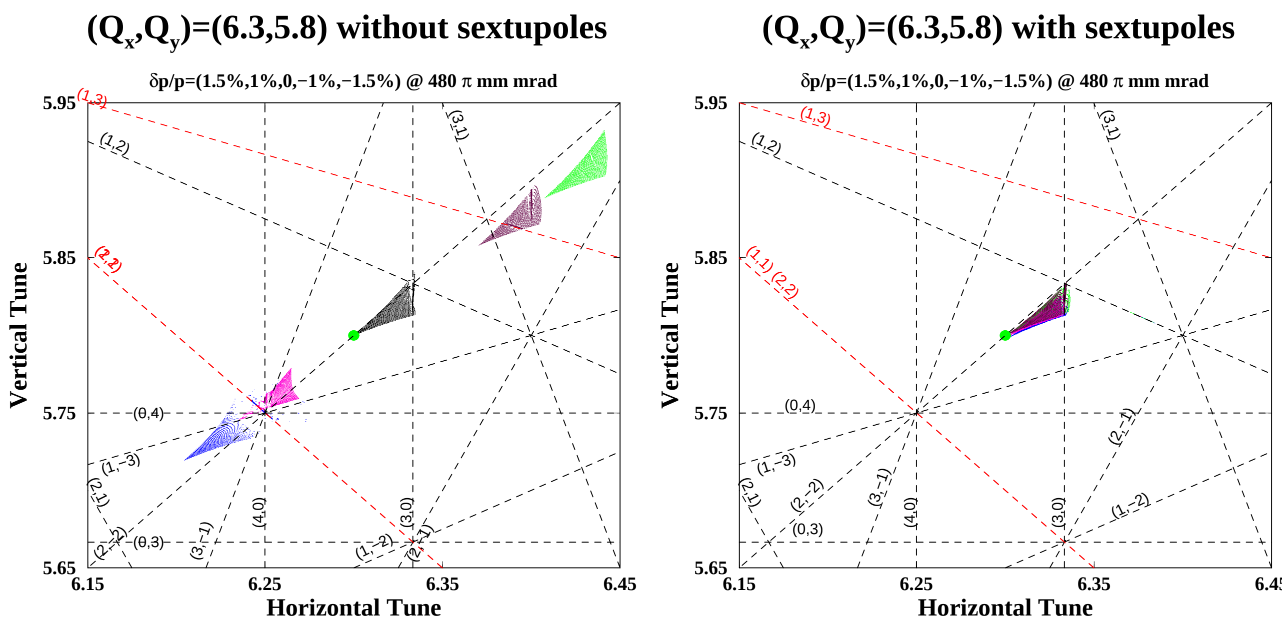

Figure 59: Frequency maps for the working point (6.3,5.8), without (left) and with (right) sextupoles.

The global dynamics of these two cases can be also displayed in the physical space of the system by mapping each initial condition with a diffusion indicator: the tune can be calculated for two equal and successive time spans which correspond to half of the total integration time τ, giving a diffusion vector:

$$\boldsymbol{D}|_{t=\tau} = \boldsymbol{\nu}|_{t\in(0,\tau/2]} - \boldsymbol{\nu}|_{t\in(\tau/2,\tau]} \ , \tag{304}$$

the amplitude of which can be used for characterizing the instability of each orbit. We can plot the points in the (I_{x0}, I_{y0})–space with a different color corresponding to different diffusion indicators in logarithmic scale: from grey for stable ($|\boldsymbol{D}| \leq 10^{-7}$) to black for strongly chaotic particles ($|\boldsymbol{D}| > 10^{-2}$). Through this representation we are able to view the traces of the resonances in the physical space, and set a pessimistic threshold for the minimum D.A.. Moreover, we can compute a diffusion quality factor defined as the average of the local diffusion coefficient to the initial amplitude of each orbit, over a domain R of the phase space:

$$D_{QF} = \langle \ \frac{|\boldsymbol{D}|}{(I_{x0}^2 + I_{y0}^2)^{1/2}} \ \rangle_R \ . \tag{305}$$

This quantity can be used for the comparison of different designs and the optimization of the correction schemes proposed.

7.4 Transition Energy Crossing

Among existing rings where the beam has to cross transition energy (AGS, CERN PS, SPS, KEK PS, FNAL Booster, etc.), beam loss and emittance growth are often observed due to chromatic nonlinearity, self-field mismatch, and instabilities [30]. At CERN SPS, the injection energy is raised to avoid transition during intense single-bunch operation. Longitudinal head-tail instability caused by nonlinear momentum compaction further complicates injection near transition. At AGS, transition jump [31] using pulsed quadrupoles has been used to minimize beam loss at high intensity. The large lattice distortion introduced by the jump system prior to the crossing severely limits machine aperture. Efforts to correct the distortion with existing sextupoles have been partially successful (Figure 60) [32].

Newly designed rings usually avoid transition either by the choice of injection and extraction energy, or by lattice manipulation creating negative dispersion in the bends. For rings that must cross transition, an optically matched transition jump using multiple quadrupole families located at different values of dispersion is preferred [33].

During acceleration in a synchrotron, the longitudinal particle motion is non-adiabatic within a characteristic time $\pm T_c$ near transition energy γ_T,

$$T_c = \left(\frac{\pi E_s \beta_s^2 \gamma_T^3}{qeV|\cos\phi_s|\dot{\gamma} h \omega_s^2} \right)^{\frac{1}{3}} \tag{306}$$

where the subscript s denotes the synchronous value. Upon crossing, the synchronous phase (ϕ_s) typically needs to be shifted by $\pi - 2\phi_s$ in a time much shorter than T_c.

7.4.1 Linear equations of motion

With a normalized time $d\tau = kdt$, $k = qeV|\cos\phi_s|/2\pi h$, the longitudinal motion is described by a Hamiltonian [164] $H(\varphi, J; \tau) = \pm J/\beta_L$. The action-angle variables (φ, J) are related to the rf phase ϕ and $W \equiv -\Delta E/h\omega_s$ by

$$\begin{aligned} \Delta\phi &= \mp\sqrt{2J/\beta_L}(\sin\varphi + \alpha_L \cos\varphi) \\ W &= -\sqrt{2J\beta_L}\cos\varphi \end{aligned}$$

where the upper (or lower) sign is for below (or above) γ_T, $\alpha_L = -\beta_L'/2$, and $'$ denotes the derivative with respect to τ. The amplitude function β_L is given by

$$\frac{1}{2}\beta_L\beta_L'' - \frac{1}{4}\beta_L'^2 + K\beta_L^2 = 1, \ K = \frac{-2\pi h^3 \omega_s^2 \eta_0}{qeV\cos\phi_s E_s \beta_s^2}$$

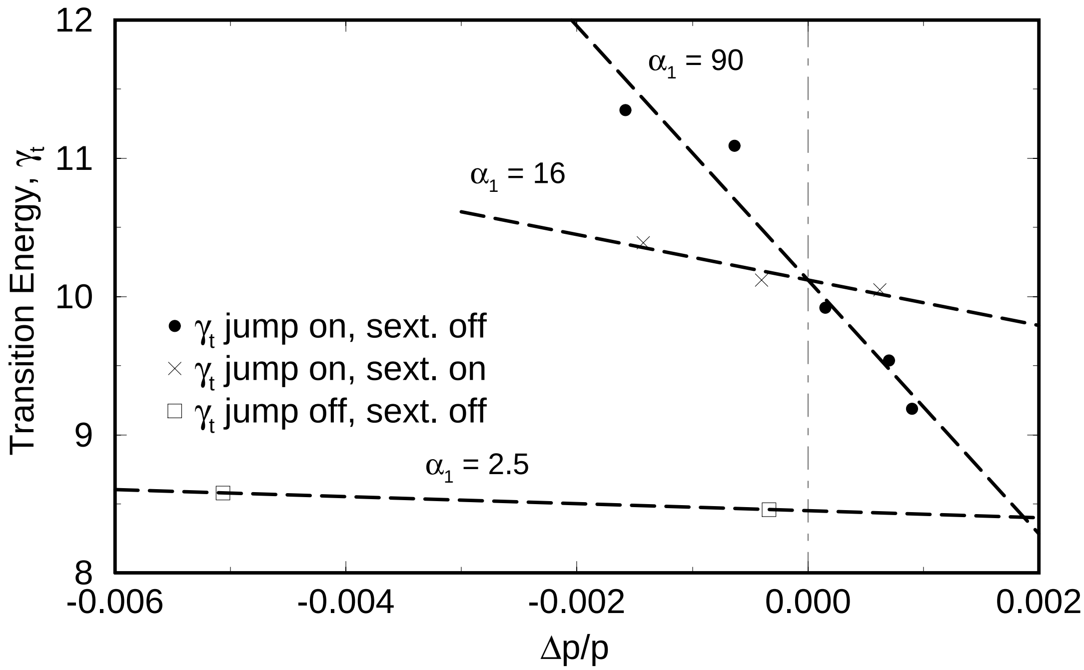

Figure 60: Measured transition energy as a function of the momentum deviation of the gold beam at AGS.

For a constant $\dot{\gamma}$ near transition,

$$\frac{\beta_L}{kT_c} = \frac{\pi}{3}x\left[\mathrm{J}^2_{-\frac{1}{3}}(y) + \mathrm{N}^2_{-\frac{1}{3}}(y)\right] \approx 1.58 - 1.15x$$

where $y = 2x^{3/2}/3$, $x = |\Delta t|/T_c$, and Δt is the time delay from γ_T. The synchrotron frequency is $\Omega_s = k\beta_L^{-1}$. The maximum excursions in ϕ and W are $\hat{\phi} = \sqrt{2\gamma_L J}$ and $\hat{W} = \sqrt{2\beta_L J}$, where $1 + \alpha_L^2 = \beta_L\gamma_L$. For a bunch of rms bunch area $S = 2\pi\langle J\rangle$, the rms phase and momentum deviations at γ_T are $\hat{\sigma}_\phi = 0.52\,(S/kT_c)^{1/2}$ and $\hat{\sigma}_\delta = 0.71h\omega_s\,(kT_cS)^{1/2}/E_s\beta_s^2$.

7.4.2 Single-particle effects

Single-particle effects include mismatching to the accelerating rf bucket, coupling to transverse motion, and various kinds of mis-timing in a time comparable to T_c.

Emittance growth due to chromatic nonlinearities (Johnsen effect) is given by

$$\frac{\Delta S}{S} \approx \begin{cases} 0.76\,\dfrac{T_{nl}}{T_c}, & \text{for } T_{nl} \ll T_c; \\ e^{\frac{4}{3}\left(\frac{T_{nl}}{T_c}\right)^{3/2}} - 1, & \text{for } T_{nl} \geq T_c, \end{cases}$$

where the total nonlinear time $\pm T_{nl}$ is given by

$$T_{nl} = \left|(\alpha_1 + \frac{3\beta_s^2}{2})\right| \frac{\sqrt{6}\hat{\sigma}_\delta\gamma_T}{\dot{\gamma}}$$

This effect was experimentally observed, and α_1 was obtained by measuring the synchrotron frequency or minimum-loss timing as a function of the beam radial position. Reducing the chromatic nonlinearity using sextupole families was proposed and demonstrated.

7.4.3 Umstätter effects

Transverse space-charge force changes the tune of each individual particle, making γ_T dependent on the azimuthal beam density. The amount of subsequent mismatch is inversely proportional to $\beta_s\gamma_s^2$, and usually negligible if γ_T is much higher than the injection energy.

7.4.4 Multi-particle mismatch

Emittance growth due to bunch mismatch under a reactive impedance $Z_\parallel$ at the bunch frequency is proportional to the ratio of the beam-induced force to the accelerating force,

$$\frac{\Delta S}{S} \approx \frac{h\hat{I}\,|Z_\parallel/n|}{3V|\cos\phi_s|\;\hat{\sigma}_\phi^2} \tag{307}$$

where $\hat{I}$ is the peak current at γ_T. Eq. 307 is valid exactly for a parabolic distribution under the space charge force.

A longitudinal resistive impedance $\mathcal{R}$ at bunch frequency causes energy dissipation, shifting the synchronous phase by $\Delta\phi_s \approx \hat{I}\mathcal{R}/V|\cos\phi_s|$ while producing a growth

$$\frac{\Delta S}{S} \approx \frac{\hat{I}\mathcal{R}}{\sqrt{6}V|\cos\phi_s|\ \hat{\sigma}_\phi}$$

The change in ϕ_s at transition can cause severe beam loading stress while the rf cavity tuning system changes the sign of the reactive beam loading compensation.

7.4.5 Instabilities

A capacitive (or inductive) longitudinal coupling impedance $Z_\parallel$ at a broad-band frequency will cause a microwave instability during a time $T_{mw} \approx 1.37\ (D_\parallel - 1)\ T_c$ after (or before) transition if

$$D_\parallel \approx \frac{4h\hat{I}\left|Z_\parallel/n\right|}{9V|\cos\phi_s|\ \hat{\sigma}_\phi^2} \geq 1 \tag{308}$$

Eq. 308 is valid exactly for a parabolic distribution under negative-mass instability above γ_T. A resistive longitudinal impedance may cause instability both below and above γ_T. Microwave instability near γ_T has been experimentally observed and simulated.

The transverse microwave instability threshold at γ_T is

$$D_\perp \approx \frac{1.5\hat{\sigma}_\delta\beta_Z}{b}D_\parallel \geq 1$$

where β_Z is the average β function at the impedance location, and b is the beam pipe radius.

When the beam stays near γ_T for a relatively long time, longitudinal head-tail and other slow-growing instabilities may also occur.

7.4.6 Simulations

Macro-particle method has been used to construct beam-induced forces in both the space and frequency domain. For a given numerical accuracy, the number of macro particles needed to simulate a reactive (or resistive) coupling is proportional to the cubic (or linear) power of the highest frequency considered.

7.4.7 Transition jump

A γ_T-jump has been demonstrated on many machines to improve crossing efficiency by effectively increasing the crossing rate. Without varying the tunes, a sudden change of γ_T is achieved by pulsing quadrupoles, often grouped in π-doublets, at locations of high dispersion. In order to minimize optical distortion and chromatic nonlinearity enhancement, "matched, first-order" schemes have been adopted for recently proposed accelerators incorporating two families of quadrupoles at regions of different dispersion. For a maximum allowable fractional growth of bunch area $G_S \equiv \Delta S/S$, the minimum size $\Delta\gamma_T$ and speed $|\dot{\gamma}_T|$ of γ_T jump is

$$\Delta\gamma_T > 2\dot{\gamma}T_{nl}, \quad \frac{|\dot{\gamma}-\dot{\gamma}_T|}{\dot{\gamma}} > \left(\frac{0.76}{G_S}\frac{T_{nl}}{T_c}\right)^{6/5}$$

to compensate for chromatic nonlinear effect,

$$\Delta\gamma_T > \frac{31E_s\beta_s^2 qeV\gamma_T^3}{h^{1/3}|\cos\phi_s|^{1/3}\omega_s^2 S^2}\left(\frac{\bar{I}\left|Z_\parallel/n\right|}{G_S V}\right)^{4/3}$$

$$\frac{|\dot{\gamma}-\dot{\gamma}_T|}{\dot{\gamma}} > \left(\frac{2hG_S\hat{I}\left|Z_\parallel/n\right|}{V|\cos\phi_s|\ \hat{\phi}^2}\right)^2$$

for self-field mismatch, and

$$\Delta\gamma_T > \frac{46E_s\beta_s^2 qeV\gamma_T^3}{h^{1/3}|\cos\phi_s|^{1/3}\omega_s^2 S^2}\left(\frac{\bar{I}\left|Z_\parallel/n\right|}{V}\right)^{4/3}$$

$$\frac{|\dot{\gamma}-\dot{\gamma}_T|}{\dot{\gamma}} > \left(\frac{8h\hat{I}\left|Z_\parallel/n\right|}{3V|\cos\phi_s|\ \hat{\phi}^2}\right)^2$$

for microwave instability, where $\hat{I}$ and $\hat{\phi}$ are values in the absence of jump, $\bar{I}=N_0qe\omega_s/2\pi$.

7.4.8 Other compensation methods

Other methods attempted or proposed include (a) minimizing the impedance at γ_T by adding reactive loading (b) rf system feedback (c) avoiding phase jump by continuously varying V and ϕ_s (d) rf manipulation to eliminate bunch-length oscillation (e) artificial blow-up of the longitudinal emittance (f) reducing rf voltage to alleviate chromatic effects (g) temporarily changing the orbit circumference using programmed V and ϕ_s (h) using a flattened rf wave to reduce $\hat{\sigma}_\delta$ and $\hat{I}$ and to provide equal acceleration for all the particles near γ_T.

Methods to avoid transition include (a) raising injection energy (b) reducing γ_T along with transverse tunes (c) creating a large or imaginary γ_T by using negative bends (d) creating a large or imaginary γ_T by using π-straight sections at small or negative dispersion

7.4.9 Applications

Operating storage rings under a quasi-isochronous condition (very small α_0) has been proposed to achieve very short bunches for free electron drivers, synchrotron light sources, next generation e^+e^- colliders, and muon colliders. These designs require both an accurate control of α_1 to provide the necessary momentum acceptance ($\sim \alpha_1^{-1}$), and effective ways to damp instabilities. Obtaining short bunches by extracting near γ_T has also been proposed for a proton driver of muon collider.

7.5 Intra-Beam Scattering

During the last decade, many theories have been developed on the subject of intra-beam Coulomb scattering of the hadron beam. These theories assume that the particle distribution remains Gaussian in the six dimensional phase space. The rates of growth in the rms beam amplitude are expressed in complex integral forms.

Based on assumptions applicable to many circular accelerators, we simplify into analytical form the growth rates of a hadron beam under Coulomb intra-beam scattering (IBS). Because of the dispersion that correlates the horizontal closed orbit to the momentum, the scaling behavior of the growth rates are drastically different at energies low and high compared with the transition energy. At high energies, the rates are approximately independent of the energy. Asymptotically, the horizontal and longitudinal beam amplitudes are linearly related by the average dispersion. At low energies, the beam evolves such that the velocity distribution in the rest frame becomes isotropic in all the directions.

7.5.1 Beam growth rates

The growth of the particle beam under intra-beam scattering is usually described by the relative time derivatives of the rms horizontal betatron amplitude σ_x, vertical amplitude σ_y, and fractional momentum deviation σ_p, respectively. Assume that the scatterings mostly occur at small scattering angles, and that the particle distribution remains Gaussian in six dimensional phase space. When the particle motions in horizontal and vertical directions are not coupled, these rates are obtained at any location of the machine

$$\begin{bmatrix} \frac{1}{\sigma_p}\frac{d\sigma_p}{dt} \\ \frac{1}{\sigma_x}\frac{d\sigma_x}{dt} \\ \frac{1}{\sigma_y}\frac{d\sigma_y}{dt} \end{bmatrix} = \frac{A_0}{2}\int \sin\theta d\theta d\phi dz \exp(-Dz)\ln(1+C^4z^2) \begin{bmatrix} n_b(1-d^2)g_1 \\ \\ a^2g_2 + (d^2+\overline{d}^2)g_1 \\ \\ b^2g_3 \end{bmatrix}, \tag{309}$$

where

$$A_0 = \frac{cr_0^2NZ^4\beta_x\beta_y}{32\pi^2A^2\sigma_x^2\sigma_y^2\sigma_p\sigma_s\beta^3\gamma^4},\ r_0 = \frac{e^2}{m_0c^2},$$

$$d = \frac{D_p\sigma_p}{(\sigma_x^2+D_p^2\sigma_p^2)^{1/2}},\ \overline{d} = \frac{\overline{D}_pd}{D_p},\ \overline{D}_p = \alpha_xD_p + \beta_xD_p',$$

$$a = \frac{\beta_xd}{D_p\gamma},\ b = \frac{\beta_y\sigma_x}{\beta_x\sigma_y}a,$$

and

$$D = \cos^2\theta + b^2\sin^2\theta\sin^2\phi + (a\sin\theta\cos\phi - \overline{d}\cos\theta)^2,$$

$$C = 2\beta\sigma_p\left[\frac{\sigma_y(1-d^2)}{r_0}\right]^{1/2},$$

$$g_1 = 1 - 3\cos^2\theta,$$

$g_2 = \cos^2\theta - 2\sin^2\theta\cos^2\phi + \sin^2\theta\sin^2\phi + 6\overline{d}\cos\theta\sin\theta\cos\phi/a,$
$g_3 = \cos^2\theta + \sin^2\theta\cos^2\phi - 2\sin^2\theta\sin^2\phi.$

Here, the prime denotes the derivative with respect to the displacement along the circumference, D_p is the horizontal dispersion, $\alpha_{x,y}$ and $\beta_{x,y}$ are the Courant-Snyder parameters, γ is the Lorentz factor, n_b is equal to 1 if the beam is azimuthally bunched, and is equal to 2 if it is not. For bunched beams, σ_s is the rms bunch length and N is the number of particles per bunch; for un-bunched beams, N is the total number of particles and $\sigma_s = L/2\sqrt{\pi}$, where L is the circumference of the machine. The quantity $d < 1$ is the effective ratio between the longitudinal and horizontal total amplitude. The actual growth rates observed over a time long compared with the revolution period, are calculated by averaging Eq. 309 over the circumference. This averaging process is implicitly implied in almost all the following equations.

Eq. 309 can in many cases be simplified into analytical forms. Firstly, the quantity $\ln(1 + C^4z^2)$ in Eq. 309 has a weak dependence on the beam configuration. It can be substituted by a constant $2L_c$, where L_c is about 20. With this simplification, the integration over z can be performed. Secondly, we assume that the accelerator consists mostly of regular cells, so that the variation in $D_p/\beta_x^{1/2}$ is small along the circumference. Terms including $\overline{D_p}$ and $\overline{d}$ in Eq. 309 are thus negligible. Replacing $\sin^2\phi$ and $\cos^2\phi$ with their average value 1/2, Eq. 309 is further simplified by integrations over θ and ϕ

$$\begin{bmatrix} \frac{1}{\sigma_p}\frac{d\sigma_p}{dt} \\ \frac{1}{\sigma_x}\frac{d\sigma_x}{dt} \\ \frac{1}{\sigma_y}\frac{d\sigma_y}{dt} \end{bmatrix} = 4\pi A_0 L_c F(\chi) \begin{bmatrix} n_b(1-d^2) \\ -a^2/2 + d^2 \\ -b^2/2 \end{bmatrix} \tag{310}$$

where

$$\chi = (a^2 + b^2)/2 \geq 0. \tag{311}$$

As shown in Figure 61, the function

$$F(\chi) = \frac{-3 + (1+2\chi)I(\chi)}{1-\chi} \tag{312}$$

with the function

$$I(\chi) = \begin{cases} \frac{1}{\sqrt{\chi(\chi-1)}}\mathrm{Arth}\sqrt{\frac{\chi-1}{\chi}} & \chi \geq 1; \\ \frac{1}{\sqrt{\chi(1-\chi)}}\arctan\sqrt{\frac{1-\chi}{\chi}} & \chi < 1 \end{cases} \tag{313}$$

is a smooth function of χ. It is positive when $\chi < 1$, zero when $\chi = 1$, and negative when $\chi > 1$. $F(\chi)$ has the asymptotic expression

$$F(\chi) = \begin{cases} \frac{\pi}{2\sqrt{\chi}} & \chi \ll 1; \\ -\frac{\ln\chi}{\chi} & \chi \gg 1. \end{cases} \tag{314}$$

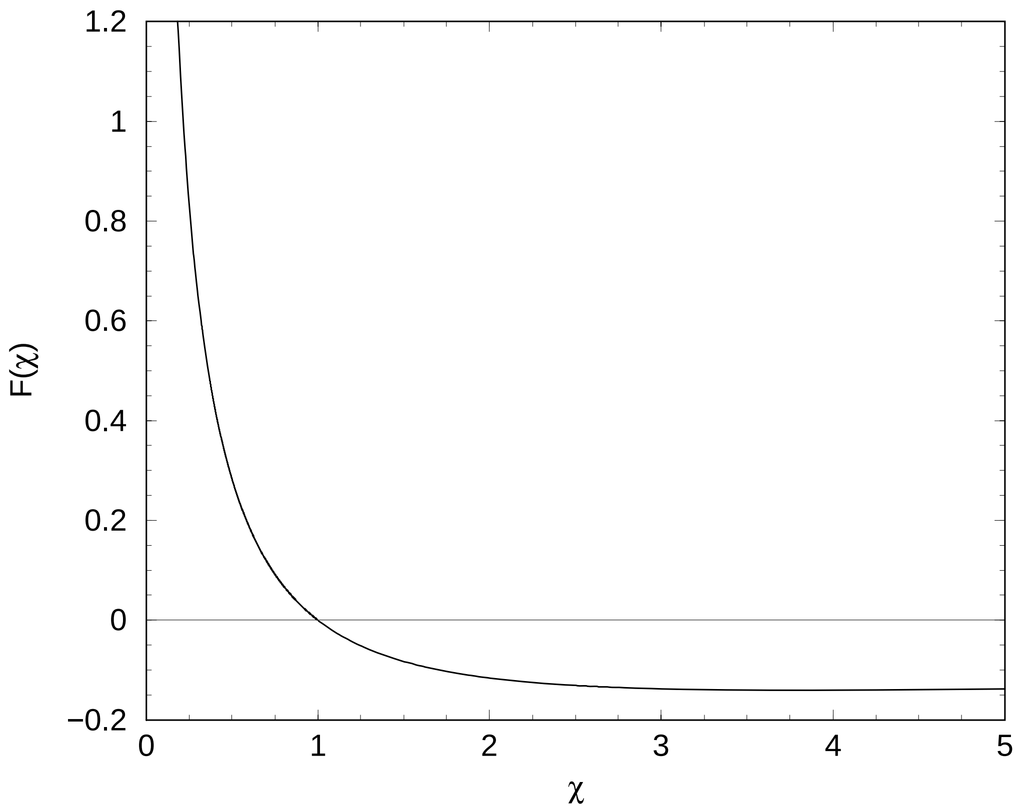

Figure 61: Function $F(\chi)$ with $0 \leq \chi < \infty$.

In terms of the normalized transverse emittance $\epsilon_{x,y} = \beta\gamma\sigma_{x,y}^2/\beta_{x,y}$ and longitudinal bunch area in phase space $S = \pi m_0 c^2 \beta\gamma\sigma_s\sigma_p/cA$, Eq. 310 can be rewritten

$$\begin{bmatrix} \frac{1}{\sigma_p}\frac{d\sigma_p}{dt} \\ \frac{1}{\sigma_x}\frac{d\sigma_x}{dt} \\ \frac{1}{\sigma_y}\frac{d\sigma_y}{dt} \end{bmatrix} = \frac{Z^4 N}{A^2}\frac{r_0^2 m_0 c^2 L_c}{8\gamma\epsilon_x\epsilon_y S} F(\chi) \begin{bmatrix} n_b(1-d^2) \\ -a^2/2 + d^2 \\ -b^2/2 \end{bmatrix} \tag{315}$$

The growth rates are shown to be linearly proportional to the number of the particle N in the beam, and are strongly dependent ($\sim Z^4/A^2$) on the charge state of the particle. Except for the form factors χ, d, a, and b that depend on the ratio of the beam amplitudes in different dimension, the rates are inversely proportional to the six dimensional phase space area.

The growths in the longitudinal and vertical amplitudes are both caused by the variation of the velocities in the corresponding direction. The growth in the horizontal amplitude, on the other hand, is caused partly from the variation in the horizontal velocity, and partly from the change in the betatron closed orbit when the momentum of the particle is varied during the collision. It can be easily verified that the first (or second) part dominates when the beam is below (or above) the transition energy of the machine.

The coupling between the horizontal and vertical motion averages the growth rates in the transverse dimension. If the motion is fully coupled within time periods much shorter than the IBS diffusion time, the average rates become

$$\begin{bmatrix} \frac{1}{\sigma_p}\frac{d\sigma_p}{dt} \\ \frac{1}{\sigma_{x,y}}\frac{d\sigma_{x,y}}{dt} \end{bmatrix} = \frac{Z^4 N}{A^2}\frac{r_0^2 m_0 c^2 L_c}{8\gamma\epsilon_x\epsilon_y S} F(\chi) \begin{bmatrix} n_b(1-d^2) \\ (-\chi + d^2)/2 \end{bmatrix} \tag{316}$$

7.5.2 Beam evolution at high energies

In a typically circular accelerator, the transition energy γ_T is approximately equal to the average value of β_x/D_p in the regular cells. When the beam energy is high compared with the transition energy, $\gamma \gg \gamma_T$, the growth in horizontal direction results mostly from the variation of the betatron orbit during the exchange of the particle momentum ($a^2 \ll d^2$). The growths in horizontal and longitudinal amplitudes are therefore proportional to each other (Eq. 310).

Consider the case that the vertical σ_y is very small, i.e. on the average

$$\frac{\sigma_y}{\sigma_y} < \frac{d}{2}\,\frac{\gamma_T}{\gamma}, \quad \gamma \gg \gamma_T \tag{317}$$

It may be verified that $\chi > 1$, and $F(\chi) < 0$. According to Eq. 310, both the horizontal and longitudinal amplitudes are damped, while the vertical one grows. The beam evolves until Eq. 317 is no longer satisfied.

When the vertical amplitude is no longer small so that $\chi < 1$, both horizontal and longitudinal amplitudes grow. Consider the effective ratio between the horizontal betatron amplitude and longitudinal amplitude

$$C_H \equiv \frac{n_b n_c \sigma_x^2}{D_p^2 \sigma_p^2} \tag{318}$$

where n_c is equal to 1 if the horizontal and vertical motions are not coupled, and is equal to 2 if they are fully coupled. Using Eq. 310, the rate of change of C_H can be derived on the average

$$\frac{dC_H}{dt} = 4\pi A_0 L_c d^2 C_H F(\chi)(1 - C_H). \tag{319}$$

This rate is positive if C_H is less than 1, and is negative if C_H is larger that 1. Therefore, the horizontal σ_x and longitudinal σ_p grow such that asymptotically the quantity C_H approaches 1, or

$$n_b n_c \sigma_x^2 \approx D_p^2 \sigma_p^2, \quad \gamma \gg \gamma_T \tag{320}$$

σ_x and σ_p are related only by the average dispersion D_p.

In a typical storage ring like the Relativistic Heavy Ion Collider (RHIC), the beams are stored at energies much higher than the transition energy. Due to coupling and injection condition, the horizontal and vertical betatron amplitudes are about the same. The growth rates can be explicitly written from Eq. 321 by using Eq. 314

$$\begin{bmatrix} \frac{1}{\sigma_p}\frac{d\sigma_p}{dt} \\ \frac{1}{\sigma_x}\frac{d\sigma_x}{dt} \end{bmatrix} = \frac{Z^4 N}{A^2}\frac{\pi r_0^2 m_0 c^2 L_c}{16\gamma_T \epsilon_x \epsilon_y S} \begin{bmatrix} n_b(1-d^2)/d \\ d/n_c \end{bmatrix} \tag{321}$$

Their dependence on the energy of the beam, which appears only in the form factor d, is usually weak. After the initial stage of storage, the asymptotic configuration Eq. 320 will be approximately reached.

7.5.3 Beam evolution at low energies

Beam evolution at energies much lower than the transition energy of the machine can be studied similarly. At low energies, $a^2 \gg d^2$, the growth in horizontal amplitude is mostly caused by the variation in the horizontal velocity alone. Eq. 310 indicates that the growths in horizontal and vertical amplitudes are proportional to each other.

Consider the case that the longitudinal σ_p is very small, i.e. on the average

$$\frac{D_p \sigma_p}{\sigma_x} < \frac{\gamma}{\gamma_T}\sqrt{\frac{2}{1+C_L}}, \quad \gamma \ll \gamma_T \tag{322}$$

where $C_L \equiv \beta_y^2 \sigma_x^2 / \beta_x^2 \sigma_y^2$ is the betatron amplitude ratio between horizontal and vertical directions. It may be verified that $\chi < 1$, and $F(\chi) > 0$. According to Eq. 310, both horizontal and vertical amplitudes are damped, while the longitudinal one grows. The beam evolves until Eq. 322 is no longer satisfied.

When the longitudinal amplitude is no longer small so that $\chi > 1$, both horizontal and vertical amplitudes grow. Using Eq. 310, the rate of change of C_L can be derived

$$\frac{dC_L}{dt} = -4\pi A_0 L_c a^2 C_L F(\chi)(1 - C_L) \tag{323}$$

This rate is positive if C_L is less than 1, and is negative if C_L is larger that 1. Therefore, the horizontal σ_x and vertical σ_y grow in such a way that asymptotically the quantity C_L approaches 1. Combining with Eq. 322 and the previous results, we therefore obtain the asymptotic beam configuration at low energies

$$\frac{\sigma_x}{\beta_x} \approx \frac{\sigma_y}{\beta_y} \approx \frac{\sigma_p}{\gamma}, \quad \gamma \ll \gamma_T. \tag{324}$$

The three quantities in Eq. 324 are proportional to the horizontal, vertical, and longitudinal velocities in the rest frame of the particles, respectively. Eq. 324 implies that the beam evolves such that the velocity distribution in the rest frame becomes isotropic in all the three directions.

7.5.4 Discussions

Based on assumptions applicable to many circular accelerators, we simplified the general integral expressions (Eq. 309) of the IBS growth rates into analytical forms (Eq. 310). The rates are expressed in terms of the beam charge state, mass, energy, phase-space area, and the machine transition energy, both for the un-coupled (Eq. 315) and fully coupled (Eq. 316) cases. They have been shown to be linearly proportional to the density of the particle in the six dimensional phase-space. Because of the dispersion that correlates the horizontal closed orbit to the momentum, the effect of intra-beam scattering are different at different energy regime. At energies much higher than the transition energy, the growth rates have been shown to be approximately independent of the energy except for the form factor d (Eq. 321).

Quantitative comparisons have been performed on the average growth rates between the simple estimate (Eq. 315) and the detailed evaluation (Eq. 309) including lattice variation using the actual RHIC lattice. For both the injection (low energy) and storage (high energy) cases, the relative deviation between them is about 20%.

The evolution of the beam in different dimensions has been investigated at energies both much higher and much lower then the transition energy. At high energies, the asymptotic horizontal and longitudinal beam amplitudes are shown to be linearly related by the average dispersion (Eq. 320). At low energies, on the other hand, the beam evolves such that the velocity distribution in the rest frame becomes isotropic in horizontal, vertical, and longitudinal directions (Eq. 324). At intermediate energies, the evolution has to be evaluated directly from Eq. 310.

During the entire analysis it has been assumed that the beam distribution remains Gaussian in the phase space. This assumption is valid only when the beam amplitudes are small compared with the aperture limitation. In the case that beam loss occurs due to aperture limitation, different approaches have to be adopted.

7.6 Electron-Cloud Effects

8 Appendices

8.1 List of Symbols

(needs re-work)

h	rf harmonic number
ω_s	angular revolution frequency
E_s	synchronous total energy
q	electric charge number
e	unit electric charge
$\hat{V}$	rf peak voltage
ϕ, ϕ_s	rf phase and rf synchronous phase
W	$\Delta E/h\omega_s$
E, ΔE	energy and energy deviation
δ	$\Delta p/p$ relative momentum deviation
p, Δp	momentum and momentum deviation
β_s	synchronous velocity in units of c
$U_{Z_\parallel}$, U_{rad}	changes in W due to impedance and radiation
η	frequency-slip factor
$\Delta\phi_{rf}$	shift in rf phase
B_s	strength of magnetic guide field
γ_s	synchronous energy in units of unit atomic mass
R_s	synchronous radius of the closed orbit
α_0, α_1, α_2, α_3	momentum-compaction factors
η_0, η_1, η_2, η_3	series expansion of η

γ_T	transition energy
$\mathcal{H}$, $\mathcal{H}_0$	Hamiltonian, and in small amplitude
$\Delta\phi$	rf phase deviation
Ω_s	synchrotron-oscillation frequency
t	time
A_B	bucket area
$\kappa(\phi_s)$	bucket-area factor
J, φ	action and angle variables
τ	reduced time
β_L, $\hat{\beta}_L$	longitudinal amplitude function, and the normalized
$\mathcal{K}$, H	reduced Hamiltonian, and the transformed
$\dot{\gamma}_s$	acceleration rate
T_c	characteristic non-adiabatic time
x	$\lvert t\rvert/T_c$
N_0	number of particles of the bunch
Ψ	particle distribution function
Ψ_H	particle equilibrium distribution
Ψ_J	distribution of action contours
Ψ_1	density perturbation
$\mathcal{H}_1$, H_1	Hamiltonian perturbation, and the transformed
$\hat{\phi}_0$, $\hat{W}_0$	phase spread and W spread
$2\pi J_0$	area enclosed by boundary contour
$Z_{\parallel}$	longitudinal coupling impedance
I, $\tilde{I}$	beam current and its Fourier transform
λ	particle density in rf phase
J_s	the Bessel function of sth order
b, a	vacuum-chamber aperture and beam radius
$\mathcal{E}_s$	azimuthal component of electric field

L	inductance
g_0	geometric factor
ε_0	electric permittivity
c	speed of light
Z_0	$(\varepsilon_0 c)^{-1} = 377$ (ohms)
$\alpha_{\phi\phi}$, $\alpha_{\phi W}$, α_{WW}	contour parameters
N_t	number of sampling particles
N_b	number of bins per 2π rf phase
l_b; l_{b1}, l_{b2}	bin length; lengths of fine and coarse bins
$\Delta\phi_b$	bin length in rf phase
s	relative distance from the bin center
$\mathrm{Sgn}(Z)$	1 for capacitive and -1 for inductive Z
U_{sc}, U_w, U_{bb}, U_R	change in W due to various kinds of impedances
$\mathcal{R}$	wall resistance
ω_c	cutoff frequency
$\mathcal{A}$	longitudinal bunch area
T_{nl}	chromatic non-linear time
ϵ_3, ϵ_4	third and fourth order non-linearity factor
ϵ_Z, ϵ_R	reactive and resistive coupling factor
*	modification due to coupling
$\hat{\lambda}$,	peak density
$\hat{\delta}$, $\hat{\varepsilon}$	relative momentum and energy spreads
$\bar{I}$	$N_0 qe\omega_s/2\pi$, average current
$\hat{I}$	peak current
T_{mw}	microwave instability growth time
D	dimensionless bunch configuration quantity
$\dot{B}_s$	magnetic-field ramping rate
γ_F	final energy for computer tracking

8.2 Acknowledgments

We thank many colleagues for information and discussion, especially D. Abell, R. Baartman, J. Beebe-Wang, M. Blaskiewicz, N. Catalan-Lasheras, Y. Cho, R. Gluckstern, R. Cappi, M. Chanel, W. Chou, V. Danilov, C. Gardner, I. Gardner, R. Garoby, I. Hofmann, J. Holmes, Y. Irie, S. Ivanov, Y.Y. Lee, T. Linnecar, R. Macek, S. Machida, N. Malitsky, Y. Mori, C. Prior, D. Raparia, G. Rees, T. Roser, H. Schonauer, E. Shaposhnikova, K. Takayama, R. Talman, N. Tsoupas, R. Webber, W. Weng, B. Zotter and the SNS team.

References

[1] E. M. McMillan, *Synchrotron a proposed high energy accelerator*, Phys. Rev. Lett., **68** (1945), 1434; V. Veksler, J. of Phys., USSR, **9** (1945), 153.

[2] E.D. Courant, M.S. Livingston, and H.S. Snyder, *The Strong-Focusing Synchrotron – A New High Energy Accelerator*, Phys. Rev. **88** (1952), 1190; N.C. Christofilos (unpublished, 1950).

[3] *Particle Accelerators*, M.S. Livingston, J.P. Blewett, McGraw-Hill (1962).

[4] *Handbook of Accelerator Physics and Engineering: a Compilation of Formulae and data*, edited by A. Chao and M. Tigner , World Scientific (1998).

[5] I.M. Kapchinskii, V.A. Teplyakov, Pribory i Teknika Eksperimenta **119** (1970), 19.

[6] 7th ICFA Workshop on Beam Halo and Scraping, edited by N. Mokhov and W. Chou, Wisconsin (1999).

[7] R. Macek, Workshop on Two-Stream Instab., Sante Fe (1999).

[8] J. Wei, D.T. Abell, J. Beebe-Wang, M. Blaskiewicz, P.R. Cameron, N. Catalan-Lasheras, G. Danby, A.V. Fedotov, C. Gardner, J. Jackson, Y.Y. Lee, H. Ludewig, N. Malitsky, W. Meng, Y. Papaphilippou, D. Raparia, N. Tsoupas, W.T. Weng, R.L. Witkover, S.Y. Zhang, Physical Review Special Topic AB, Vol. 3, 080101, (2000); SNS/BNL Tech. note 66 (1999) and 76 (2000), Brookhaven National Laboratory.

[9] JHF Design Manual; S. Machida, private communications.

[10] Y. Cho, Y.-C. Chae, H. Friedsam, D. Horan, R. Kustom, E. Lessner, W. McDowell, D. McGhee, H. Moe, R. Nielsen, G. Norek, K. Peterson, K. Thomson and M. White, in *Proceedings of the 1996 European Particle Accelerator Conference, Sitges, Spain, 1996*, edited by R. Pascual, p. 521.

[11] *Spallation Neutron Source: Description of Accelerator and Target*, RAL Report RL 82-006, ed. B. Boardman (1982); European Spallation Source Study, ESS-96-53-M (1996).

[12] N. Catalan-Lasheras, Y.Y. Lee, H. Ludewig, N. Simos, J.Wei, in *Proceedings of the 2000 European Particle Accelerator Conference, Vienna, Austria, 2000*, p 924.

[13] R. Nawrocky, U. Bergmann, and D.P. Siddons, *A Bunch Killer for the NSLS X-Ray Electron Storage Ring*, in *Proceedings of the 1993 Particle Accelerator Conference, Washington D.C., 1993*, p.2145; R.L. Witkover, P.R. Cameron, T.J. Shea, R.C. Connolly, M. Kesselman, in *Proceedings of the 1999 Particle Accelerator Conference, New York, 1999*, edited by A. Luccio and W. MacKay, p. 2250. C. Montag, J. Klute, in *Proceedings of the 2000 European Particle Accelerator Conference, Vienna, Austria, 2000* (to be published).

[14] G. Rees, in *Proceedings of the 1994 European Particle Accelerator Conference, London, 1994*, p.241; [4] p.497

[15] G. Rees [4] p. 497; C. Prior, G. Rees, 12th HIF sym. (1997)

[16] J. Beebe-Wang, Y. Y. Lee, D. Raparia, and J. Wei C. R. Prior,S. Machida, in *Proceedings of the 2000 European Particle Accelerator Conference, Vienna, Austria, 2000*, p. 1465; J. Galambos, S. Danilov, D. Jeon, J. A. Holmes, D. K. Olsen, F. Neri and M. Plum, Physical Review Special Topic AB, Vol. 3, 034201, (2000)

[17] W. Chou; E. Shaposhnikova, CERN ICFA Workshop (2000)

[18] Y. Suzuki, I. Yamane, Workshop on Injection and Extraction, Abingdon (1999)

[19] A. Fedotov, D. T. Abell, Y. Y. Lee, N. Malitsky, Y. Papaphilippou, J. Wei, in *Proceedings of the 2000 European Particle Accelerator Conference, Vienna, Austria, 2000*, p.1492.

[20] T. Roser, ICFA Newsletter **20** (1999); M. Yoshii, CERN ICFA Workshop (2000)

[21] Y. Mori, ICFA Newsletter **21** (2000); C. Ohmori, E. Ezura, M. Fujieda, Y. Mori, R. Muramatsu, H. Nakayama, Y. Sato, A. Takagi, M. Toda, T. Uesugi, M. Yamamoto, M. Yoshii, M. Kanazawa, K. Noda,, in *Proceedings of the 1999 Particle Accelerator Conference, New York, 1999*, p.413

[22] *TRIUMF Kaon Factory Definition Study* (1990)

[23] J. Wei, J. Beebe-Wang, M. Blaskiewicz, M. Brennan, P. Cameron, N. Catalan-Lasheras, G. Danby, C. Gardner, H.C. Hseuh, J. Jackson, Y.Y. Lee, A.U. Luccio, H. Ludewig, N. Malitsky, W. Meng, D. Raparia, A. Soukas, N. Tsoupas, J. Tuozzolo, R. Witkover, A. Zaltsman, S. Y. Zhang, S. Danilov, J.D. Galambos, J.G. Wang, G.H. Rees, *Low-Loss Rapid-Cycling-Synchrotron Design for the Spallation Neutron Source*, in *Proceedings of the 2000 European Particle Accelerator Conference, Vienna, Austria, 2000*, p. 981.

[24] N. Tsoupas C. J. Gardner, Y. Y. Lee, Y. Papaphilippou, J. Wei, in *Proceedings of the 2000 European Particle Accelerator Conference, Vienna, Austria, 2000*, p. 1581.

[25] G. Danby, J. Jackson, C. Spataro, in *Proceedings of the 1999 Particle Accelerator Conference, New York, 1999*, p.3333

[26] J. Wei, R. Talman, *Theorem on Magnet Fringe Field*, Part. Accel. **55** (1996), 339; J. Wei, Y. Papaphilippou, R. Talman, *Scaling Law for the Impact of Magnet Fringe Fields*, in *Proceedings of the 2000 European Particle Accelerator Conference, Vienna, Austria, 2000*, p. 1092.

[27] Y. Papaphilippou and D. Abell, in *Proceedings of the 2000 European Particle Accelerator Conference, Vienna, Austria, 2000*, p. 1453.

[28] N. Tsoupas M. Blaskiewicz, Y. Y. Lee, J. L. Mi, A. Soukas, J. G. Wang, J. Wei, S. Y. Zhang, in *Proceedings of the 2000 European Particle Accelerator Conference, Vienna, Austria, 2000*, p. 2270.

[29] C. Gardner, G. Danby, J. W. Glenn, J. Jackson, A. Soukas, W. van Asselt, C. Whalen, Y. Shoji, in *Proceedings of the 1994 European Particle Accelerator Conference, London, 1994* p.979.

[30] K. Johnsen, CERN Symp. on High-Energy Acc., **1** (1956), 106; K. Takayama, D. Arakawa, J. Kishiro, K. Koba, M. Yoshii, Phys. Rev. Lett. **78** (1997), 871 J. Wei, *Longitudinal Dynamics of the Non-Adiabatic Regime in the Alternating-Gradient Synchrotrons*, Ph.D. dissertation, Stony Brook (1990).

[31] W. Hardt, D. Möhl, CERN ISR-300/GS/69-16 (1969); W.W. Lee, L.C. Teng, IEEE Trans. NS-18 (1971), p.1057.

[32] J. Wei, J.M. Brennan, L. Ahrens, M. Blaskiewicz, D-P. Deng, W.W. MacKay, S. Peggs, T. Satogata, D. Trbojevic, A. Warner, and W. Van Asselt, *Effects of Enhanced Chromatic Nonlinearity during the AGS γ_T Jump*, in *Proceedings of the 1995 Particle Accelerator Conference, Dallas, Texas, 1995*, p.3334.

[33] T. Risselada, CERN PS/90-15 (1990); S. Peggs, S. Tepikian, D. Trbojevic, in *Proceedings of the 1993 Particle Accelerator Conference, Washington, D.C., 1993* p.168.

[34] B. Zotter, Two-Stream Instab. Workshop, Sante Fe (1999).

[35] M. Blaskiewicz, in *Proceedings of the 2000 European Particle Accelerator Conference, Vienna, Austria, 2000*, p. 1110.

[36] W. Weng, in *Proceedings of the 1997 Particle Accelerator Conference, Vancouver, 1997*, p.42.

[37] ICFA Beam Dynamics Newsletter **21** (2000).

[38] H. Goldstein, *Classical Mechanics*, (Addison-Wesley, Reading Massachusetts, 1980).

[39] J.D. Jackson, *Classical Electrodynamics*, 3rd edition, (John Wiley and Sons, New York, 1999).

[40] B.W. Montague, 5th advanced CERN Accelerator School, Rhodes 1993, *CERN Yellow Report*, **95-06**, Vol.1 (1995).

[41] E.D. Courant and H.S. Snyder, Annals of Physics, 1, (1957).

[42] G. Floquet, *Ann. 'Ec. Norm.*, **1**, 13 (1883).

[43] J. Rossbach and P. Schmüser, 5th general CERN Accelerator School, Rhodes 1993, *CERN Yellow Report*, **94-01**, Vol.1 (1994).

[44] M. Linstead, *Astron. Nach.*, **103**, 211 (1882).

[45] H. Poincaré, *Les Méthodes Nouvelles de la Mechanique Celèste*, 3rd edition, (Gauthier-Villars, Paris, 1892).

[46] H. Von-Zeipel, *Ark. Astron. Mat. Fys.*, **11**, No. 1 (1916).

[47] A.J. Lichtenberg and M.A. Lieberman, *Rwegular and Chaotic Dynamics*, 2nd edition, (Springer-Verlag, New York, 1992).

[48] K. Meyer and L. Hall, *Introduction to Non-linear Dynamical Systems and the N-Body problem*, (Springer-Verlag, New York, 1992).

[49] A.J. Dragt and J. M. Finn, *J. Math. Phys.*, **17**, 2215 (1976).

[50] A. N. Kolmogorov, *Dokl. Akad. Nauk. SSSR*, **98**, 527 (1954).

[51] V. I. Arnold, *Soviet Math. Dokl.*, **3**, 136 (1962); J. Moser, *Nachr. Akad. Wiss. Götingen Math. Phys. K1*, 1 (1962).

[52] A. Schoch, "Theory of linear and non-linear perturbations of betatron oscillations in alternating gradient sychnotrons", *CERN Yellow Report*, **57-21** (1958).

[53] R. Hagedorn, *CERN Report*, **57-1, 57-14**, (1957).

[54] G. Guignard, *CERN Yellow Report*, **76-06** (1976).

[55] G. Guignard, *CERN Yellow Report*, **78-11** (1978).

[56] B.V. Chirikov, *Plasma Phys.*, **1**, 253 (1960); B.V. Chirikov, *Phys. Rep.*, **52**, 265 (1979)

[57] G. Contopoulos, *J. Math. Phys.*, **7**, 788 (1966);

[58] C.J. Gardner, Closed orbit distortion and correction in the four-fold symmetric NSNS ring, BNL/SNS Technical Note 31, 1997 (unpublished); C.J. Gardner, Closed orbit distortion and correction in the 248 SNS accumulator ring lattice, BNL/SNS Technical Note 82, 2000 (unpublished).

[59] S. Mashida and Y. Shoji, AIP Conf.Proc., **377**, 160-168, 1995.

[60] J. Holmes, *et al.*, to be presented in PAC'2001, Chicago, 2001.

[61] Y. Shoji and H. Sato, *Nucl. Instr. Meth. Phys. Res.*, **399**, 5-10, 1997.

[62] G. Ripken, DESY Internal Rept. R1-70/04 (1970).

[63] F. Méot, Particle Accelerators, **55**, 329 (1996).

[64] M. Berz, B. Erdélyi and K. Makino, Non-linear effects in muon accelerators, (preprint).

[65] K.G. Steffen, *High Energy Beam Optics* (Interscience, New York, 1965).

[66] K.L. Brown and R.V. Servranckx, First- and second-order charged particle optics, in *Proceedings on Physics of High Energy Particle Optics*, BNL/SUNY Summer School, 1983, edited by M. Month, P.F. Dahl and M. Dienes (American Institute of Physics Conference Proceedings No.127, New York, 1985), p. 62.

[67] C.J. Gardner, Three-dimensional field expansions in magnets: A primer, BNL/SNS Technical Note No.53, 1998 (unpublished).

[68] Vector Fields, Ltd, Oxford England.

[69] M. Venturini and A.J. Dragt, Nucl. Instrum. Methods **427**, 387 (1999).

[70] A.J. Dragt, D.R. Douglas, F. Neri, E. Forest, L.M. Healy, P. Schütt, J. van Zeijts, MARYLIE 3.0 User's Manual, University of Maryland, Physics Department Report, 1999 (unpublished).

[71] G.H. Hoffstätter and M. Berz, Phys.Rev E **54**, 5664 (1996).

[72] B. Erdélyi, M. Berz and M. Lindemann, Differential algebra based magnetic field computations and accurate field maps, (preprint).

[73] K. Makino and M. Berz, Nucl. Instrum. Methods **427**, 338 (1999).

[74] H.A. Enge, Deflecting magnets, in *Focusing of charged particles*, volume 2, edited by A. Septier (Academic Press, NY and London 1967).

[75] E. Forest, J. Milutinovic, Nucl.Inst. and Meth. A269, 474, 1988.

[76] E. Forest, *Beam Dynamics - A new attitude and framework*, Harwood Acad. Pub., Amsterdam, 1998.

[77] E. Forest, M. Berz, and J. Irwin, "Normal form methods for complicated periodic systems: a complete solution using differential algebra", *Part. Acc.*, **24**, 91-113, (1989).

[78] A. Bazzani, E. Todesco, G. Turchetti, and G. Servizi, "A normal form approach to the theory of nonlinear betatronic motion", *CERN Yellow Report*, **94-02** (1994).

[79] J. Laskar, Astron. Astroph. 198, 341, (1988).

[80] J. Laskar, Icarus 88, 266, (1990).

[81] J. Laskar, et al., Physica D 56, 253, (1992).

[82] J. Laskar, Physica D 67, 257 (1993).

[83] H.S. Dumas and J. Laskar, Phys. Rev. Let. 70, 2975, (1993).

[84] J. Laskar and D. Robin, Part. Acc. 54, 183, (1996).

[85] J. Laskar, NATO-ASI, S'Agaro, Spain, 1996.

[86] Y. Papaphilippou, PAC'99, New York, 1554, (1999).

[87] G.E. Lee-Whiting, Nucl.Inst. and Meth. 103, 117, 1972.

[88] I.S. Gradshteyn and I.M. Ryzhik, *Table of Integrals, Series, and Products*, Corrected and enlarged edition, (Academic Press Inc., San Diego, CA, 1980).

[89] M. Berz, B. Erdélyi and K. Makino, PRST-AB **3:124001** (2000).

[90] E. Forest, D. Robin, A. Zholents, M.Donald, R.Helm, J. Irwin and H. Moshammer, Sources of amplitude dependent tune shift in the PEP-II design and their compensation with octupoles, *Proceedings of the 4th European Particle Accelerator Conference*, London, 1994, edited by V. Suller and C. Petit-Jean-Genaz, (World Scientific, River Edge NJ 1994), p. 1033.

[91] F. Zimmermann, Tune shift with amplitude induced by quadrupole fringe fields, CERN-SL-2000-009 AP, 2000 (unpublished).

[92] F. Zimmermann, C. Johnstone, M. Berz, B. Erdélyi and K. Makino and W. Wan, Fringe fields and dynamic aperture in the FNAL muon storage ring, CERN-SL-2000-011, 2000 (unpublished).

[93] F. Zimmermann, Fringe fields, dynamic aperture and transverse depolarisation in the CERN muon storage ring, CERN-SL-2000-012 AP, 2000 (unpublished).

[94] M. Berz, B. Erdélyi and K. Makino, Towards accurate simulation of fringe field effects, (preprint).

[95] A.W. Chao, Physics of Collective Beam Instabilities in High Energy Accelerators (Wiley 1993).

[96] P.J. Bryant and K. Johnsen, The Principles of Circular Accelerators and Storage Rings (Cambridge University Press 1993).

[97] B. Zotter, Incoherent Q-shift of a flat, off-centered particle beam in an elliptical vacuum chamber, CERN 74-38 (July 1974).

[98] B. Zotter, Image fields of an off-center particle beam in an elliptic vacuum chamber, CERN 74-11 (February 1974).

[99] G. Guignard, CERN 77-10 (1977).

[100] M. Reiser, Theory and Design of Charged Particles Beams (Wiley 1994).

[101] R.C. Davidson, Physics of Nonneutral Plasmas (Addison-Wesley 1990).

[102] R.L. Gluckstern, A.V. Fedotov, S. Kurennoy, R. Ryne, Phys. Rev. E, V. 58, p. 4977 (1998).

[103] R.L. Gluckstern and A.V. Fedotov, Phys. Rev. ST AB, V. 2, 054201 (1999).

[104] The utility of rms approach was first demonstrated by P. Lapostolle for stationary distributions (CERN/ISR/D1/70-36); R.L. Gluckstern later showed that the rms version of KV equations remain valid for beam with axial symmetry (1970 Linac Conference, unpublished); these results were extended by F. Sacherer to distributions with elliptical symmetry (IEEE Trans. Nucl. Sci. NS-18, p. 1105, 1971).

[105] D.C. Morin, MURA Report 649 (Ph.D. thesis, University of Wisconsin, 1962).

[106] P. Lapostolle, Conf. on High Energy Acc. (Dubna, Russia, 1963), p. 1235.

[107] L. Smith, Conf. on High Energy Acc. (Dubna, Russia, 1963), p. 1232.

[108] F. Sacherer, Lawrence Rad. Lab Report UCRL-18454 (Ph.D. thesis, University of California, 1968).

[109] R.L. Gluckstern, Proceedings of LINAC'70 (Fermilab, Batavia, 1970), p. 811.

[110] I. Hofmann and K. Beckert, IEEE Trans. Nucl. Sci. NS-32 (PAC'85), p. 2264.

[111] S. Machida, Nucl. Inst. Meth. A309 (1991), p. 43; AIP Conf. Proceedings 448, (New York, 1998), p. 73.

[112] R. Baartman, AIP Conf. Proceedings 448, (New York, 1998), p. 56.

[113] A.V. Fedotov, R.L. Gluckstern and M. Venturini, ICFA Workshop (Wisconsin, USA, 1999), p. 27.

[114] M. Venturini and R.L. Gluckstern, Phys. Rev. ST AB, V. 3, 034203 (2000).

[115] I. Hofmann, Phys. Rev. E 57, p. 4713 (1998).

[116] J. Struckmeier et al., Part. Accel. 15, p. 47 (1984).

[117] J. Holmes et al., Proceedings of EPAC'00 (Vienna), p. 936 (2000).

[118] J. Holmes et al., to be presented at PAC'01 (Chicago, USA, 2001).

[119] A.G. Ruggiero, V.G. Vaccaro, CERN Report, CERN ISR-TH/68-33 (1968).

[120] E. Keil and W. Schnell, CERN Report TH-RF/69-48 (1969); V.K. Neil and A.M. Sessler, Rev. Sci. Instr. 36, p. 429 (1965).

[121] I. Hofmann and O. Boine-Frankenheim, AIP Conf. Proceedings 496 (BNL, Upton, New York), p.86 (1999)

[122] M. Blaskiewicz, Proceedings of PAC'99 (New York, USA), p. 1611 (1999).

[123] L.J. Laslett, V.K. Neil, A.M. Sessler, Rev. Sci. Instr. 36, p. 436 (1965); K. Hubner, V.G. Vaccaro, CERN Report, CERN ISR-TH/70-44 (1970).

[124] D. Boussard, CERN Lab II /RF/ Int 75-2 (1975); R.D. Ruth and J.M. Wang, IEEE Trans. Nucl. Sci., NS-28, 2405 (1981).

[125] D. Mohl, Particle Accel., V. 50, p. 177 (1995).

[126] Workshop on Instabilities of High Intensity Hadron Beams in Rings, AIP Conference Proceedings 496 (Upton, New York, 1999).

[127] R.L. Gluckstern and A.V. Fedotov, ICFA Workshop (Wisconsin, USA, 1999), p.22.

[128] S. Strasburg and R.C. Davidson, Phys. Rev. E, V. 61, p. 5753 (2000).

[129] J.A. Holmes et al., Phys. Rev. ST AB, Vol. 2, 114202 (1999).

[130] B.W. Montague, CERN Report 68-38 (1968).

[131] Y. Shoji and H. Sato, KEK Preprint 97-38 (1997).

[132] J. Wei et al., Phys. Rev. STAB, V. 3, 080101 (2000).

[133] A.V. Fedotov et al, "Effect of space charge on stability of beam distribution in the SNS", to be presented at PAC'01 (Chicago, USA, 2001).

[134] A.V. Fedotov, J. Holmes and R.L. Gluckstern, submitted for publication to Phys. Rev. ST AB (2001).

[135] R.W. Hockney, J.W. Eastwood, Computer Simulation Using Particles (Adam Hilger, New York) (1981).

[136] R. Ryne et al., Proceedings of LINAC'98 (Chicago, USA), p. 701 (1998).

[137] J. Galambos et al., ORBIT's User's Manual, SNS/ORNL/AP Technical Note 011 (1999).

[138] F.W. Jones, "Developments in the ACCSIM code", PAC'97, p.2597 (1997).

[139] A. Friedman et al., Phys. Fluids B, Plasma Physics 4, p. 2203 (1992).

[140] C. Prior, "The Multi-Particle Code Track 2D, A Guide for Users CLRC", Rutherford Appelton Lab, UK (1993).

[141] N. Malitsky and R. Talman, AIP Proceedings 391, p.337 (1996).

[142] N. Malitsky et al., Proceedings of PAC'99 (New York), p. 2713 (1999).

[143] A.V. Fedotov, N. Malitsky and J. Wei, BNL/SNS Technical Note 086 (2001).

[144] L. Schachinger and R. Talman, Particle Accel., Vol. 22, p.35 (1987).

[145] A.J. Dragt, D.R. Douglas, F. Neri, E. Forest, L.M. Healy, P. Schutt, and J. van Zeijts, MARYLIE 3.0 Users Manual, University of Maryland, Physics Department Report (1999).

[146] Y. Papaphilippou and D.T. Abell, Proceedings of EPAC 2000, Vienna, Austria, p. 1453 (2000).

[147] A.V. Fedotov, D.T. Abell, Y.Y. Lee, N. Malitsky, Y. Papaphilippou, and J. Wei, Proceedings of EPAC 2000, Vienna, Austria, p. 1492 (2000).

[148] A.V. Fedotov, D.T. Abell, J. Beebe-Wang, Y.Y. Lee, N. Malitsky, J. Wei, and R.L. Gluckstern, Proceedings of EPAC 2000, Vienna, Austria, p. 1289 (2000).

[149] J. Beebe-Wang, A.V. Fedotov, J. Wei, and S. Machida, Proceedings of EPAC 2000, Vienna, Austria, p. 1286 (2000); and references there in.

[150] A. Shishlo, private communications.

[151] S. Danilov and J. Holmes, SNS/ORNL, private communication.

[152] L.D. Landau, J. Phys. USSR, V. 10, p. 25 (1946).

[153] K.W. Robinson, Cambridge Electron Accel. Report CEAL-1010 (1964).

[154] K. Hubner, P. Strolin, V. Vaccaro and B. Zotter, CERN/ISR-RF-TH/70-2 (1970).

[155] M. Blaskiewicz, Phys. Rev. ST AB, V. 1, 044201 (1998).

[156] H.G. Hereward, CERN-71-15 (1971).

[157] H. Grunder and G. Lambertson, Proc. 8th Int. Conf. HEACC, p. 308 (1971).

[158] K.Y. Ng, "Physics of collective beam instabilities", US Particle Accelerator School (June 2000), Fermilab-Cont-00/142-T, 2000.

[159] D.H. Fitzgerald et al., Proceedings of PAC'99 (New York, 1999), p.518.

[160] D.T. Abell, Y.Y. Lee, W. Meng, Proceedings of EPAC'00 (Vienna, Austria, 2000), p. 2107.

[161] A.V. Fedotov, Y.Papaphilippou, J. Wei, and J. Holmes, BNL/SNS Technical Note 091 (2001).

[162] R.J. Damburg and V.V. Kolosov, "Rydberg States of Atoms and Molecules" (Cambridge University Press, 1983), pp. 31-71.

[163] N. Catalan-Lasheras et al., SNS/ORNL Tech. Note 07 (2001).

[164] J. Wei, *Longitudinal Dynamics of the Non-Adiabatic Regime on Alternating-Gradient Synchrotrons*, Ph.D. dissertation, Stony Brook (1990); rev. 1994